REPORT DOCUMENTATION PAGE

Form Approved
OMB No. 0704-0188

PLEASE DO NOT RETURN YOUR FORM TO THE ABOVE ORGANIZATION.

1. REPORT DATE *(DD-MM-YYYY)*	2. REPORT TYPE	3. DATES COVERED *(From - To)*
10/13/2010	Final	Sept. 2009 - Sept. 2010

4. TITLE AND SUBTITLE

Single-photon nonlinear optics in integrated hollow-core waveguides

5a. CONTRACT NUMBER

FA 9550-05-1-0432

5b. GRANT NUMBER

5c. PROGRAM ELEMENT NUMBER

6. AUTHOR(S)

~~Holger~~ Schmidt, Holger
Hawkins, Aaron R.
Wu, Bin
Hulbert, John F.

5d. PROJECT NUMBER

5e. TASK NUMBER

5f. WORK UNIT NUMBER

7. PERFORMING ORGANIZATION NAME(S) AND ADDRESS(ES)

UC Santa Cruz
1156 High St.
Santa Cruz, CA 95064

8. PERFORMING ORGANIZATION REPORT NUMBER

9. SPONSORING/MONITORING AGENCY NAME(S) AND ADDRESS(ES)

AFOSR
875 North Randolph St.
Suite 325, Rm 3112
Arlington, VA 22203

10. SPONSOR/MONITOR'S ACRONYM(S)

AFOSR

11. SPONSOR/MONITOR'S REPORT NUMBER(S)

12. DISTRIBUTION/AVAILABILITY STATEMENT

Approved for public release

13. SUPPLEMENTARY NOTES

14. ABSTRACT

In the course of this project, novel technology for building atomic vapor chips was developed. Hollow-core waveguides and alkali atom (Rb) vapor were combined for the first time in a self-contained platform. The chips were successfully used to demonstrate linear and nonlinear atomic spectroscopy, EIT and world-record slow light on a chip.

15. SUBJECT TERMS

16. SECURITY CLASSIFICATION OF:			17. LIMITATION OF ABSTRACT	18. NUMBER OF PAGES	19a. NAME OF RESPONSIBLE PERSON
a. REPORT	b. ABSTRACT	c. THIS PAGE			HOLGER SCHMIDT
			SAR		19b. TELEPHONE NUMBER *(Include area code)* 831 459-1482

Final report for contract FA9550-05-1-0432

Project title: Single-photon nonlinear optics in integrated hollow-core waveguides

PI: Holger Schmidt (UC Santa Cruz)

Co-PI: Aaron Hawkins (Brigham Young University, subcontract)

Project start: 07/01/05

A. Executive summary

The overarching goal of the project was to develop a brand new type of miniaturized rubidium (Rb) cells in integrated ARROW waveguides and to demonstrate their use for quantum interference effects such as EIT, slow light, and low-level quantum-optical devices.

The project was extraordinarily successful. We successfully demonstrated the first fully self-contained chip-scale atomic spectroscopy chip along with world record slow light on a photonic chip. These results have been disseminated in numerous publications and invited conference presentations (see below), most notably two seminal Nature Photonics articles and an invited review for Laser and Photonics Reviews. Our new technology is attracting growing interest from researchers and media across the globe and has large potential for future expansion and improvement.

Two student theses were completed in direct connection with this project. Both are attached here as appendices to provide further details on the methods and results developed under this grant:

(a) PhD thesis, Bin Wu (UCSC), Executive summary: A novel integrated optical device based on anti-resonant reflecting optical waveguide (ARROW) for atomic spectroscopy was proposed and demonstrated. A new type of hollow-core waveguide called self-aligned pedestal (SAP) waveguides with vastly improved performance developed. The first linear and nonlinear Rb spectroscopy on a photonic chip was demonstrated. The optical density is comparable with the commercially available Rb cell at higher temperatures. Electromagnetically induced transparency (EIT) and the first slow light experiment in atomic vapors on chip are reported. The group velocity of the light pulse was slowed down by a world-record factor of 1,200.

(b) M.S. thesis, Don Conkey (BYU), Executive summary: The integration of atomic vapor cells with anti-resonant reflecting optical waveguides (ARROWs) fabricated on silicon chips is presented. To demonstrate the effectiveness of the ARROW as a vapor cell, a platform consisting of solid and hollow core waveguides integrated with rubidium vapor cells was developed. A variety of sealing techniques were tested for vapor cell integration with the ARROW chip and for compatibility with rubidium. Liquefied rubidium was transferred from a bulk supply into an on-chip vapor cell in an anaerobic atmosphere glovebox. Optical absorption measurements confirmed the presence of rubidium vapor within the hollow waveguide platform. Further analysis of the measurements revealed high optical density of rubidium atoms in the hollow core. Saturated absorption spectroscopy measurements verified that the on-chip integrated vapor cell was suitable for common precision spectroscopy applications.

One senior undergraduate thesis was written (T. Vogt, UCSC, Dean's Award for Undergraduate Research). In addition, three more theses are currently being completed (John Hulbert, PhD, BYU; M. Oehlberg, MS, UCSC; Katie Hurd, MS, BYU). Furthermore, numerous other PhD thesis were informed by

this work or contain elements related to this project (Dongliang Yin, UCSC; Philip Measor, UCSC; Evan Lunt, BYU; John Barber, BYU).

People involved in project:

- Prof. Holger Schmidt (UCSC)
- Prof. Aaron Hawkins (BYU)
- Dr. Wenge Yang (UCSC)
- Dongliang Yin (UCSC)
- Philip Measor (UCSC)
- Bin Wu (UCSC)
- Mark Oehlberg (UCSC)
- Trevor Vogt (UCSC)
- John Hulbert (BYU)
- Evan Lunt (BYU)
- Katie Hurd (BYU)
- Don Conkey (BYU)
- John Barber (BYU)

Journal Publications:

[1] B. Wu, J.F. Hulbert, K. Hurd, E.J. Lunt, A.R. Hawkins, and H. Schmidt, “Slow light on a chip via atomic quantum state control.”, Nature Photonics **4**, 776 (2010).

[2] E.J. Lunt, B. Wu, J.M. Keeley, P. Measor, H. Schmidt, and A.R. Hawkins, “Improving Hollow ARROW Waveguides on Self-Aligned Pedestals for Improved Geometry and Transmission”, IEEE Phot. Tech. Lett. **22**, 1041 (2010).

[3] H. Schmidt and A.R. Hawkins, “Atomic Spectroscopy and Quantum Optics in Hollow-core Waveguides”, Laser and Photonics Reviews **4**, 720 (2010).

[4] B. Wu, J.F. Hulbert, A.R. Hawkins, and H. Schmidt, "Planar Hollow-core Waveguide Technology for Atomic Spectroscopy and Quantum Interference in Alkali Vapors", Journal of Lightwave Technology **26**, 3727-3733 (2008).

[5] B. Wu, J. Hulbert, A.R. Hawkins, and H. Schmidt, "Quantum interference effects in rubidium vapor on a chip", Proc. SPIE 6904, 69040E (2008).

[6] J.F. Hulbert, B.T. Carroll, A.R. Hawkins, B. Wu, and H. Schmidt, "Sealing techniques for on-chip atomic vapor cells", Proc. SPIE 6904, 69040N (2008).

[7] A.R. Hawkins, J.F. Hulbert, B.T. Carroll, B. Wu, and H. Schmidt, "Fabrication methods for compact atomic spectroscopy", Proc. SPIE 6898, 689817 (2008).

[8] W. Yang, D.B. Conkey, B. Wu, D. Yin, A.R. Hawkins, and H. Schmidt, "Atomic spectroscopy on a chip", Nature Photonics **1**, 331 (2007).

[9] H. Schmidt, W. Yang, B. Wu, D. Yin, D.B. Conkey, J. Hulbert, and A.R. Hawkins, "Rubidium spectroscopy on a chip", Proceedings of the SPIE, 6482:64820P (2007).

[10] A.R. Hawkins, E.J. Lunt, M.R. Holmes, B.S. Phillips, D. Yin, M. Rudenko, B. Wu, and H. Schmidt, "Advances in integrated hollow waveguides for on-chip sensors", Proceedings of the SPIE, 6462:64620U (2007).

[11] D.B. Conkey, R.L. Brenning, A.R. Hawkins, W. Yang, B. Wu, and H. Schmidt, "Microfabrication of Integrated Atomic Vapor Cells", Proceedings of the SPIE, 6475:647518 (2007).

[12] H. Schmidt, D. Yin, W. Yang, B. Wu, D.B. Conkey, J.P. Barber, and A.R. Hawkins, "Towards integration of quantum interference in alkali atoms on a chip", Proceedings of the SPIE, 6130:613006 (2006).

[13] J.P. Barber, E. Lunt, Z. George, D. Yin, H. Schmidt, and A.R. Hawkins, "Integrated Hollow Waveguides with Arch-shaped Cores", Photonics Technology Letters, **18**, 28 (2006).

[14] D. Yin, J.P. Barber, A.R. Hawkins, and H. Schmidt, "Waveguide loss optimization in hollow-core ARROW waveguides", Optics Express **13**, 9331 (2005).

Conference proceedings:

[1] H. Schmidt, “Slow light and EIT on a hollow-core waveguide spectroscopy chip”, **Invited talk**, 41st Winter Colloquium on the Physics of Quantum Electronics, Snowbird, UT, January 2-6 (2011).

[2] B. Wu. J. F. Hulbert, K. Hurd, A.R. Hawkins, and H. Schmidt, “Slow light and EIT in atomic spectroscopy chips”, **Invited talk**, Photonics West, San Jose, CA, January 22-27, 2011.

[3] E.J. Lunt, B.S. Phillips, J. Keeley, A.R. Hawkins, P. Measor, B. Wu, and H. Schmidt, "Hollow ARROW Waveguides on Self-Aligned Pedestals for High-Sensitivity Fluorescence Sensing", Photonics West, San Jose, CA, January 24-29, 2010.

[4] B. Wu, J. Hulbert, A.R. Hawkins, and H. Schmidt, "EIT in an integrated Rb vapor cell", OSA Summer Topical Meeting, Nonlinear Optics, Honolulu, HI, July 12-17, (2009).

[5] H. Schmidt, "Atomic spectroscopy on a chip using hollow-core waveguides", **Invited Talk**, Second Workshop on Integrated Atomic Systems (IAS), Seattle, WA, February 18-19, 2009.

[6] H. Schmidt, "Atomic spectroscopy and quantum interference on a chip", **Invited Talk**, 39th Winter Colloquium on the Physics of Quantum Electronics, Snowbird, UT, Jan 4-8, 2009.

[7] H. Schmidt, "Atomic spectroscopy and quantum interference in on-chip hollow-core waveguides", **Invited Talk**, 92st Annual Meeting of the OSA, Rochester, NY, Oct 19-23, 2008.

[8] A.R. Hawkins, J.F. Hulbert, B.T. Carroll, B. Wu, and H. Schmidt, "Fabrication methods for compact atomic spectroscopy", **Invited Talk**, Photonics West Conference, San Jose, CA, Jan 24, 2008.

[9] J.F. Hulbert, B.T. Carroll, A.R. Hawkins, B. Wu, and H. Schmidt, "Sealing techniques for on-chip atomic vapor cells", Photonics West Conference, San Jose, CA, Jan 22, 2008.

[10] H. Schmidt, B. Wu, J.F. Hulbert, and A.R. Hawkins, "Quantum interference effects in rubidium vapor on a chip", **Invited Talk**, Photonics West Conference, San Jose, CA, Jan 22, 2008.

[11] H. Schmidt, W.Yang, B. Wu, D. Conkey, J. Hulbert, A.R. Hawkins, "Saturation absorption spectroscopy in an integrated rubidium vapor cell", OSA Summer Topical Meeting: Nonlinear Optics, Kona HI, July 30 - Aug 3, 2007.

[12] H. Schmidt, "Integrated semiconductor chips for EIT", **Invited talk**, CLEO/QELS conference, Baltimore, MD, May 6-11, 2007.

[13] H. Schmidt, W. Yang, B. Wu, D. Yin, D.B. Conkey, J. Hulbert, and A.R. Hawkins, "Rubidium spectroscopy on a chip", **Invited talk**, Photonics West Conference, San Jose, CA, Jan 21-25, 2007.

[14] D.B. Conkey, R.L. Brenning, A.R. Hawkins, W. Yang, B. Wu, and H. Schmidt, "Microfabrication of Integrated Atomic Vapor Cells", Photonics West Conference, San Jose, CA, Jan 21-25, 2007.

[15] A.R. Hawkins, E.J. Lunt, M.R. Holmes, B.S. Phillips, D. Yin, M. Rudenko, B. Wu, H. Schmidt, "Advances in integrated hollow waveguides for on-chip sensors", **Invited talk**, Photonics West Conference, San Jose, CA, Jan 21-25, 2007.

[16] W. Yang, D. Yin, B. Wu, D.B. Conkey, E.J. Lunt, A.R. Hawkins, and H. Schmidt, "Monolithically integrated atomic vapor cell for quantum optics on a chip", Frontiers in Optics 2006/Laser Science XXII conferences, 90th Annual Meeting of the OSA, Rochester NY, October 8-12, 2006.

[17] H. Schmidt, D. Yin, W. Yang, B. Wu, D. Conkey, J. Barber, and A. Hawkins, "Towards integration of quantum interference in alkali atoms on a chip", Photonics West Conference, San Jose, CA, Jan 21-26, 2006.

[18] D. Yin, A.R. Hawkins, and H. Schmidt, "Design of Integrated Hollow-Core Waveguides for EIT on a Chip", Frontiers in Optics/Laser Science Conference, Optical Society of America, Tucson, AZ, October 16-20 (2005).

In the following pages, we summarize the work carried out in the areas of hollow-core waveguide design, fabrication, and spectroscopy.

B. Fabrication

B.1. Rubidium cell fabrication

A new technique for photonic rubidium cell fabrication was developed and successfully implemented on a silicon chip containing ARROW waveguides. The figure below shows the generic process flowchart for integrated rubidium vapor cells.

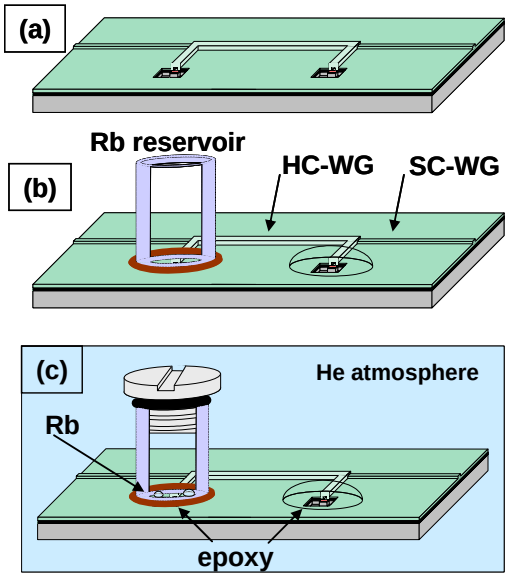

Rb cell fabrication flowchart

After building the hollow-core waveguides on a silicon wafer using a previously developed sacrificial core layer process, one of the open ends is sealed with epoxy while a reservoir is placed over the other. The

reservoir is subsequently placed into a glove box with an inert atmosphere and rubidium is added from an ampoule. Finally, the reservoir is sealed.

We have utilized different types of reservoirs and sealing methods, including glass, stainless steel, and copper. These types are shown in the figure below. The best results to date leading to the highest sample yields are achieved with the crimped copper reservoirs.

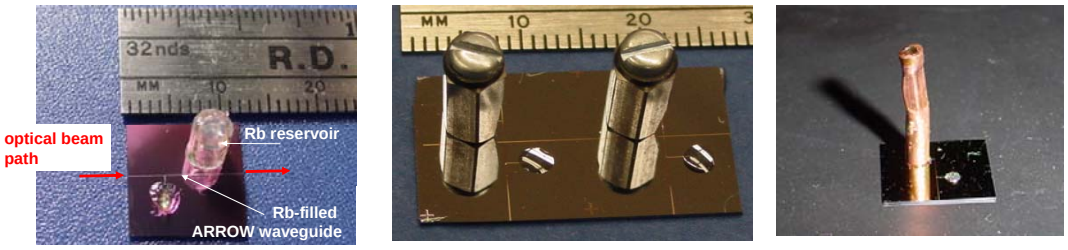

Different integrated Rb reservoirs on ARROW chip.

We successfully implemented the integration of rubidium vapor with hollow-core waveguides. In addition, we added the capability to evacuate the reservoirs to well-defined pressures in different atmospheres (nitrogen, helium). This is essential for buffer gas control in quantum coherence studies.

The figure below shows the example of a minicell made using a crimped copper seal. The figure on the left shows the crimping tool that produces an airtight seal. The center image shows a minicell filled with rubidium and sealed by a crimped copper stub. The image on the right shows the yield of functional minicells (absorption observed at room temperature) over different generations of sealing methods. With the sealed copper method, all minicells showed absorption.

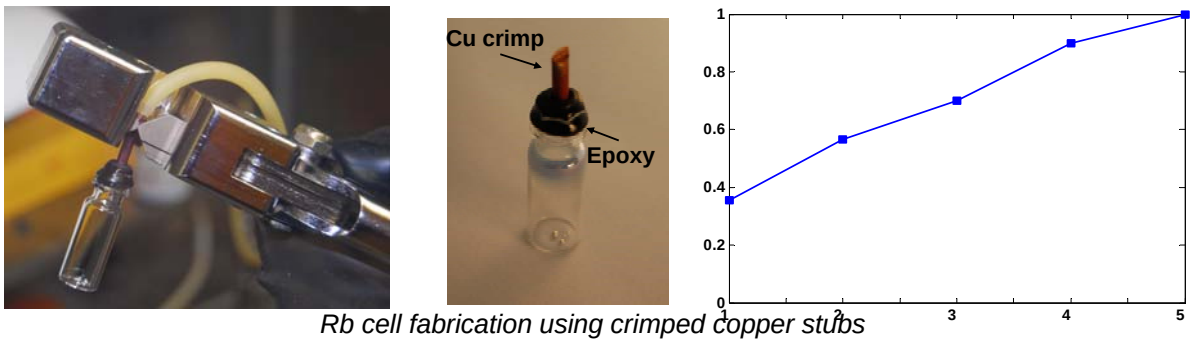

Rb cell fabrication using crimped copper stubs

In order to quantify the aging process of the rubidium seals, minicells made with Aremco 2310 epoxy were stored at 70, 80, and 90 ˚C to cause premature ageing. The devices failed after 11.6 days at 70 ˚C, 5.7 days at 80 ˚C, and 3.1 days at 90 ˚C. We defined device failure as a 50% drop in the Rb vapor density. A modified version of the Arrhenius equation was used to predict lifetime. By plotting the empirically gathered data from the accelerated lifetime tests, t being days to failure and T being the temperature, we can solve for the activation energy E_a as shown below. These results correspond with an E_a of 0.71 eV. These experiments predict a room temperature device lifetime of 1.2 years, but an increase of just 10 ˚C cuts that lifetime by 60 percent.

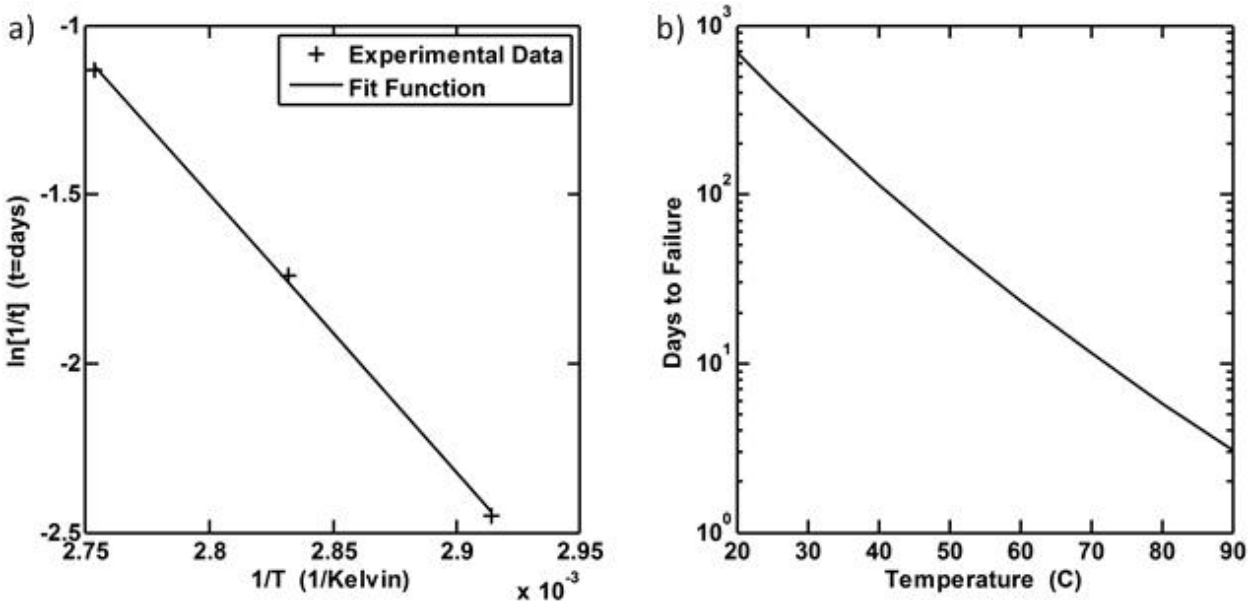

(a) Fitted Arrhenius equation to empirically gathered lifetime vs. temperature data. (b) Lifetime expectancy vs. temperature projection plot.

Subsequently, another promising approach was initiated with the goal of eliminating any epoxy in the sealing process since the epoxy seal seemed to limit the cell stability if the cell is subjected to repeated heating cycles. The figure on the left below shows a minicell that is soldered to the copper segment. The figure in the center shows that the atomic density in the cell is very repeatable over several heating cycles, returning back to its initial value at room temperature in contrast to epoxy-based versions. The plot on the right shows that this cell is able to maintain the density over more than a month despite the fact that it had been exposed to high temperatures for several times.

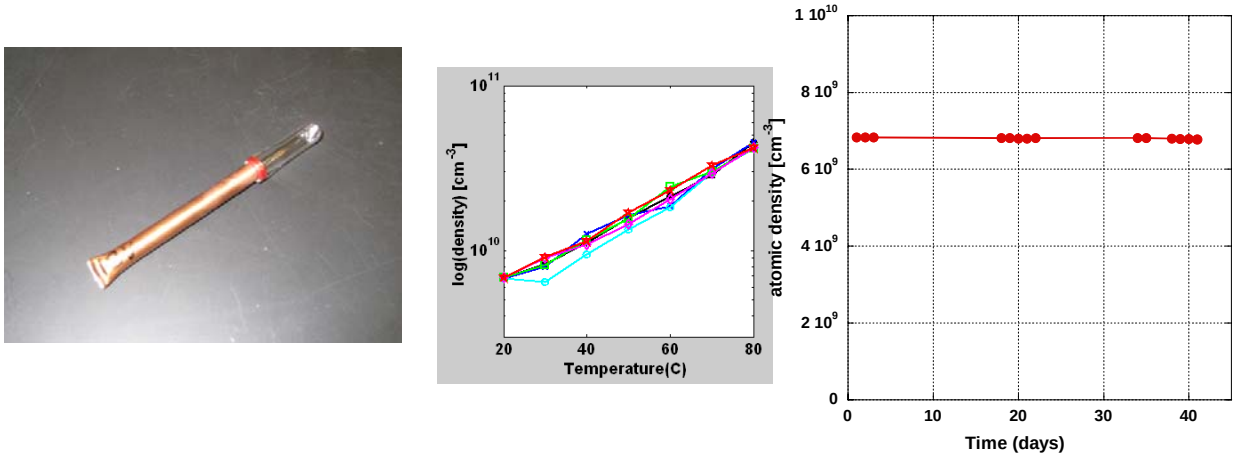

Epoxy-free Rb minicell and performance over repeated heating cycles.

An essential requirement for observing quantum interference effects on a chip is coating the waveguide walls with an organic layer that ameliorates coherence dephasing collisions. To this end, a process had to be developed that works with the integrated chip environment. The flowchart for this process is shown below along with an image of the completed chip with the two copper reservoirs after addition of an ODMS coating but before rubidium filling and sealing. This method was successfully used to create the slow light devices reported in 2010.

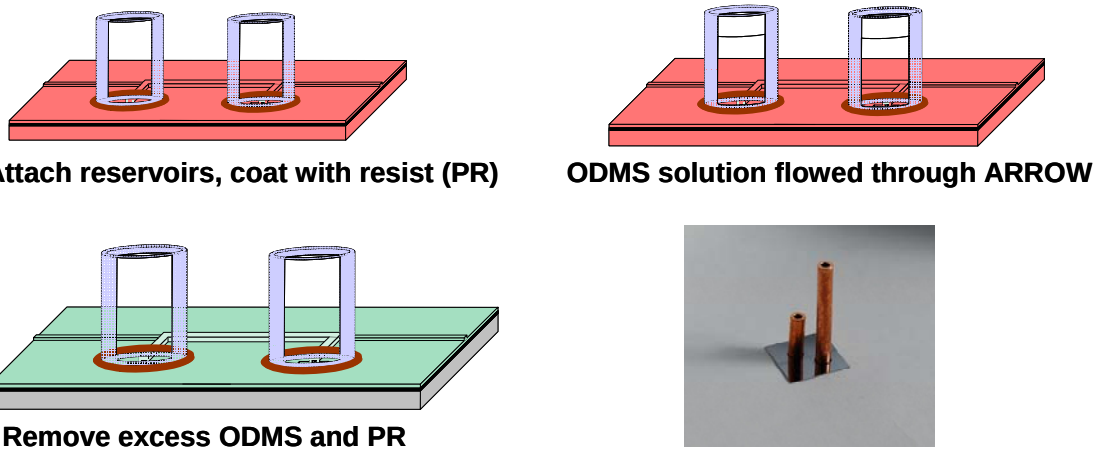

Fabrication flowchart for filling hollow-core waveguides with ODMS coating

C. Experiments and Spectroscopy

C.1. Novel hollow-core waveguides

The figure on the left below shows the impressive improvements in the EIT performance that can be expected simply by reducing the waveguide loss in the ARROW chip and thus increasing the available coupling power. Specifically, a reduction in waveguide loss from 10/cm to 1/cm could increase the measured EIT depth form ~10 to ~90 percent. We have shown a couple of years ago that lower loss is feasible by placing the hollow-core waveguides on top of a pedestal etched into the silicon substrate. The figure on the right displays the calculated loss spectra for two updated broadband waveguide designs that exhibit a low-loss region across both rubidium D-lines. Clearly, the spectrum shows that a pedestal design can lower the loss substantially while not affecting the available transmission bandwidth.

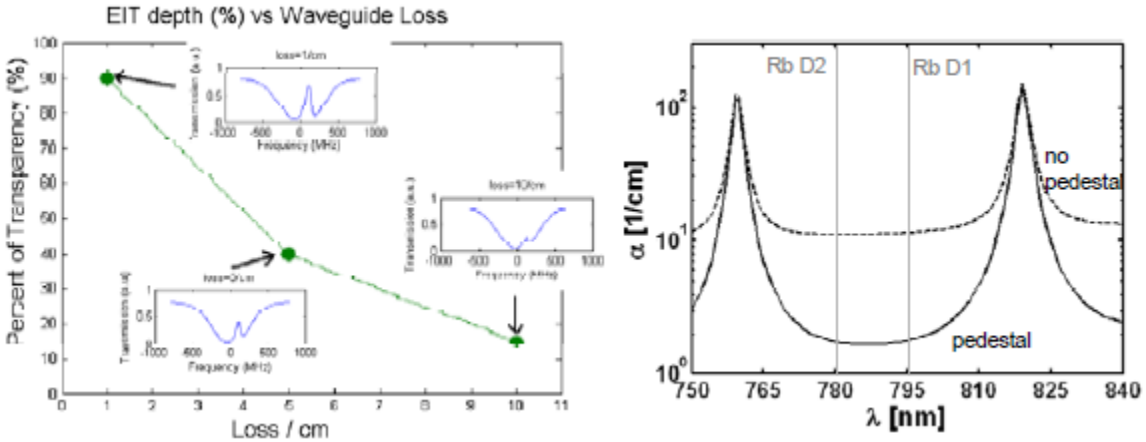

Left: Calculated EIT spectra and EIT dip depths for varying waveguide loss; right: calculated waveguide loss for two different broadband designs.

Up to now, we had not used pedestal waveguides for rubidium spectroscopy on a chip because these samples are more complex to fabricated and the pedestals showed large and varying nonidealities. The

emergence of “shoulders” due to the alignment of a hollow core on a wider pedestal is highlighted by the arrow in the figure on the left below.

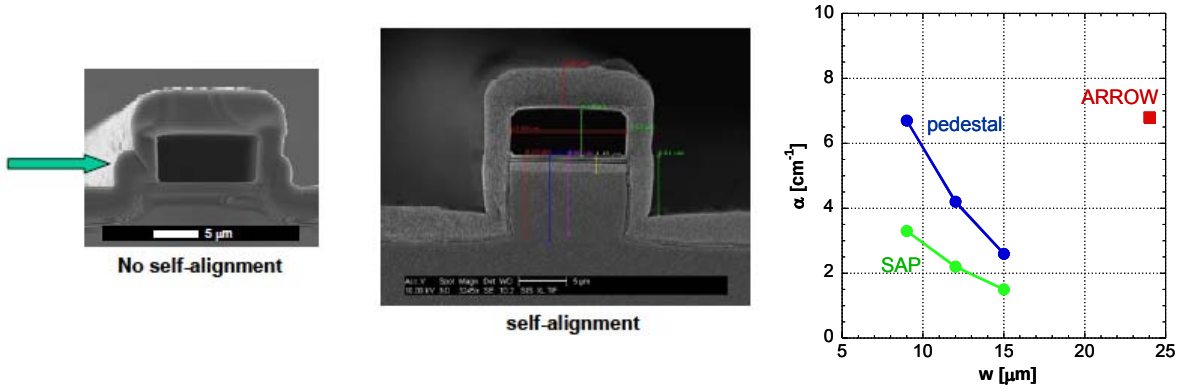

Improvement in pedestal fabrication process.

We have now solved this problem by developing a self-aligned lithography process. In this case, the sacrificial layer that forms the waveguide core is also used as an etch mask for creating the pedestal. The outcome of this process is shown in the center SEM. The improvements in waveguide loss from forming a clean self-aligned pedestal (SAP) with fully vertical sidewalls are shown on the right. The development of this process was possible through acquisition of a new dedicated ICP-RIE etcher at BYU.

C.2. Atomic spectroscopy on a chip

At UCSC, versatile spectroscopy setups with three external cavity diode lasers were built for spectroscopic experiments (two at 795nm, one at 780nm), allowing for different types of EIT-based experiments, including Λ-type EIT on the Rb D1-line, V-type EIT on the D2-line, four-wave mixing and parametric generation as well as giant Kerr nonlinearities.

With this setup, we were able to carry out atomic spectroscopy using bulk rubidium cells, minicells (chromatography bottles), and integrated waveguide-based cells. The minicells are used to optimize sealing methods and assess longevity of the samples.

We then carried out spectroscopy on the integrated ARROW cells and were able to demonstrate atomic spectroscopy on an integrated optics chip for the first time. The Rb spectrum across the D2 line was probed as a function of temperature and compared to a conventional bulk cell. The figure below shows the comparison of bulk and ARROW-spectra at 70C along with the Rb energy level scheme.

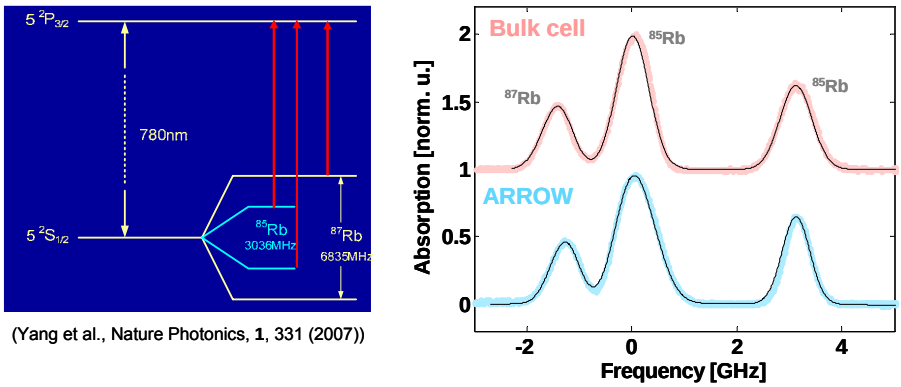

(Yang et al., Nature Photonics, **1**, 331 (2007))

Rb level scheme and D2 absorption spectra on a chip.

Both atomic density and optical density were compared for the two cells as a function of temperature showing that the integrated cell can perform almost as well as a bulk cell. However, due to its small size the optical volume is reduced by a factor of 80,000,000 and the nonlinear intensity is increased by a factor 90,000, promising strongly enhanced nonlinear optical effects. These results are summarized in the figure below.

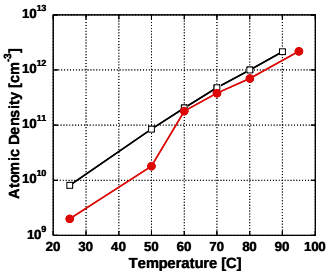

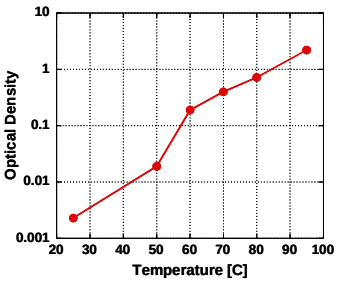

	dimensions [μm x μm x μm]	V [pl]	I [norm. u.]
Bulk cell	25,000 x 25,000 x 50,000	3.1 x 10^{10}	1
ARROW	5 x 12 x 5000	300	90,000
ARROW Improvement	Mode area: 14 λ^2	8 x 10^7 (bulk)	90,000 (bulk)

Performance comparison between integrated and conventional rubidium cell.

The simplest nonlinear optical experiment that can be realized with such a cell is saturated absorption spectroscopy (SAS). Because SAS uses counter-propagating pump and probe beams, it is an excellent application to showcase the advantages of our integrated approach. Since both beams travel in the same waveguide mode, perfect alignment of pump and probe beam throughout the cell are guaranteed without alignment efforts. The schematic of the experiment and our setup are shown below.

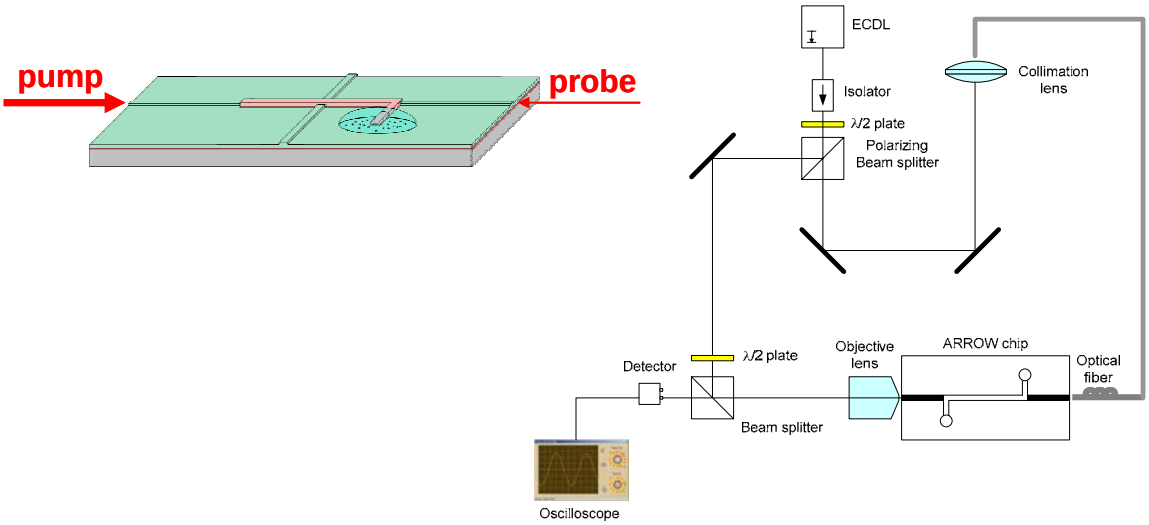

SAS spectroscopy scheme and experimental setup.

We were able to demonstrate SAS and observe narrow Lamb dips in the hyperfine absorption spectrum. We also achieved good agreement with theory as shown in the images below and found a SAS dip broadening of 46MHz which is in good agreement to the expectation one would get from transit time broadening, i.e. the finite interaction time of the beam with a Rb atom as it traverses the mode. This is also the source of broadening in hollow-core PCF fiber. The demonstration of SAS has immediate practical applications towards laser frequency stabilization using the narrow Lamb dip as a reference. In addition, it shows that narrow features are observable in on-chip cells which was a good sign for observing quantum coherence effects such as slow light and giant Kerr nonlinearities.

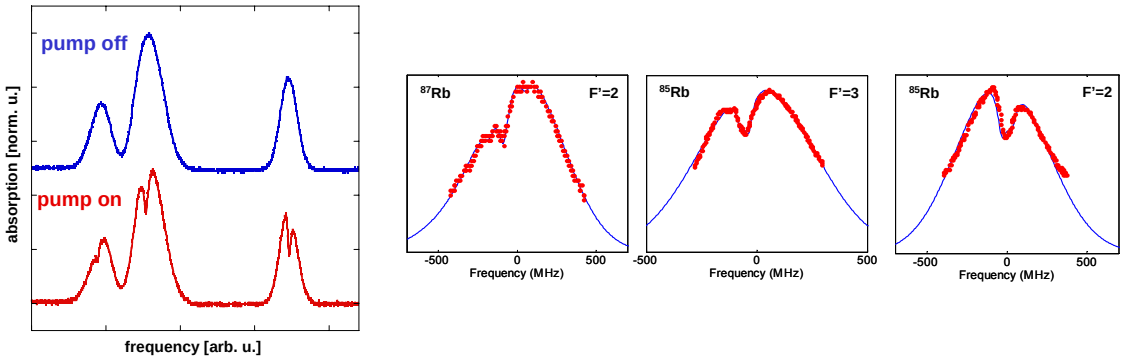

SAS spectra and fits with theory.

C.3. Nonlinear spectroscopy on minicells

One of the project goals was generation of single photon pairs from rubidium atoms on a chip. This can be accomplished in a nonlinear parametric generation scheme illustrated in the figure on the left below. Three lasers at frequencies ω_C, ω_S, and ω_C are sent into the rubidium cell, and a probe field at ω_P is generated (see center figure for the beam geometry used). This scheme was successfully implemented in a glass minicell, and the figure on the right shows the generated power at ω_P as a function of detuning of the ω_S-laser from its corresponding resonance. A typical resonant behavior of the generation rate is observed in agreement with expectations.

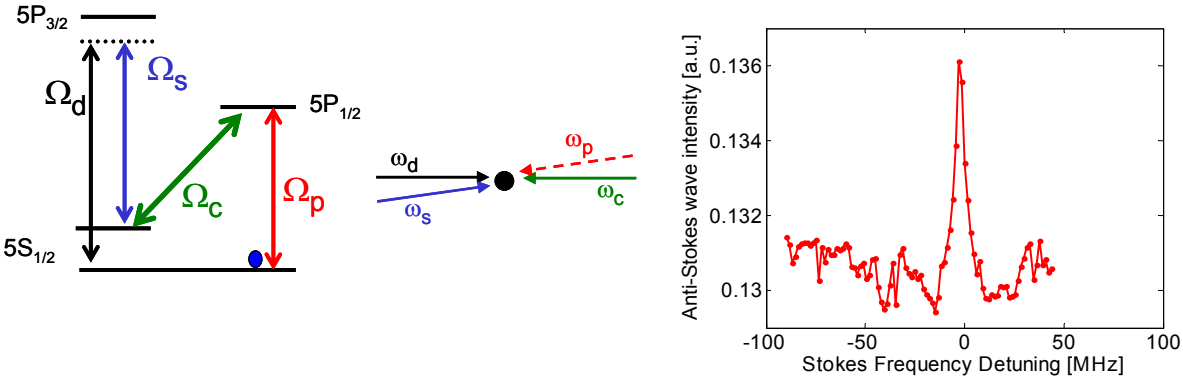

Nonlinear parametric generation experiment in rubidium minicells.

This experiment showed that nonlinear photon generation can successfully be implemented in home-built rubidium cells.

C.4. Laser induced atomic desorption (LIAD) in minicells

It is well known that alkali atoms can be optically released from cell walls, resulting in increased atomic density in the cell. This phenomenon known as laser-induced atomic desorption (LIAD) proved essential in the fiber-based EIT experiments by the Gaeta group and others.

In order to investigate the importance of LIAD on our platforms we built a LIAD setup as shown below on the left. A desorption laser at 770nm and of varying power was sent into a minicell filled with rubidium, and the resulting atomic density was measured for different desorption laser powers.

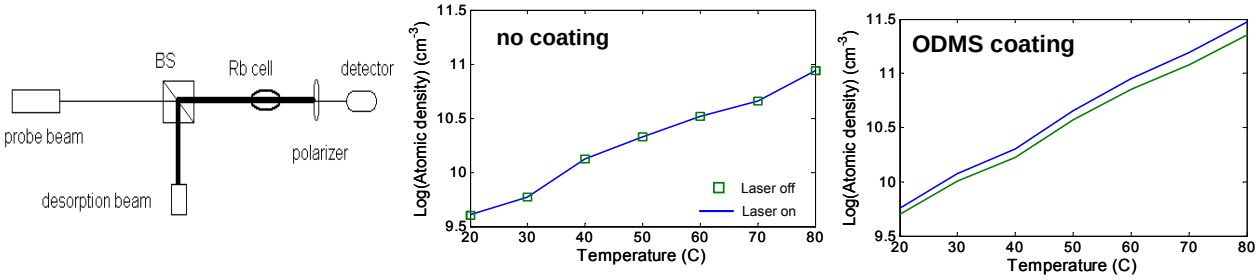

LIAD experiment in glass minicells.

The experimental results in the center and right panels show that a desorption effect could only be detected for the minicells that had an ODMS coating. Uncoated samples, or samples coated with silicon dioxide or nitride showed no dependence of the atomic density on the presence of the desorption laser.

The figure below shows the LIAD effect on the ODMS-coated minicell as a function of temperature and laser power, respectively. It can be seen that a relatively temperature-independent increase in density can be achieved that can reach up to 15% for the highest laser powers used.

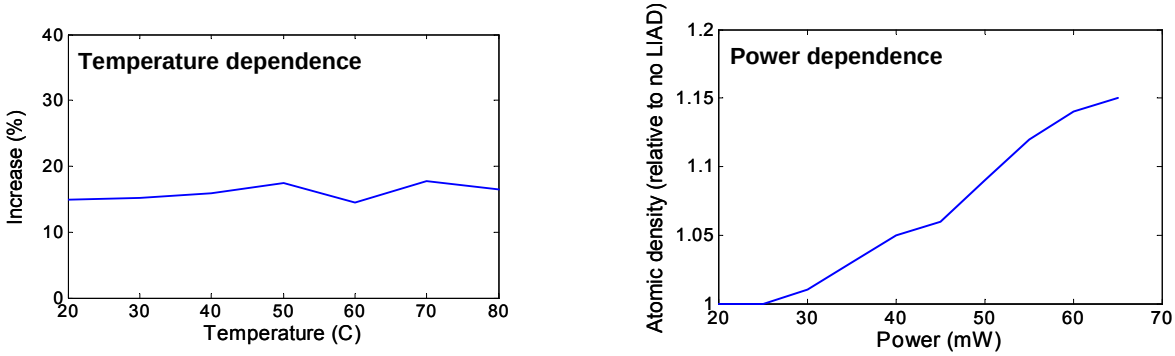

Laser-induced desorption results on ODMS-coated mincells..

C.5. Novel method for EIT spectroscopy

Typically, quantum interference experiments are carried out by fixing the coupling beam at the |2>-|3> resonance and detuning the probe beam across the atomic resonance as illustrated in Fig. (a) below. This results in the well-known EIT dip in the absorption coefficient as shown at the bottom. The downsides of this scheme are the relatively slow decay to zero and fluctuating baselines in experiments. This can make it difficult to identify a clear baseline (zero absorption) to assess switching efficiencies and perform reliable fits to extract salient parameters, especially at low light levels where the data can be noisy. Fig. (b) shows an alternative to this setup where the roles of the beams are reversed. Since the probe is fixed at the |1>-|3> resonance, we obtain a constant, very high absorption levels in an optically dense vapor as soon as the coupling beam is detuned from the narrow EIT dip. This is highlighted by the green arrows in the figure.

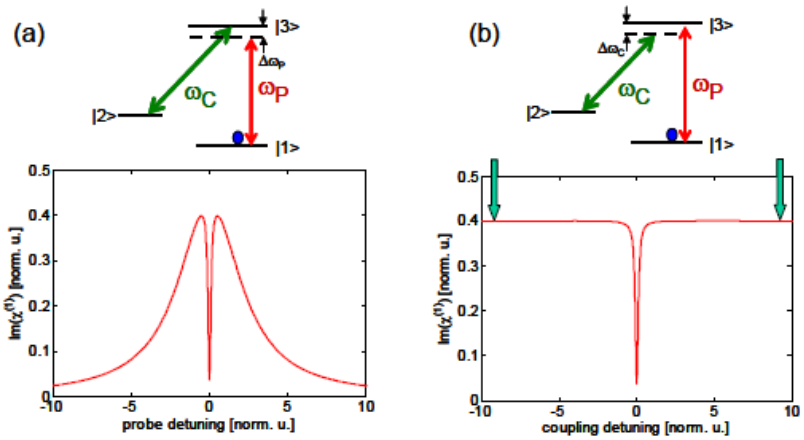

EIT experiment schemes: (a) fixed coupling, variable probe; (b) fixed probe, variable coupling.

Below we show an experiment carried out with this new scheme. The transmission at the Rb D2 line is shown as function of coupling detuning and shows both a characteristic EIT peak (in transmission) and a very clean and flat baseline, only limited by digitization noise from the scope. This approach can be used to carry out linear and nonlinear EIT experiments in ARROW chips and other environments.

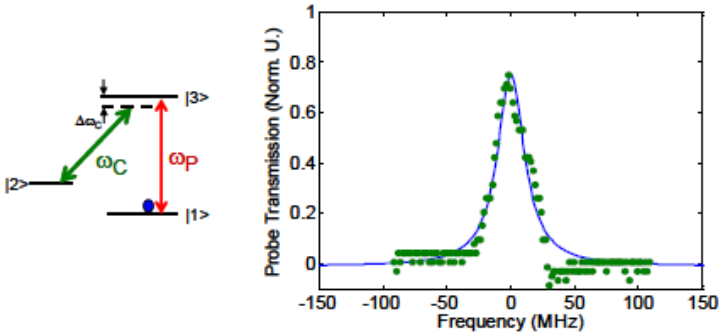

Experimental result for EIT measured by tuning the coupling field and fixing the probe frequency.

C.6. EIT on a chip

In order to see quantum interference on a chip, it is necessary to maximize the electron coherence time. It is well known that the effect of wall collisions present in integrated structures can be mitigated by coating the walls with an organic material. We have successfully coated straight hollow ARROW waveguides with ODMS and shown that the effect on optical mode quality is negligible. This is shown in the figure below.

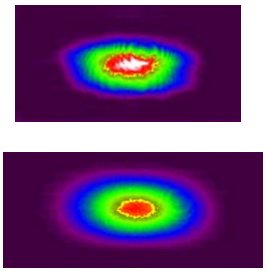

Sample #	Uncoated		Coated	
	Output Power (uW)	Mode Quality	Output Power (uW)	Mode Quality
C1	72	Perfect	65	Perfect
C2	153	Perfect	111	Perfect
C3	82	Perfect	93	Perfect
C4	70	Perfect	78	Perfect
C5	121	Perfect	105	Perfect
C6	179	Perfect	156	Perfect
C7	159	Perfect	122	Perfect

Left: Hollow-core waveguide modes before (top) and after (bottom) coating the waveguide walls. Right: comparison of several waveguides on the same chip.

Using ODMS-coated ARROW waveguides, we were able to achieve the first demonstration of Λ-EIT on an integrated optical chip. In the first such experiment, the ARROW waveguide chip was heated up to 90C and spectroscopy was carried out on the rubidium D2 line. Coupling and probe laser fields were sent through the chip collinearly and with identical polarizations. The probe laser signal was recovered using a lock-in modulation scheme. The figure below shows a comparison of the D2 hyperfine spectrum with the coupling laser on and off.

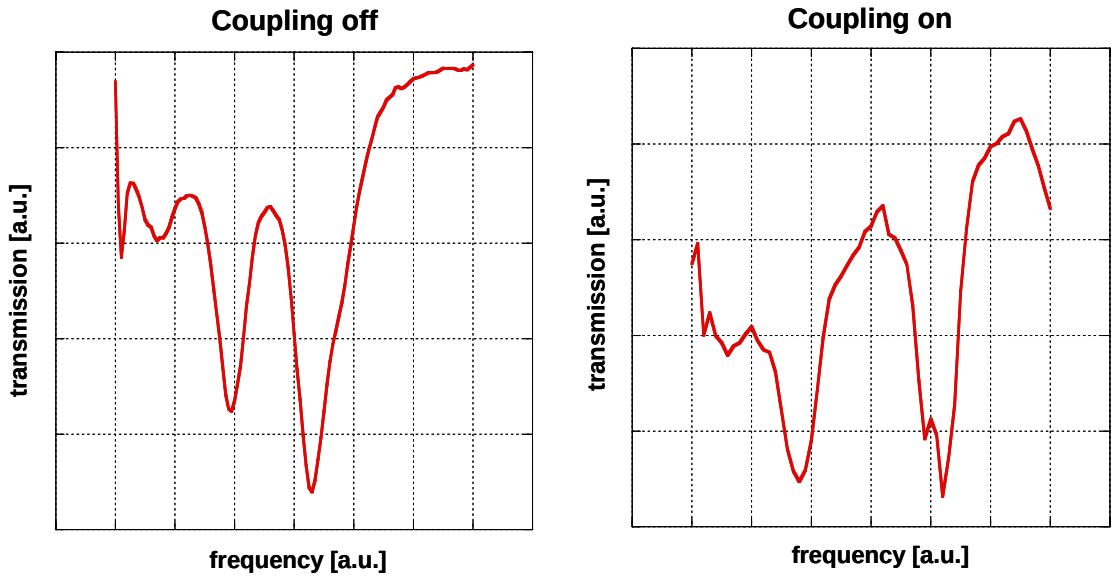

EIT in an integrated optical chip

A transmission peak in the rightmost transmission dip can clearly be seen in the presence of the coupling field. This increase in laser transmission is the hallmark of electromagnetically induced transparency (EIT).

The figure below shows the emergence of the EIT dip as the coupling laser power is gradually increased.

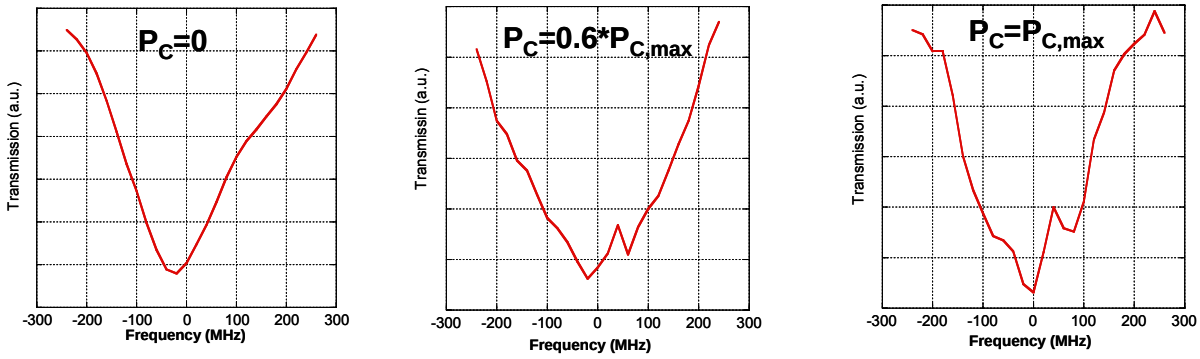

Power dependence of EIT feature.

This first demonstration of quantum interference on a chip through micron-scale waveguides is an essential step towards nonlinear photon generation on the same platform.

The left figure below shows the experimental setup. The center figure shows once more the resulting transmission spectrum obtained in a conventional manner by detuning the probe laser, this time however along with a two-parameter fit (blue line) that allows us to determine the local coupling field power in the waveguide. The agreement with the data is very good, and the quality is limited by the finite frequency step size of the New Focus laser that was used in this experiment.

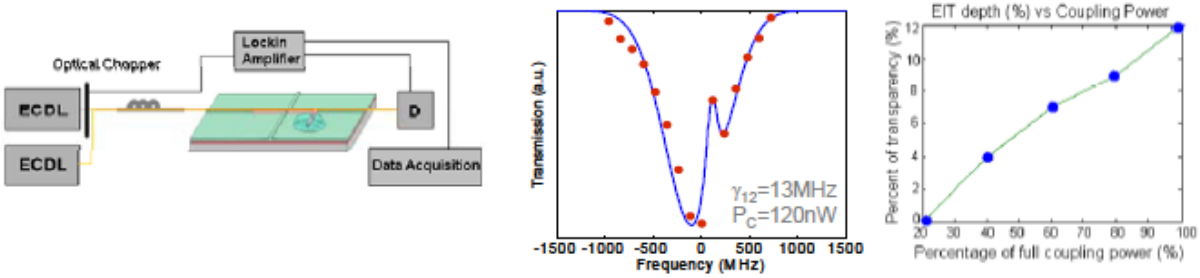

EIT in an integrated optical chip. Left: Setup; center: spectrum with fit; right: dependence of EIT depth on coupling power.

Specifically, a dephasing rate of 13MHz was extracted, suggesting that the ODMS coating ameliorated the coherence dephasing induced by wall collisions. The figure on the right shows the dependence of the EIT dip depth on the coupling laser power, exhibiting the expected increase in depth with coupling power.

In a second, improved version of this experiment, continuous wave (cw) light from two Vescent external cavity diode lasers with better frequency resolution was coupled into a single-mode fiber which was aligned to the input facet of the spectroscopy chip. The coupling laser was tuned to the $5S_{1/2}(F=3) \rightarrow 5P_{3/2}(F=3)$ hyperfine transition of the D2 line in ^{85}Rb, and the probe laser was tuned across the $5S_{1/2}(F=2) \rightarrow 5P_{3/2}(F=3)$ resonance with a 3.035 GHz larger frequency, corresponding to the hyperfine splitting of the $5S_{1/2}$ ground states. The figure below shows the measured probe transmission spectrum for input powers at the chip facet of 18.2mW (coupling field) and 3.6mW (probe field), respectively.

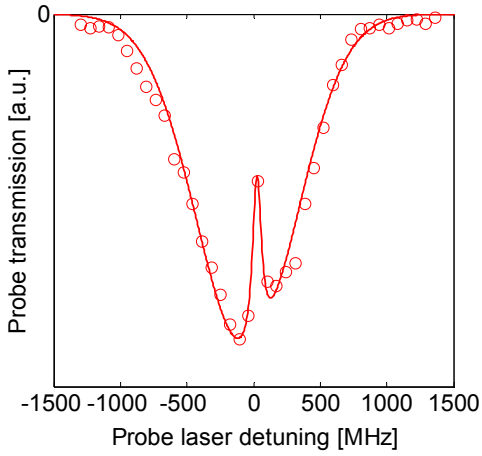

Improved EIT with 44% transparency.

A narrow transmission peak of ~50MHz width is clearly visible amidst the Doppler-broadened profile. It shows the clear hallmark of EIT in optically thick media, an extremely asymmetric transparency peak due to Fano-type interference between dressed states that appears whenever the condition $\Omega_C^2 >> \gamma_{13}\gamma_{12}$ is fulfilled (γ_{13}: |3>-|1> coherence decay rate, Ω_C: coupling Rabi frequency). For the present experimental parameters, 44% of the transmission through the optically dense vapor was restored by the quantum

coherence effect. The data were modeled with the linear atomic susceptibility including Doppler broadening and using Ω_C and the coherence dephasing rate due to wall collisions, $\gamma_{12,WC}$, as free parameters. The fit (line) shows excellent agreement with the data for $\Omega_C/2\pi$=201.6MHz and $\gamma_{12,WC}/2\pi$=4.0MHz, corresponding to an average coupling power of only 1.06μW in the hollow-core waveguide to create the atomic spin coherence. The dephasing rate due to wall collisions is substantially smaller than the 33MHz one would expect if every collision at the most probable atomic velocity along the shortest dimension of the waveguide resulted in loss of coherence. This results points to the efficiency of the ODMS coating and a loss of coherence after an average of 10.5 wall collisions.

C.7. Slow light on a chip

The goal of this project was not only to demonstrate the feasibility of robust quantum interference in a photonic spectroscopy chip, but also to utilize this new system to demonstrate applications such as slow light, all-optical switching and cross-phase modulation of short laser pulses. An important step in this direction was to make our optical spectroscopy setups compatible with short pulse detection. To this end, an acousto-optical modulator (AOM) was incorporated into the setup. This device is capable of producing short pulses on the order of tens of nanoseconds long and is used in numerous quantum interference experiments. The figure below shows the result of a slow-light experiment carried out in a bulk Rb cell with pulses generated in this fashion.

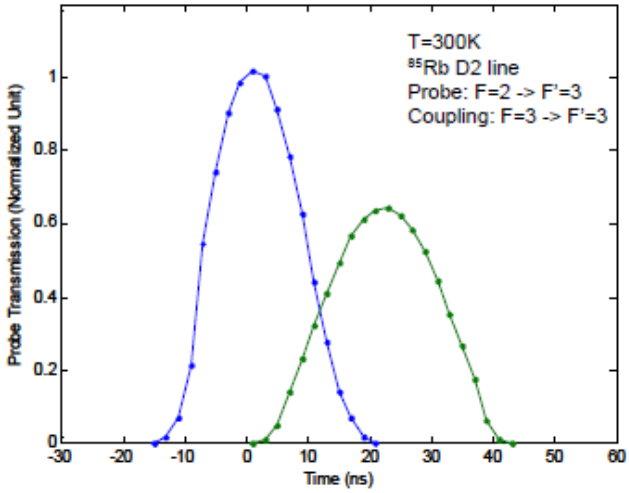

Pulsed slow light experiment on Rb bulk cell using new AOM-based setup.

A probe pulse was generated at a repetition rate of 5MHz and an input coupling power of 16.5mW was used. An experimental delay of ~1 pulse length by 22ns was observed in excellent agreement with theoretical expectations. This results showed that nonlinear optical experiments with nanosecond pulses are possible on our testbed.

To demonstrate slow light on the chip, the probe laser was modulated with the acousto-optic modulator (AOM) to create 20ns long pulses at a repetition rate of 5 MHz. A portion of the probe beam was routed directly to a detector as a reference while the remaining pulse traveled through the chip together with the cw coupling beam. The left figure below shows the first observation of slow light via quantum state control on a chip. A large delay between the two probe pulses (depicted as circles and square symbols, respectively) was observed. The figure on the right shows the group index n_G (filled squares) and the group velocity v_G (open circles) as a function of coupling power as extracted from the measured pulse delays. For the lowest coupling power used, a reduction in the speed of light by a factor 1,200 is observed along with a commensurate increase in the group index. This is seven times slower than recent reports in

photonic crystal waveguides, and corresponds to a spatial compression of the 6m long probe pulse to 5mm on the chip. The solid lines in Fig. 3b represent the results of parameter-free calculations of n_G and v_G based on the values extracted from the EIT spectrum, showing very good agreement between theory and experiment.

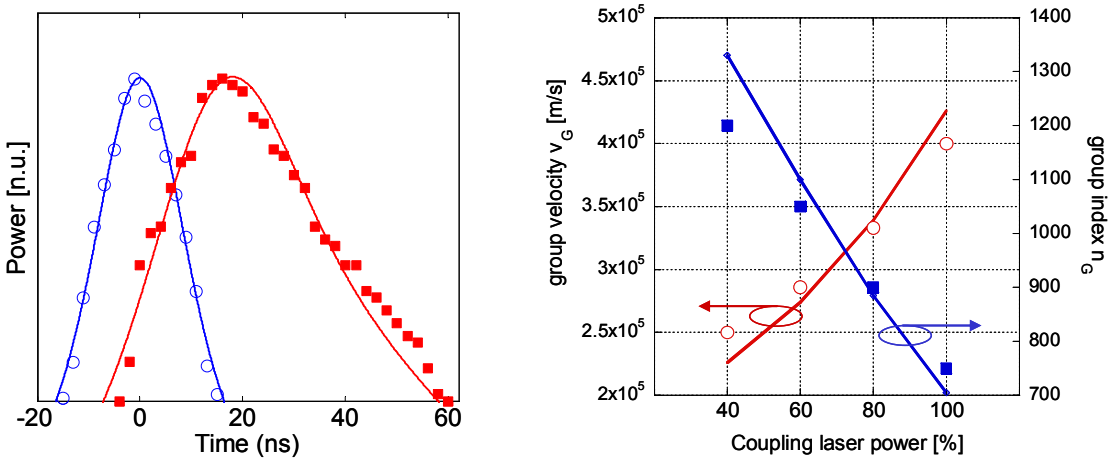

Slow light on a chip. Left: Probe laser pulses for reference beam (open circles) and beam traveling through Rubidium chip experiencing slow light effect (filled squares) for 40% of maximum input pulse power. The line for the reference pulse represents a fit with a sech^2 pulse shape. The line for the delayed pulse represents a parameter-free calculation of the output pulse including group velocity dispersion and absorption effects. Right: Measured group velocity (open circles) and group index (filled squares) versus relative coupling laser power. The lines represent parameter-free calculations based on the vapor properties extracted from the EIT spectrum.

The left figure below shows the extracted pulse delay versus coupling power. A maximum delay of 16ns corresponding to a delay by 80% of the pulse width is observed. The delay is smaller at higher coupling power since the widening transparency hole results in a decrease in dispersion dn/dω that determines v_G=c/(n+ω•dn/dω), where *n* is the phase index and ω is the light frequency. The FWHM pulse width is depicted in the right figure and shows increasing broadening as the coupling power is reduced.

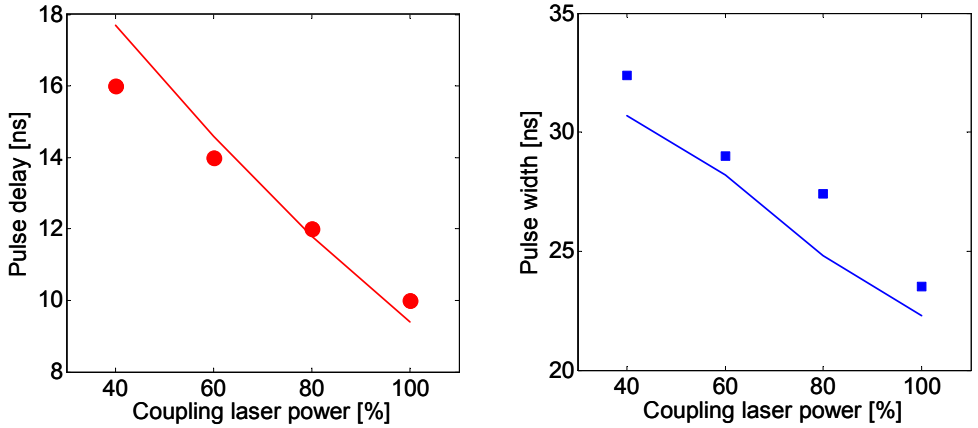

Slow light characteristics. Left: Probe pulse delay versus relative coupling laser power (data: filled circles). Right: Probe pulse width versus relative coupling laser power (data: filled squares). The lines in both graphs are parameter-free calculations based on the vapour properties extracted from the EIT spectrum.

This effect is due to both group velocity dispersion $\beta_2(\omega)$ and frequency-dependent absorption $\alpha(\omega)$ across the transparency peak. We modeled the propagation of the electric field pulse E(z,t) across a waveguide of length *L* in the frequency domain via:

$$E(L,t) = \int_{-\infty}^{\infty} E(0,\omega) e^{-\alpha(\omega)L} e^{\frac{i}{2}\beta_2\omega^2 z} e^{i\omega t} d\omega \qquad (1)$$

Both $\beta_2(\omega)$ and $\alpha(\omega)$ can be extracted from the EIT profile, and a sech^2 input pulse shape was assumed. The pulse broadening calculated without any free parameters from Eqn. (1) is shown in the right figure (line) and shows very good agreement with the data. Moreover, the calculated output pulse shape matches the observed slow light pulse very well as seen in the preceding figure (line).

C.8. Portable integrated atomic spectroscopy system

Another goal of efforts was to build a portable rubidium spectroscopy platform built around hollow-core ARROW waveguide chips.

One component of this effort was the development of a robust package for the chip that can be combined with fiber-optic integration. The figure below shows a major step in this direction. Here, an ARROW-chip was placed on an aluminum based for improved handling, and the protruding crimped copper reservoir was protected by aluminum plates for increased mechanical stability.

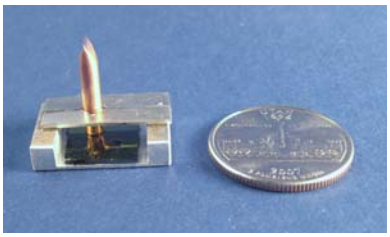

Image of rubidium spectroscopy chip in protective aluminum package.

A second effort was directed towards integrating all elements (sources, detectors, and Rb chips) on a single, portable breadboard for proof-of principle demonstration. To this end, we developed layouts of the completed breadboard setup to optimize arrangements and minimize the space requirements.

The figure below shows side and top views of such a layout containing two lasers for nonlinear generation, three rubidium spectroscopy chips (two for frequency stabilization and one for nonlinear generation), and the required optical elements.

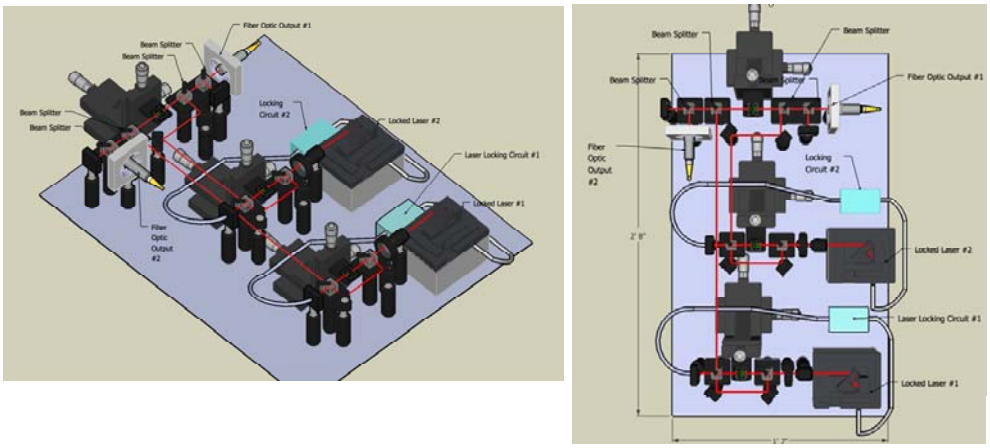

Layout for portable photon generation system

Finally, the various lasers involved in the nonlinear optical generation scheme need to maintain their emission frequency with high precision in order to allow for resolving the very narrow EIT feature. We developed our own frequency locking circuits based on a design from Wieman et al. The figure below shows the circuit diagram and the completed locking circuit box. The figure on the right shows a comparison of the frequency stability of a laser with the locking circuit on and off. An improvement in stability by a factor of over 5,000 from 60MHz to 12kHz was demonstrated.

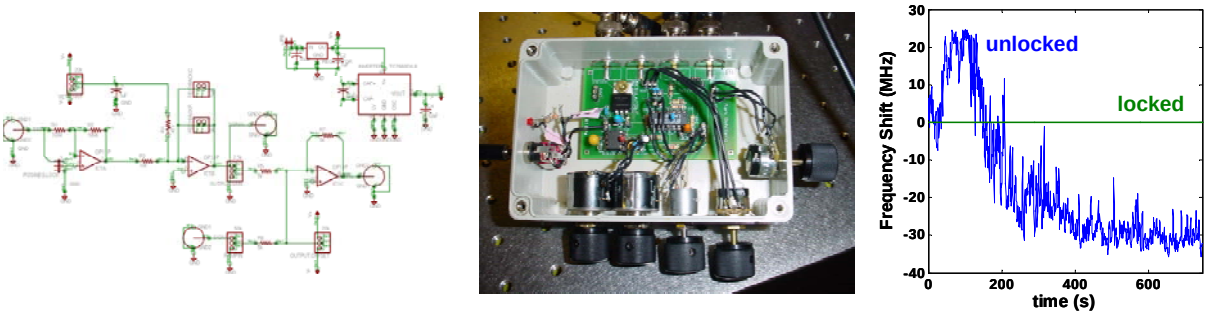

Laser frequency locking circuit, physical implementation, and performance.

In order to minimize the footprint of the setup, we completely redesigned and built an ECDL with substantially reduced footprint and additional tweaks for better alignment.

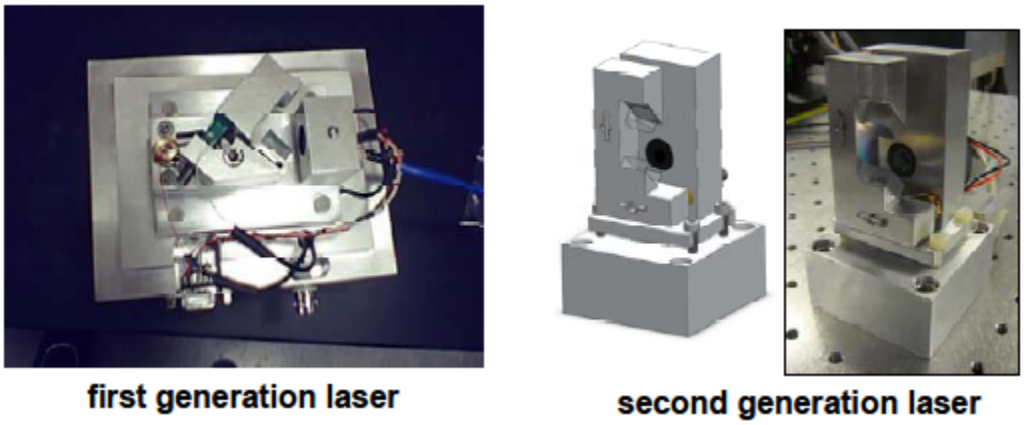

Home-built ECDLs. Left: First generation; right: Drawing and photo of completely redesigned and miniaturized laser.

The laser was designed, machined, and tested exclusively by EE undergraduate student Trevor Vogt at UCSC as part of his senior thesis. The laser is fully operational and Trevor received a much-deserved Dean's Award for Undergraduate Research for his work.

Subsequently, we implemented two additional methods to improve the laser locking performance: DAVLL (dichroic atomic vapor laser locking, not shown) and DFDL (Doppler-free dichroic locking). DFDL combines the principles of DAVLL (generation of a suitable feedback signal from differential absorption in Zeeman-split lines) and saturated absorption spectroscopy, allowing us to use the lamb dips of a SAS spectrum to implement the DAVLL principle. The experimental setup is shown on the left in the figure below, and the DFDL error signal is shown in blue on the right, indicating high stability after an initial settling period. Further tests are still ongoing to assess the performance of this method.

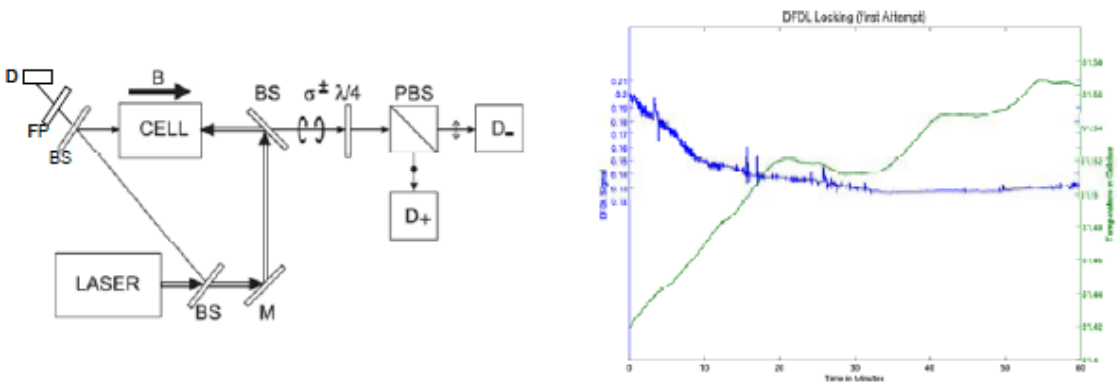

DFDL locking of ECDL laser. Left: Setup; right: DFDL laser locking signal (blue) and reference cell temperature (green).

Finally, the figure below shows a completed portable 1'x1' setup for saturated absorption spectroscopy. The home-built ECDL laser and the integrated Rb chip are highlighted by the yellow circles in the top right while the bottom right image provides a different perspective with a better view of the integrated chip. Tests of SAS with this platform are still ongoing.

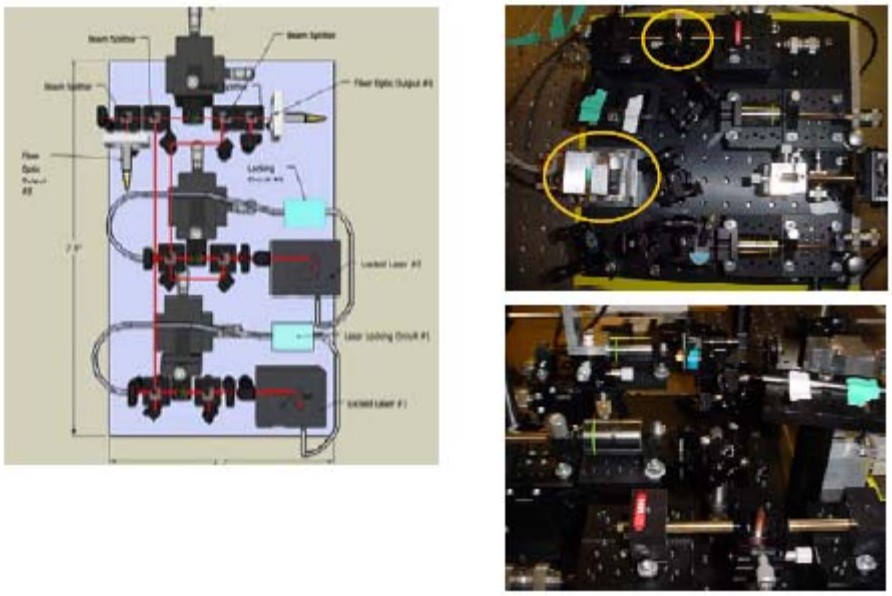

Portable SAS setup. Left: Schematic layout, right: photographs of completed setup.

C.10 Summary

In this project, we have introduced a completely new integrated atomic spectroscopy platform with the following new and unique features:

- planar photonic integration of atomic medium and optical paths
- small optical modes for maximized nonlinear optical effects
- fully self-contained
- operates at or above room temperature
- exhibits large and robust quantum interference

- exhibits the largest slow light effects on a chip to date
- integration in larger photonic systems

During the course of this project, we had to create new hollow-core optical waveguides with low loss, develop fabrication methods for incorporating alkali atoms with hollow-core optical waveguides, develop a method to coat ARROW waveguide channels with an organic monolayer and develop the theory to analyze optical quantum interference effects with strongly spatially varying coupling fields. None of these capabilities were available before this project started.

We feel that it is safe to say that our work has been transformative and opened new avenues for atomic spectroscopy. In addition to the narrowly focused goals of this project (slow light and low-level nonlinear optics), our new ARROW-based platform has clearly a large number of applications, including precision spectroscopy, atomic manipulation on a chip, and slow and stopped light devices using a variety of experimental techniques.

UNIVERSITY OF CALIFORNIA

SANTA CRUZ

RB CELL INTEGRATED HOLLOW CORE WAVEGUIDE DEVICES FOR SPECTROSCOPY AND QUANTUM COHERENCE APPLICATIONS

A dissertation submitted in partial satisfaction
of the requirements for the degree of

DOCTOR OF PHILOSOPHY

in

ELECTRICAL ENGINEERING

by

Bin Wu

September 2010

The Dissertation of Bin Wu
is approved:

_____
Professor Holger Schmidt

_____
Professor Claire Gu

_____
Professor Jin Zhang

_____
Tyrus Miller
Vice Provost and Dean of Graduate Studies

Table of Contents

List of Figures ix

List of Tables xviii

Abstract xix

Acknowledgement xxi

Introduction 1

1.1 Motivation 1

1.2 Introduction of electromagnetically induced transparency 3

1.3 Motivation for using rubidium 10

1.4. Introduction of Rb spectroscopy with Doppler Broadening 11

1.4.1 Doppler broadened Rb spectroscopy 11

1.4.2 Doppler broadened linewidth extractions 13

1.5 Introduction to Slow Light 14

1.5.1 Theory of slow light 14

1.5.2 Fundamental theory of slow light 16

1.5.3 Double Atomic Resonance Reduces Dispersion 19

1.5.4 Tunable Double Resonance and Electromagnetically Induced Transparency 19

1.5.5 Photonic Resonances: Bragg Gratings 21

1.5.6 Double-Resonant Photonic Structures 22

1.5.7 Coupled Ring Resonators 22

1.5.8 Slow Light in Optical Fibers 23

1.5.9 Experimental demonstrations of slow light techniques 26

1.6. ARROW waveguides 30

1.7 Chapter arrangement 32

Chapter 2 Theory of ARROW and EIT 35

2.1. Introduction of ARROW 36

2.2 Loss calculation of ARROW 38

2.2.1 Matrix formulism for mode loss calculation 38

2.2.2 Loss calculation of 2D ARROW waveguide. 42

2.2.3 Loss optimization 43

2.3 Fabrication 44

2.3.1 Fabrication of non-preetched ARROW 45

2.3.2 Fabrication of preetched ARROW 46

2.4. Testing of ARROW Performance 49

2.5 Theory of EIT 53

2.5.1 Basic physics of EIT 53

2.5.2 Rabi frequency 55

2.5.3 Closed system for Lambda Type EIT 55

Chapter 3 Rubidium Cell Integration 61

3.1. Current vapor cell technology 61

3.1.1 Bulk cell 61

3.1.2 Anodic boding for micro-cell 62
3.2 Fabrication of rubidium filled minicell 64
3.2.1 Geometry for integrated ARROW waveguides with Rb cell 64
3.2.2 Fabrication of minicell 65
3.2.3 The absorption testing result of minicell 67
3.3 Integration of rubidium cell onto ARROW waveguide 70
3.3.1 First generation of rubidium loaded ARROW 70
3.3.2 Second generation of rubidium loaded ARROW 71
3.4 Improvement of ARROW fabrication 72
3.4.1 Cleaning Technique 72
3.4.2 ODMS coating rubidium loaded ARROW 73
Chapter 4 Rubidium Spectroscopy in Rb loaded ARROWs 77
4.1 Theory of rubidium spectroscopy 77
4.1.1 Atomic Transitions of Rubidium 77
4.1.2 Hyperfine Splitting 79
4.1.3 Doppler Broadened Spectroscopy 81
4.2 Rb spectroscopy in bulk cell 84
4.2.1 Experimental setup 84
4.2.2 Using interferometry technique to improve the experiment 85
4.3. Rubidium spectroscopy in minicells 89
4.3.1 Experiment setup 89

4.3.2 Experimental result 90
4.3.3 Multi-cycle heating test for characterizing minicell performance 91
4.3.4 Pressure control in Rb loaded minicells 95
4.4. Spectroscopy in Rb-loaded ARROWs 97
4.4.1 Experimental setup for Rb loaded ARROW 97
4.4.2 Experimental results 98
4.5 Fittings of rubidium spectroscopy 100
4.5.1 Equations and methods 100
4.6 Theory of saturated absorption spectroscopy 102
4.6.1 The zero-velocity dips 102
4.6.2 The crossover dips 105
4.7 Saturated absorption spectroscopy in Rb loaded ARROW 109
4.7.1 Experimental setup 109
4.7.2 Experimental results 110
4.8. Fittings of SAS 111
4.8.1 Equations for fitting 111
4.8.2 Fitting results of SAS 112
4.9 Summary 119
Chapter 5 EIT in Rb loaded ARROWs 120
5.1 EIT in bulk cell 120
5.1.1 Lambda type EIT (bulk cell) 121

5.1.1.1 Experimental setup 121
5.1.1.2 Experimental result 122
5.1.2 Vee type EIT (bulk cell) 124
5.1.2.1 Experimental setup 124
5.1.2.2 Experimental result 125
5.2 Extraction of atomic density 127
5.3 Laser induced atomic desorption (LIAD) experiment 127
5.4 EIT in minicells 137
5.4.1 Lambda type EIT Setup in Rb loaded minicell 137
5.4.2 Experimental result 138
5.5 EIT in Rb loaded ARROW 142
5.5.1 Experimental setup for EIT in Rb loaded ARROW 142
5.5.2 Experimental result 144
5.6 Fitting of EIT spectrum 151
5.6.1 Theory for fitting 151
5.6.2 The method for fitting 152
5.6.3 Fitting result 153
5.6.4 Fitting with the consideration of waveguide loss. 157
5.6.5 Experiment with coupling frequency detuning 163
5.7 Summary 165
Chapter 6 Slow Light on a Chip 166

6.1 Slow light experiment in Rb loaded ARROW 166
6.1.1 Experimental setup 166
6.1.2 Experimental result 167
6.2 Simulations of pulse propagation in slow light with Rb loaded ARROW . 172
6.3 Simulations of slow light experiment with waveguide loss 181
6.4 Summary 187
Chapter 7 Summary and outlook 188
Appendix A Experimental Operations 196
A.1 Laser Operations 196
A.1.1 Vescent laser (trouble shooting) 196
A.1.2 Newfocus laser 198
A.2 Coupling lens calculation (fiber coupling, waveguide coupling) 199
A.3 Temperature calibration of Current control 199
Appendix B 202
B.1 Aim 202
B.2 Method 202
B.3. Result 203
Bibliography 212

List of Figures

Figure 1.1 Three-level scheme for EIT 4

Figure 1.2 (a) Normal transmission curve with atomic absorption (b) Transmission curve with EIT 6

Figure 1.3 (a) Normal dispersion curve with atomic absorption (b) Dispersion curve with EIT 8

Figure 1.4 Rubidium energy diagram 12

Figure 1.5 Rb spectrum (D2 line) with Doppler broadening 13

Figure 1.6 Two level atomic system 16

Figure 1.7 Refractive index profile for slow light in EIT 20

Figure 1.8 Photograph of 4-inch silicon wafer with 32 atomic spectroscopy cells 33

Figure 2.1 Cross section of the ARROW waveguide (a low-index core (thickness d_c, index n_c) is surrounded by ARROW cladding layers (indices n_1, n_2) on both sides; also depicted are the relevant polarization directions of the electric field (TE polarization is parallel and TM is perpendicular to the layers). Propagation occurs along the z-direction with a propagation constant β and the wave is to be confined in the transverse (y) direction. The cladding layers act as Fabry-Perot cavities for propagation with the transverse wave

vector k_T in the y direction.) 37
Figure 2.2 Diagram of multi-layer structure 39
Figure 2.3 Light ray tracing in a general waveguide 41
Figure 2.4 Phase conditions for different polarizations 42
Figure 2.5 Fabrication process of ARROW waveguides 46
Figure 2.6 SEM pictures of ARROW: (a) Non-preetched ARROW (b) Preetched ARROW 47
Figure 2.7 Fabrication process of SAP ARROW waveguides. 49
Figure 2.8 The experimental setup for measuring ARROW loss. 51
Figure 2.9 Loss measurement of ARROW waveguide (a) Transmission vs different waveguide lengths with different waveguide widths. Lines: fits; symbols: experimental data; (b) The measurement results of waveguide loss for both previous-designed ARROWs (open circles) and SAP ARROWs (open squares). 52
Figure 2.10 Three types of configuration for EIT: (a) Vee type (b) Ladder type (c) Lambda type 54
Figure 2.11 Configuration of a three-level Lambda Type EIT system 56
Figure 2.12 (a) Transmission vs probe detuning in EIT; (b) Refractive index vs probe detuning in EIT 59
Figure 3.1 Picture of the conventional Rb bulk cell 62
Figure 3.2 Illustration of a compact Rb vapor cell from anodic bonding 63

Figure 3.3 Rubidium cell integrated ARROW waveguide 65

Figure 3.4 Illustration of a sealing technique testing platform called a minicell 67

Figure 3.5 Rubidium spectroscopy at 780nm D2 line (all the dips here correspond to different atomic transitions with Rb level schemes referring to section 1.4.1). 68

Figure 3.6 Performance testing of rubidium minicells 69

Figure 3.7 The first generation of Rb loaded ARROW 71

Figure 3.8 Second generation of Rb loaded ARROW 72

Figure 3.9 The fabrication process of applying ODMS coating: (a) Attaching reservoirs. (b) ODMS solution flowed through ARROW. (c) Remove excess ODMS. (d) ODMS layer on silicon nitride surface. 74

Figure 3.10 Images of optical modes taken at the end of hollow waveguides illuminated by a single-mode fiber at the opposite side. (a) Waveguide with no ODMS coating on its interior walls. (b) Waveguide with ODMS coating on its interior walls..... 75

Figure 4.1 Energy level diagram of Rubidium (D1 and D2 lines)..... 78

Figure 4.2 D2 line rubidium spectroscopy with Doppler broadening 81

Figure 4.3 Doppler broadening linewidth (FWHM) v.s. Temperature 84

Figure 4.4 Experimental Setup of rubidium spectroscopy in bulk cell..... 85

Figure 4.5 Rubidium spectroscopy with the interferometer rectification..... 86

Figure 4.6 (a) The rubidium spectroscopy and interferometer fringes before

rectification; (b) The rubidium spectroscopy and interferometer fringes after rectification 88

Figure 4.7 Experimental setup of Rb spectroscopy in minicell 89

Figure 4.8 Rubidium spectroscopy from first crimped minicell of D1 line..... 90

Figure 4.9 Multi-cycle heating and cooling test of minicells: (a) Multi-cycles heating and cooling test of rubidium in a minicell with old fabrication method (b) Multi-cycles heating and cooling test of rubidium in a minicell with improved fabrication method (crimped minicell) 93

Fig 4.10 Atomic density evolution with cycles of heating and cooling. Crimped minicell (stars), Non-crimped minicell (circles); X-axis: 1: before heating. 2: after first heating and cooling cycle. 3: after second heating and cooling cycle. 4: after third heating and cooling cycle. Y-axis: atomic density normalized to the original value at 1..... 94

Figure 4.11 (a) Rubidium absorption spectra of minicells with no buffer gas (squares) and 2 torr buffer gas (circles). (b) Absorption spectra linewidths of minicells with no buffer (squares) and 2 torr buffer gas (circles)..... 96

Figure 4.12 Experiment setup of Rb spectroscopy in Rb loaded ARROW 97

Figure 4.13 (a) Rb absorption spectra at different temperatures with bulk cell; (b) Rb absorption spectra at different temperatures with Rb loaded ARROWs. 98

Figure 4.14 The absorption linewidths are extracted for both bulk cell (solid

circles), Rb loaded ARROWs (open squares), and theoretical values (open circles) v.s. different temperatures. 99

Figure 4.15 The fitting of Rb absorption spectra in both bulk cell and Rb loaded ARROW..... 101

Figure 4.16 Sketch of setup and result of linear (a) Rb spectroscopy and Saturated (b) Rb spectroscopy..... 103

Figure 4.17 Illustration of cause for crossover dips..... 106

Figure 4.18 The experimental setup of SAS in Rb loaded ARROW..... 109

Figure 4.19 Saturated absorption spectroscopy in Rb loaded ARROW. 110

Figure 4.20 The fitting results of SAS experiments in bulk cell (a) ^{87}Rb F=2 transition (b) ^{85}Rb F=3 transition (c) ^{85}Rb F=2 transition 115

Figure 4.21 The fitting results of SAS experiments in bulk cell (a) ^{87}Rb F=2 transition (b) ^{85}Rb F=3 transition (c) ^{85}Rb F=2 transition 118

Figure 5.1 Three type of EIT configurations: (a) Lambda type; (b) Vee type; (c) Ladder type 120

Figure 5.2 Experimental setup of Lambda type EIT..... 122

Figure 5.3 Transmission spectrum of Lambda type EIT in bulk Rb cell..... 123

Figure 5.4 The experimental setup for V-type EIT 125

Figure 5.5 Transmission spectrum of Vee type EIT..... 126

Figure 5.6 Experimental setup of LIAD in minicells. 129

Figure 5.7 LIAD experiments in (a) no coating minicell (b) SiO_2 coating minicell

(c) SiN coating minicell (d) ODMS coating minicell 133
Figure 5.8 Light induced density increase v.s. temperature 134
Figure 5.9 Atomic density increase v.s. desorption laser power 135
Figure 5.10 Dynamic LIAD v.s. exposure time 136
Figure 5.11 Lambda type EIT experiment setup in minicell 137
Figure 5.12 EIT spectra in minicells for different coupling powers: (a)P_c=10mW (b)P_c=5mW (c)P_c=1mW 141
Figure 5.13 EIT transparency percentage (filled circles) vs coupling Rabi frequency. 142
Figure 5.14 Experimental setup for EIT in Rb loaded ARROW 143
Figure 5.15 EIT spectra in Rb loaded ARROWs with different coupling powers 150
Figure 5.16 EIT depth vs coupling power in Rb loaded ARROW 151
Figure 5.17 The flow chart for fitting of EIT spectrum 153
Figure 5.18 Fitting of EIT spectra in Rb loaded ARROWs. (a) Fitting with 100% coupling power (b) Fitting with 80% coupling power (c) Fitting with 60% coupling power (d) Fitting with 40% coupling power (e) Fitting with 20% coupling power 156
Figure 5.19 The calculated EIT spectra with different waveguide loss 158
Figure 5.20 Flow chart of EIT spectrum fitting with waveguide loss 159
Figure 5.21 Fittings of EIT spectra with waveguide loss: (a) Fitting with 100%

coupling power (b) Fitting with 80% coupling power (c) Fitting with 60% coupling power (d) Fitting with 40% coupling power (e) Fitting with 20% coupling power..... 162

Figure 5.22 EIT spectra with coupling frequency detuning with different coupling powers (a) 100% coupling power (filled circles); (b) 80% coupling power (filled squares); (c) 60% coupling power (open circles)) 164

Figure 6.1 Experimental setup of slow light in Rb loaded ARROW..... 167

Figure 6.2 The Lambda type EIT used for slow light experiment..... 168

Figure 6.3 Experimental result of slow light with different coupling powers: (a) 100% full coupling power (b) 80% full coupling power (c) 60% full coupling power (d) 40% full coupling power..... 171

Figure 6.4 (a) Pulse delay v.s. Coupling power (b) Pulse broadening vs Coupling power..... 172

Figure 6.5 Reference pulse (input pulse) is plotted with $sech^2$ pulse shape compared to the experimental data. 173

Figure 6.6 (a) Fitting of EIT spectrum with full coupling power and (b) β_2 (the second order derivative of refractive index respect to frequency) v.s. probe frequency with full coupling power..... 175

Figure 6.7 Simulations of output pulses from Rb loaded ARROWs: (a) 100% full coupling power (b) 80% full coupling power (c) 60% full coupling power (d) 40% full coupling power..... 178

Figure 6.8 The group velocity and group index vs coupling power (experimental data of group velocity (open circles) and group index (filled squares) versus relative coupling laser power. The lines represent parameter-free calculations based extracted from the EIT spectrum) 180

Figure 6.9 Experiment (symbols) and theory (lines) are compared for pulse delay and pulse width. 181

Figure 6.10 Simulations of output pulses with waveguide loss: (a) 100% full coupling power (b) 80% full coupling power (c) 60% full coupling power (d) 40% full coupling..... 185

Figure 6.11 Pulse width with different coupling powers (stars: experimental data; solid line: calculations with waveguide loss; dashed line: calculations with single Rabi frequency) 186

Figure 7.1 Four-level system for parametric oscillation generation 191

Figure 7.2 (a) The efficiency of parametric generation v.s. pump power (with the fixed signal power at 10nW). (b) The efficiency of parametric generation v.s. pump power.and signal power (with the fixed pump power at $1\,\mu W$). 194

Figure B.1 AL3 – Epoxy (The absorption decreased dramatically after one cycle of heating and cooling, in the second round heating and cooling, absorption signal can only be observed when heated to 60c)..... 203

Figure B.2 AL4 – Gold (No degradation. There is less than 5% atomic density variation with three cycles of heating and cooling.) 204

Figure B.3 AL5 – Chromium (No degradation. There is less than 5% atomic density variation with three cycles of heating and cooling.) 205
Figure B.4 AL6 – Palladium (No degradation. There is less than 5% atomic density variation with three cycles of heating and cooling.) 206
Figure B.5 AL7 – Plexiglass (Some degradation, 85.53% atomic density remains after three cycles of heating and cooling.) 207
Figure B.6 AL8 - Aluminum (Some degradation, 81.13% atomic density remains after three cycles of heating and cooling.) 208
Figure B.7 AL9 –Tin (Some degradation, 85.92% atomic density remains after three cycles of heating and cooling.) 209
Figure B.8 AL10 - Nickel (No degradation. There is less than 5% atomic density variation with three cycles of heating and cooling.) 210

List of Tables

Table 2.1 Design parameters of self aligned pedestal ARROWs..... 44

Table 5.1 The desorption techniques used in PCF based experiments 128

Table 5.2 Fitting parameters of coupling Rabi frequencies and EIT transparency depths at different input coupling powers..... 157

Table A.1 Coupling lens calculation 199

Table A.2 Calibration of TEC plate for ARROW chip testing..... 200

Table A.3 Calibration of oven box for minicell testing 201

Table B.1 Summary of material compatibility testing 211

Abstract

RB CELL INTEGRATED HOLLOW CORE WAVEGUIDE DEVICES FOR SPECTROSCOPY AND QUANTUM COHERENCE APPLICATIONS

by

Bin Wu

The motivation behind the current trend towards miniaturization of optical communication devices is to pursue robustness, efficiency, versatility, and low cost. Integrated optical devices for communication network are, therefore, very desirable. For instance, optical delay lines and optical data storage units can provide innovative solutions to the next generation of all-optical network which would greatly overcome the bandwidth and speed limitations of the current telecommunication network. The emergence of an integrated optical logic unit on the chip scale will be compatible with today's mass production in semiconductor industry and hence have the potential to be integrated in the future photonic circuit for all optical network.

Clearly, the debut of the on chip optical logic units would be a revolution for present opto-electronic based telecommunication network. Here, we propose a novel integrated optical device based on anti-resonant reflecting optical waveguide (ARROW). The confinement of light inside the low index medium in such a waveguide structure is coming from the high reflection coefficient from the multilayer structure around the core acting as a Bragg reflector. After taking all the fabrication reality into

consideration, the design of this new type of waveguide is optimized. A type of new waveguide called self-aligned pedestal (SAP) waveguides was developed and the loss value was improved more than twice compared to the previous waveguides. Effective light guiding is achieved in this hollow core ARROW waveguide, which is then used as the platform to integrate Rb vapor cell on top for spectroscopy and quantum optics experiments based on a quantum coherence effect called electromagnetically induced transparency (EIT).

Aside from being able to guide light into and out of the Rb cell integrated waveguide, we demonstrated the first linear and nonlinear Rb spectroscopy on a chip. The optical density is comparable with the commercially available Rb cell at higher temperatures. Moreover, electromagnetically induced transparency (EIT) is realized on this self-contained Rb cell integrated ARROW chip which has great potential for applications as optical buffers, optical data storage, and optical switching. Based on this EIT effect, we demonstrated the first slow light experiment in atomic vapors on chip. The group velocity of the light pulse can be slowed down by a factor of 1200 as the world record with our Rb cell integrated device which opens a new direction for on-chip-scale optical logic unit devices.

Acknowledgement

I would like to express my deep and sincere gratitude to my advisor, Prof. Holger Schmidt. His wide knowledge and his logical way of thinking have been of great value for me. His understanding, encouraging and personal guidance have provided a solid basis for the present thesis. Without his continuous support, I would not be able to accomplish all the research work I have done.

I would also like to thank the other members of my committee, Prof. Claire Gu, and Prof. Jin, Zhang, for their various directions and contributions.

I am especially indebted to Prof. Aaron R. Hawkins, John Hulbert, Katie Hurd and Evan Lunt for providing me with so many great samples and for many useful discussions.

I am very grateful to Dr. Wenge Yang for his direction on conducting the general spectroscopy and EIT experiment in rubidium cell.

I would also like to acknowledge Mark Oehlberg for helping me with frequency stabilization of the external cavity diode lasers.

Special thanks to Mr. Robert Hoelle for his direction on utilizing FIB and SEM.

I have greatly enjoyed working with many students here at UCSC and I want to especially thank Dr. Philip Measor, Mikhail Rudenko, Rebekah Brandt, Jason Mcdowell, Kaelyn Leake, Yu Yahagi, Shou Liu, as well as some former members Dr. Dongliang Yin, Dr. Suqin Wang, Dr. Aiqing Chen and Dr. Zhigang Liu for all their advices and discussions of all aspects of life.

The writing of a dissertation can be a lonely and isolating experience, yet it is obviously not possible without the personal and practical support of numerous people. Thus my sincere gratitude goes to my parents Xida Wu and Wenhua Chang, my husband Xinghua Hu, and my friends Meng Zhang and Xuchu Hu, Chenyu Zhang, Zak, Amanda, Sue, Alice, Nacici Xie, Jessie, Higgle, Jiligulu et al.

Introduction

1.1 Motivation

Today's network of information is still based on the original model of the computer network which was initially established by Advanced Research Projects Agency (ARPA) funding the design of the Advanced Research Projects Agency Network (ARPANET). With the development of information science and technology, network today has reached an extremely high level of performance, such as the speedy and reliable information exchange in between servers and users, the increasing compatibility of carrying information for communications.

One of the biggest advances in present computer networks, such as internet, is the utilization of optical fibers as the information transmission media for communication purposes. Optoelectronic technology and optical networking have become the key to enabling the communications infrastructure through the enormous increase of bandwidth and the large decrease of bit-error rate inherent in traditional electromagnetic signal-based communications. Hence, this is one of the most important evidences to show that photonics is a relatively promising candidate for replacing today's radio frequency based network which is limited by the speed of electrons.

Moreover, from the angle of fundamental physics, Einstein's special relativity theory sets up an upper limitation of the speed of the information transmission which is the

vacuum speed of light. In this sense, an all-optical network is possibly the most reachable advanced network based on today's understanding of nature.

As we all know, the present network still heavily relies on electronic components for information storage, switches, routers etc. which are all necessary for networks functioning. In order to build up an all optical network, all the components mentioned above should be possibly replaced by corresponding optical counterparts, such as optical switches, optical buffers, and optical data storage units.

There have been intensive researches towards the realization of optical networks [1-25].

From all these research work, we can see that all-optical network is definitely an ultimate goal for scientists and engineers related to these specialized fields to achieve.

As an important example, optical logic continues to develop new capabilities. Recently, at Harvard, researchers were able to slow and then stop (hold stationary) a pulse of light [74]. The immediately visible opportunities are for better optical memories and to manage data rates inside a device. More opportunities will appear in information storage and information buffering units. Moreover, scientists also demonstrated all optical switching based on different technologies. [111].

All optical information processing technology which can be practically utilized in networks should have two fundamental characteristics: functioning feasibility and integrating compatibility. Feasibility means that the technology using for optical

information processing should exhibit the proper functions of logic units, such as delay, switching and storage. At the same time, integration compatibility indicates the possibility of scaling down the logic units into a miniaturized size so that it can be really and finally used for mass production compatible with today's semiconductor industry.

In this work, we proposed a way of achieving the above mentioned two aims simultaneously with a self-contained Rb cell integrated with hollow core anti-resonant reflection optical waveguides (ARROWs). With this integrated and miniaturized device, we can actually manipulate light for information processing applications such as optical buffer, optical switching, and optical information storage based on a quantum coherence effect named electromagnetically induced transparency (EIT).

1.2 Introduction of electromagnetically induced transparency

There are many approaches of realizing optical information processing, such as optical buffers for pulse delay, optical information storage and fast optical switching. One possible and promising method is electromagnetically induced transparency (EIT) which refers to a quantum interference phenomenon involving with two optical fields known as coupling and probe fields [84]. With the presence of a strong coupling field, the optical response of an atomic medium can be modified due to the laser-induced

coherence of atomic states. An atomic level scheme for EIT is shown in figure1.1. This leads to the quantum interference between the excitation pathways between atomic energy levels. In this case, the optical response of the atomic medium changed in the form of eliminating the absorption of the weak probe field as shown in figure1.2.

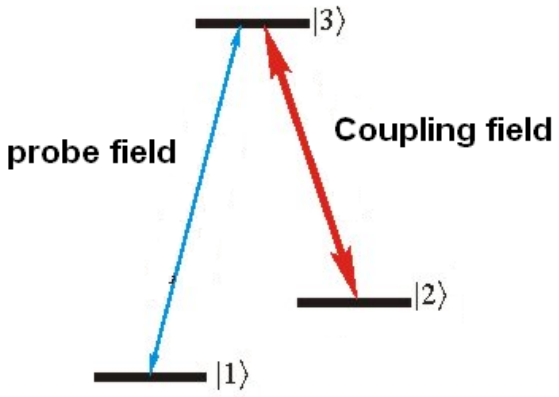

Figure 1.1 Three-level scheme for EIT

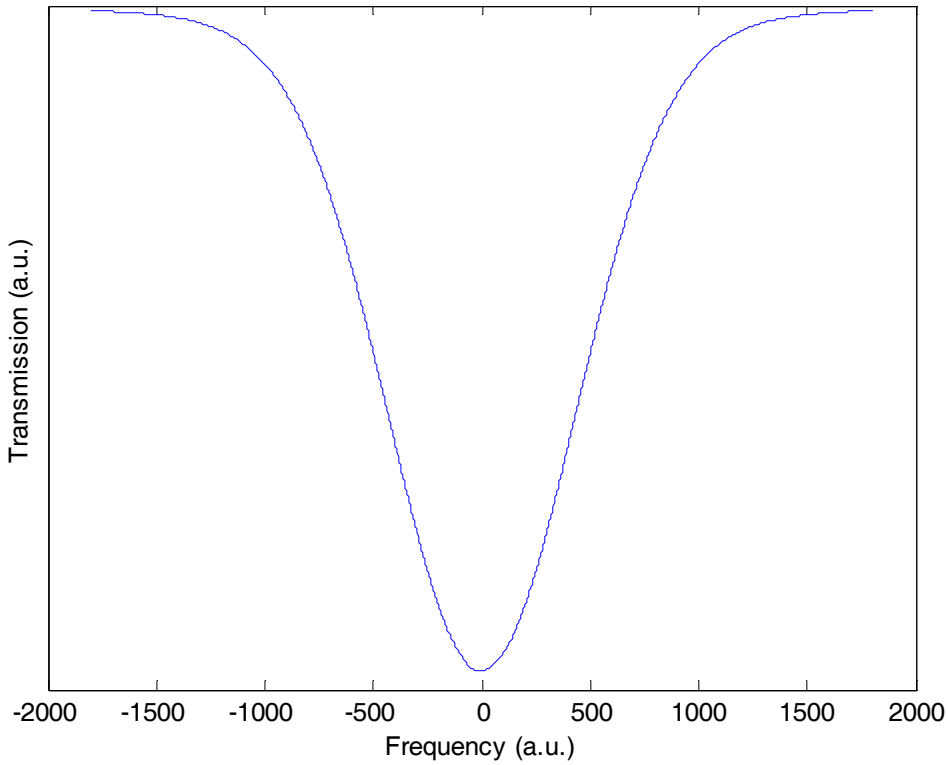
Transmission (a.u.)
-2000
-1500
-1000
-500
0
500
1000
1500
2000
Frequency (a.u.)

(a)

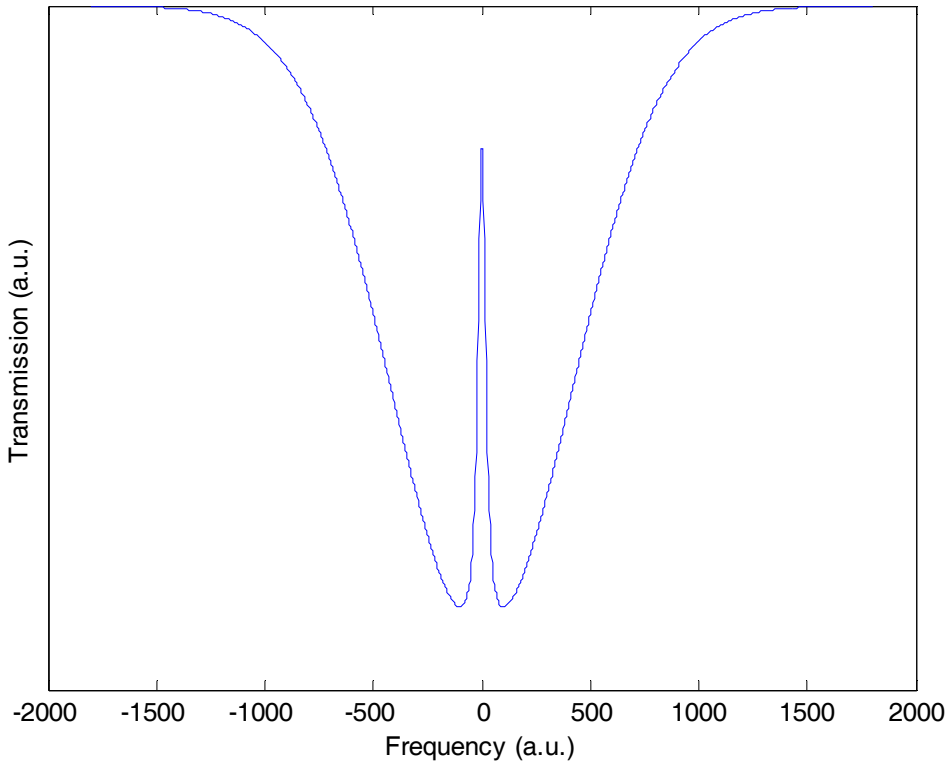

(b)

Figure 1.2 (a) Normal transmission curve with atomic absorption (b) Transmission curve with EIT

With this fore-mentioned feature, the transmission of a continuously detuned probe field would have a narrow transparency window [figure1.2(b)] across the atomic resonance which in turn gives a modified steep dispersion curve around the narrow transparency window [figure1.2 (b)] due to the Kramers–Kronig relation

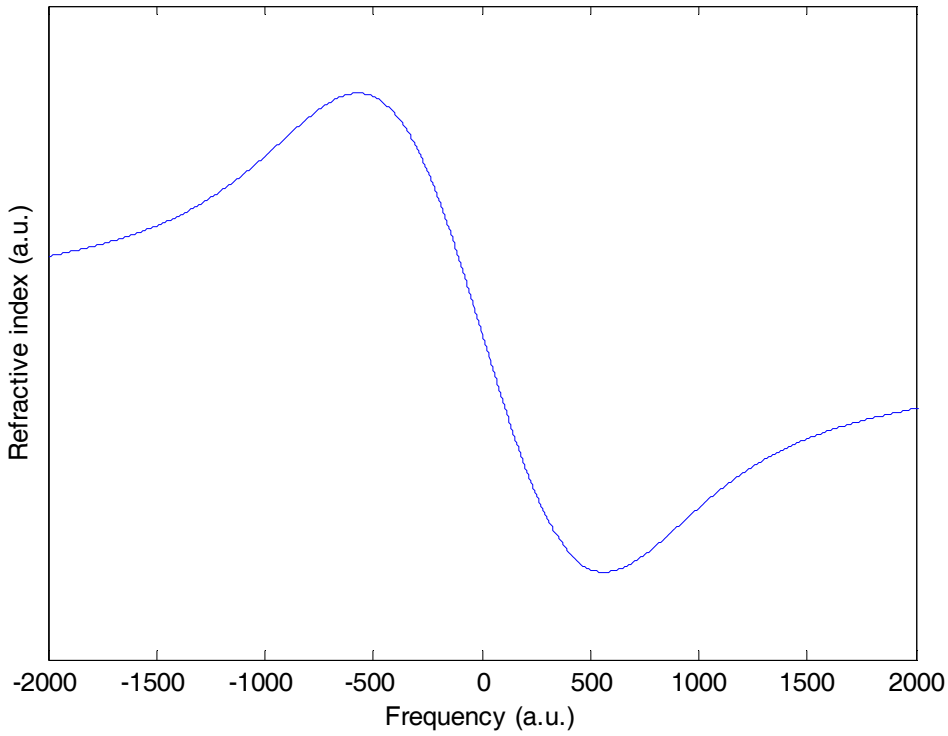
Refractive index (a.u.)
-2000
-1500
-1000
-500
0
500
1000
1500
2000
Frequency (a.u.)

(a)

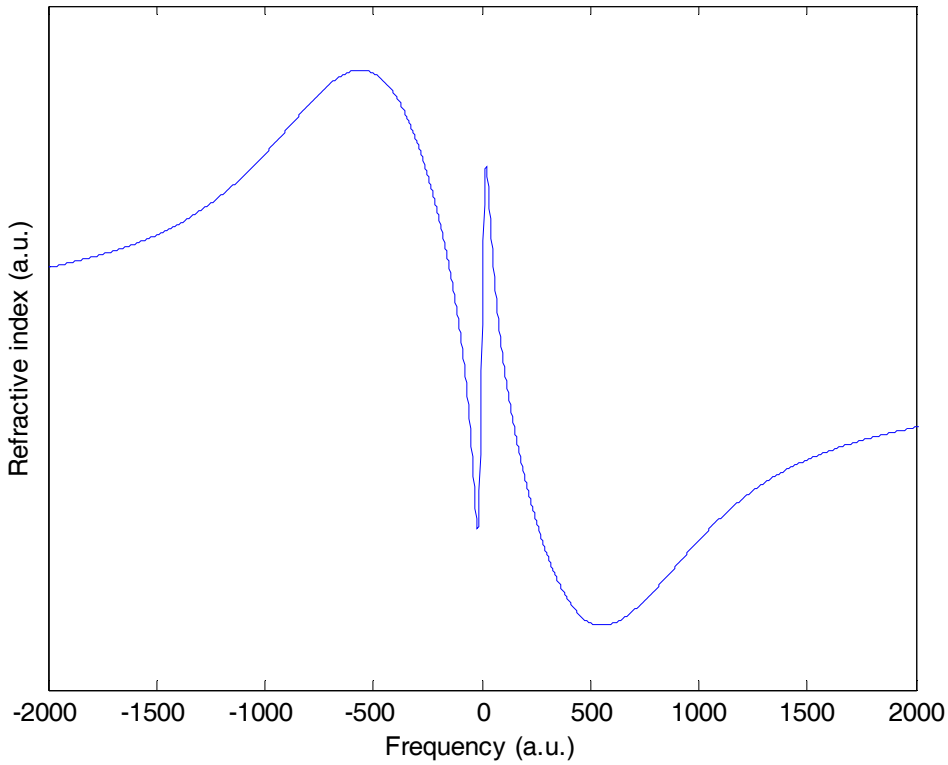

(b)

Figure 1.3 (a) Normal dispersion curve with atomic absorption (b) Dispersion curve with EIT

The absorption of a light field inside the medium can be described by taking the imaginary part of the linear susceptibility mathematically representing the linear response of an atom to light field. Meanwhile, the real part of the linear susceptibility χ physically represents the refractive index. Therefore, both the transmission spectrum and the dispersion curve (the index response versus optical frequency) of a weak probe

field can be changed by introducing a strong coupling field based on this EIT technique. Figure1.2 and figure 1.3 show the comparison between the normal atomic absorption and dispersion curves and the EIT absorption and dispersion curves.

With the modification of its linear susceptibility, the large dispersion curve gives rise to a large refractive index change within a certain spectral range i.e. a large group index ($n_g = n + \omega(dn/d\omega)$). This large n_g would result in a prominent slow down of group velocity ($v_g=c/n_g$) which is termed as 'slow light'. This technique can be directly used as an optical buffer for pulse (working as information carrier) delay. Furthermore, the speed of light pulse can be conveniently controlled by changing the power of the coupling laser. With the decrease of coupling power, the speed of light pulse can be further reduced.

In particular, if the coupling beam is turned off after the probe signal pulse has been compressed into the EIT medium, its group velocity is reduced to zero. At this point, information originally carried by the photons (pulse shape, amplitude, length, polarization, etc.) is fully mapped onto the long-lived ground or spin states of the atoms. As long as this "light storage" is sufficiently smooth, it always remains within the transparency window. The stored light pulse can be easily retrieved by simply turning the control beam back on and thus opens the possibility of optical information storage. Moreover, with this EIT effect, not only the linear susceptibility of the medium is modified, the higher order nonlinear susceptibility associated with various nonlinear

optics effects is also modified. In fact, it can greatly enhanced nonlinear optics effects originated from its large increase of the nonlinear susceptibilities while maintaining the problem unabsorbed, such as nonlinear Kerr effect [26], parametric oscillations [27], sum frequency generation [112], all-optical switching [113]. which can find many applications in all optical network.

1.3 Motivation for using rubidium

As a result, EIT is a very promising technique for achieving various critical components in optical information process. There are several media for establishing this quantum coherence effect which have been demonstrated recently including both gas and solid state materials such as in [28, 29, 30, 31]. Among all these media, alkali atomic vapor may be one of the most favorable candidates. Since alkali metals such as Rubidium or Cesium have remarkable optical properties which make their vapors very attractive for numerous applications. These include well-established uses in precision spectroscopy as frequency standards or references [1,2]. For example, narrow spectral features on the order of the natural atomic linewidth can be the standards for frequency stabilization of a semiconductor laser by sending a small portion of the laser into an atomic vapor and feeding the transmitted signal back to the laser diode controller. Alternatively, these features are used as the references for atomic clocks. More recently, alkali vapors have been the subject of intense research on optical quantum coherence

effect. Due to the existence of long-lived metastable electronic states in the hyperfine levels of the alkali atoms, it is possible to establish long time coherences between these electronic states that have significant impact on the optical properties of medium. As a result, numerous optical effects have been observed in alkali vapor including EIT, slow light, stopped light, highly efficient nonlinear optics effects such as four wave mixing, paired photon generation and cross phase modulation. [31,34-38]. Therefore, in our system, we employ rubidium vapor as the medium to realize EIT as well as many other effects based on EIT (such as slow light, nonlinear optics). In order to introduce the gas phase medium in the industrially compatible 2D waveguide platform, a hollow core for confining Rb atoms needs to be constructed within the waveguide structure and light guiding in this hollow core region is required for the interaction of both coupling and probe fields with the Rb atomic vapor.

1.4. Introduction of Rb spectroscopy with Doppler Broadening

1.4.1 Doppler broadened Rb spectroscopy

An energy diagram of Rubidium D2 line is shown in figure 1.4. [121]

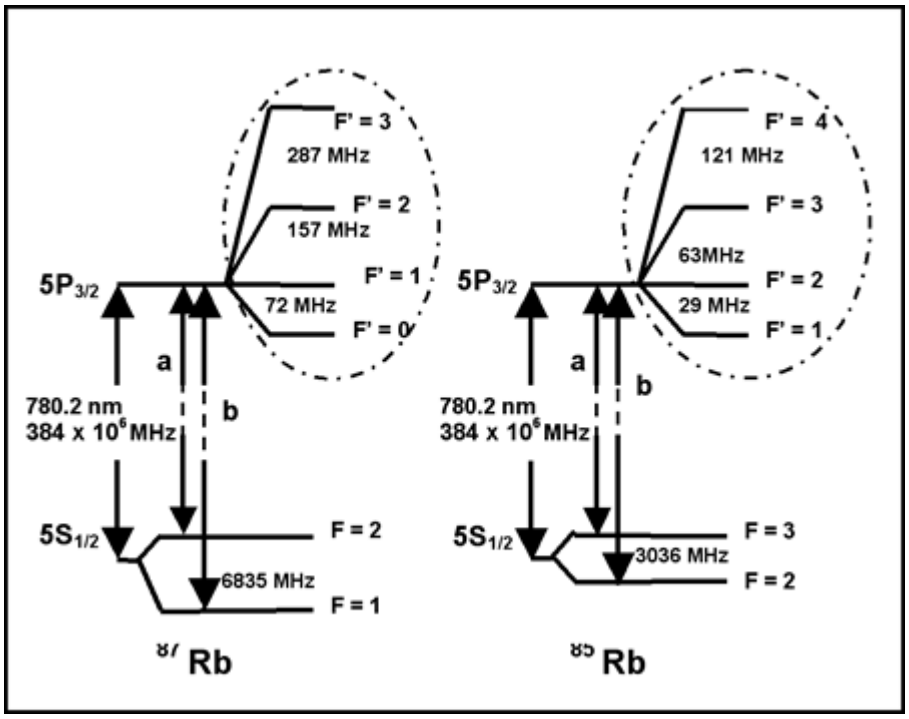

Figure 1.4 Rubidium energy diagram

The full spectrum, revealing the four absorption peaks, is known as the Doppler broadened spectrum as shown in figure 1.5. The resolution limit for atomic spectra in the visible region is often determined by Doppler broadening. The frequency of the light emitted by an atom will be Doppler shifted because of the thermal motion of the atoms. A stationary detector measuring the frequency of the light emitted by atoms traveling towards or away from the detector with speed v will measure a Doppler shift towards a higher or lower frequency, respectively, when compared to the frequency of light emitted by the same species of atoms at rest. The light from a stationary source absorbed by atoms traveling towards or away from the source with speed v will have a lower or higher frequency, respectively, than that absorbed by atoms at rest.

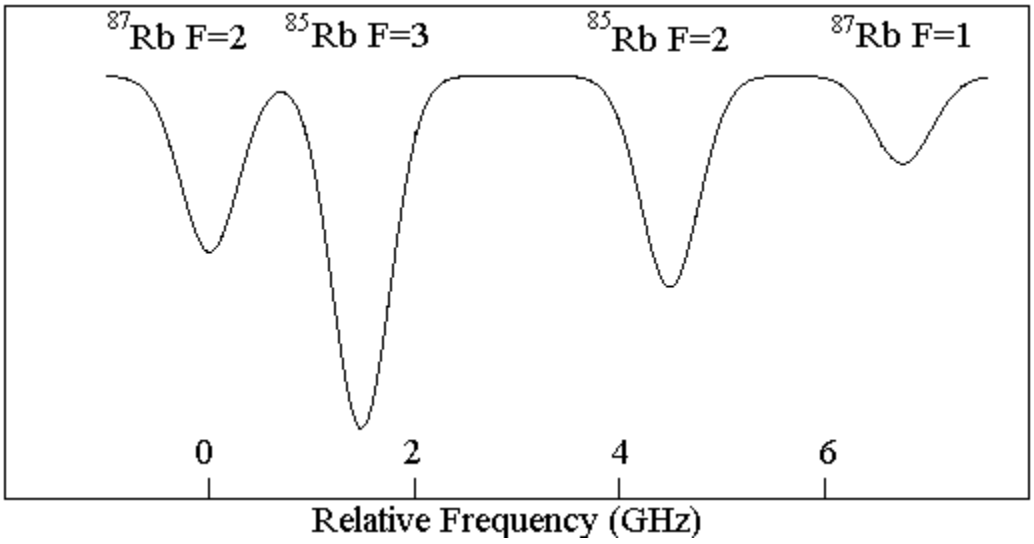

Figure 1.5 Rb spectrum (D2 line) with Doppler broadening

1.4.2 Doppler broadened linewidth extractions

The transmission (output intensity) curve of a Rb absorption dip can be calculated as the following equation:

$$I_{out} = I_{in} \exp^{-\alpha L} \quad (1.1)$$

Where α (the absorption coefficient between level i and j) is given by:

$$\alpha = \frac{\omega_{ij} n_0}{c} \frac{N \mu_{ij}^2}{\hbar \gamma_{ij}} \frac{1}{1 + \frac{\Delta \omega_{ij}}{\gamma_{ij}}} \quad (1.2)$$

Where ω_{ij} is the atomic resonance frequency, n_0 is the refractive index at this

frequency, c is the speed of light at vacuum, N is the atomic density, μ_{ij} is the dipole moment of the transition, $\Delta\omega_{ij}$ is the laser detuning deviated from ω_{ij}, γ_{ij} describes the absorption dip linewidth which is related to the Doppler broadening by the following equation:

$$\Delta\omega_d = 2\gamma_{ij} \quad (1.3)$$

So the spectrum profile of Doppler broadening is given by:

$$I_{out} = I_{in}(1/\sqrt{2}\pi\Delta\omega_d)\exp(-(\omega-\omega_0)^2/(2\Delta\omega_d{}^2)) \quad (1.4)$$

$\Delta\omega_d$ is the Doppler width (FWHM), ω_0 is the central angular frequency. As a result, the Doppler width as well as the atomic density can be extracted by fitting this Gaussian type curves for multi Rb absorption peaks (transmission dips).

1.5 Introduction to Slow Light

1.5.1 Theory of slow light

The subject of slow light has caused keen interest in the past decade, mostly because of the groundbreaking successes of achieving very slow propagation velocity [73] and stopping the light entirely [74]. Following these pioneering results, a large amount of work has been performed in recent years, with slow light propagation attained in diverse media such as metal vapors with and without electromagnetically induced transparency (EIT), rare-earth-doped materials, Raman and Brillouin fiber optical

amplifiers, photonic crystal waveguides, and microresonators. A number of interesting linear and nonlinear optical devices have been proposed, including optical buffers, switches, and interferometers. [105-109]

It should be mentioned that the history of light propagating with reduced group velocity goes back to the 19th century when the classical theory of dispersion of electromagnetic waves was first formulated. Slow wave propagation was also observed and widely used in the microwave range as early as the 1940s [75]. The first experimental observation of slow light in the nonlinear regime was made in 1967 by McCall and Hahn when they studied the effect of self-induced transparency in ruby [76]. Soon afterward Grischkowsky and others observed slow light in the linear regime [77].Yet it was only with the discovery of EIT that slow light science was given a strong impetus—and this can be explained by the simple fact as we have mentioned before that EIT is a promising method of obtaining strong optical resonance without extensive loss and dispersion.

With all the diversity of slow light schemes they can be all characterized by a single common feature—the existence of a sharp single resonance or multiple resonances. The resonance can be defined by a simple atomic transition, by a Bragg grating, by a microresonator or other resonant photonic structure, or by an external laser as in the schemes involving various nonlinear processes—resonant scattering, spectral hole burning, or four-wave mixing.

1.5.2 Fundamental theory of slow light

As shown in figure 1.6, the energy diagram in a two level atomic system is as following:

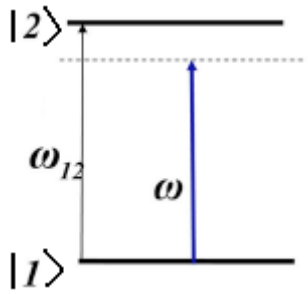

Figure 1.6 Two level atomic system

The complex refractive index as $\tilde{n}(\omega) = \varepsilon^{1/2}(\omega)$, and for the frequencies relatively close to the resonance $|\omega_{12} - \omega| \ll \omega$, we obtain:

$$\begin{aligned}\tilde{n}(\omega) &= \left(\overline{n}^2 + \frac{\Omega_p^2}{\omega_{12}^2 - \omega^2 - j\omega\gamma_{12}} \right)^{\frac{1}{2}} \\ &\approx \overline{n} + \frac{1}{2\overline{n}} \frac{\Omega_p^2}{\omega_{12}^2 - \omega^2 - j\omega\gamma_{12}} \\ &\approx \overline{n} + \frac{1}{4\overline{n}\omega} \frac{\Omega_p^2(\omega_{12} - \omega)}{(\omega_{12} - \omega)^2 + \gamma_{12}^2/4} + \frac{j}{8\overline{n}\omega} \frac{\Omega_p^2 \gamma_{12}}{(\omega_{12} - \omega)^2 + \gamma_{12}^2/4}\end{aligned} \quad (1.5)$$

From real and imaginary parts of equation (1.4) the absorption coefficient can be

expressed by:

$$\alpha(\omega) = \frac{2\omega}{c}\,\mathrm{Im}(\tilde{n}) \approx \frac{1}{4\bar{n}c}\,\frac{\Omega_p^2\gamma_{12}}{(\omega_{12}-\omega)^2+\gamma_{12}^2/4} \qquad (1.6)$$

And the refractive index is given by:

$$n(\omega) = \mathrm{Re}(\tilde{n}) \approx \bar{n} + \frac{1}{4\bar{n}\omega}\,\frac{\Omega_p^2(\omega_{12}-\omega)}{(\omega_{12}-\omega)^2+\gamma_{12}^2/4} = \bar{n} + \frac{c}{\omega}\alpha(\omega)\frac{\omega_{12}-\omega}{\gamma_{12}} \qquad (1.7)$$

The absorption spectrum presents a Lorentzian peak with a full width at half maximum (FWHM) of exactly γ_{12} .The last relation in equation (1.6) and (1.7) is a particular form of the more general Kramer–Kronig relation between the real and the imaginary parts of dielectric constant,

$$\mathrm{Re}\big(\varepsilon(\omega)\big) = 1 + \frac{1}{\pi}P\int_{-\infty}^{\infty}\frac{\mathrm{Im}(\varepsilon(\omega'))}{\omega'-\omega}$$

$$\mathrm{Im}\big(\varepsilon(\omega)\big) = -\frac{1}{\pi}P\int_{-\infty}^{\infty}\frac{\mathrm{Re}(\varepsilon(\omega'))-1}{\omega'-\omega} \qquad (1.8)$$

Let us now consider a plane wave of frequency ω propagating in the medium defined by equation (1.5) and (1.6):

$$E(z,t) = E_0\exp(jkz - j\omega t) \qquad (1.9)$$

With the wave vector,

$$k(\omega) = n(\omega)\frac{\omega}{c} \qquad (1.9)$$

The velocity with which the phase of the plane wave propagates,

$$v_p(\omega) = \frac{\omega}{k} = \frac{c}{n}(\omega) \qquad (1.10)$$

deviates from its background value $c / \overline{n}$ near the resonance, but, as mentioned above, these changes do not lead to the slow light phenomenon. In fact, the phase velocity is meaningful only for purely monochromatic light, i.e., for the harmonic wave with no features, which carries no information. The information propagates in the form of a wave packet comprising more than a single frequency. In this section, we consider a Gaussian wave packet with the FWHM equal to Δt :

$$E(t) = E_0 e^{-2\ln 2(\frac{t^2}{\Delta t^2})} \qquad (1.11)$$

The frequency spectrum of the Gaussian wave packet is also Gaussian:

$$E(\omega) = E_0^2 e^{-4\ln 2[\frac{(\omega-\omega_0)^2}{\Delta\omega_{1/2}^2}]} \qquad (1.12)$$

where the spectral FWHM $\Delta\omega_{1/2}$ is:

$$\Delta\omega_{1/2} = \frac{4In2}{\Delta t} \qquad (1.13)$$

The envelope of the wave packet propagates with the group velocity defined as the slope of the dispersion curve

$$v_g = \frac{\partial\omega}{\partial k} \qquad (1.14)$$

Therefore,

$$v_g^{-1}(\omega) = \frac{\partial k(\omega)}{\partial \omega} = \frac{1}{c}\left(n(\omega)\omega + \omega \frac{\partial n(\omega)}{\partial \omega} \right) = v_p^{-1}(\omega) + \omega \frac{\partial n(\omega)}{\partial \omega} \tag{1.15}$$

Clearly the group velocity can be significantly smaller or larger than the phase velocity, depending on the sign of the derivative of the index in equation (1.15).

1.5.3 Double Atomic Resonance Reduces Dispersion

The first practical slow light results were achieved by using the phenomenon of EIT [78,79], where the double resonance is created by strong coupling beam, the main features of the double-resonant atomic schemes can be understood more easily if one considers that closely spaced narrow resonances do occur naturally in metal vapors, such, as, for instance, in ^{85}Rb [80], where two D2 resonances near 780 nm separated by 3 GHz have been used in the most successful slow light experiments in atomic medium.

1.5.4 Tunable Double Resonance and Electromagnetically Induced Transparency

The double atomic resonant scheme described cannot be adapted to variable bandwidth because the width of the pass band cannot be changed. To change the pass band width, one can consider the alternative of spectral hole burning in the inhomogeneously broadened transition [81,82]. A strong pump pulse creates a situation in which the absorption in the frequency range becomes depleted. The profile of the absorption

spectrum is remarkably like the double-resonant profile. With the refractive index profile shown in figure 1.7, one can see that a strong reduction of group velocity can be expected near the center of the spectral hole.

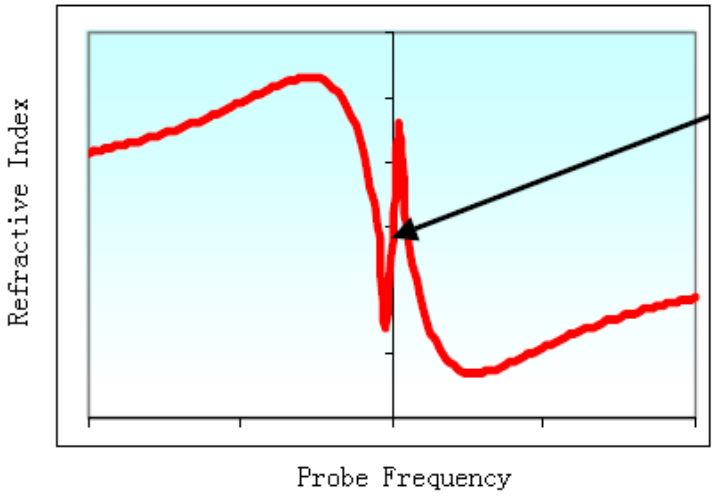

Figure 1.7 Refractive index profile for slow light in EIT

By changing the spectrum of the coupling, for instance, using intensity or frequency modulation, one can change $\Delta\omega$ [83] to achieve the maximum delay without distortion for a given bit rate. In ref [83], delays of 2 bit intervals were achieved for a moderate bandwidth of 100 MHz but only in a 40 cm long Rb vapor delay line. Since the background absorption in the hole burning is always high, it is the dispersion of loss that causes the signal distortion and is in fact an ultimate limitation in this scheme. The scheme also suffers from the large energy dissipation as the coupling is absorbed. To avoid large background absorption and to achieve wide pass band tenability one uses an entirely different slow light scheme based on EIT, first considered by Harris

[84–86].

Thus the slow light effect has a rather simple physical interpretation. While in the simple single or double-resonant slow light scheme the energy is transferred from the electromagnetic wave to the atomic excitation and back, in the EIT scheme the process involves more steps, as the signal photon propagates in the EIT medium it transfers its energy to the excitation of the atomic transition. Because of the presence of strong coupling wave, the excitation is almost instantly transferred to the long-lived excitation between levels. Then the process occurs in reverse, and the energy is transferred back to the transition and finally back into the photon. Then the process repeats itself. Overall, most of the time the energy is stored in the form of atomic states excitations, and thus it propagates with a very slow group velocity. Furthermore, the actual absorption event occurs only when the excitation loses coherence and the energy cannot get back to the photon. Naturally, it is the dephasing rate of this excitation that determines the residual absorption loss.

1.5.5 Photonic Resonances: Bragg Gratings

As is already mentioned, in the case of atomic resonance the apparent slow down of light is caused by the resonant energy transfer to and from the excitation of atomic polarization. An entirely different resonance is the photonic resonance in which the energy is resonantly transferred between two or more modes of electromagnetic

radiation. When the transfer takes place between forward and backward propagating wave slow light, the group velocity is reduced, and we once again see the slow light phenomenon, but with an entirely different nature from the slow light in atomic media. [87-89]

1.5.6 Double-Resonant Photonic Structures

The photonic double resonance can be easily implemented by simply combining two Bragg gratings with slightly different periods. Such combination was first suggested for dispersion compensation [87,88] and then considered for application in electro-optic modulators [89]. As long as one deals with linear devices, such as delay lines, one can simply cascade two Bragg gratings sequentially, and the resulting dispersion curve will be simply the mean of the individual dispersion curves.

1.5.7 Coupled Ring Resonators

Coupled resonators are similar to atoms in their ability to delay the light. The slow down factors in them are not as spectacular as in EIT slow light buffers, yet they can potentially operate at much higher bit rates [116]. Another distinctive feature of all photonic structures— the slow down effect in them is the consequence of energy being transferred back and forth between the forward and the backward waves, or simply of light making circles in the ring resonator. The energy is never transferred from the

electromagnetic wave to the medium as in the case of atomic slow light schemes. As a result the strength of the electromagnetic field inside photonic structures does increase, which is very advantageous for various nonlinear optical devices. Also, as was already mentioned, the losses in photonic structures are determined only by fabrication techniques and not by the fundamental coherence times; therefore, in principle photonic structures should perform with less loss than atomic ones.

1.5.8 Slow Light in Optical Fibers

In the prior Sections, slow light in the vicinity of atomic resonance is described and photonic resonances that are always associated with loss. In the case of atomic resonance the loss is inherent and can be traced to dephasing of atomic polarization. In the case of photonic resonances the loss occurs simply because the light spends more time inside the delay line (or, in one case, it takes a longer effective path by bouncing back and forth or making circles). But it is well known that strong dispersion also takes place in the spectral vicinity of the resonant gain. The advantages of using gain are many fold: first, one is not faced with attenuation, and, second, the gain can be changed at will by changing the pump strength and spectrum—hence the delay and the bandwidth can be made tunable.

In the Stimulated Brillouin Scattering (SBS) process, a high-frequency acoustic wave is induced in the material via electrostriction, for which the density of a material

increases in regions of high optical intensity. The process of SBS can be described classically as a nonlinear interaction between the pump and a probe field through the induced acoustic wave of frequency [90]. The acoustic wave in turn modulates the refractive index of the medium and scatters pump light into the probe wave when its frequency is downshifted by the acoustic frequency. This process leads to a strong coupling among the three waves when this resonance condition is satisfied, which results in exponential amplification of the probe wave.

Tunable slow light delay via SBS in an optical fiber was first demonstrated independently by Song et al. [91] and Okawachi et al. [92]. In the experiment preformed in [91] delay could be tuned continuously by as much as 25 ns by adjusting the intensity of the pump field, and the technique can be applied to pulses as short as 15 ns. A fractional slow light delay of 1.3 was achieved for the 15 ns long input pulse with a pulse broadening of 1.4. Following the first demonstrations of SBS slow light in optical fibers, there has been considerable interest in exploiting the method for telecommunication applications. One branch of research has focused on reducing pulse distortion by reducing the distortion caused by the gain dispersion performance [93–98] by essentially trying to shape the Brillouin gain with multiple pumps. In numerous experimental demonstrations with multiple closely spaced SBS gain lines generated by a multi-frequency pump, a significant increases in slow light pulse delay was achieved as compared with the optimum single-SBS-line delay. Another branch of research has focused on broadband SBS slow light [99–103]. The width of the resonance that makes

the slow light effect possible limits the minimum duration of the optical pulse that can be effectively delayed without much distortion and therefore limits the maximum data rate of the optical system. Herraez et al. [99] were the first to increase the SBS slow light bandwidth and achieved a bandwidth of about 325 MHz by broadening the spectrum of the SBS pump field. Zhu et al. extended this work to achieve a SBS slow light bandwidth as large as 12.6 GHz, thereby supporting a data rate of more than 10 Gbits/ s [100].The latest results on expanding bandwidth are summarized in the review article [104] An alternative way to achieve tunable delays in optical fibers is via stimulated Raman scattering (SRS), which can also be achieved in optical fibers. SRS arises from exciting vibrations in individual molecules, also known as optical phonons—as opposed to exciting sound waves (acoustic phonons) as in the SBS process. The optical phonons, unlike acoustic phonons, are localized and have very short lifetimes, measured in picoseconds or fractions of picoseconds. Furthermore, in amorphous materials, such as glass, the frequencies of optical phonons are spread over a large interval (measured in terahertz)—hence the Raman gain is much boarder than the Brillouin gain, but is also much smaller in absolute value.

Sharping et al. demonstrated an ultrafast all-optical controllable delay in a fiber Raman amplifier [105]. In this experiment a 430 fs pulse is delayed by 85% of its pulse width by using SRS in a 1 km long high-nonlinearity fiber. The ability to accommodate the bandwidth of pulses shorter than 1 ps in a fiber-based system makes SRS slow light useful for producing controllable delays in ultrahigh-bandwidth telecommunication

systems.

In addition to optical fibers, SRS slow light has also been demonstrated in a silicon-on-insulator planar waveguide [106]. Since Si is a single-crystalline material, the Raman gain is concentrated into the narrower bandwidth than in glass, but this bandwidth is still sufficient for delaying short optical pulses of 3 ps for 4 ps in a very short 8 mm waveguide. This scheme represents an important step in the development of chip-scale photonics devices for telecommunication and optical signal processing. Slow light propagation was also demonstrated in Er-doped fibers [107, 108] using coherent population oscillations, but the bandwidth, related to the relaxation time in the Er ion was only of the order of kilohertz. Other methods included using the parametric gain [109] in the optical fiber as well as taking advantage of EIT in hollow optical fibers.

1.5.9 Experimental demonstrations of slow light techniques

(1). In [81]

(1.1) Media: Ruby

(1.2) Theory: homogeneously broadened absorption spectrum caused by coherent population oscillations

(1.3) Group velocity: 57.5 ±0.5 m/s

(1.4) Wavelength: Argon ion laser 514.5nm

(1.5) Conclusion: This technique for producing slow light is very easy to implement. It requires the use of only a single laser. In addition, since the location of the spectral hole follows exactly any drift in the laser frequency, the laser does not need to be frequency locked to any particular transition frequency. In fact, the laser does not even have to operate in a single longitudinal mode since all the modes will experience an identical delay. Also, since the slow light can be produced in a solid and at room temperature, this technique offers the possibility of applications in photonics such as fully integrated, controllable optical delay lines. However, the large decoherence rate in solid state materials is the main concern for application of this type of experiment.

(2). In [82]

(2.1) Media: alexandrite crystal

(2.2) Theory：the influence of coherent population oscillations involving chromium ions in either mirror or inversion sites within the crystal lattice

(2.3) Group velocity: 91m/s

(2.4) Wavelength: Arion laser that we operate at either 476 or 488 nm

(2.5) Conclusion: This phenomenon occurs as a result of coherent population oscillations between the ground and excited states in an alexandrite crystal. It needs taking account of the different absorption characteristics of Cr3+ ions in mirror or inversion sites.

(3). In [91]

(3.1) Media: silicon single mode fiber

(3.2) Theory: SBS. The long lifetime of acoustic waves in silica (about 10 ns) results in a very narrowband resonant coupling that translates into narrowband gain or loss for the interacting lightwaves. In optical fibers, the gain or loss spectral distribution faithfully follows a Lorentzian distribution, which is centred at the Brillouin frequency shift ν_B (10–11 GHz at λ = 1,550 nm) and has a 30-MHz FWHM)

(3.3) Wavelength: semiconductor 1550nm

(3.4) Tunability: ΔT can be simply and optically controlled by varying the pump power

(3.5) Group velocity: 71000 m/s

(3.6) Conclusion: Even though impressive delays were obtained in these pioneering experiments they were achieved in kilometer-long fibers, and these delays represent only a minor fraction of the total transit time. The modification of the absolute group velocity is small, far from the amazing results obtained in atomic media.

(4) In [105]

(4.1) Media: High nonlinear dispersion shifted fiber

(4.2) Theory: an all-optical tunable pulse delay scheme that utilizes the power-dependent variation of the refractive index that accompanies stimulated Raman scattering in an optical fiber.

(4.3) Delay: Using this technique, delay 430-fs pulses by up to 85% of a pulse width is

achieved.

(4.4) Group velocity: 299,999,967 m/s

(4.5) Conclusion: The ability to accommodate the bandwidth of pulses shorter than 1 ps in a fiber-based system makes this technique potentially viable for producing controllable delays in ultra-high bandwidth telecommunication systems.

(5) In [109]

(5.1) Media: dispersion shifted fiber

(5.2) Theory: Kerr optical nonlinearity has been proposed. In this process the idler wave is another optical wave and the three waves involved in the interaction are co-propagating. They must obey a phase-matching condition that is more rigorous than for SRS, but less strict when compared with SBS and its counter-propagating-wave requirement. In addition, the linewidth of the interaction can be widely tuned by carefully placing pump and signal wavelengths within the fiber dispersion curve.

(5.3) Delay: In this way, delays of up to 160 ps using 70-ps pulses were obtained in a 2-km fiber using 1 W pump power, with a bandwidth capability of many tens of gigahertz.

(5.4) Group velocity: 299,992,800 m/s

(5.5) Conclusion: Despite the lower efficiency of this parametric process when compared with stimulated scattering (SBS and SRS), this approach offers the best natural delaying capability for bandwidths of tens to hundreds of gigahertz.

(6) In [107]

(6.1) Media: Erbium doped fiber

(6.2) Theory: a very narrow resonance is created with a bandwidth essentially determined by the erbium lifetime (around 10 ms).

(6.3) Delay: large delays up to a fraction of a millisecond can be obtained, but with only a moderate bandwidth in the kilohertz range.

(6.4) Group velocity: 25,000 m/s

(6.5) Conclusion: As a result, this approach is of limited use for real signal-processing applications, but is a good tool for investigating large velocity changes.

1.6. ARROW waveguides

As discussed in the above section, an approach to confining atoms on chip is needed for achieving EIT and optical nonlinear experiments. Therefore, a low-index guiding waveguide with Rb reservoirs attached is required for filling Rb atomic vapor in the interactive waveguide core region in order to achieve EIT effect on a miniaturized and integrated platform. As the phase index of Rb atomic vapor is approximately equal to 1, the ability to confine light in a low-index core media is required. There are several ways of confining light in a hollow core area while maintaining a reasonable loss along the propagation length [39-43]. In our work, we used the self-designed and fabricated

ARROW waveguides as the platform for the Rb vapor cell integration. This ARROW based device can actually achieve complete self-contained small-scale device compared to those system using photonic crystal fiber (PCF) which may need large vacuum pump or comparatively complicated Rb loading procedure. Moreover, the suitable connections between the hollow core region and input and output light paths are built up by depositing solid core waveguides on both ends of hollow core waveguide. The figure 1.4 shows a photograph of the self-contained Rb cell integrated ARROW. Furthermore, this ARROW based device would be more compatible with today's mass production of semiconductor wafers and have the potential to be integrated with a 2D planar all optical data process module including on-chip lasers, detectors, filters, etc. Rest of the thesis will deal with all these components in details.

The principle of confining light in ARROWs is akin to Bragg reflectors in which a stack of multiple layers of alternating materials with varying refractive index and well-chosen thicknesses of these dielectric layers (waveguide cladding), resulting in periodic variation in the effective refractive index of the guiding mode. Each layer boundary causes a partial reflection of an optical wave. For electromagnetic waves whose wavelength is close to the design wavelength, the many reflections combine with constructive interference, and the layers act as a Fabry-Perot high-quality reflector. The range of wavelengths that are reflected is called the photonic bandgap. Within this range of wavelengths, light is "forbidden" to propagate in the cladding structure and thus confined in the hollow core area of the ARROW waveguides.

In our work, we have proposed and demonstrated a complete and comprehensive waveguide platform which contains both hollow core ARROW waveguides and solid rib waveguide for simultaneously achieving the purposes of confining a light mode in a hollow core region containing Rb atomic vapor and guiding light in and out with outside connections such as optical fibers and objective lenses. This complete system has the advantage of separating Rb loading path and light guiding path so that this simple Rb loading method may greatly reduce the complexity of the whole device.

Based on this Rb loaded ARROW waveguide, we have demonstrated linear Rb spectroscopy, saturated absorption spectroscopy, electromagnetically induced transparency, and slow light experiments which have indicated the great potentials for the application of our self-contained quantum coherence control Rb vapor chip in optical information process.

1.7 Chapter arrangement

In figure 1.8, a photograph of 4-inch silicon wafer with 32 atomic spectroscopy cells is shown which demonstrates the ability of potential mass production. The self contained Rb cell is integrated on an ARROW chip. The details of design, fabrication, and applications of this Rb cell integrated ARROW will be addressed in the rest of the thesis.

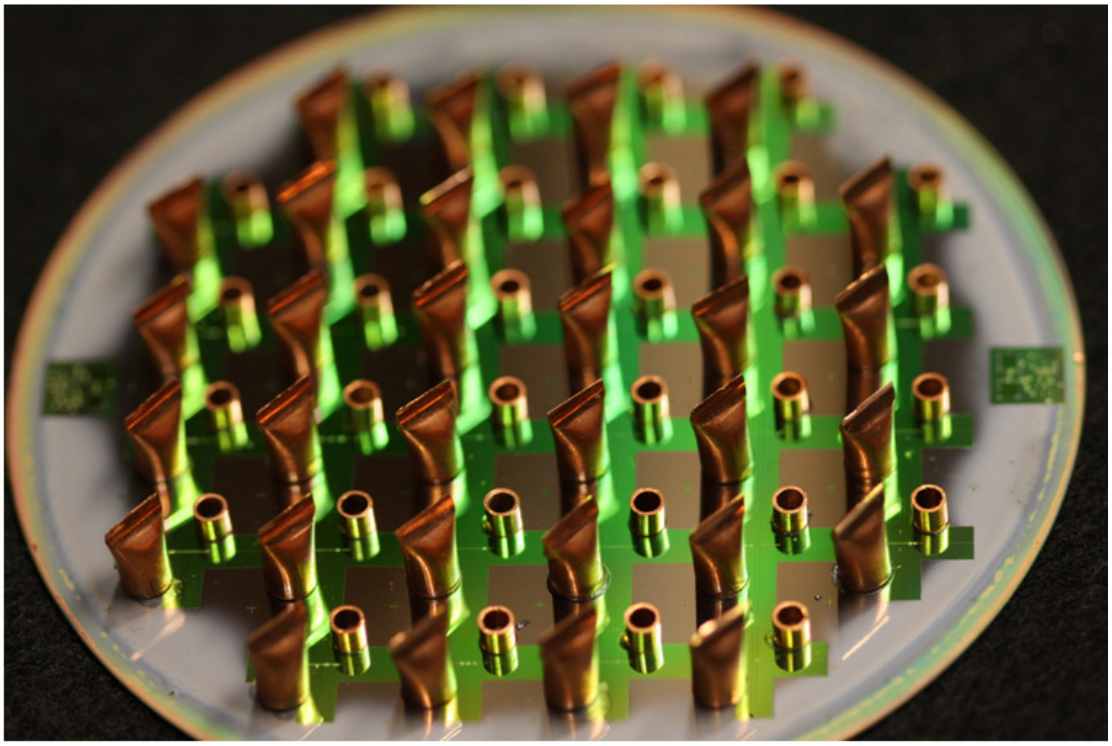

Figure 1.8 Photograph of 4-inch silicon wafer with 32 atomic spectroscopy cells

The remainder of this thesis is organized as follows. In chapter 2, the entire theory base used to design and optimize ARROW waveguides is discussed. We will elaborate on the design criteria, loss calculation, and measurement results of the ARROW waveguides. Moreover, the physics behind EIT will be addressed and discussed in details.

In chapter 3, the fabrication process and testing of the optical performance of the rubidium loaded ARROWs is presented. We also describe the loss optimization and characterize different fabrication improvements of Rb cell integrated ARROWs.

Demonstration of both linear and nonlinear rubidium spectroscopy in our rubidium cell

integrated ARROW chip is discussed in chapter 4.

In chapter 5, we present the detailed experimental results of electromagnetically induced transparency experiments. A theoretical model is constructed to fit the experiment data.

Slow down the group velocity of a light pulse based on the EIT technique and the theory of fitting this experiment are discussed in chapter 6.

Finally we conclude in chapter 7 by summarizing our work, addressing some remaining issues, and pointing out possible future directions.

Chapter 2 Theory of ARROW and EIT

This chapter is divided into two parts: the theory of anti-resonant reflecting optical waveguide (ARROW) and the theory of EIT (electromagnetically induced transparency).

For the first part, we begin with introducing the fundamental working principle of an ARROW waveguide. Then the anti-resonant condition to deduce the optimized cladding thickness is discussed. Furthermore, the details of waveguide loss calculation will be addressed including 1D and 2D ARROW models. Then a hybrid of both ridge waveguide and hollow core ARROW waveguide will be discussed and its fabrication process will be elaborated with an emphasis on implementing the Rb cell integrated on this 2D waveguide platform.

For the second part, we attempt to outline the physics of EIT by introducing the dressed state picture and density matrix formalism. Then the mechanisms of several interesting optical effects created by this EIT technique will be addressed including slow light, giant Kerr effect and parametric oscillation which may find various important applications in quantum communications.

2.1. Introduction of ARROW

Unlike conventional dielectric waveguides, an ARROW partially depends on anti-resonant reflection for wave guidance. The index of the core can be less than that of the substrate. Therefore the waveguide modes are leaky, and the radiation losses to the substrate cannot be ignored. This is especially important for the ARROW structure at the anti-resonant condition since the radiation losses of the guided modes are considerably increased.

For a rubidium cell integrated waveguide platform, the low refractive index of the rubidium vapor ($n \cong 1$) requires a low-index light guiding geometry for the effective interaction between light and medium. There are some possible ways of achieving this low-index guiding in the core region by Bragg fibers [39], photonic crystal fibers [41] or 2D photonic crystal slab waveguide [44]. The method proposed here is an approach based on the antiresonant reflecting optical waveguides (ARROWs). Light guiding in ARROWs is achieved by defining the cladding of the waveguide with multiple dielectric layers that act as Fabry-Perot reflectors.

The layer structure and the index profile of a typical ARROW waveguide are shown in Figure 2.1. The cladding layers act as Fabry-Perot cavities for propagation with the transverse wave vector k_T in the y direction. If each of these cavities is designed to be antiresonant for k_T, the light wave experiences high reflectivity in the transverse direction and remains confined to the core. The antiresonant condition for the round

trip phase shift in the i-th cladding layer is given by:

$$\Phi = 2t_i k_T + \Phi_r = (2N-1)\pi; N = 1,2,... \quad (2.1)$$

where Φ is the total phase shift from reflection at the two interfaces with the adjacent layers. The thickness t of each high-index cladding layer needs to be chosen so that it satisfies the desired interference condition by the following equation:

$$t_i = \frac{\lambda}{4n_i}(2M+1)\left(1-\frac{n_c^2}{n_i^2}+\frac{\lambda^2}{4n_i^2 d_c^2}\right)^{-\frac{1}{2}}; M = 0,1,2,... \qquad (2.2)$$

Low loss propagation of leaky modes in ARROWs was first proposed by Duguay [45] for the original utilization with solid cores in optoelectronics and photonics for high-power and cascade lasers. ARROW waveguides offer many advantages such as excellent suppression of higher order modes and the reduction of periodicity compared Bragg fibers and PCFs.

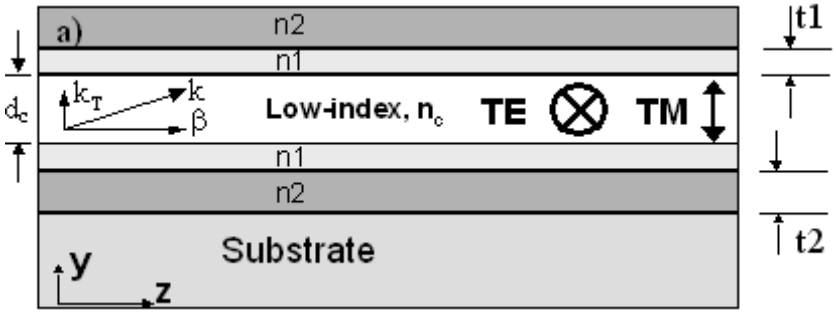

Figure 2.1 Cross section of the ARROW waveguide (a low-index core (thickness d_c, index n_c) is surrounded by ARROW cladding layers (indices n_1, n_2) on both sides; also depicted are the relevant polarization directions of the electric field (TE

polarization is parallel and TM is perpendicular to the layers). Propagation occurs along the z-direction with a propagation constant β and the wave is to be confined in the transverse (y) direction. The cladding layers act as Fabry-Perot cavities for propagation with the transverse wave vector k_T in the y direction.)

2.2 Loss calculation of ARROW

2.2.1 Matrix formulism for mode loss calculation

In this section, we will focus on calculating the mode loss of 1D waveguide. The most accurate way of solving this problem is certainly to solve the wave equation of multilayer structure analytically to find the complex propagation constant. (Since the imaginary part of the propagation constant corresponds to the loss of the leaky mode during its propagation.) But in practical, it is mathematically difficult to find the solution of the eigenvalue equation in the case when a plot of the mode loss versus a large number of free parameters such as wavelength different refractive indices and different layer thickness.

So here we use a matrix formulism [46] for the isotropic-layered media under the assumption that a plane wave is a very good approximation to calculate the loss coefficient of the mode in ARROW waveguide. For a general multi-layer dielectric medium as show in figure2.2, n_0 is the incident layer and n_s is the outside boundary layer. The light propagates in the z direction. The whole medium is assumed to be

homogeneous in the z direction, the electric field of a plane wave that satisfies Maxwell's equations has the form:

$$E = E(y)e^{i(\omega t - \beta z)} \quad (2.3)$$

Where β is the z component of the wave vector and ω is the angular frequency. The electromagnetic wave is assumed to propagate in the yz plane, and hence E and H are parallel to the x direction for the s and p waves, respectively. The electric field E(y) consists of a right-traveling and a left-traveling wave and can be written as:

$$E(y) = \mathrm{Re}^{-ik_y y} + Le^{-ik_y y} = A(y) + B(y) \quad (2.4)$$

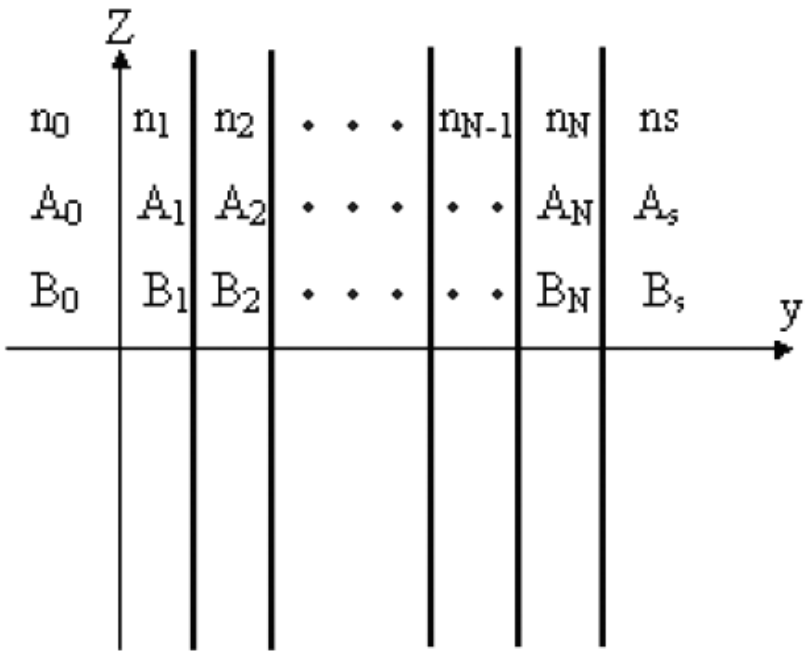

Figure 2.2 Diagram of multi-layer structure

Where A(y) represents the amplitude of the right traveling wave and B(y) represents that of the left-traveling wave. As depicted in the matrix formulation for layered medium, the traveling waves for both directions of the mutilayer medium as illustrated in figure 2.2 are related by a 2×2 matrix in the following way:

$$\begin{bmatrix} A_0 \\ B_0 \end{bmatrix} = \begin{bmatrix} M_{11} & M_{12} \\ M_{21} & M_{22} \end{bmatrix} \begin{bmatrix} A_s \\ B_s \end{bmatrix} \qquad (2.5)$$

If the incident angle of the light is specified, the 2×2 matrix can be easily solved by using the boundary condition of the interface between each two layers, which is the continuity of E_x and H_z at the interface for s wave and the continuity of H_x and E_z at the interface for p wave respectively. Then the reflectance of the multilayer structure can be calculated from (2.5). If the light is incident from medium n_0, the reflection coefficient is given by:

$$r = \left(\frac{B_0}{A_0} \right)_{B_s=0} = \frac{M_{21}}{M_{11}} \qquad (2.6)$$

For finally calculating the loss coefficient, let us first consider a waveguide configuration as shown in the figure 2.3

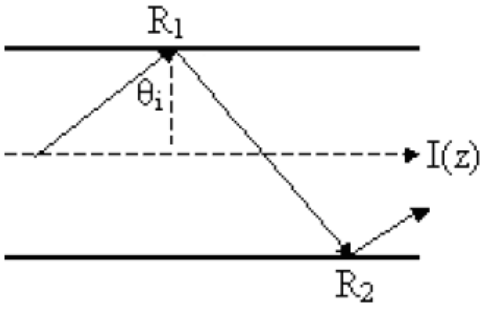

Figure 2.3 Light ray tracing in a general waveguide

R1 and R2 represent the reflectance of the multilayer structure on both sides of the core. The propagation intensity of the leaky modes of the waveguide can be written as:

$$I(z) = I_0 e^{-\alpha z} \qquad (2.7)$$

Differentiating both side of the formula (2.7) with respect to z, we obtain:

$$\alpha = -\frac{1}{I}\frac{dI}{dz} \qquad (2.8)$$

One round trip is taken as the step along the light propagation direction, dI and dz then can be written as:

$$dI = -I(1-R_1+1-R_2); dz = 2d\frac{\sin\theta_i}{\cos\theta_i} \qquad (2.9)$$

Where d is the thickness of the core; R1 and R2 are the reflectances of the multilayer structure on both sides of the core. Substituting (2.9) into (2.8), we obtain:

$$\alpha = \frac{(1-R_1+1-R_2)\cos\theta_i}{2d\sin\theta_i} \qquad (2.10)$$

As a result, the loss coefficient of the leaky mode can now be calculated by knowing the reflectance of the multilayer structure around the core and incident angle of the mode. The reflection coefficient can be deduced from equation (2.6) as discussed above. In the case that the difference of the refractive index is relatively large between core and cladding, the incident angle of the m_{th} core leaky mode of a slab waveguide can be approximately given by [47]:

$$\theta_i \approx \cos^{-1}\left(\frac{\pi(m+1)}{k_0 n_{core} d}\right) \quad (2.11)$$

2.2.2 Loss calculation of 2D ARROW waveguide.

When it comes to the loss optimization of 2D ARROW waveguides, another important issue is the polarization dependence. Since different polarizations will have different phase shifts at the reflection, the optimized thickness is not always the same between the TE and TM modes. It sometimes satisfies the antiresonant condition and sometimes the resonant condition, all depending on the polarization and the incident angle of the light. As illustrated in figure 2.4:

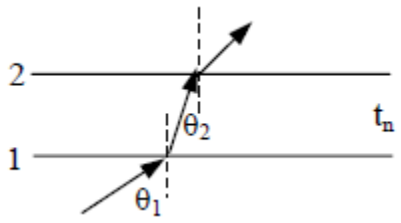

Figure 2.4 Phase conditions for different polarizations

Where θ1,2 and θB1,2 stands for the different incident angles and the Brewster angles at the top and bottom interface of the cladding. The incident angle is the angle between the incident light and the normal of the incident plane. The Brewster angle is the incident angle when the reflectance of the p wave is zero and is given by [24]:

$$\tan(\theta_B) = \frac{n_2}{n_1} \quad (2.12)$$

For TE waves, when $n_{i-1}<n_i<n_{i+1}$, the resonant condition is satisfied; when $n_i>n_{i-1},n_{i+1}$, the antiresonant condition is satisfied.

For TM waves, when $n_{i-1}<n_i<n_{i+1}$, if $\theta_{1,2} >\theta_{B1,2}$ and $\theta_{1,2} <\theta_{B1,2,}$ the resonant condition is satisfied. Otherwise, the antiresonant condition is satisfied. Also, when $n_i>n_{i-1},n_{i+1}$, if $\theta_{1,2} >\theta_{B1,2}$ and $\theta_{1,2} <\theta_{B1,2}$, the antiresonant condition is satisfied. Otherwise, the resonant condition is satisfied.

2.2.3 Loss optimization

A new design taking into consideration the polarization orientations and the conformality ratio (In the real fabrication of the top layers, the thickness of the top and lateral parts are different because of the gravity. The comformality ratio is defined as the ratio between the thickness of the top part of the layer and that of the lateral part of

the layer) and the mechanical stability requirements (The most outside oxide layer should be thicker than 3μm to maintain the structure mechanical stable).

The parameters shown in the following table are the calculated result of top and bottom layer thickness of each layer. These parameters are used to finally calculate the waveguide loss as shown in table 2.1 as well.

	Bottom Layers	Top layers	Loss
SAP ARROW (Air-core) @ 785nm	SiO2/SiN/SiO2/SiN/SiO2/SiN 150/110/165/100/190/90	SiN/SiO2/SiN/SiO2/SiN/SiO2 61/324/94/284/234/4010	0.86/cm @ 785nm

Table 2.1 Design parameters of self aligned pedestal ARROWs

2.3 Fabrication

In this section, the fabrication processes of two types of ARROWs are presented: non-preetched ARROW and preetched ARROW. The latter ARROW structure is a reformed version of the former ARROW structure which greatly reduces the loss and therefore highly improves the device performance.

2.3.1 Fabrication of non-preetched ARROW

The ARROW fabrication process utilizes standard semiconductor processes [12,13]. This makes fabrication of multiple devices simultaneously possible (32 devices on a whole semiconductor wafer). ARROWs are fabricated on <100> crystal orientation silicon wafers to allow the devices to be cleaved perpendicular to the waveguides. The process begins by depositing the bottom dielectric layers of silicon dioxide and silicon nitride using plasma enhanced chemical vapor deposition (PECVD). Following the bottom layers, the sacrificial core is fabricated using SU-8 (SU-8 is a commonly used epoxy-based negative photoresist.) spun on to a specified thickness, patterned, and developed (Figure 2.5a). The top dielectric layers are then deposited over and around the sacrificial core using PECVD. The top oxide layer is deposited thicker than the other layers specified by the design parameters above. This thick oxide layer provides structural strength for the waveguides (Figure 2.5b) [14]. Ridge waveguides etched into the top, thick silicon dioxide layer provide a means for coupling light into the hollow core without exposing the hollow waveguide to the surrounding air [15]. The ridge waveguide is patterned with an SU8 mask and etched using a reactive ion etcher (Figure 2.5c). The next step is to expose the sacrificial cores to air to allow them to be etched and removed. This is also done in the reactive ion etcher with the pattern masked by SU8 (Figure 2.5d). To complete the ARROWs and make them hollow, they are placed in a highly selective acid bath to etch the sacrificial core (Figure 2.5e). The openings in figure 2.5e can later be used to attach a reservoir that does not interfere

with the optical beam path.

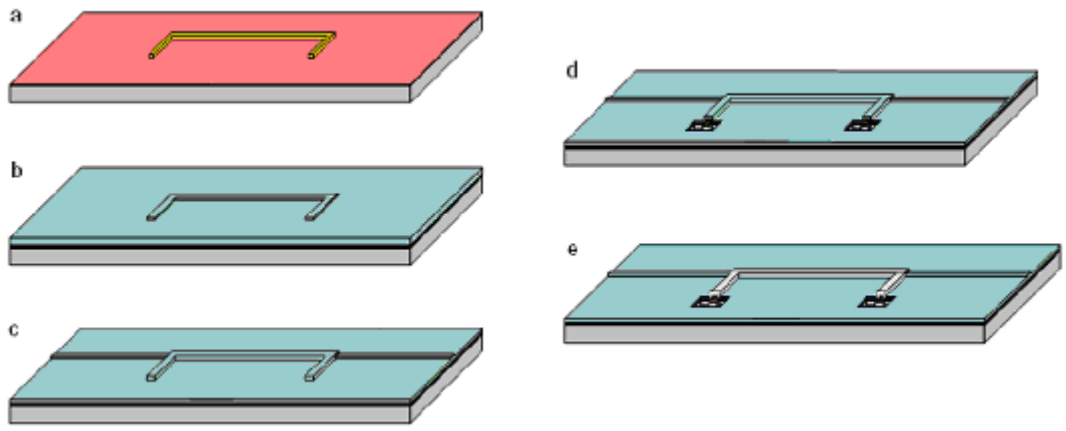

Figure 2.5 Fabrication process of ARROW waveguides

2.3.2 Fabrication of preetched ARROW

The fabrication process outlined above (Section 2.3.1) yields a rectangular core (Figure 2.6(a)) [12,16]. The thick top oxide layer extends laterally out from the waveguide as can be seen in Figure 2.6. This high index layer yields higher loss in the waveguide than if air were laterally extending out from the waveguide. Fabricating the ARROW on a raised pedestal creates a waveguide where air extends laterally from the waveguide [12,16]. This is realized by adding a fabrication process called self aligned pedestal (SAP) process.

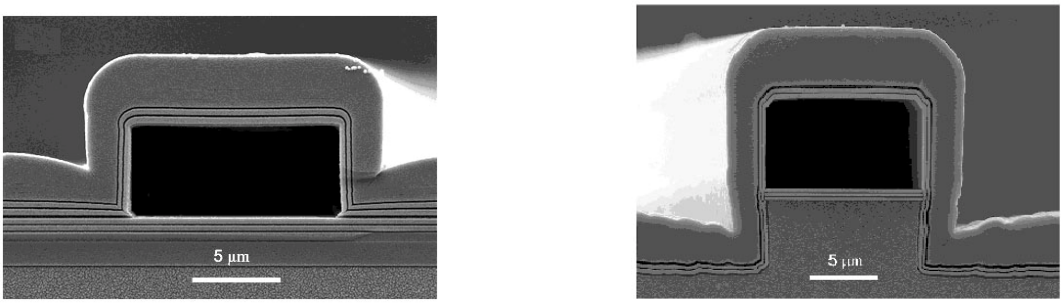

(a) (b)

Figure 2.6 SEM pictures of ARROW: (a) Non-preetched ARROW (b) Preetched ARROW

In order to fabricate self-aligned pedestal (SAP) ARROWs, a process based upon anisotropic plasma etching was chosen. The rest of the fabrication process is similar to that for ARROWs on planar substrates, based on PECVD and sacrificial etching [5]. First, layers of silicon dioxide (SiO_2) and silicon nitride (SiN) are deposited by PECVD on a silicon substrate at 250◦ C (see Fig. 2.7 (a)). These layers are deposited with controlled refractive indexes and precise thicknesses so that each layer satisfies the antiresonant condition [7]. Next, the SU8 sacrificial core is deposited and defined by photolithography. After this, the self-aligned pedestal is created by anisotropic plasma etching. Selective etching is required so that the SU8 core is not removed while etching through 1-1.5 µm of PECVD SiO_2 and SiN layers and 4-5 µm of the silicon substrate to form a pedestal with sufficient height. Etching of the PECVD layers is performed in a single etch step at an average rate of 170 nm/min. Etching of the silicon substrate is performed with alternating sidewall passivation and etch steps, repeated

many times, with an etch rate of about 18 nm/sec.

The CHF_3 in the etching recipes provides sidewall passivation and increases the anisotropy of the etching. During etching, a fluorocarbon passivation film is deposited isotropically on the surface. Ion bombardment keeps horizontal surfaces clear of the film, while the film accumulates on and protects vertical surfaces. After etching is completed, the accumulated passivation film, commonly called post-etch residue, remains on the sides of the pedestal and the sacrificial core, and must be removed prior to deposition of the top antiresonant layers.

Various approaches have been used to remove this etch residue, including O_2 and H_2 plasmas, hydroxylamine, super-critical CO_2 (SCCO2) [12], and radical anions [13]. A cleaning procedure is developed using a mixture of H_2O_2 and the resist remover RS-6 (Cyantek Corp.), which contains TMAH. To remove the etch residue, our samples are immersed in the mixture (1:10 H_2 O_2 :RS-6) at 40◦ C for 5 minutes and then rinsed in deionized water. This cleaning process is performed after the SiO_2 /SiN etch and again after the silicon etching and effectively removes the etch residue without damaging the SU8 core.

Another common problem encountered with anisotropic etching is the formation of etch grass. This occurs when surface defects and contamination function as micromasks and lead to the formation of small pillars on the etched surface. This issue can be particularly severe in our self-aligned pedestal etching, as the PECVD SiN and SiO_2 layers have many defects in them which can function as micromasks. We have

found that the most effective way to remove this etch grass is to employ an isotropic silicon etch at the end of the pedestal etching. This etch process attacks the sides of the etch grass and etches away the silicon base to the point that the grass collapses, so it can be later rinsed away.

After the pedestal etching is completed and the etch residue and etch grass are removed, the top antiresonant layers are deposited by PECVD (see Fig. 2.7 (c)). Finally, the ends of the sacrificial core are exposed, either by cleaving the wafer or by plasma etching, and the core is removed in a piranha etch (1:1 H_2O_2 :H_2SO_4 , 100◦ C), completing the hollow waveguide, as shown in Fig. 2.7 (d).

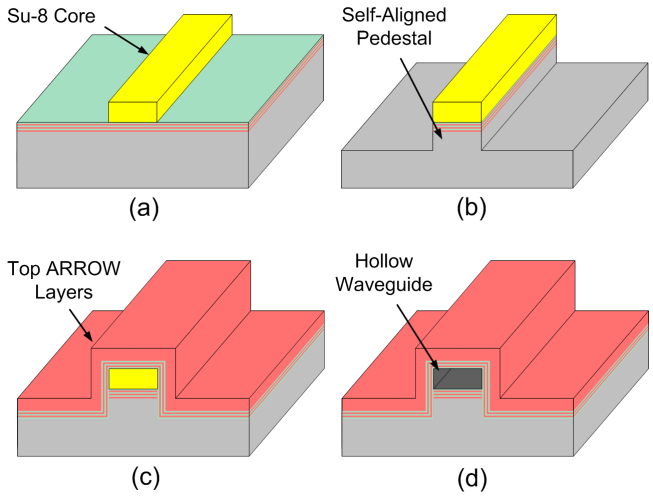

Figure 2.7 Fabrication process of SAP ARROW waveguides.

2.4. Testing of ARROW Performance

In order to characterize the waveguide performance, straight SAP ARROW

waveguides were fabricated with cores 5.8 μm tall and 9, 12, and 15 μm wide. In the ARROW waveguide, the waveguide loss comes from two major sources, one is the leaky mode loss due to the complex propagation constant, and the other one is the scattering loss due to the roughness of the fabricated layers. In order to quantify the loss value of waveguides, several methods for measuring optical attenuation as a function of propagation distance in a waveguide have been reported [48-50]. One of these methods is to determine the waveguide loss by measuring the intensity of the scattered light as a function of distance along the guide, either by imaging the guided light streak on an array of detectors [48] or by using a fiber bundle [49]. This method is implemented in our ARROW waveguides, since the hollow core ARROW is covered by multilayer cladding on top which leads to weak scattering for detection. Another solution used to determine the attenuation is to outcouple the guide beam with a contact prism coupler. [50,51] By sliding the prism coupler along the guide, the distance dependent attenuation is obtained. This method requires a relatively complicated setup to maintain the prism in good contact with waveguide surface during the experiment. Also this method is destructive to the waveguide. Because the waveguide surface may be damaged by the sliding of the contacting prism.

Taking the dilemma of experiment complexity and measurement accuracy into account, we used a cutback method. The experimental setup is shown in figure 2.8. First, we measured the output of many waveguides at different lengths by cutting them piece by piece. We then average the data for each length to eliminate the variation of the

coupling between waveguide and fiber. The extraction of waveguide attenuation coefficient over the distance is also feasible in the cutting-back loss measurement of ARROW waveguides.

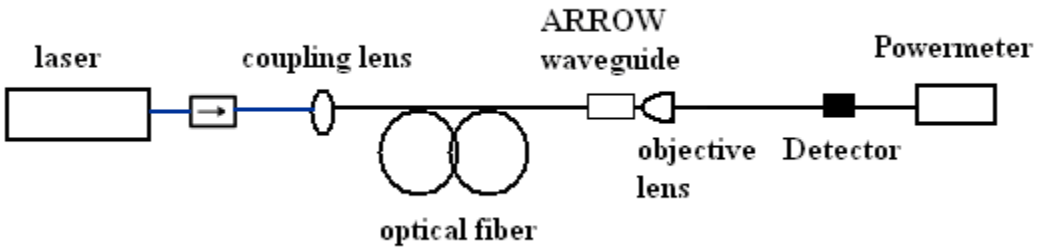

Figure 2.8 The experimental setup for measuring ARROW loss.

As seen from figure 2.8, during our loss measurement, we start with a long waveguide and cut it shorter and shorter to measure the output at different lengths. Then the absorption coefficient (α) and the coupling efficiency between optical fiber and ARROW waveguide (κ) can be extracted by fitting α and κ to the following equation:

$$I_{out} / I_{in} = \kappa \exp(-\alpha L)\ I_{out} / I_{in} = \kappa \exp(-\alpha L) \quad (2.13)$$

The result of the loss measurement is shown in figure 2.9.

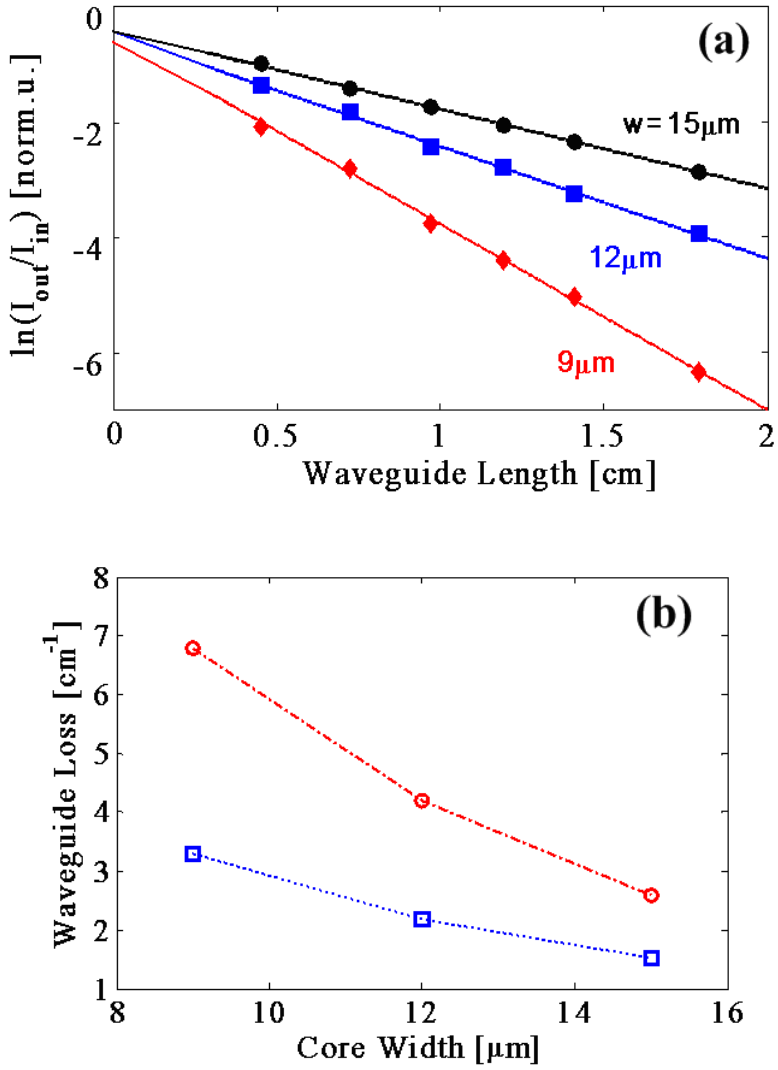

Figure 2.9 Loss measurement of ARROW waveguide (a) Transmission vs different waveguide lengths with different waveguide widths. Lines: fits; symbols: experimental data; (b) The measurement results of waveguide loss for both previous-designed ARROWs (open circles) and SAP ARROWs (open squares).

Using this cutback method with light at 785 nm and air-filled cores, average waveguide

losses are determined to be 3.31, 2.19, and 1.54 cm^{-1} for 9, 12, and 15 μm-wide waveguides, respectively (see Fig. 2.9). Previously, the lowest loss for air-core hollow ARROWs is achieved using the pre-etched pedestal design and was 2.6 cm^{-1} for a 5.8x15 μm hollow core, as shown in Fig. 2.6 (b) [11]. Comparing waveguide losses for the SAP ARROWs and our previous best results for air-core ARROWs, we see that the losses at 785 nm are greatly reduced for the SAP ARROWs, as shown in Fig. 2.8 (b).

2.5 Theory of EIT

2.5.1 Basic physics of EIT

Electromagnetically induced transparency (EIT) is a quantum coherence phenomenon which has intrigued scientists for more than twenty years since it was first discovered by Imamoglu and Harris in 1989 [52]. Since then, a large part of the research in this field was focused on observing and studying the fundamental physics behind the unique light-matter interactions that are caused by this quantum interference phenomenon.

This interference is an analogy to constructive and destructive interference between classical wave interference. However, compared to the classical wave interference whose field amplitudes are interfering between two spatially overlapped beams, the quantum interference describes the interference phenomenon between transition pathways induced with internal quantum states of atoms and molecules coupled to one

or more laser fields. In particular, three-level atomic and molecular systems coupled with two laser fields exhibit interference effects that can result in cancellation of absorption at a resonance transition frequency and other modifications of the optical responses of a medium. This above mentioned phenomenon for eliminating the absorption of one laser field by applying another strong laser field within a three-level system is so called electromagnetically induced transparency.

EIT is commonly observed in three-level systems. Figure 2.9 shows three typical three-level systems for EIT (Λ type, V type, Ladder Type).

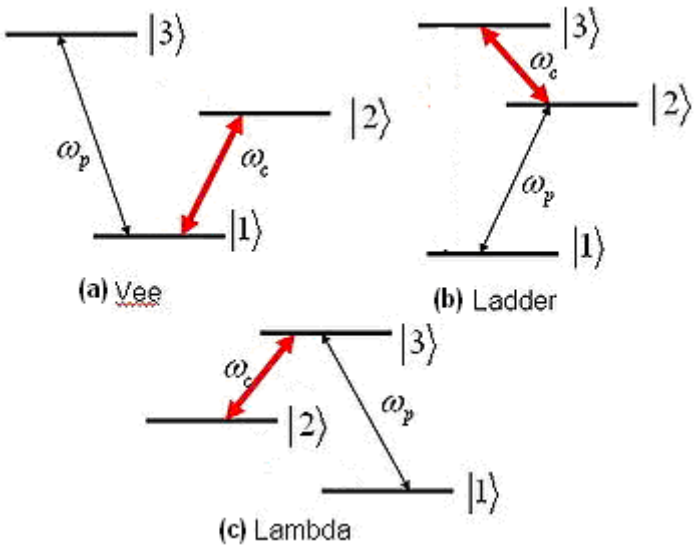

Figure 2.10 Three types of configuration for EIT: (a) Vee type (b) Ladder type (c) Lambda type

The effect requires a small ground state decoherence rate, so that the largest effects are typically observed in hyperfine split states of alkali atoms. This type of interference is

induced by an applied laser field concerned with the laser control of the optical properties of atomic media. The cancellation of absorption for a probe field tuned in resonance to an atomic transition, for which strong absorption would normally be expected, can be achieved in this case. Therefore, EIT effect caused by the interference between coherent excitations in the atom by the electromagnetic fields can render an initially highly opaque media almost transparent.

2.5.2 Rabi frequency

Rabi frequency refers the strength of the coupling between the light and the transition for a given atomic transition. It is related to the electrical field of the incident laser field:

$$\Omega_{i,j} = \frac{\mu_{i,j} \cdot E_0}{\hbar} \tag{2.14}$$

2.5.3 Closed system for Lambda Type EIT

In this section we look into the closed three-level atom system (as seen in Fig. 2.10) with incoherent pumping. The equations of motion for the density matrix elements in a rotating frame can be written as [68]:

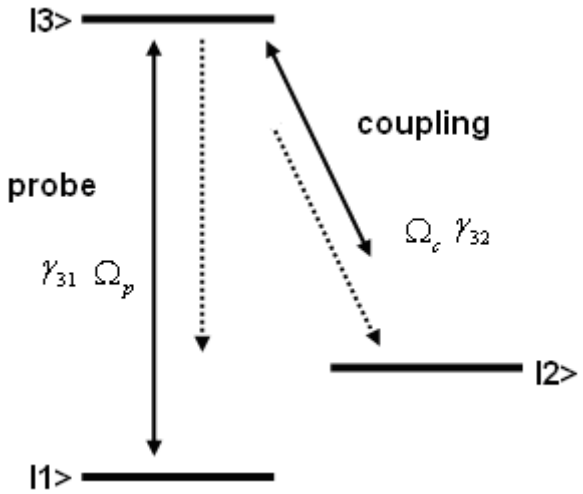

Figure 2.11 Configuration of a three-level Lambda Type EIT system

$$\dot{\rho}_{11} = \gamma_{31}\rho_{33} + i\Omega_p(\rho_{31} - \rho_{13})$$

$$\dot{\rho}_{22} = \gamma_{32}\rho_{33} + i\Omega_c(\rho_{32} - \rho_{23})$$

$$\dot{\rho}_{33} = -\gamma_{31}\rho_{11} - \gamma_{32}\rho_{22} + i\Omega_c\rho_{13} + i\Omega_p\rho_{23}$$

$$\dot{\rho}_{31} = -(\gamma_{31} + i\Delta_1)\rho_{31} - i\Omega_p(\rho_{33} - \rho_{11}) + i\Omega_c^*\rho_{21}$$

$$\dot{\rho}_{21} = -(\gamma_{21} + i\Delta_1 - i\Delta_2)\rho_{21} - i\Omega_p\rho_{23} + i\Omega_c\rho_{31}$$

$$\dot{\rho}_{23} = -(\gamma_{23} + i\Delta_1)\rho_{23} - i\Omega_p\rho_{21} - i\Omega_c(\rho_{22} - \rho_{33}) \qquad (2.15)$$

Where $\Delta_1 = \omega_{31} - \omega_p$, $\Delta_2 = \omega_{32} - \omega_c$ are the detunings of probe and coupling lasers. ω_p, ω_c are the angular frequencies of the probe and coupling fields.

γ_{13}, γ_{23} are the spontaneous decay rates from the excited state $|3\rangle$ to two ground states $|1\rangle$ and $|2\rangle$. γ_{12} is the non-radiative decay rate between the two ground states $|1\rangle$ and $|2\rangle$ (as denoted in figure 2.11).

Now to the first order in Ω_p, ρ_{13} (which governs the macroscopic polarization P) is then:

$$\rho_{31} = \frac{i\Omega_p / 2}{i\Delta_1 - \gamma_{31} + \frac{\Omega_c^2 / 4}{i(\Delta_1 - \Delta_2) - \gamma_{12}}} \qquad (2.16)$$

The linear susceptibility of the atomic system can be written as:

$$\chi = \frac{2N\mu_{31}^2}{\hbar\Omega_p}\rho_{31} \quad (2.17)$$

Here EIT can be achieved in the case of $\Omega_c >> \gamma_{12}$.

Based on equation (2.17), the transmission and dispersion curve of EIT vs. probe frequency detuning are plotted in figure 2.11 with the following assumptions of parameters: $\gamma_{23} = \gamma_{13} = 3\text{MHz}$, $\gamma_{12} = 0.1\text{MHz}$, $\Omega_c = 120\text{MHz}$.

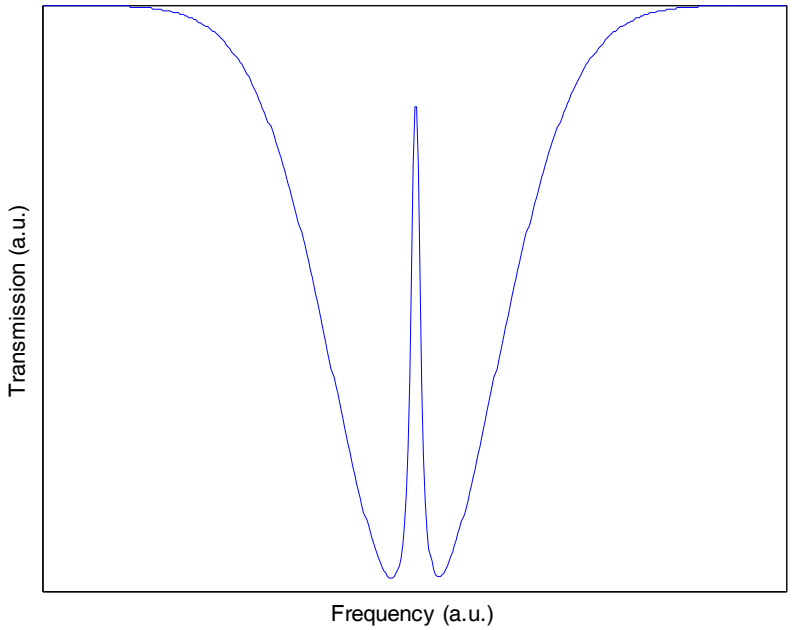

(a)

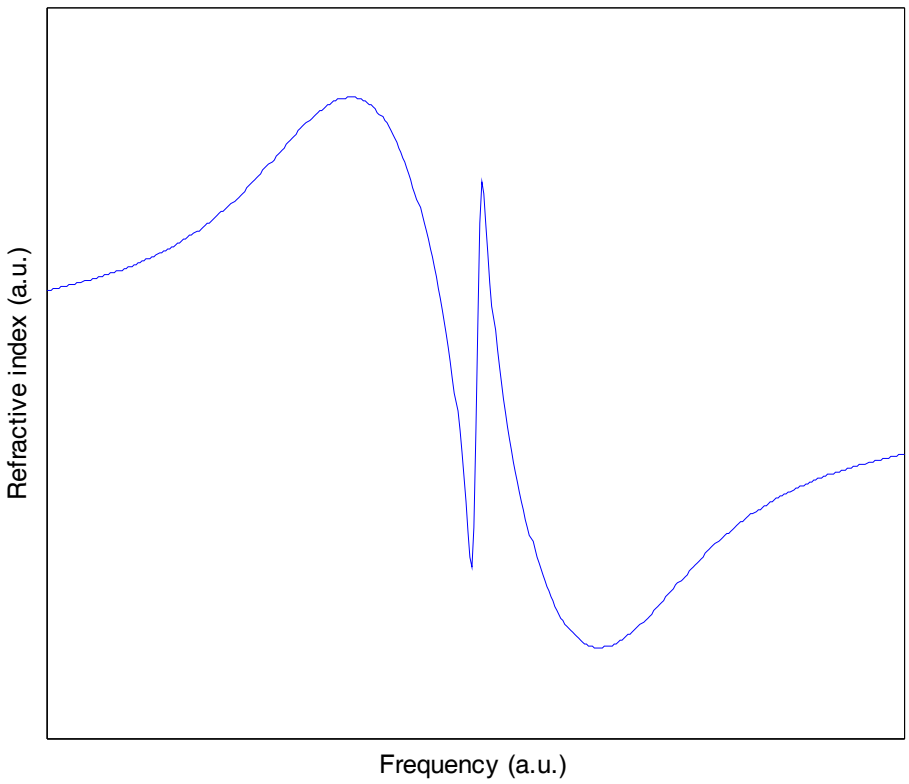

(b)

Figure 2.12 (a) Transmission vs probe detuning in EIT; (b) Refractive index vs probe detuning in EIT

From the figure above, we can clearly see that with this EIT effect, the absorption can be cancelled across the probe atomic transition. Accordingly, the dispersion properties of the medium may be greatly modified; for instance the usual correlation of high refractive index with high absorption can be broken, leading to the creation of media

with very unusual optical properties. The possible importance of this EIT effect to further applications in linear and nonlinear optics will be discussed in the following section.

The appeal of EIT effects in nonlinear optics arises from the fact that large nonlinearities can be achieved while simultaneously eliminating linear absorption, e.g. in sum-frequency generation or four-wave mixing [53,54]. Expansion of the three-level scheme to a complete four-level scheme allows for observation of giant Kerr nonlinearities as described by Schmidt and Imamoglu [26].

Highly efficient photon generation based on EIT is also feasible. In 1998, Lukin et al. described the enhancement of parametric processes and the possibility of mirrorless parametric amplification in a double-Lambda EIT-scheme [55]. They also showed that the parametric process is particularly efficient for counter-propagating pump fields, which was later observed by Zibrov et al.[56]. In an expansion of this earlier work, Eisaman et al. recently demonstrated generation of few-photon light pulses in a Lambda -scheme [57]. As can be seen, nonlinear optical processes based on EIT in alkali atoms have shown great potential for devices operating at or near the single-photon level, providing strong incentive for using integrated optics.

Moreover, as the EIT experiments are conducted in hot Rb atoms, they are subject to Doppler broadening (see section 4.1.3). The consideration of both pumping and probe lasers passing through a Doppler-broadened atomic vapor will be addressed in the experimental curve fitting sections (see section 4.5.1 and section 5.6.1.).

Chapter 3 Rubidium Cell Integration

In this chapter, the integration of rubidium cell into ARROW waveguides is introduced by attaching a rubidium reservoir onto the opening at the end of the hollow core ARROW. Some possible techniques for attaching and sealing the rubidium reservoirs on chip are discussed in the following section. A preliminary testing for checking the performance of different sealing epoxies is done with a home-made miniaturized rubidium cell (termed minicell).

3.1. Current vapor cell technology

We will briefly discuss two types of atomic vapor cell (bulk cell and anodic bonding) currently being made and their fabrication methods.

3.1.1 Bulk cell

The most common cell uses a conventional glass enclosure filled with an atomic vapor like the one shown in Fig. 3.1. The creation of these cells utilizes a large and complex system of glass tubes, ampoules, and valves created using glass blowing techniques. These cells are usually cylindrical in nature. Light is incident on the flat ends of the

cylinder to lessen the amount of light lost to diffraction. The cell originally has one or more openings in the form of a glass tube. Through these glass tubes the cell is put under vacuum and rubidium vapor is introduced from a source on the other end of the glass tube. Once the cell is under vacuum and rubidium vapor is introduced, the glass tube is heated to the glass melting point, twisted, and pulled. This seals and separates the cell from the rest of the system. These cells are usually fairly large, somewhere in the multiple centimeter range. Because of the large size and the need for table top sized optical systems to align and focus beams, bulk cells are most commonly found in research settings.

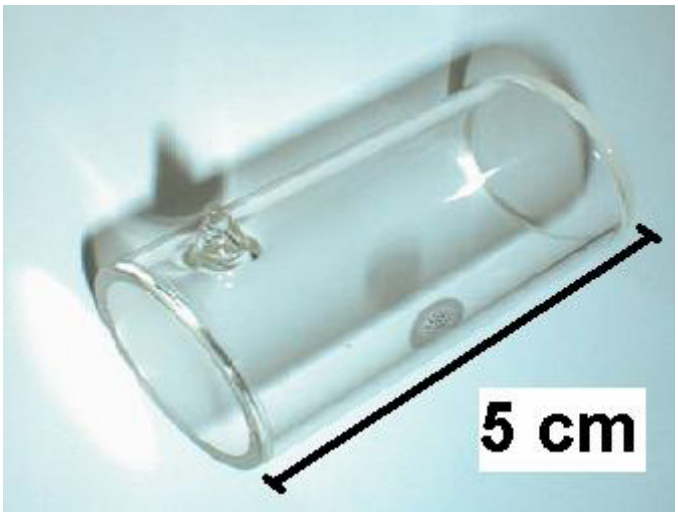

Figure 3.1 Picture of the conventional Rb bulk cell

3.1.2 Anodic boding for micro-cell

NIST developed a method to build a more compact atomic vapor platform [58,59].

Their method uses well proven silicon and wafer bonding micro-fabrication methods that not only allow for smaller sizes, but allow for multiple devices to be created in one batch. First, holes are etched through a silicon wafer either by a chemical wet etch or a reactive ion etch. A glass wafer is then anodically bonded to one side of the silicon wafer. Rubidium or cesium is then deposited into the holes etched out of the silicon wafer. Another glass wafer is then sealed to the top of the silicon wafer. This is done under vacuum. In the end, a vapor cell is formed in the hole etched out of the silicon sandwiched between two glass wafers. To generate the desired absorption spectroscopy, a laser is directed through the rubidium cell via the glass wafer windows as illustrated in Fig. 3.2. This compact size has enabled NIST cells to be mounted on circuit boards and opened the door for a number of practical uses of atomic vapor cells. NIST recently reported the successful creation of a compact frequency reference by mounting one of their cells on a small circuit board [60].

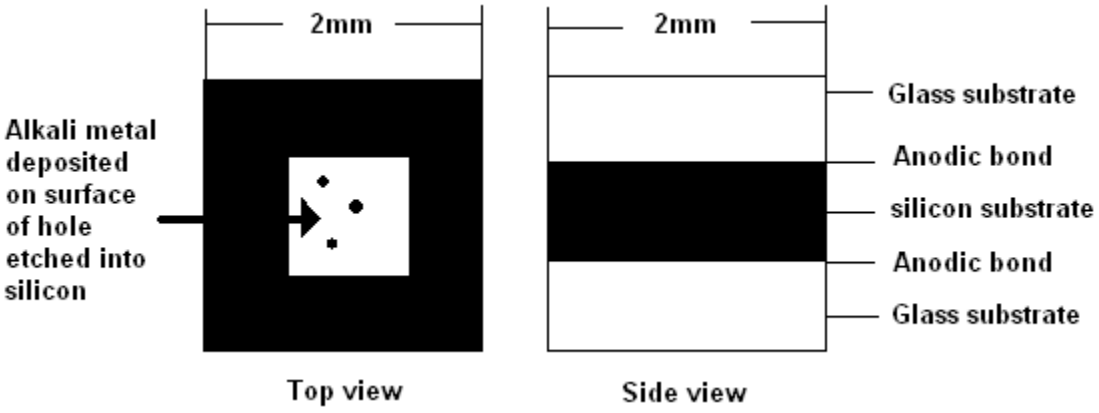

Figure 3.2 Illustration of a compact Rb vapor cell from anodic bonding

It should be noted that another recently developed compact atomic spectroscopy platform utilizes a hollow-core photonic crystal fiber (PCF) filled with atomic vapor [61-64]. Light interacts with the vapor as it propagates down the fiber. Since the light is confined in the fiber, this method allows for long interaction lengths without sacrificing beam width and requiring a large system of optical apparatus. However, currently this methodology utilizes large vacuum cells at each end of the fiber making it difficult to incorporate in an integrated system.

3.2 Fabrication of rubidium filled minicell

3.2.1 Geometry for integrated ARROW waveguides with Rb cell

Even though the NIST cell is a large improvement over classical bulk cells in the push for compact spectroscopy, there is still room for improvement. With respect to most devices in the microfabrication field, the NIST cells dimensions of several millimeters in all three dimensions is rather bulky, especially after packaging and mounting. Also, creating integrated optical systems is difficult due to the need for vertical incident light. In our approach, we also take advantage of microfabrication techniques to create atomic vapor cell systems that have micrometer dimensions and utilize in-plane incident light.

ARROW platforms are created using microfabrication methods which has been

addressed in the previous chapter. In our atomic vapor systems we utilize what we call an S-mask ARROW configuration. We fabricate our hollow core in an S-like pattern with solid cores at the top and bottom of the 'S'. Openings into the hollow core are etched out at the tip of each end of the S shape. The sacrificial core is removed through these holes and ultimately atomic vapor is introduced through them as well and sealed into the hollow core. Fig. 3.3 shows a typical ARROW based absorption spectroscopy setup. A reservoir containing rubidium is assembled over one end of the hollow core while the other end is sealed off with epoxy. Optical fiber couples light into the on-chip solid core waveguide which then couples the light into the hollow core atomic vapor cell. Likewise, light is coupled out via another on-chip solid core waveguide into an optical fiber.

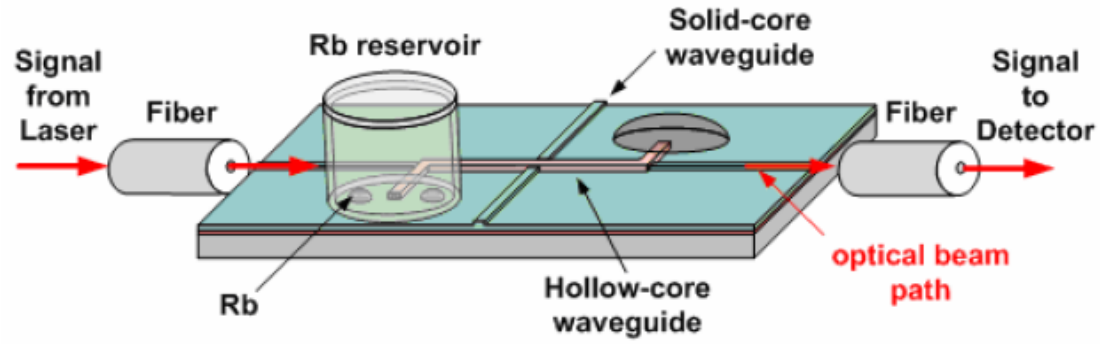

Figure 3.3 Rubidium cell integrated ARROW waveguide

3.2.2 Fabrication of minicell

One of the most important parts of designing these ARROW based on-chip atomic

vapor cells, are the rubidium introduction and sealing techniques. Because of the small volumes and configuration of the ARROW devices, this has proven to be challenging as the rubidium is very reactive with air.

Attaching a reservoir using anodic bonding techniques is hard to implement because the ARROW platform surface is not flat. The hollow core and solid core waveguides etched into the silicon wafer form ridges that would prevent good anodic bonding. This means that a 3-D structure of some sort must be constructed to act as a rubidium reservoir. Another important factor in sealing atomic vapor cells is that both the atmosphere and pressure need to be controlled. Rubidium, which is used as the EIT media in our cells, is highly reactive to air and must be introduced into the cells in an inert gas atmosphere or under vacuum.

In order to test the effectiveness of the epoxy used for sealing rubidium reservoir onto ARROW chip, we first fabricate a type of minicell (as seen in Figure3.4) with the same type of epoxy which is later transferred to the real rubidium loaded ARROW waveguides.

We have experimented with many different types of materials and epoxies to test their sealing potential and compatibility with rubidium (see appendix1). Since the creation of a working ARROW requires a lot of time and resources, the majority of the sealing testing is done with devices we call minicells. Minicells consist of a cylindrical glass body made out of a tube or vial with various sealing technique sealing the device. An example of a minicell is shown in Fig. 3.4. After the minicell is created with the sealing

method in question, light is shone through the glass cylinder to test for absorption. Data from these absorption tests help to determine optimal sealing materials and techniques.

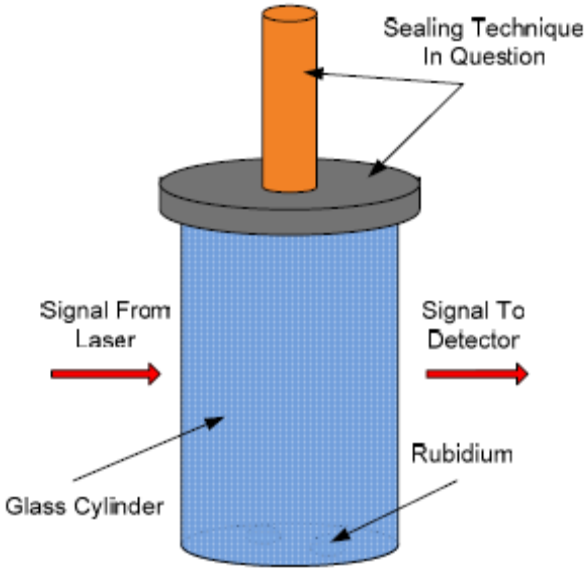

Figure 3.4 Illustration of a sealing technique testing platform called a minicell

3.2.3 The absorption testing result of minicell

A typical rubidium spectrum (Rubidium D2 is shown in figure 3.5).

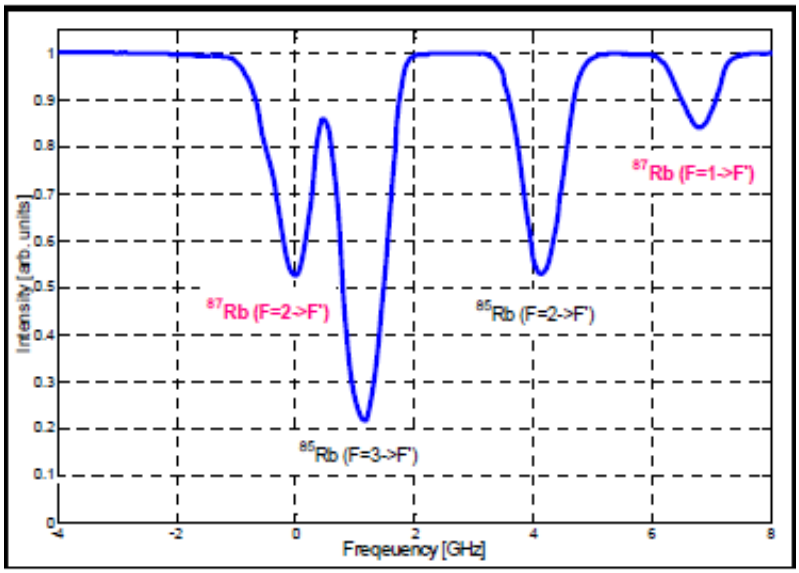

Figure 3.5 Rubidium spectroscopy at 780nm D2 line (all the dips here correspond to different atomic transitions with Rb level schemes referring to section 1.4.1).

By extracting the atomic density from the rubidium absorption curve from each testing, we can actually monitor the performance of the minicell. A more recent version of this process uses copper standoffs and sealing is accomplished by a combination of epoxy (Aremco 2310 epoxy, Aremco Products, Inc.) adhesive around the bottom edge of the standoff and crimping of the top of the standoff with a commercial crimping tool. A minicell sealed using this method is shown in the inset to Fig. 3.6(a). Metallic rubidium droplets are visible at the bottom. The vapor density in the cells is extracted from the hyperfine absorption spectra. Fig. 3.6(a) shows how the atomic density evolves as it is subjected to repeated heating and cooling of the cell. It is seen that the density increases with temperature as expected and that the cell slowly degrades with each heating cycle,

likely due to microscopic leaks that lead to slow oxidation of the Rb. Fig. 3.6(b) shows a side-by-side comparison of the reduction in peak atomic density for two different epoxies (Aremco 2310: open squares; Devcon clear epoxy: filled circles), showing how important the choice of sealing material is. Minicells fabricated by copper crimping can be heated repeatedly and are stable over several months. The results of such a long term test are shown in Fig. 3.6(c) where measurements of the normalized rubidium density are depicted over a span of three months.

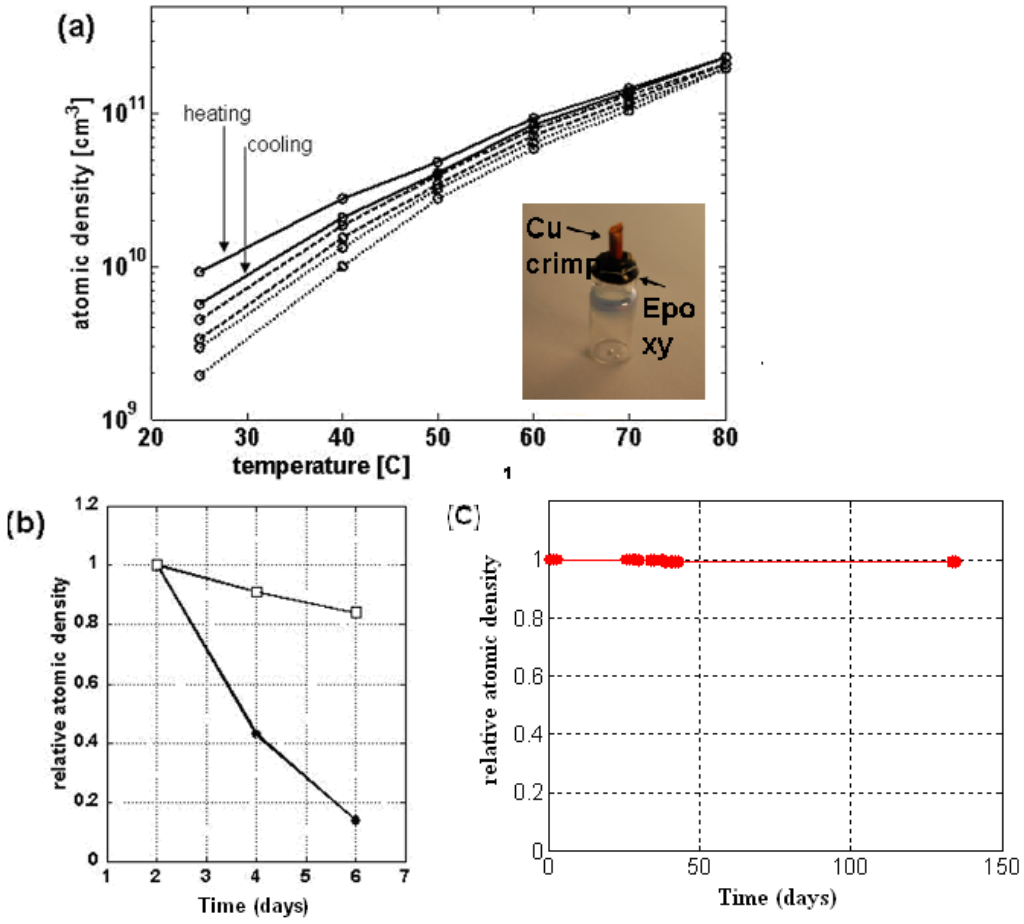

Figure 3.6 Performance testing of rubidium minicells

As a result, a reliable fabrication method with long term stability was developed and can be readily translated to integrated ARROW waveguides. An additional advantage of using a crimped copper stub is the ability to control the pressure inside the rubidium reservoir by attaching it to a vacuum pump immediately before pinching off the top end.

3.3 Integration of rubidium cell onto ARROW waveguide

3.3.1 First generation of rubidium loaded ARROW

Our first generation sealing technique consisted of mounting a stainless steel standoff on one end of a hollow waveguide using epoxy while the other end was sealed off with a dab of epoxy (figure 3.7). The rubidium was then loaded into the stainless steel reservoir. A screw with a rubber gasket sealed the reservoir and formed an atomic vapor source. All of this was done in a glovebox with a helium atmosphere. Absorption was successfully observed using this sealing technique. However, the pressure control in this method relies on the fact that helium can escape through the rubber seal, leaving behind a vacuum due to differential pressure with the atmosphere. Since pressure cannot be easily controlled, this sealing technique is less than ideal.

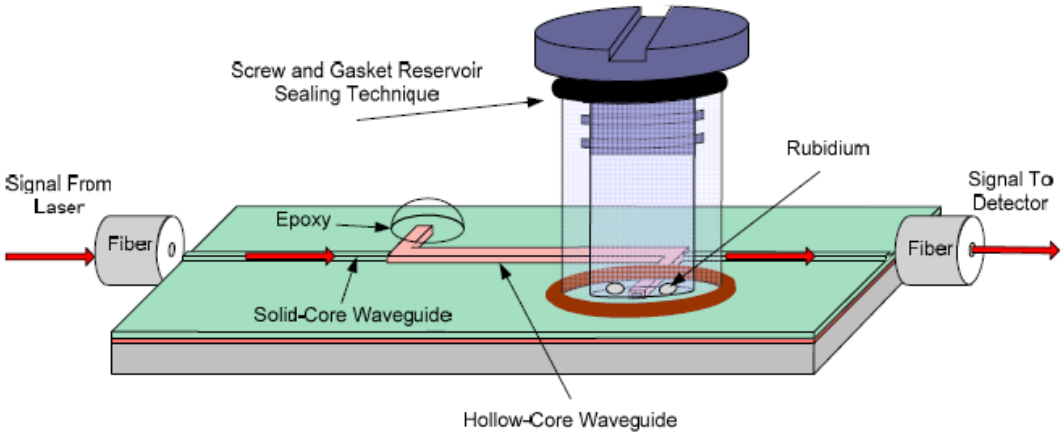

Figure 3.7 The first generation of Rb loaded ARROW

3.3.2 Second generation of rubidium loaded ARROW

Our second generation, and current sealing technique, is somewhat similar to the glass blowing approach used in the bulk cell in that a tube connected to a vacuum is used to evacuate our cells. We attach an approximately 1inch long, 1/8 inch diameter copper tube to one end of the hollow core and seal the other end with epoxy much like we did with the stainless steel reservoir (figure 3.8). The copper stub is then loaded with rubidium while inside a glovebox filled with nitrogen. We have found that it is easier to maintain lower oxygen levels in the glovebox when filled with nitrogen compared to helium. Once the copper reservoir is loaded with rubidium, a rubber hose is attached to the end of the stub and the cell is evacuated to the desired pressure. When the desired pressure is reached, the end of the copper stub is sealed shut with cold-weld pinch-off pliers. This sealing technique allows us to have greater control over the device

parameters and gives much more consistent seals from chip to chip than the first method.

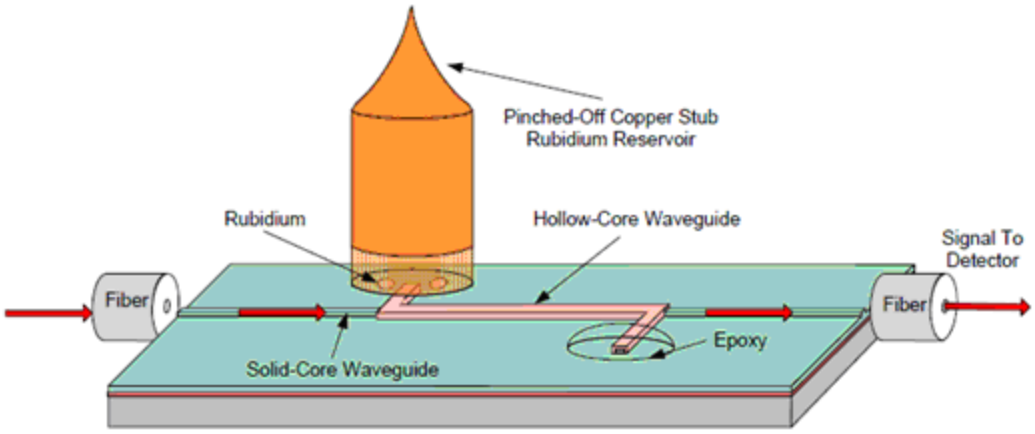

Figure 3.8 Second generation of Rb loaded ARROW

3.4 Improvement of ARROW fabrication

3.4.1 Cleaning Technique

It is also important to note that we have been experimenting with different cleaning techniques to better the performance and longevity of our devices. Currently, devices are washed in solvents (acetone, ipa or water), quickly dipped in acid on the copper stubs to remove oxides, followed by long-duration dehydration bakes (at 150c, for 90min) that also help fully cure the epoxies.

3.4.2 ODMS coating rubidium loaded ARROW

One consideration that must be made if small diameter hollow waveguides are to be used for quantum interference experiments is how the collisions of atoms with the sides of the waveguides will effect our measurements. Collisions with the sidewall can lead to coherence dephasing and for cross-section dimensions on the order of 10μm and a rubidium thermal velocity at room temperature of 240 m/s, we would expect a dephasing event every 40 ns. This is too short to observe many of the quantum interference effects we are interested in. Fortunately this problem can be mediated by adding a buffer gas into the waveguide and/or coating the walls of the waveguide with an organic surface coating. These coatings are known to passivate the surface of silica glass. This decreases both the occurrence of rubidium atoms adhering to the waveguide walls and the number of rubidium atom interactions with the walls, thus increasing the effectiveness of the waveguide as a quantum interference device.

A standard coating for glass vapor cells has been paraffin but coating the interior of a small diameter waveguide with paraffin is difficult because it tends to coat in layers at least as thick as the openings to the waveguides themselves. Two research groups working with rubidium vapors in photonic crystal fibers have reported using both octadecyldimethyl-methoxysilane (ODMS) [65] and polydimethylsiloxane (PDMS) [66] successfully as a surface coating inside their fibers. Both of these compounds form monolayer coatings to the fiber's silica surface that does not significantly affect the optical mode. It is reported that observations of EIT in these fibers is due in large part to

these coatings. The inner walls of our hollow ARROWs are formed from silicon nitride instead of silica. We have conducted a number of experiments to confirm that ODMS can provide an effective coating on a silicon nitride surface by measuring the surface energy before and after the coating is applied. The following figure (3.9) shows a fabrication process of applying the ODMS monolayer onto the Rb loaded ARROW.

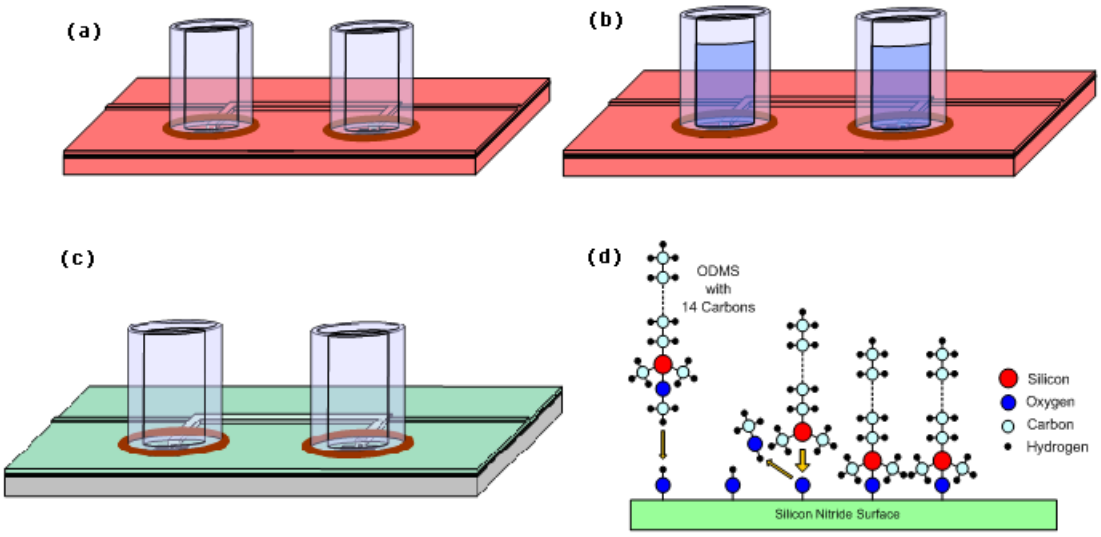

Figure 3.9 The fabrication process of applying ODMS coating: (a) Attaching reservoirs. (b) ODMS solution flowed through ARROW. (c) Remove excess ODMS. (d) ODMS layer on silicon nitride surface.

In addition to demonstrating the ability to coat the ARROW nitride layers effectively with ODMS, it is also essential to verify that the coatings do not adversely affect the optical properties of the waveguides. To this end, we coated a number of test waveguides with ODMS and evaluated their optical properties before and after the

coating process. These waveguides are straight hollow-core waveguides without solid-core waveguide sections and open on both ends. Both the optical mode profile and the transmitted power are recorded for comparison. Fig. 3.8 (a) and (b) show the mode profiles of one of these waveguides before and after ODMS coating, respectively. As can be seen, we observe no significant degradation after the ODMS coating and are confident this method can be used to suppress collision dephasing in rubidium filled ARROWs [67].

(a) (b)

Figure 3.10 Images of optical modes taken at the end of hollow waveguides illuminated by a single-mode fiber at the opposite side. (a) Waveguide with no ODMS coating on its interior walls. (b) Waveguide with ODMS coating on its interior walls.

In summary, a number of techniques are currently being pursued to miniaturize and simplify systems for atomic spectroscopy and quantum interference investigations. A viable lab-on-a-chip solution is to use hollow ARROW waveguide platforms. The possible methods of integrating Rb cells on ARROWs are investigated. Different sealing techniques are experimented by testing home-made minicells whose sealing

methods are later transferred to fabricate Rb loaded ARROWs. In order to minimize the dephasing rate in quantum coherence effects, an ODMS coating is deposited onto the inner wall of the hollow-core waveguide. This facilitates the realization of EIT experiment and slow light experiment in Rb loaded ARROWs.

Chapter 4 Rubidium Spectroscopy in Rb loaded ARROWs

4.1 Theory of rubidium spectroscopy

4.1.1 Atomic Transitions of Rubidium

There are two, naturally occurring isotopes of Rb: ^{85}Rb with nuclear spin I = 5/2 and natural abundance 72.17% and ^{87}Rb with nuclear spin I = 3/2 and natural abundance 27.83%. The energy diagram of these two isotopes is shown in the Figure 4.1.

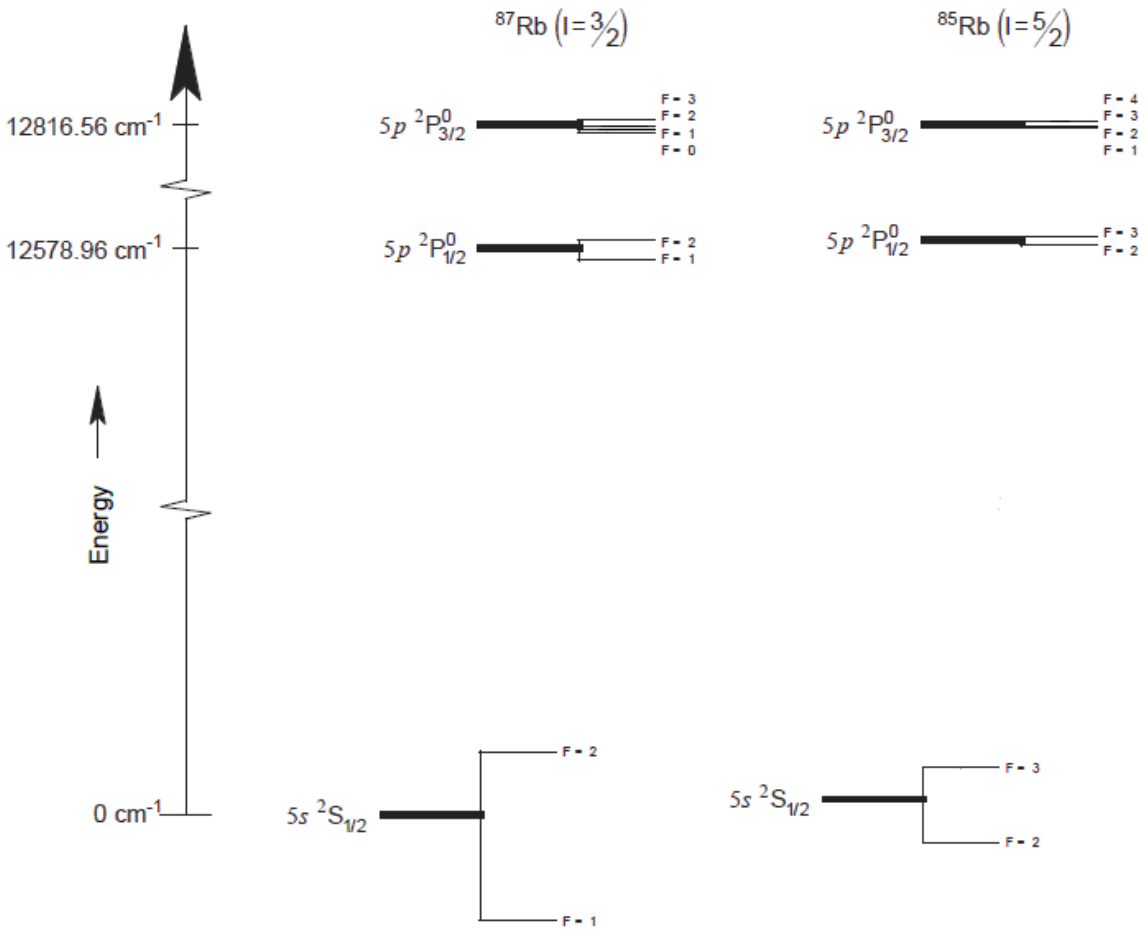

Figure 4.1 Energy level diagram of Rubidium (D1 and D2 lines)

The structural underpinnings of Rb responsible for the transition of an electron from one state to another are as follows [114]: the ground state electron configuration of Rb is $[1s^2, 2s^2, 2p^6, 3s^2, 3p^6, 3d^{10}, 4s^2, 4p^6], 5s^1$. Only the valence shell (5s) is unfilled with one electron. As a result, the structure of energy levels is similar to that of hydrogen. As for the core Rb+ ion, it is spherically symmetric, resulting in a total angular momentum (L), spin angular momentum (S), and thus spin-orbit L-S coupled angular momentum

(J = |J| = |L + S|) of zero. Consequently, with all the core ion quantum numbers equal to zero, the observed energy transitions with the associated changes in L-S coupled quantum numbers comes from the valence electron only. Stated in L-S coupling notation: (nl)2S+1Lj, (where n and l are the principle and angular momentum quantum numbers respectively), the ground electronic state is (5s)2 $S_{1/2}$, and the first electronic excited state is found in the (5p)2 orbital. Here S = 1/2 and L = p = l = 1, leaving two possible values for J (i.e., |L–S|, …, J, …, |L+S|; in integer steps) equal to 1/2 and 3/2 . As a result, two possible energy levels exist for these given n and l values. The first, less energetic excited state is referred to as the D1 line and has the following quantum numbers: $(5p)^2$ $P_{1/2}$. The second, more energetic excited state is referred to as the D2 line and has these quantum numbers: $(5p)^2$ $P_{3/2}$. This splitting of the S=1/2 and L=1 state into two finer (J = 1/2, and 3/2) states is known as the magnetic fine structure states of the atom, where the former state corresponds to a transition from the ground state with a wavelength of 794.8 nm, whereas the latter transition corresponds to a wavelength of 780.0 nm. The following experiments are mainly done with 780nm diode lasers, and therefore we focus on the D2 line.

4.1.2 Hyperfine Splitting

The spin quantum number of the nucleus (I) and the nuclear quadrapole moment lead to even finer splittings in the energy spacing of the atom, known as the atomic hyperfine

structure. In zero or even very weak magnetic fields, I and J couple together and lead to what is known as the grand total angular momentum quantum number of the whole atom: F = |F| = |I + J|, where |I–J|, …, F, …, |I+J| in integer steps. Now, it must be noted that ^{85}Rb has I = 5/2, whereas ^{87}Rb has I = 3/2. Therefore, considering only the D2 line where J= 3/2, the two isotopes each have differing states. That is, with J = 3/2 and I= 5/2, ^{85}Rb has the following possibilities for F states: F= 1, 2, 3, and 4, whereas with I = 3/2, ^{87}Rb has these following values of F states: F= 0, 1, 2, and 3. The ground state quantum numbers for ^{85}Rb are J =1/2, and I = 5/2, resulting in the possible F states: 1,2, and 3, whereas the ground state quantum numbers for ^{87}Rb are J = 1/2 and I = 3/2 resulting in these possible F states: F = 0,1, and 2. Evidently, in both cases the ground state is split into two hyperfine levels, making the total number of possible transitions in each isotope, from the ground state to the excited D2 line, not eight, but six. This is due to the fact that transitions from one energy level to another must obey certain quantum mechanical selection rules that prohibit two of the transitions above. These selection rules for the exchange of one value of quantum number for another in a given transition, for the quantum numbers F, J, L and M, dictate that no quantum number may change by more than 1. In other words, the difference between the value of a ground state and an excited state quantum number can either be 0 or 1. The only exception is that L can only change by one, not by zero. Thus, in the case of transitions from the F values of 2 and 3 for ^{85}Rb, and 1 and 2 for ^{87}Rb, to the four corresponding excited state F values of each isotope, there can only be six possible transitions as illustrated in the

hyperfine energy manifold of Rb.

4.1.3 Doppler Broadened Spectroscopy

The full spectrum, revealing the four absorption peaks, is known as the Doppler broadened spectrum as illustrated in figure 4.2.

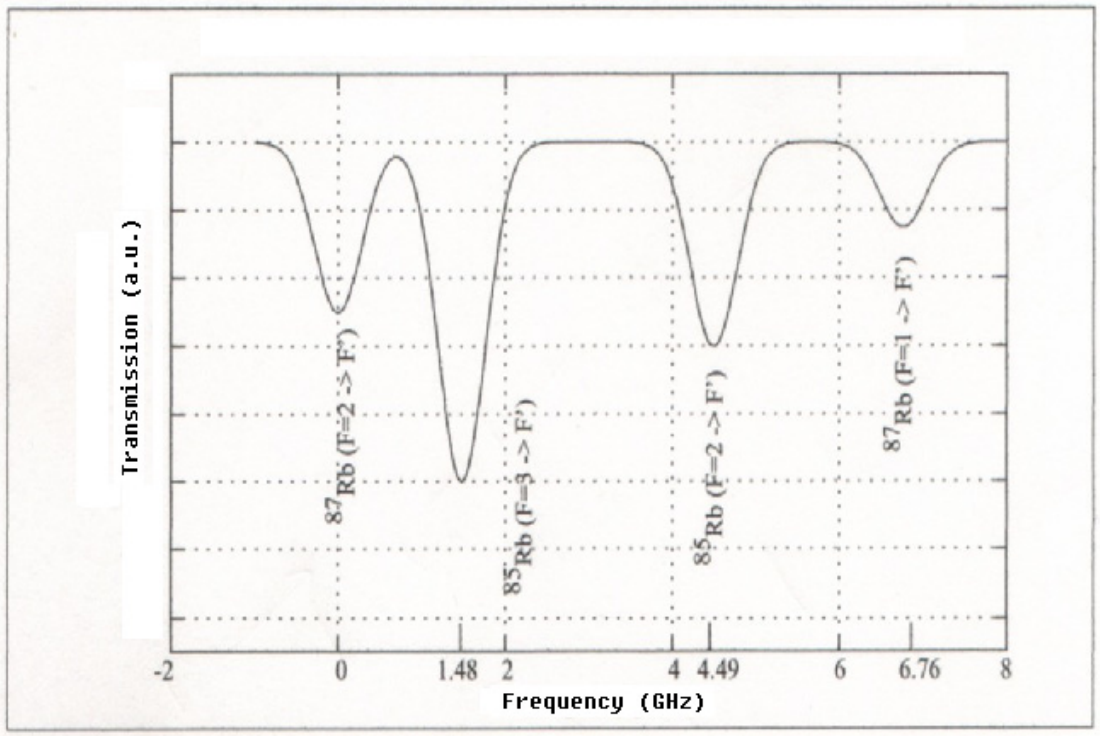

Figure 4.2 D2 line rubidium spectroscopy with Doppler broadening

With reference to the six possible transitions from ground to excited states in the two isotopes mentioned above, the four peaks correspond to two sets of transitions, each of which stems from the two ground states of both isotopes. The two outer peaks of the

full profile of the transitions (from the $5S_{1/2}$ to the $5P_{3/2}$ states) correspond to transitions from the F =1 and 2 ground states of ^{87}Rb, and the two inner peaks correspond to transitions from the F=2 and 3 ground states of ^{85}Rb. Within each peak, transitions to the three excited states that obey the DF selection rules mentioned above, are obscured by Doppler broadening.

This Doppler broadening of the D2 transition peaks refers to the fact that within the Rb vapor cell, the atoms are moving with a Boltzman velocity distribution corresponding to room temperature. The Boltzman velocity probability distribution is as follows:

$$\mathrm{P}\left(V_X\right) = \exp\left(-MV_X^2 / 2\mathrm{k}_B\mathrm{T}\right) \qquad (4.1)$$

and the Doppler width is given by:

$$\Delta\omega_d = (8\mathrm{k}_B \ln 2)^{1/2} (T / M)^{1/2} \omega_0 \qquad (4.2)$$

where x refers to the direction of the beam, V_x is the x component of the velocity of the Rb atoms in the vapor cell, M is the atomic mass, T is the temperature, ω_0 is the central frequency and k_B is the Boltzman constant. Using the laser beam's direction of propagation as a reference for the positive direction, entering the cell from one end and exiting at the other, the atoms move with a velocity component either parallel to (x-direction) or anti-parallel to the beam. Thus, the Doppler profile is a direct verification of the fact that atoms in the vapor cell will absorb light that is detuned off of the atomic transition frequency with different velocities. The zero velocity group or class of atoms is the only group that does not contribute to the Doppler broadening and

corresponds to the summit of the Doppler peak and the lab frame transition frequency. Atoms with positive velocities with respect to the beam see the incident beam red shifted to the transition frequency and correspond to the higher frequency side of the Doppler peak, whereas atoms with negative velocities see the incident beam blue shifted to the transition frequency and correspond to the lower frequency side of the Doppler profile. This is the very source of the Doppler broadening as seen in figure4.2. That is, each portion of the Doppler profile corresponds to a different velocity class of atoms which see different degrees of Doppler shifting of the incident beam frequency to the transition frequency.

Since the magnitude of the detected absorption is proportional to the number of atoms with certain velocity, the Doppler profile thus has the shape of the Maxwell-Boltzman distribution, i.e., a Gaussian, which gives the relative number of atoms in each velocity class. The relation between the velocity of the Rb atoms and the Doppler shifted frequency is:

$$\nu' = \nu_0(1 + \nu_X / c) \qquad (4.3)$$

where ν_0 is the transition frequency of the Rb, and ν' is the incident beam frequency. Since ν_0 is constant, the preceding equation (4.3) illustrates the one-to-one correspondence between the absorbed (incident) frequency ν', and the atomic velocity v_x. Doppler broadening leads to a FWHM of about 505 MHz around room temperature. A theoretical calculation of Doppler broadening (FWHM) with the increasing temperatures was shown as in figure 4.3.

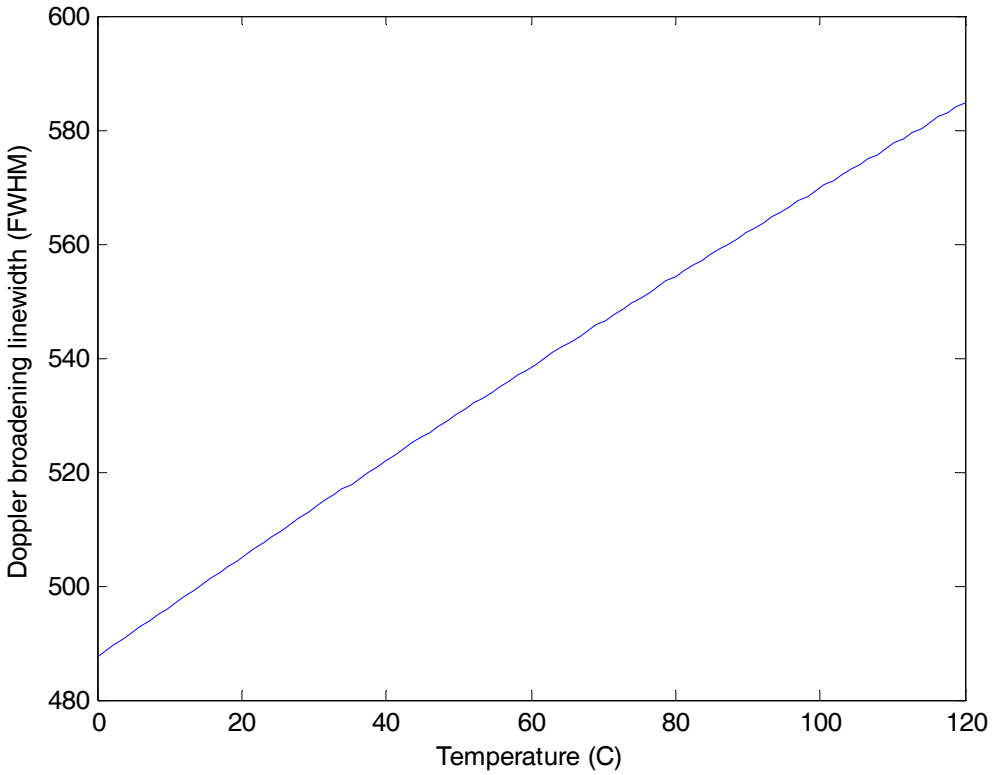

Figure 4.3 Doppler broadening linewidth (FWHM) v.s. Temperature

4.2 Rb spectroscopy in bulk cell

4.2.1 Experimental setup

The rubidium spectroscopy is conducted as illustrated in figure 4.4. A laser beam from an external cavity diode laser (ECDL) tuned to the atomic D2 transition is directed through the rubidium bulk cell and the light is then collected by an optical detector (sometimes, a lens may be needed to focus the entire beam spot into the detection area

on the detector for a clear rubidium absorption signal). The signal is then recorded in the oscilloscope.

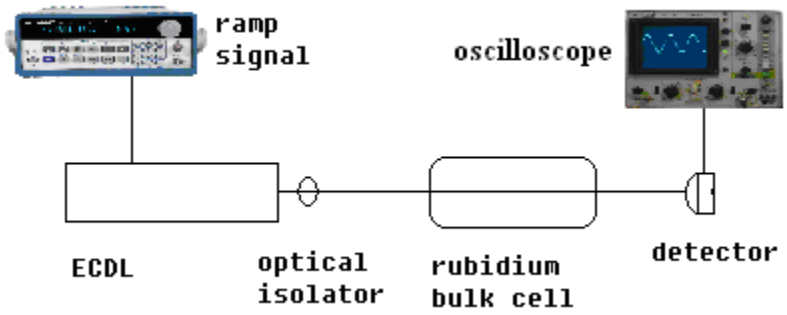

Figure 4.4 Experimental Setup of rubidium spectroscopy in bulk cell

4.2.2 Using interferometry technique to improve the experiment

An original rubidium spectrum directly obtained from the experiment (Newfocus Vortex Series D2line ECDL) is illustrated in figure 4.6 (a). The upper curve is the fringes from an interferometer as shown in figure 4.6 (a) and the lower curve is the rubidium spectroscopy in the bulk cell. It is obvious to identify from the unequal space of the fringes that the piezoelectric motor built in the ECDL has a nonlinear response to the applied voltage. Therefore, the absorption peaks in figure 4.6 (a) have very different widths due to the nonlinearity of the piezo.

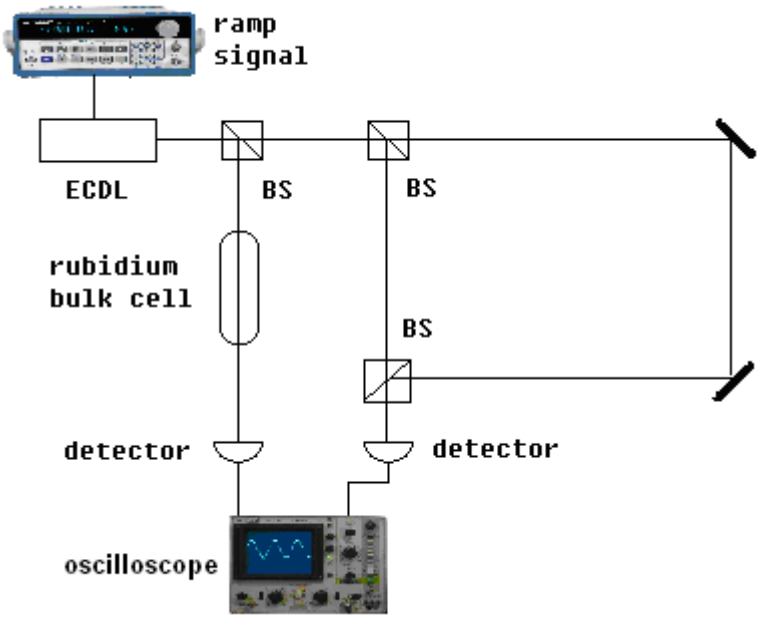

Figure 4.5 Rubidium spectroscopy with the interferometer rectification

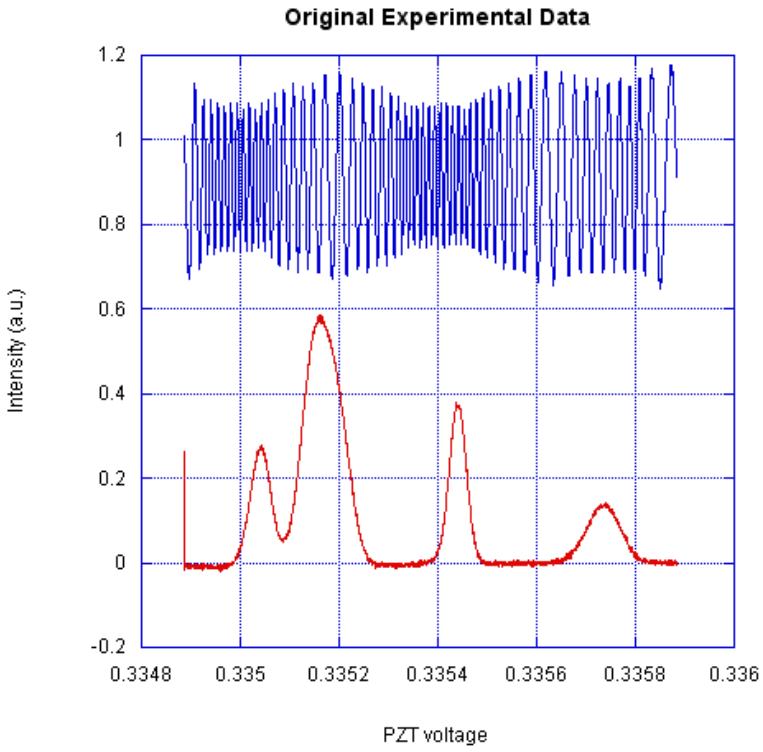
Original Experimental Data
1.2
1
0.8
0.6
0.4
0.2
0
-0.2
Intensity (a.u.)
0.3348
0.335
0.3352
0.3354
0.3356
0.3358
0.336
PZT voltage

(a)

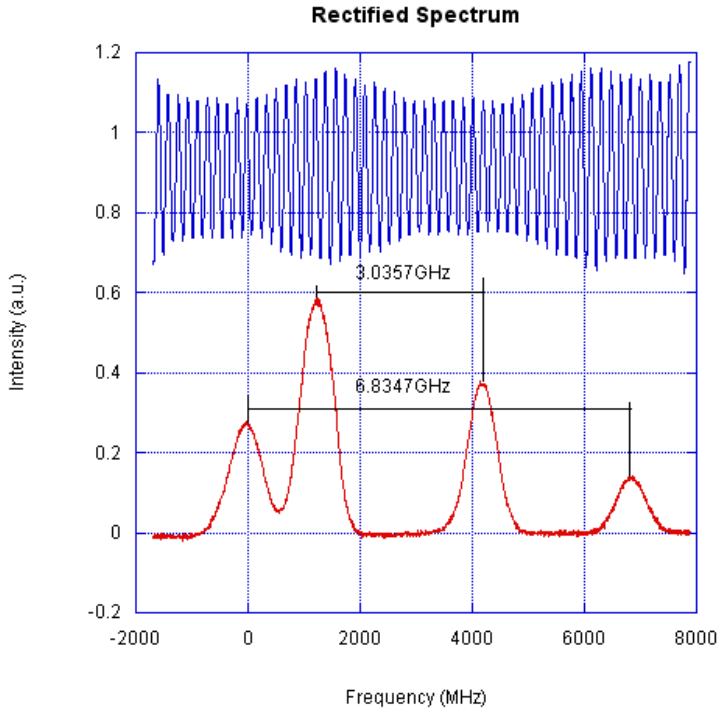

(b)

Figure 4.6 (a) The rubidium spectroscopy and interferometer fringes before rectification; (b) The rubidium spectroscopy and interferometer fringes after rectification

In order to overcome this artificial nonlinearity introduced by the ECDL, a software rectification method is employed to intentionally even the space between the fringes and then rectify the corresponding data points for the rubidium absorption spectrum.

After this software rectification, the evened fringes and rectified spectrum are drawn in figure 4.6 (b). As a result, the rubidium absorption spectrum is now illustrated in the linear scale, that can be calibrated by the known hyperfine splitting in ^{85}Rb and ^{87}Rb, respectively.

4.3. Rubidium spectroscopy in minicells

4.3.1 Experiment setup

The experimental setup for rubidium spectroscopy in mincells is illustrated in figure 4.7. The whole setup is similar to the spectroscopy testing of bulk cell except that the bulk cell is replaced by a minicell aligned in a heating oven with input and output windows which is used for temperature controlling of minicells.

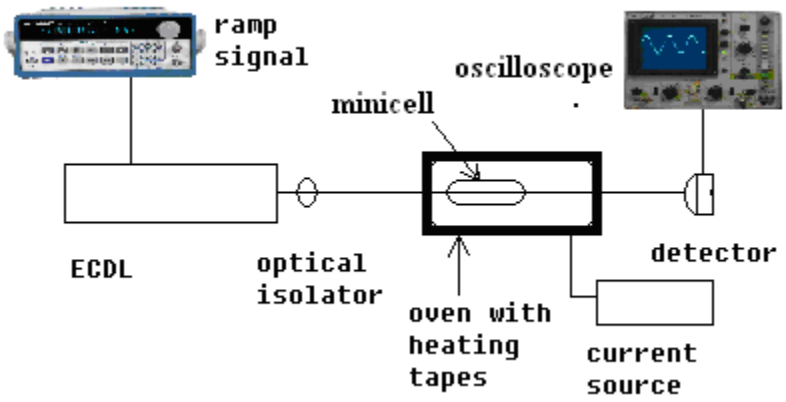

Figure 4.7 Experimental setup of Rb spectroscopy in minicell

4.3.2 Experimental result

As we have mentioned in the previous chapter, the minicell with crimped copper tube on top was identified as the sealing technique to be transferred to fabricate the Rb loaded ARROW. In figure 4.8, an example of rubidium spectroscopy (D1) in a minicell (the first crimped minicell with rubidium absorption signal) is demonstrated. As seen in this figure, part of the D1 line (795nm) is obtained by scanning the probe laser frequency. Dips from left to right indicate different atomic transitions: first: ^{85}Rb F=1->F'=1 and F=1->F'=2; second: ^{87}Rb F=1->F'=1; third: ^{87}Rb F=1-> F'=2.

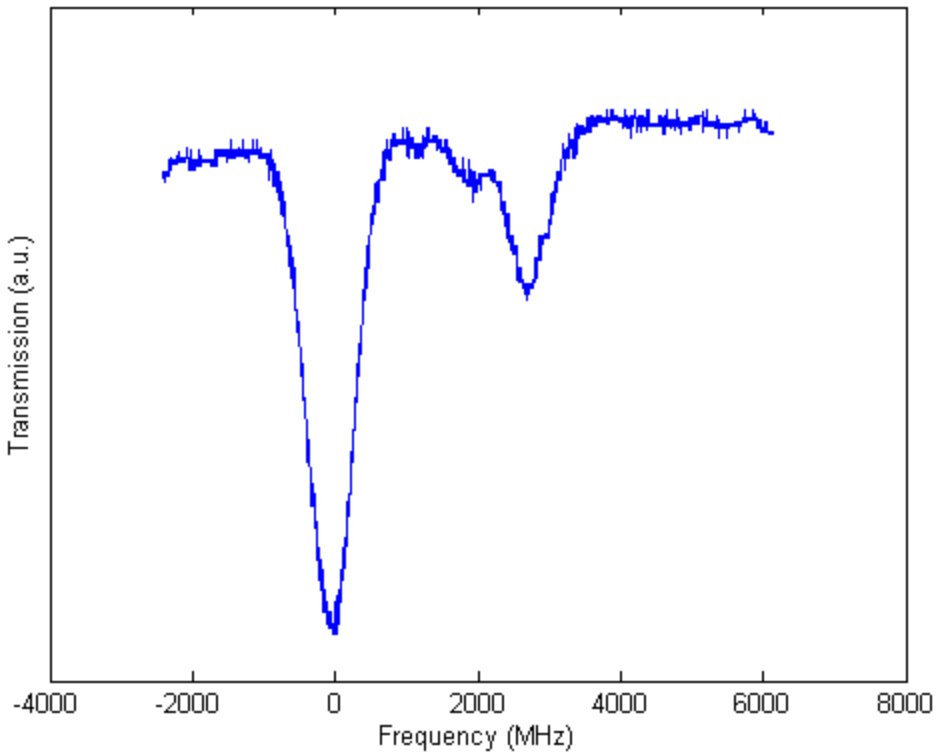

Figure 4.8 Rubidium spectroscopy from first crimped minicell of D1 line.

4.3.3 Multi-cycle heating test for characterizing minicell performance

From the fundamental physics, we know that the atomic density of rubidium vapor may increase with heating (i.e. higher temperature renders larger atomic density). A larger atomic density gives a deeper absorption signal and hence a better EIT signal as well as nonlinear optics responses. Therefore, it is necessary to heat up our Rb samples at different temperatures.

However, with our experiment, we find out that the epoxy used for sealing rubidium may degrade during the heating process. Therefore, it is necessary to test the minicells with several heating and cooling cycles at different temperatures. Figure 4.9 shows two multi-cycle heating and cooling tests at several different temperatures.

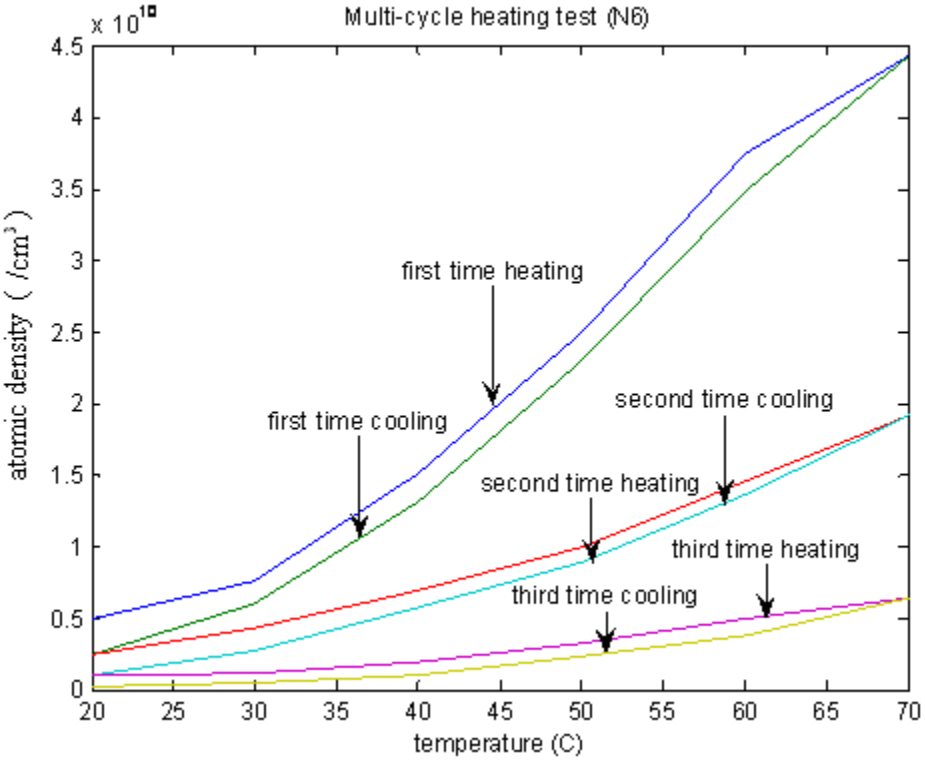
Multi-cycle heating test (N6)
x 10^18
atomic density (/cm^3)
temperature (C)
first time heating
first time cooling
second time cooling
second time heating
third time heating
third time cooling
4.5
4
3.5
3
2.5
2
1.5
1
0.5
0
20
25
30
35
40
45
50
55
60
65
70

(a)

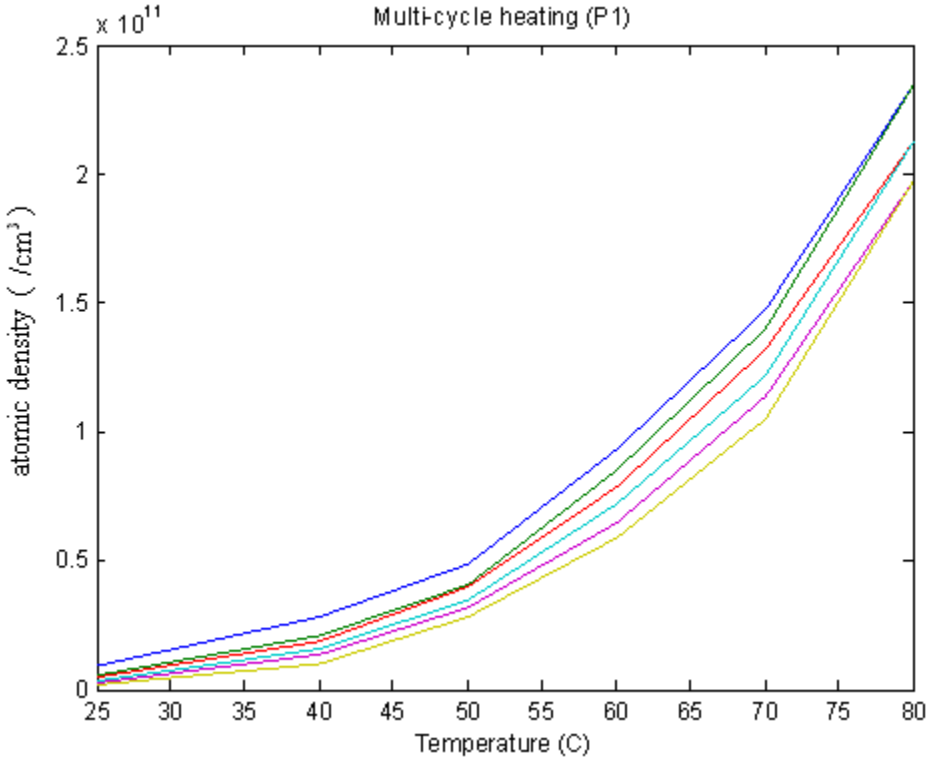

(b)

Figure 4.9 Multi-cycle heating and cooling test of minicells: (a) Multi-cycles heating and cooling test of rubidium in a minicell with old fabrication method (b) Multi-cycles heating and cooling test of rubidium in a minicell with improved fabrication method (crimped minicell)

The degradation of atomic density at room temperature between figure 4.9 (a) and figure 4.9 (b) are compared in figure 4.10.

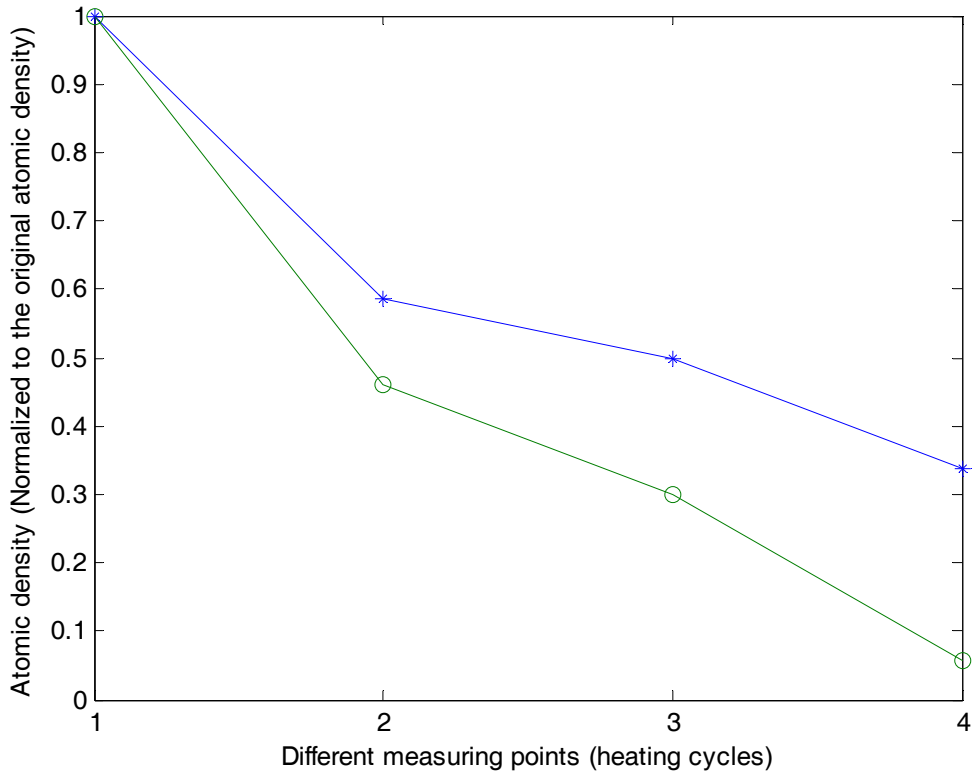

Fig 4.10 Atomic density evolution with cycles of heating and cooling. Crimped minicell (stars), Non-crimped minicell (circles); X-axis: 1: before heating. 2: after first heating and cooling cycle. 3: after second heating and cooling cycle. 4: after third heating and cooling cycle. Y-axis: atomic density normalized to the original value at 1.

From the comparison, the great improvement (more than 6 times of the percentage of atomic density remained after three cycles of heating and cooling) has been achieved by choosing the effective epoxy (Amcrobie8510) and the crimped top to the minicells.

4.3.4 Pressure control in Rb loaded minicells

We have successfully demonstrated the dependence of the absorption dip linewidths on pressure inside our vapor cells. With our ability to control the internal pressure of our atomic vapor cells, minicells were created with the crimped top and the data were measured as seen in Fig. 4.10.

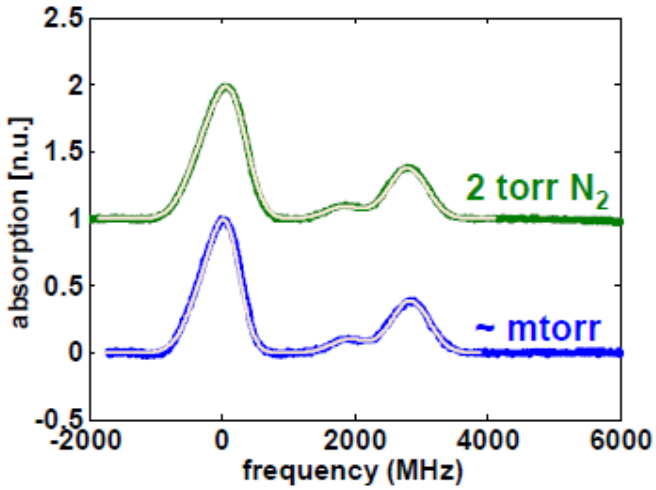

(a)

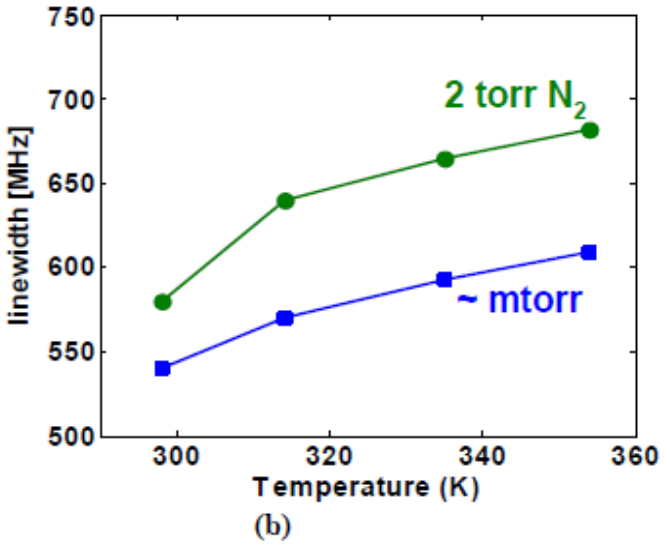

Figure 4.11 (a) Rubidium absorption spectra of minicells with no buffer gas (squares) and 2 torr buffer gas (circles). (b) Absorption spectra linewidths of minicells with no buffer (squares) and 2 torr buffer gas (circles).

Fig. 4.11 (a) compares the two absorption spectra while Fig. 4.11 (b) plots the linewidth (which is the FWHM Doppler extracted by fitting the Rb absorption spectra as shown in fig. 4.11(a). See section 4.5.1 for details.) versus the temperature of the minicells. As expected, higher pressures inside the cells result in linewidth broadening due to interactions between the Rb atoms and the residual nitrogen atoms. This is a demonstration of our ability to control the gas pressures for our devices which may be used for various applications in future experiments.

4.4. Spectroscopy in Rb-loaded ARROWs

4.4.1 Experimental setup for Rb loaded ARROW

The experimental setup is illustrated in figure 4.12. The Rb loaded ARROW is mounted on a XY stage which is placed after a fiber chuck mounted on a XYZ stage and before an objective lens mounted on a XYZ stage.

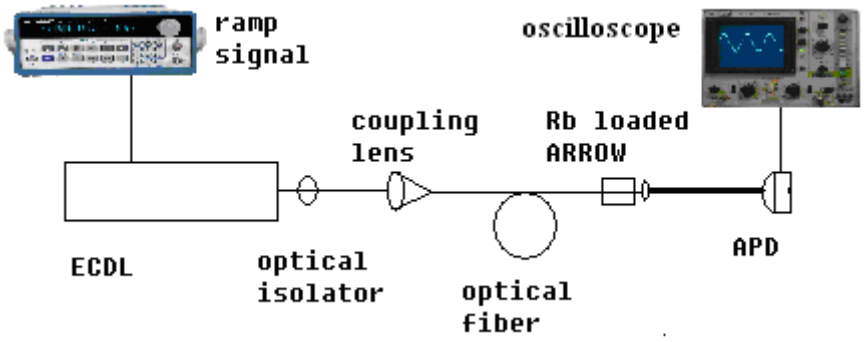

Figure 4.12 Experiment setup of Rb spectroscopy in Rb loaded ARROW

The laser beam is coupled into an optical fiber (Here we use a 8°fiber to eliminate the oscillations due to the interference between the parallel fiber ends.) Then the fiber end is placed adjacent to the input end of the waveguide chip. The output light is collected and imaged by an objective lens onto an avalanche photo diode (APD). The internal gain of APD would help the collection of small signal out of the Rb loaded ARROW chip.

4.4.2 Experimental results

In order to further characterize the optical properties of the integrated rubidium cell, the chip was heated to different temperatures between 60 and 95℃ and the measured spectra are compared to spectra that are taken from a conventional bulk rubidium cell at the same temperatures. Figure 4.13 shows the results of this comparison with the normalized bulk cell spectra shown in Fig. 4.13 (a) and the ARROW spectra in Fig. 4.13 (b).

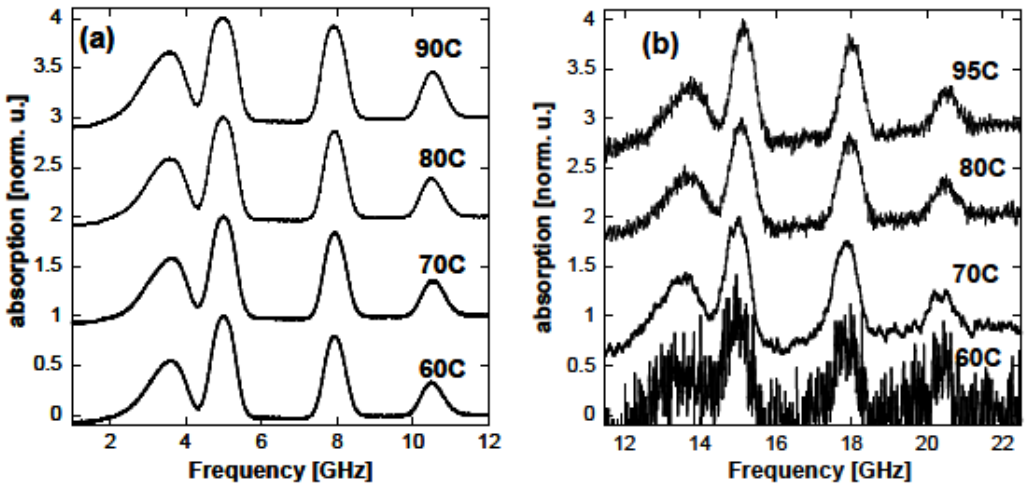

Figure 4.13 (a) Rb absorption spectra at different temperatures with bulk cell; (b) Rb absorption spectra at different temperatures with Rb loaded ARROWs.

The figure shows that the spectra are similar in shape without dramatically changing over the observed temperature range. The ARROW spectra are generally noisier, in particular at lower temperatures where the atomic density is still low. The effect of

increasing optical density is observed at the highest temperatures in the bulk cell when the strongest absorption peaks show noticeable flattening. The increase in optical density in the ARROW cell is clearly visualized in Fig.4.13 (b). Clearly, much larger absorption and therefore atomic density in the optical beam path is achieved at the higher temperature.

Fig.4.14 shows the dependence of the absorption line width of the high-frequency ^{87}Rb peak for the two cell types as a function of cell temperature. An overall increase in broadening is observed in both cases due to increased Doppler broadening. Interestingly, the broadening for the ARROW cell remains below the bulk cell for all temperatures, likely due to the lower atomic density.

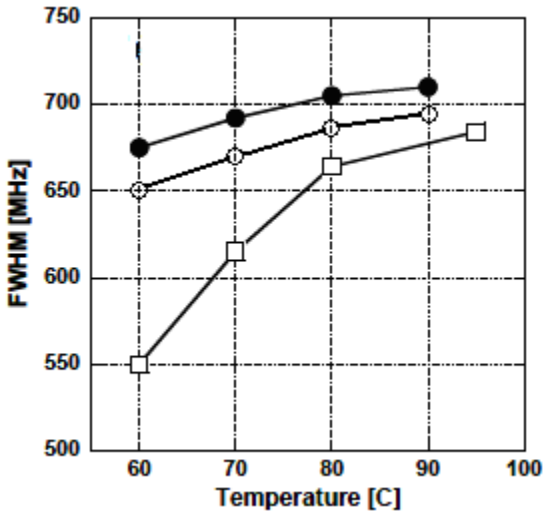

Figure 4.14 The absorption linewidths are extracted for both bulk cell (solid circles), Rb loaded ARROWs (open squares), and theoretical values (open circles) v.s.

different temperatures.

The results demonstrated in this section validate the integrated ARROW approach to carrying out atomic spectroscopy on a chip. The behavior of the cell is comparable to standard bulk cell and significant optical densities (OD is defined as $OD = -\log(I_{out} / I_{in}) = \alpha L$) can be achieved over short distances of only a few millimeters on the optical chip. The measurements discussed here open the way for more comprehensive spectroscopic studies including a detailed analysis of the observed linewidths, saturation absorption spectroscopy using counter-propagating beams, nonlinear frequency generation taking advantage of the small mode areas and high intensities inside the hollow-core ARROW, and realization of quantum coherence effects including EIT and slow light on a chip.

4.5 Fittings of rubidium spectroscopy

4.5.1 Equations and methods

The intensity profile centered at each atomic transition is given by [117]:

$$I_{out} = I_{in} \exp(-\frac{2\omega_{ij} n_0}{c} \frac{N\mu_{ij}^2}{\hbar\Delta\omega_d} \frac{1}{1+\frac{2\Delta\omega_{ij}}{\Delta\omega_d}}) \qquad (4.4)$$

Where $\Delta\omega_d$ is the Doppler width. ω_{ij} is the central frequency, n_0 is the refractive

index at this frequency, c is the speed of light at vacuum, N is the atomic density, μ_{ij} is the dipole moment of the transition, $\Delta\omega_{ij}$ is the laser detuning from ω_{ij}.

For a complete scanning of spectrum, different dips stand for different absorption transitions, so the total absorption curve is a sum of all these transitions at slightly different center frequencies:

$$I_{tot} = I_1 + I_2 + I_3 + \ldots \qquad (4.5)$$

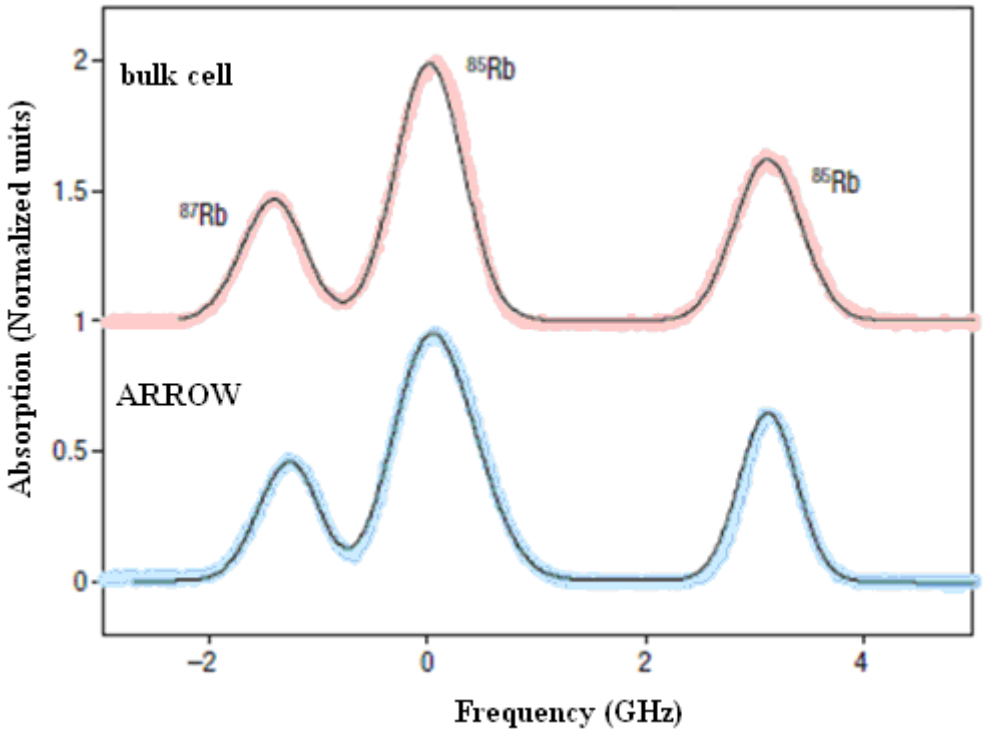

Figure 4.15 The fitting of Rb absorption spectra in both bulk cell and Rb loaded ARROW

The fitting is performed by varying the Doppler width in a reasonable range (typically

from 450MHz to 650MHz) and finding optimum result of the theoretical curve compared by the experimental data by least square fitting.

Figure 4.15 shows an excellent agreement with the experimental data (at 70℃) and the theoretical data. The extracted Doppler width is 576MHz.

4.6 Theory of saturated absorption spectroscopy

4.6.1 The zero-velocity dips

For experiments requiring greater precision, i.e. a smaller FWHM, a technique known as saturation spectroscopy has been developed that significantly reduces the FWHM of the Doppler broadened peaks [114]. By overlapping the probe beam that produces the original Doppler broadened peaks with an intense, counter-propagating saturating (or pump) beam (~several times more intense and derived from the same laser) within the vapor cell, the spectrum from the zero velocity group of atoms is able to be selected out. The technique of saturation spectroscopy operates by taking advantage of a peculiar interaction between atomic velocity classes and the overlapping beams mentioned, in a way such that when the laser is tuned to precisely the atomic transition frequency, the fine structure, initially obscured by Doppler broadening is exposed. These Doppler free peaks with a FWHM of about 20 to 50 MHz depict the hyperfine structure of the atomic transitions as illustrated in figure 4.16.

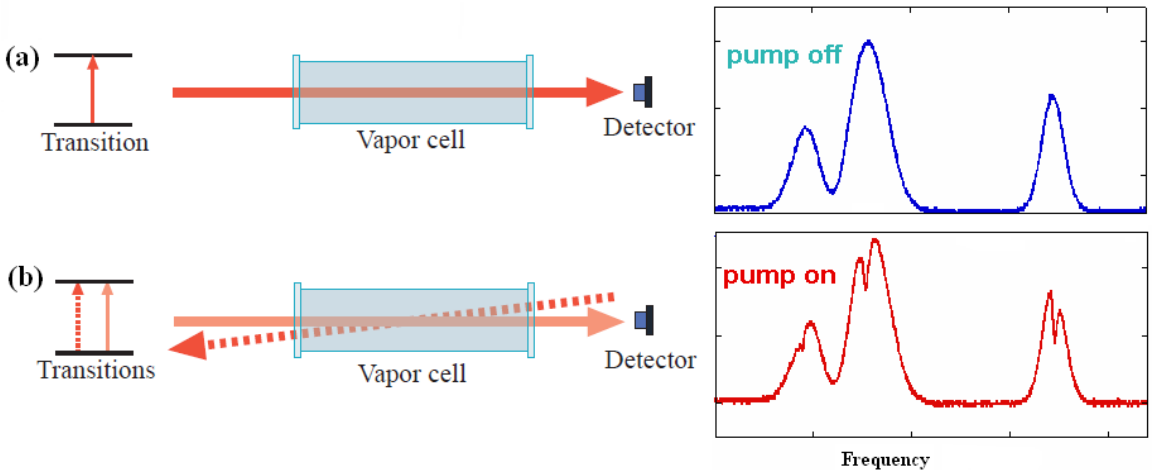

Figure 4.16 Sketch of setup and result of linear (a) Rb spectroscopy and Saturated (b) Rb spectroscopy.

Now, once the counter-propagating pump beam overlaps one of the probe beams, the situation remains relatively unchanged with respect to the absorption profile, since the two beams interact with different velocity classes of atoms. That is, since the two beams are of the same frequency they each interact with atoms moving with similar speeds and thus similar Doppler transition frequencies. But since the beams are counter-propagating they interact with atoms with opposite directions of movement. At one particular value of frequency in the sweep, each of the two beams interacts with atoms on opposite sides of the Doppler profile. The absorbed light in both cases is either blue-shifted or red-shifted. Assuming it is blue-shifted, once the sweep goes up in frequency, the two beams switch sides of the Doppler profile, and the respective atoms now see the light red-shifted. This is just another way of saying that the production of the Doppler peak is independent of the direction of the laser beam in the

lab. And since the two beams interact with a different set of atoms altogether, they have no effect on one another. As a result, the probe beam reports a signal to the photodiode that is unperturbed by the presence of the pump beam.

However, when the laser is nearly tuned to the zero velocity transition frequency during the scanning, the two beams have no choice but to interact with the same set of zero velocity atoms. The result is that the absorption of the probe beam is reduced at one spot along the Doppler broadened profile. Namely, during the course of a sweep across an absorption peak, the photodiode reports the original Doppler broadened profile, but the absorption is suddenly reduced and the intensity goes up at one location once the sweep reaches the transition frequency of the zero velocity atoms. Once the laser is tuned to the atomic transition frequency, both beams interact with the same atoms, but the pump beam, being much more intense, has a much larger probability of interaction. Once an atom is excited it cannot be re-excited until it decays. In other words, once the pump beam excites a certain atom, it is removed from the pool of excitable atoms available to the probe beam. And once the two beams are overlapped, the absorption of the probe beam is reduced by a factor governed by the number of zero velocity atoms that are excited by the pump beam. As a result, the signal reported by the overlapping probe beam tuned to the atomic transition reveals Doppler broadened peaks with small dips (called Lamb dips) corresponding to the absorption frequencies of the zero velocity class of atoms only. Since the un-broadened absorption profile is a result of revealing other broadening mechanisms in our system (in ARROW, the time

of flight broadening dominates due to its micro-scale dimensions), which have a Lorentzian lineshape, these Lamp dips inherit the very same Lorentzian lineshape.

4.6.2 The crossover dips

The final spectrum reveals not only the Doppler free peaks that have been discussed, but additional spurious peaks, appearing between each real absorption peak [114]. These spurious peaks are known as cross-over peaks and can arise when there is more than one hyperfine transition under the same Doppler profile, allowing the laser beam the possibility of interacting with two different velocity classes of atoms at the same time. At this point it is useful to recall that the Doppler profile is a composite effect of the different velocity classes of atoms that see a range of frequencies Doppler shifted to the atomic transition frequency of Rb. As such, given two different hyperfine transition frequencies (termed ν_1 and ν_2) under the same Doppler profile corresponding to two different nonzero velocities, V_1 and V_2 respectively, there are potentially certain laser frequencies, ν_L that will be concurrently Doppler shifted to both ν_1 and ν_2 and absorbed by the two different sets of atoms at the same time as shown in figure 4.17.

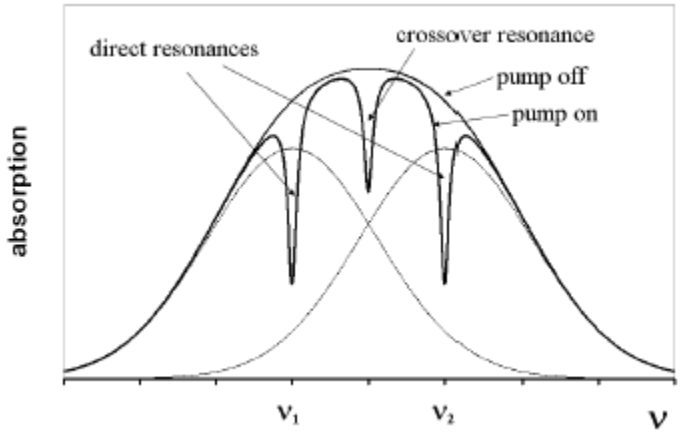

Figure 4.17 Illustration of cause for crossover dips

In particular, it turns out that the frequency spacing between the hyperfine transitions is such that a single beam must interact with atoms moving in opposite directions for cross-over peaks to arise. Thus, for a given output frequency, blue shifted transitions in atoms moving in one direction and red shifted transitions in atoms moving in the opposite direction are both excited to their respective transitions by the same beam at the same time. It is important to emphasize that the atomic interaction in each of these two cases corresponds to two completely different hyperfine transitions, for it is impossible for a single frequency to be simultaneously red shifted and blue shifted to the same transition frequency. Now, if both the probe beam and saturating beam are present, the following scenario is established such that each beam interacts with two groups of atoms moving in opposite directions. Since the probe beam and saturating beam are of the same frequency, they each interact with two distinct atomic velocity

classes having the same speed, but with opposite directions of movement.

Thus, in order to produce cross-over peaks at least four groups of atoms are involved, moving with different velocities: $\pm V_1$, and $\pm V_2$ corresponding to ν_1 and ν_2 respectively, where the probe interacts with, for example, the $+V_1$ and $-V_2$ velocity class and the pump beam with the $-V_1$ and $+V_2$ velocity classes. (Here the direction of the probe beam is taken as positive.) So far, given the present situation, the pump beam and probe beam do not interact with same atoms. The probe beam then, although interacting with two atomic velocity classes at the same time, is simply contributing to the Doppler profile as before, but in a two-fold manner. In fact, it is safe to say the reference beam interacts in exactly the same way the probe beam does here and any effect like the sharing of beam intensity between two transitions (resulting in a sudden increase in absorption) can be canceled out. Now it is conceivable that the laser frequency can be swept to a given frequency, ν_{LC} such that the $-V_1$ velocity class (red shifted to ν_1) of the pump beam is the very same velocity class as $-V_2$ (i.e., $-V_1 = -V_2$) corresponding to the probe beam (blue shifted to ν_2). The same would of course be true for the $+V_1$ and $-V_2$ velocity classes due to the symmetry of the velocities described above. A circumstance has thus evolved where the probe and pump beam interact with the same nonzero velocity class of atoms. As a result, like the case for the zero velocity class of atoms discussed earlier, there is a reduction in the absorption of the probe beam and consequently a detected absorption peak.

In summary, a crossover occurs when the laser frequency ν_{LC} is such that atoms

with velocity -V see the pump beam Doppler red shifted to the transition frequency at a lab frame value of ν_1 and at the same time, see the probe beam blue shifted to the lab frame value of ν_2 and vice-versa for atoms moving with velocity +V, where $\nu_1 = \nu_L(1 - V/c)$, and $\nu_2 = \nu_L(1 + V/c)$. Since the pump beam is so much more intense, the interaction with the pump beam is dramatically favored. Solving for ν_L gives: $\nu_L=(\nu_1 +\nu_2)/2$, which places each crossover halfway between successive Doppler free transitions.

4.6.3 Time of flight broadening

In our SAS experiment with Rb loaded ARROWs, the time of flight (TOF) broadening needs to be considered due to the fact that the atoms in a gas move across the full width of micro-scale optical beam with which they are interacting in a transit time which is small compared with the energy decay lifetime. The transit time T_{tr} is given by:

$$T_{tr} = d / v \quad (4.6)$$

Where d is the optical mode diameter and v is the atomic velocity. Therefore, the estimated broadening due to the limited transit time is:

$$\Delta\nu_{tr} \approx 1 / T_{tr} \quad (4.7)$$

In our experiments, with the typical velocity of gas phase Rb atoms (263m/s at room temperature T=20℃). The calculated TOF broadening: $\Delta\nu_{tr} \approx 35\text{MHz}$ with an average diameter of 7.52 μm.

4.7 Saturated absorption spectroscopy in Rb loaded ARROW

4.7.1 Experimental setup

The experiment setup of saturated absorption spectroscopy (SAS) is shown in figure 4.18. The first beam splitter is used to separate the laser light into a strong pump beam and a weak probe beam. The probe beam is then coupled into the optical fiber and directed into the Rb loaded ARROW. The strong coupling beam is directed back into the opposite direction of the Rb loaded ARROW by an objective lens. Therefore, the two beams counter propagate each other and meet in the Rb loaded hollow ARROW.

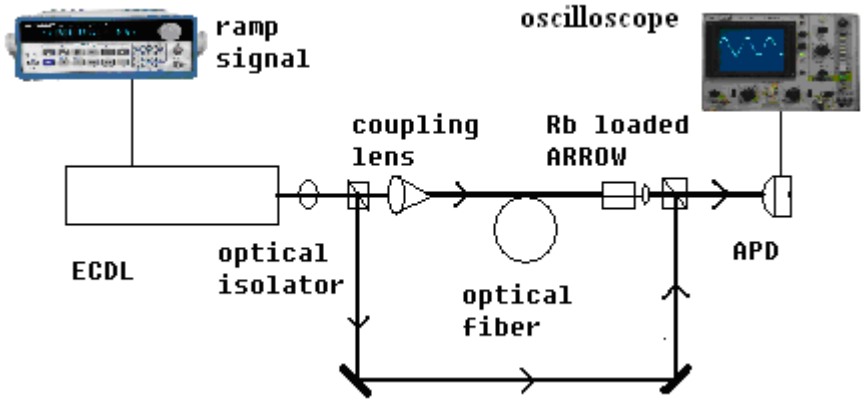

Figure 4.18 The experimental setup of SAS in Rb loaded ARROW

In these optical experiments, the chips are mounted on a waveguide translation stage. Light from tunable external cavity diode lasers was coupled into the solid-core

ARROW as shown in Fig.4.18 using end-coupling from a single-mode fiber. Transmitted light is collected with an objective lens, focused on an APD, and recorded as a function of frequency.

4.7.2 Experimental results

In figure 4.19, the saturated absorption spectroscopy is demonstrated in Rb loaded ARROW [119].

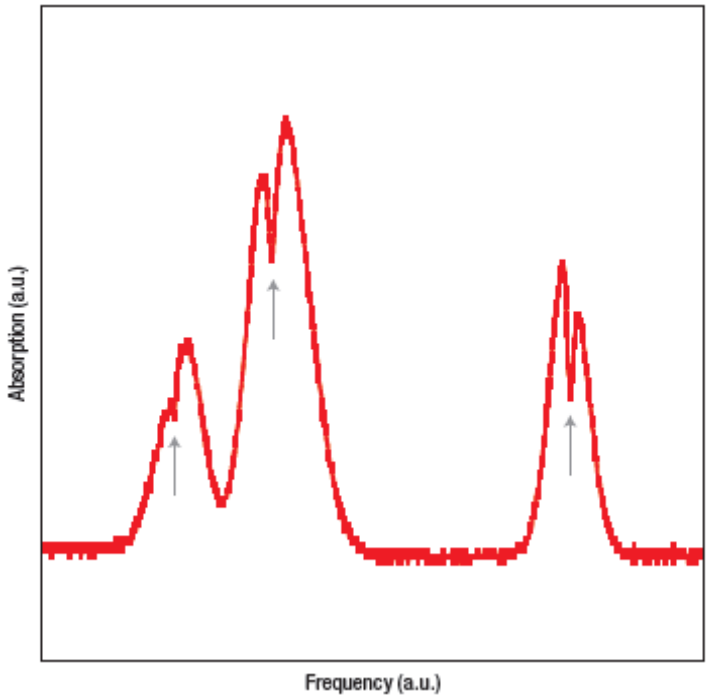

Figure 4.19 Saturated absorption spectroscopy in Rb loaded ARROW.

In our integrated ARROW cell, the alignment for overlapping probe and coupling

beams is automatically accomplished by the optical waveguides, another advantage of the use of integrated optical elements. Figure 4.19 shows the SAS spectrum observed in the ARROW cell and clearly shows the characteristic Lamb dips. A width of approximately 34±2 MHz is observed, which is consistent with additional homogeneous time of flight broadening.

Figure 4.17 (a) displays the comparison between the atomic densities of bulk cell and Rb loaded ARROW in the successive experiment. As we may see, the atomic density is comparable for Rb loaded ARROWs with that of the bulk cell at 60℃. Figure4.17 (b) shows the optical density calculated for Rb loaded ARROWs at different temperatures.

4.8. Fittings of SAS

4.8.1 Equations for fitting

We now calculate the resonance shapes of saturation absorption spectroscopy of Rb. First, the optical pumping effect contributes to a principal resonance as [110]:

$$L = N_g I_{ij} S_0 \frac{(\Delta\nu/2)^2}{(\nu-\nu_k)^2+(\Delta\nu/2)^2} \qquad (4.8)$$

Where the N_g is the ground state population, $\Delta\nu$ is the saturation linewidht,

saturation factor S_0 is defined as:

$$S_0 = \frac{I_p / I_{eff}}{(1 + I_p / I_{eff})^{1/2}[1 + (1 + I_p / I_{eff})^{1/2}]} \qquad (4.9)$$

Where I_{eff} is the saturated intensity of specified atomic spectroscopy. (For Rb, $I_{eff} = 2.6 mW / cm^2$)

4.8.2 Fitting results of SAS

In figure 4.20, the fitting results and the original experimental data are all plotted for the SAS in bulk cell. The saturation coefficient is S_0=8. And the line width $\Delta\nu$ is =42 MHz.

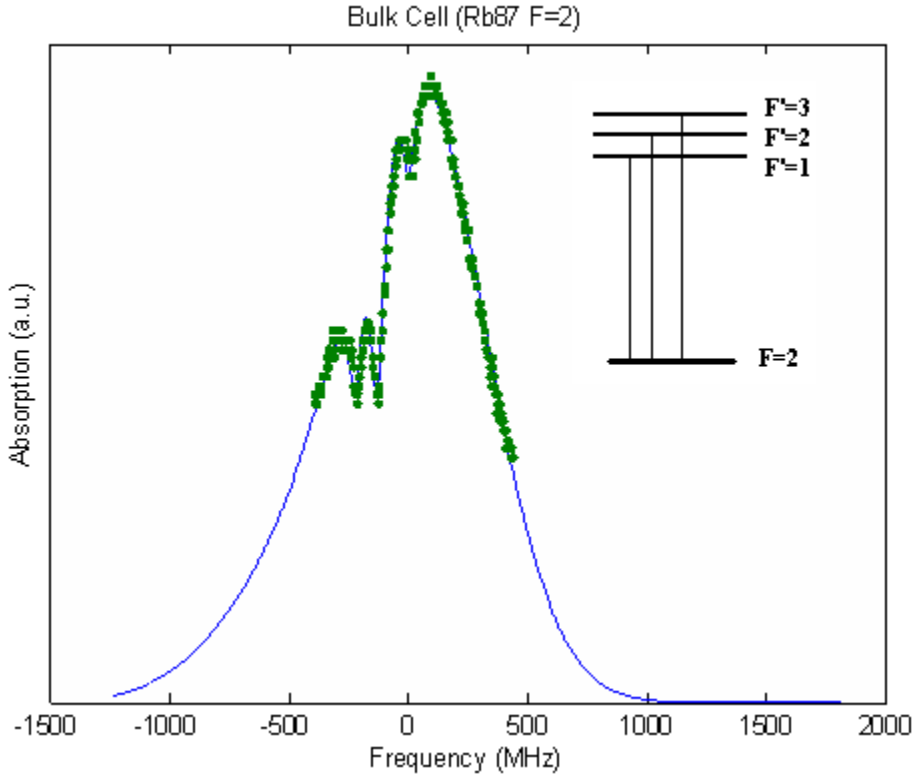
Bulk Cell (Rb87 F=2)
Absorption (a.u.)
-1500
-1000
-500
0
500
1000
1500
2000
Frequency (MHz)
F'=3
F'=2
F'=1
F=2

(a)

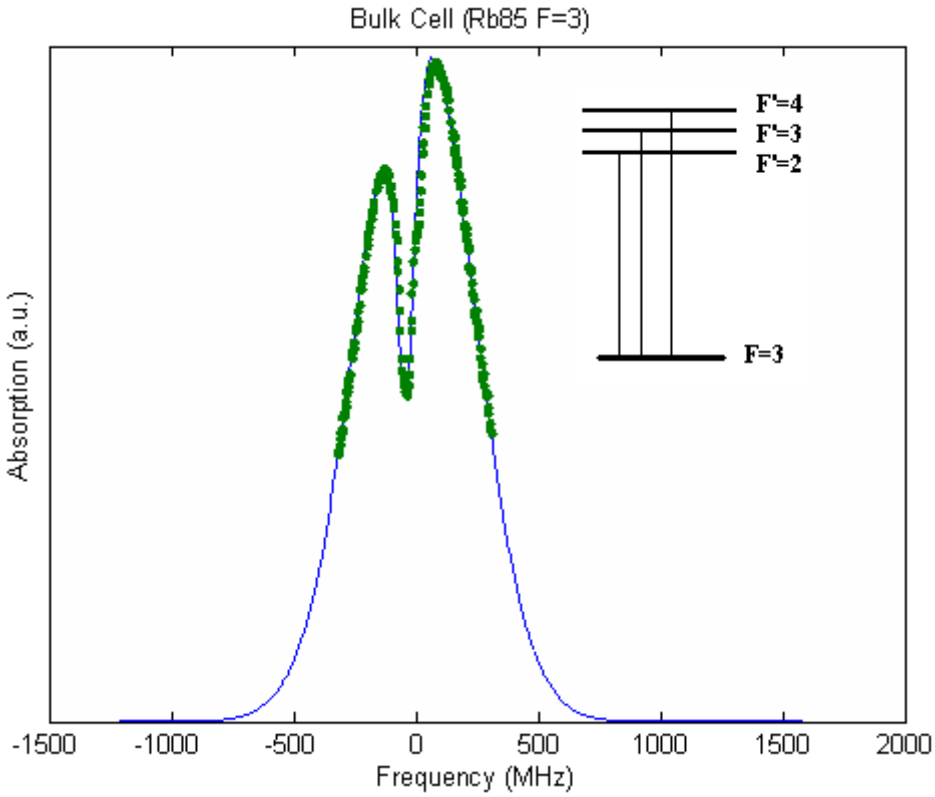
Bulk Cell (Rb85 F=3)
F'=4
F'=3
F'=2
F=3
Absorption (a.u.)
-1500
-1000
-500
0
500
1000
1500
2000
Frequency (MHz)

(b)

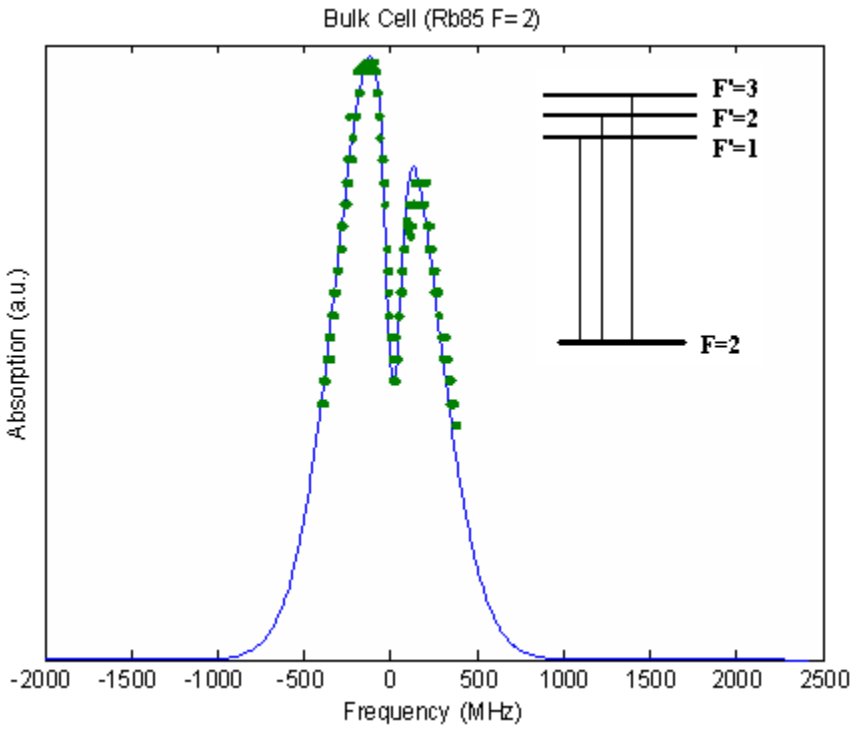

(c)

Figure 4.20 The fitting results of SAS experiments in bulk cell (a) ^{87}Rb F=2 transition (b) ^{85}Rb F=3 transition (c) ^{85}Rb F=2 transition

In figure 4.21, the fitting results and the original experimental data are all plotted for the SAS in Rb loaded ARROW. The saturation coefficient is S_0 =2. And the line width $\Delta\nu$ is =46 MHz.

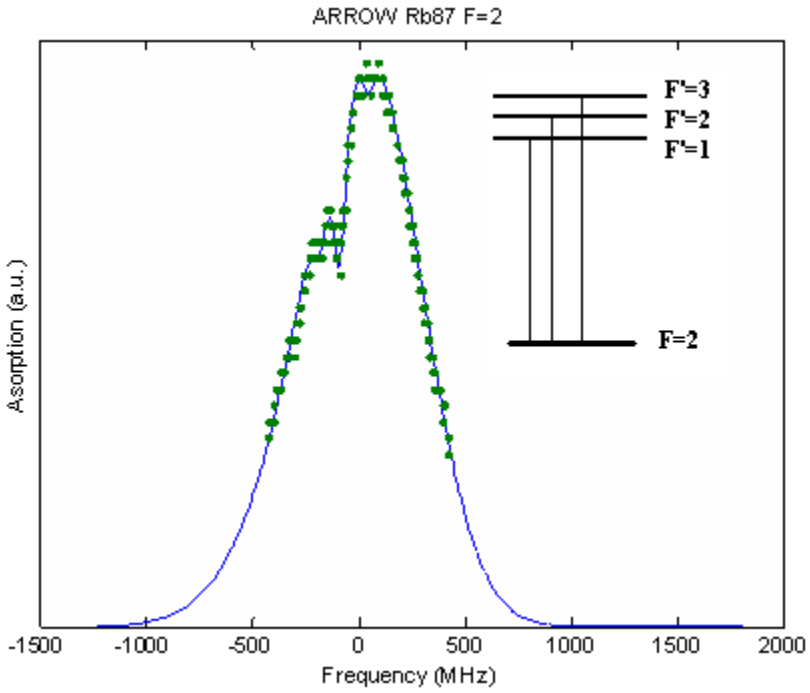
ARROW Rb87 F=2
Asorption (a.u.)
Frequency (MHz)
-1500
-1000
-500
0
500
1000
1500
2000
F'=3
F'=2
F'=1
F=2

(a)

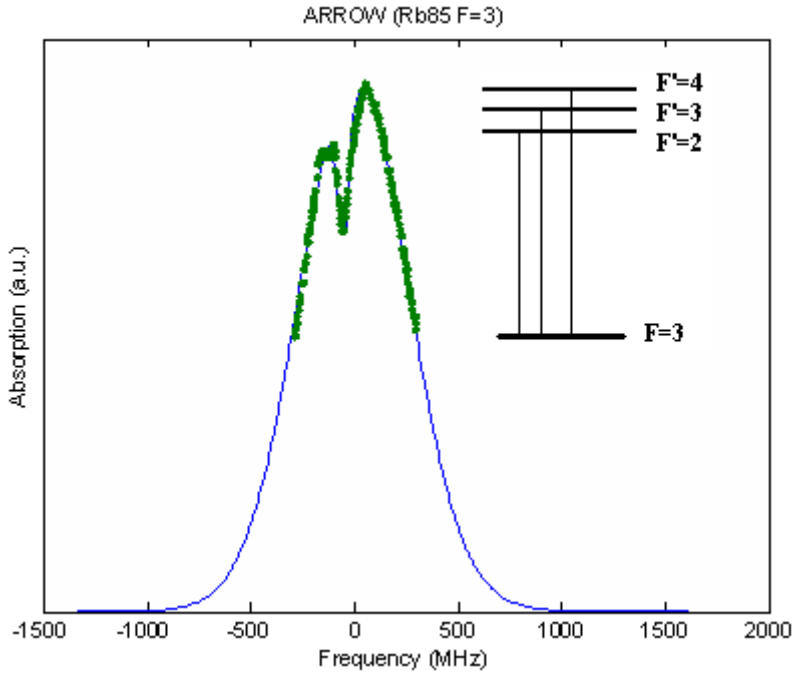
ARROW (Rb85 F=3)
F'=4
F'=3
F'=2
F=3
Absorption (a.u.)
-1500
-1000
-500
0
500
1000
1500
2000
Frequency (MHz)

(b)

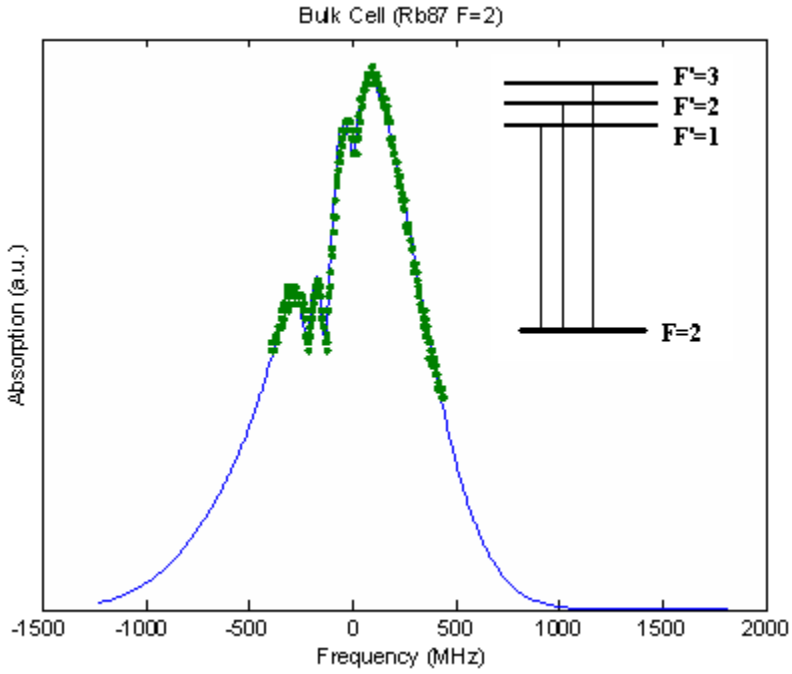

(c)

Figure 4.21 The fitting results of SAS experiments in bulk cell (a) ^{87}Rb F=2 transition (b) ^{85}Rb F=3 transition (c) ^{85}Rb F=2 transition

Between the comparison of the saturation coefficients of both bulk cell (S_0=8) and ARROW (S_0=2), it is clear that the performance of ARROW for SAS experiments is on the same level with the commercially available bulk cell.

4.9 Summary

In this chapter, we investigated the suitability of the ARROW cell for common precision spectroscopy applications. Here we describe the first monolithically integrated, planar rubidium cell on a chip. We demonstrate, experimentally, the key requirements for integrated atomic spectroscopy, including confinement of both light and rubidium vapor in micrometer-scale hollow-core waveguides, large optical density over chip-scale distances, high intensities (on the order of $10W/m^2$) for efficient nonlinear effects, and fiber-optics-based saturation absorption spectroscopy on a chip.

Chapter 5 EIT in Rb loaded ARROWs

5.1 EIT in bulk cell

As we described in the theoretical part, there are basically three types of EIT configurations: Lambda type, Vee type and Ladder type (as illustrated in figure 5.1).

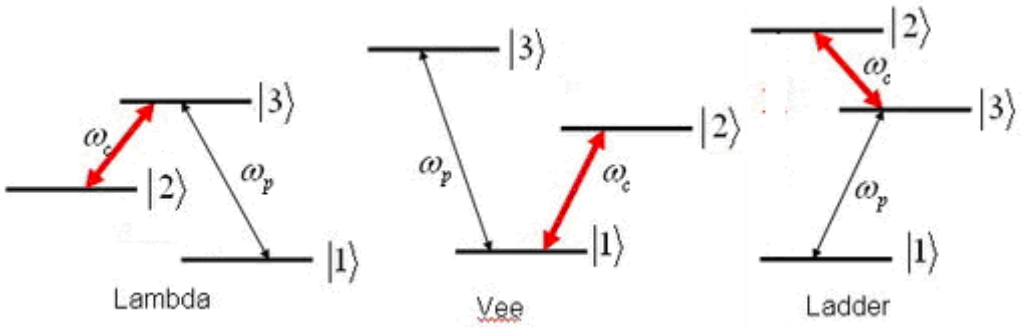

(a) (b) (c)

Figure 5.1 Three type of EIT configurations: (a) Lambda type; (b) Vee type; (c) Ladder type

In this section, we will present two types of EIT experiments: Lambda type EIT and Vee type EIT both in bulk cell.

5.1.1 Lambda type EIT (bulk cell)

5.1.1.1 Experimental setup

The experimental arrangement is give in figure 5.2. The Doppler free configuration for coherence effects in the Lambda type system is that the coupling beam and the probe beam propagate collinearly, because the Doppler shift of the probe laser and pumping laser for the same group of atoms with velocity v can be canceled. This configuration can reduce the requirement for the pumping intensity to create effective coherence [68]. The probe and pumping beams are orthogonally polarized and are separated with a polarizing beam splitter after passing through the rubidium cell. The 75mm-long rubidium vapor cell is kept at a room temperature of about 20℃. The natural linewidth of the excited state is 6MHz. Both diode lasers have wavelengths near 794.8nm. The probe laser is about 120μW, with a beam size of 1mm in diameter. The coupling beam is about 12.3mW with a beam size of 2mm in diameter. Both of these beams are focused with a lens before entering the cell, which overlap with each other in the active rubidium vapor region.

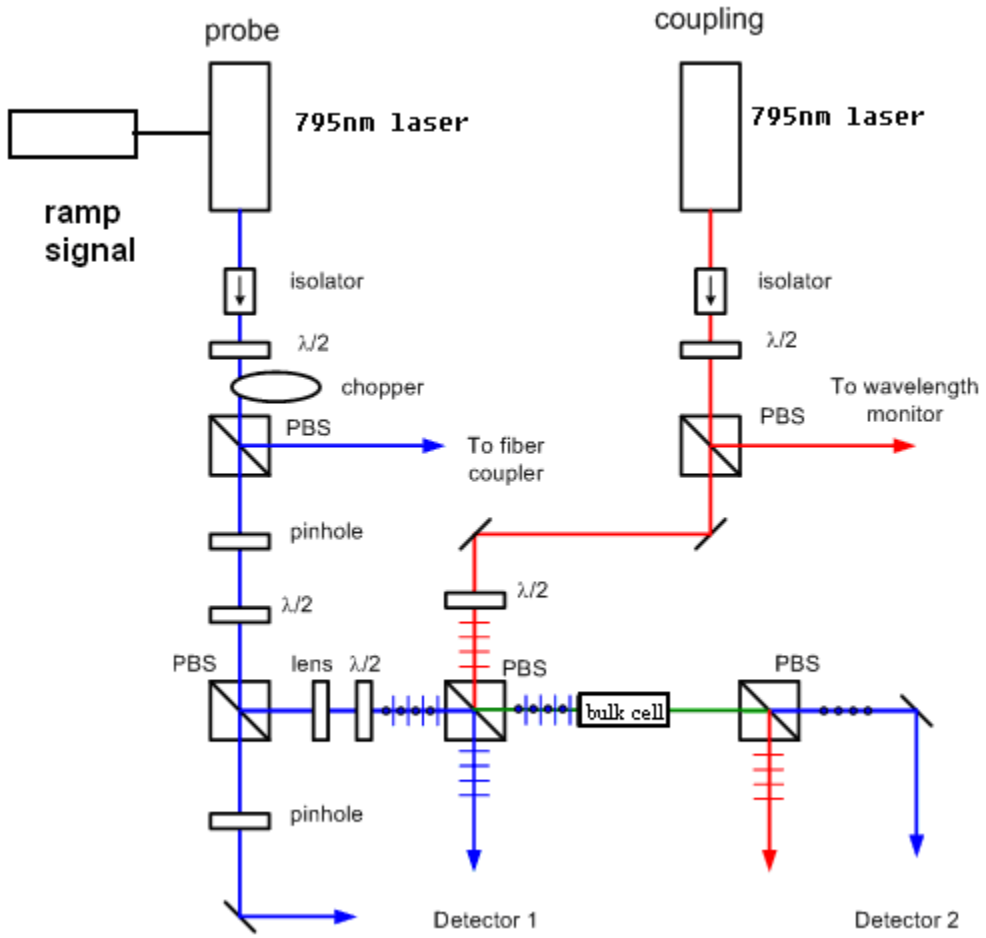

Figure 5.2 Experimental setup of Lambda type EIT

5.1.1.2 Experimental result

The Lambda type EIT spectrum is illustrated in figure 5.3. The transmission peak is generated by tuning the probe laser across the $5S_{1/2}$ F=1 -> $5P_{1/2}$ F'=2 transition. And when the coupling laser is centered at the $5S_{1/2}$ F=2 -> $5P_{1/2}$ F'=2 transition, the EIT transparency can be observed as illustrated in figure 5.3. (inset is the three-level atomic

configuration for lambda type EIT.)

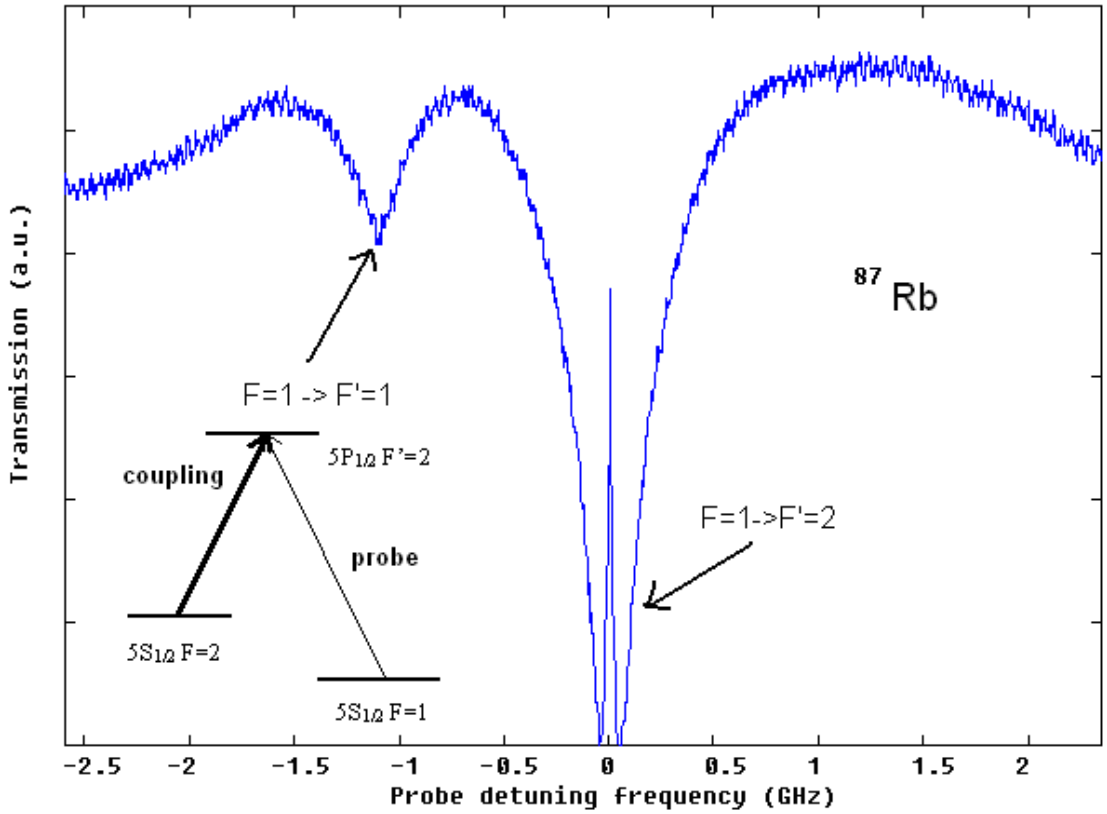

Figure 5.3 Transmission spectrum of Lambda type EIT in bulk Rb cell

From the transmission spectrum, it is clear that a 80% transparency is created at the central frequency with the zero probe detuning when the strong coupling field is presented.

5.1.2 Vee type EIT (bulk cell)

5.1.2.1 Experimental setup

The experimental setup of V type EIT is similar to Lambda type EIT except that one of the rubidium D1 line (795nm) lasers is replaced by rubidium D2 line (780nm) laser. In this configuration, the coupling beam (780nm) and probe beam (795nm) co propagate and overlap through rubidium cell and are separated by the polarization directions. Therefore, the probe is scanned and directed into a photodetector after going through the rubidium cell. The whole experimental setup is illustrated in figure 5.4.

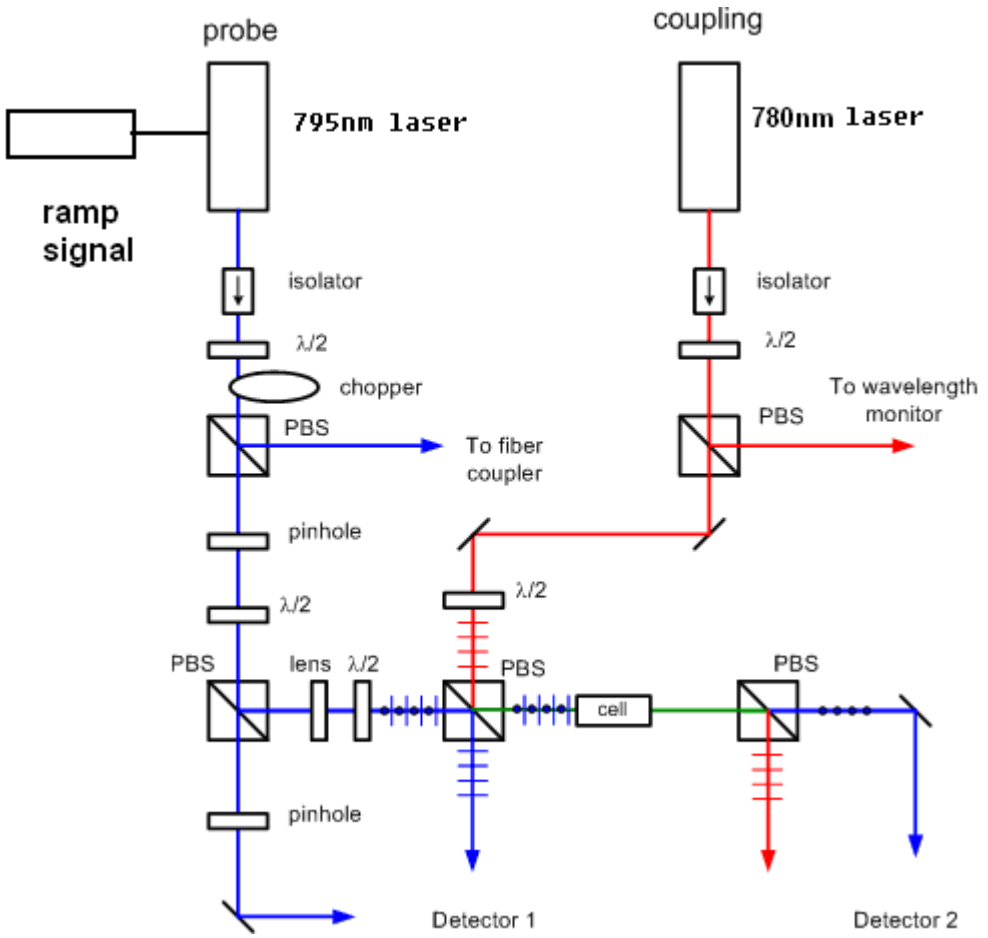

Figure 5.4 The experimental setup for V-type EIT

5.1.2.2 Experimental result

The V type EIT experimental result is illustrated in figure 5.5. We can observe the suppression of absorption by measuring the probe transmission as a function of probe frequency. The probe is scanned over the ^{87}Rb $S_{1/2}$ F=2->$P_{1/2}$ F'=1 D1 line and the coupling is tuned at the ^{87}Rb $S_{1/2}$ F=2 ->$P_{3/2}$ F'=1 D2 line. As a result, the EIT

transparency is clearly observed when the probe power is set to be 120 μW and the coupling power is set to be 5.3mW at room temperature.

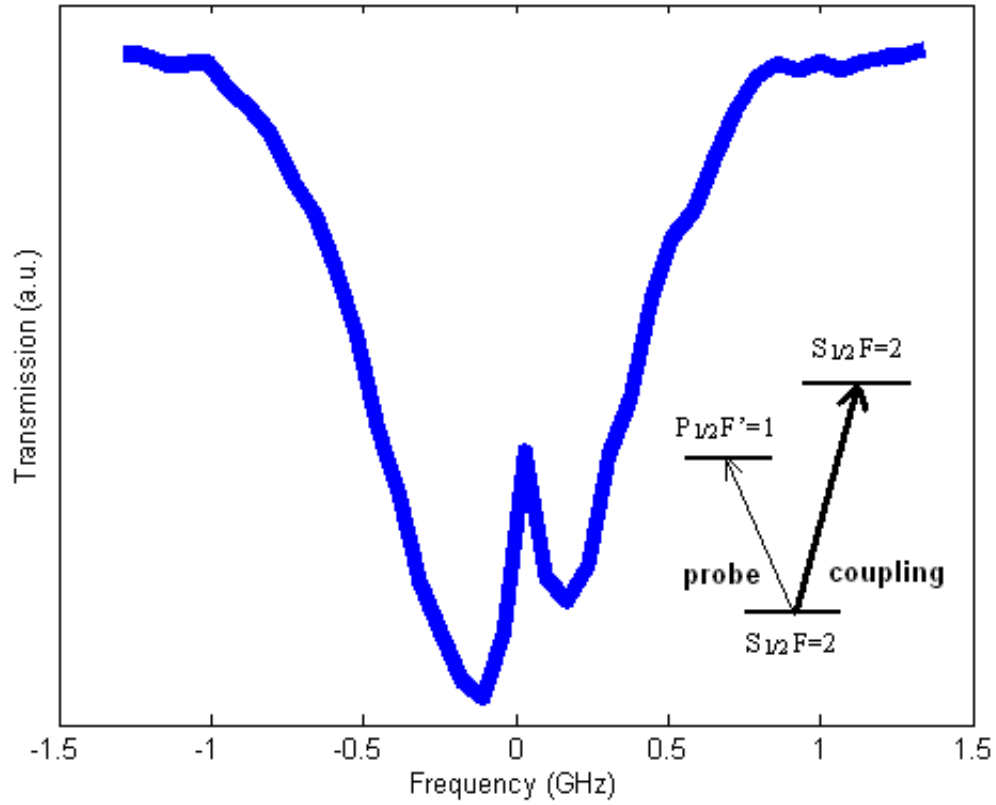

Figure 5.5 Transmission spectrum of Vee type EIT

As the dephasing rate of V-type EIT is larger than that of the Lambda type, the transparency depth observed in this type EIT (Figure 5.5, EIT depth is 30%) is typically smaller than the transparency observed in Lambda type EIT (Figure 5.3 EIT depth is 80%.). Therefore, Lambda type configuration is more favorable for EIT experiment.

5.2 Extraction of atomic density

The atomic density can be extracted by fitting the Rb absorption spectrum. The absorption profile can be determined by the following equation:

$$I_{out} = I_{in} \exp(-\alpha L) \quad (5.1)$$

Where L is the interaction length of Rb atoms and light and α is the absorption coefficient defined by:

$$\sigma_{ij} = \frac{\omega_{ij} \left|\mu_{ij}\right|^2}{c\varepsilon_0 \hbar \gamma_{12}} \quad \alpha = N\sigma \quad (5.2)$$

N is the atomic density, and σ is the absorption cross section given by:

$$\sigma_{ij} = \frac{\omega_{ij} \left|\mu_{ij}\right|^2}{c\varepsilon_0 \hbar \gamma_{ij}} \quad (5.3)$$

Where ω_{ij} is the resonance frequency, μ_{ij} is the dipole moment, γ_{ij} is the decay rate.

5.3 Laser induced atomic desorption (LIAD) experiment

As we have discussed before, the atomic density is a crucial part for achieving the effective EIT as well as other nonlinear optics phenomena that rely on large optical depth. Here, we introduced a technique to increase the atomic density by using a strong laser beam to simulate a desorption process which would release a large amount of Rb

atoms sticking on the inner surface of the hollow core waveguide wall. [69,70,71,72]

Title	Wavelength	Power	Coating	Notes
Low-light-level optical interaction with Rubidium vapor in a photonic band-gap fiber PRL 97,023603	770nm	1mW	ODMS	In this paper, they did not observe measurable desorption in uncoated fibers.
Generation of large alkali vapor densities inside bare hollow-core photonic band gap fiber Opt.Exp.16,18976	805nm	20-90mW	Non-coating fiber	Exposing fiber to ambient Rubidium vapor at 70c for three weeks.
On-demand all optical generation of controlled Rb vapor densities in photonic bad gap fibers PRA,79,063809	806nm 770nm	10-15mW	Coated fiber Non-coating fiber	No big difference of dynamic desorption response between coated and uncoated fibers.
Ultralow power four wave mixing with Rb in a hollow core photonic band gap fiber PRL,103,043602	808nm	3mW	Non-coating fiber	

Table 5.1 The desorption techniques used in PCF based experiments

The above table shows several desorption geometries increasing the Rb atomic density for different experiments.

The experimental setup of LIAD is illustrated in figure 5.6.

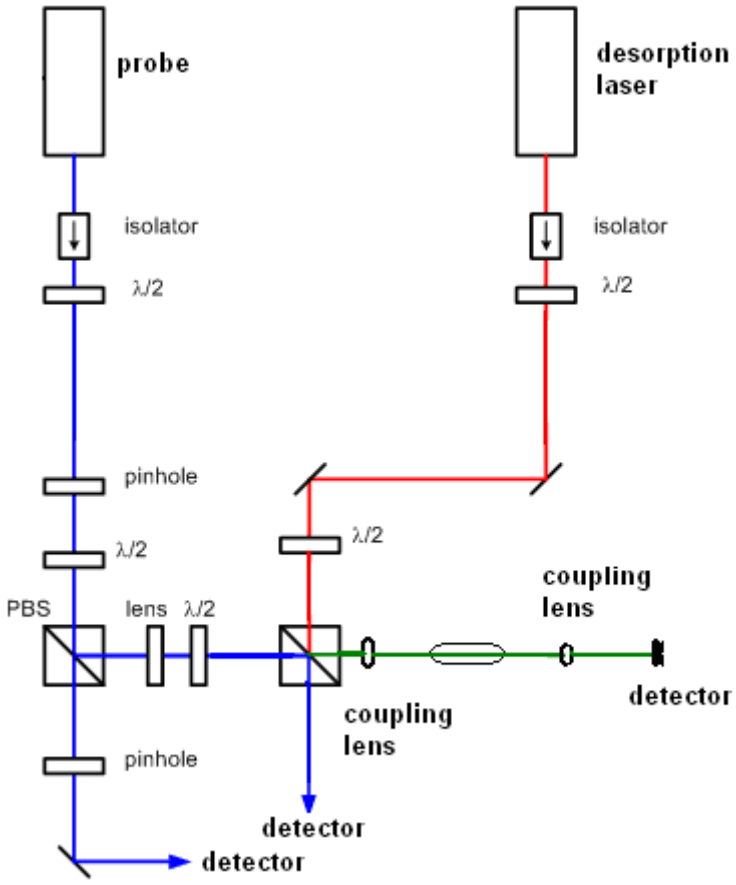

Figure 5.6 Experimental setup of LIAD in minicells.

Minicells with different coatings were fabricated for testing in the LIAD experiment. The desorption experiment is done by probing the atomic density with a weak probe laser for two cases when the strong desorption beam is off and on. Figure 5.7 illustrates the comparison of the atomic densities with and without the desorption beam for each individual mincell. In this experiment, the desorption beam is introduced by a laser diode with 770nm wavelength and maximum 65mW output power.

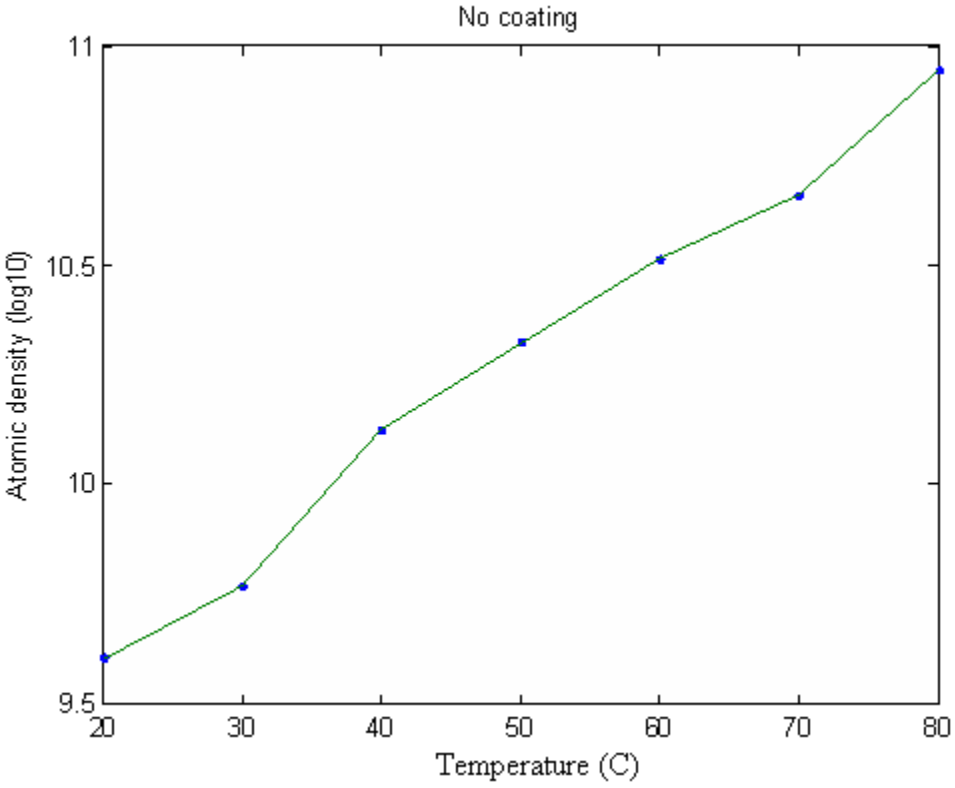
No coating
11
10.5
10
9.5
Atomic density (log10)
20
30
40
50
60
70
80
Temperature (C)

(a)

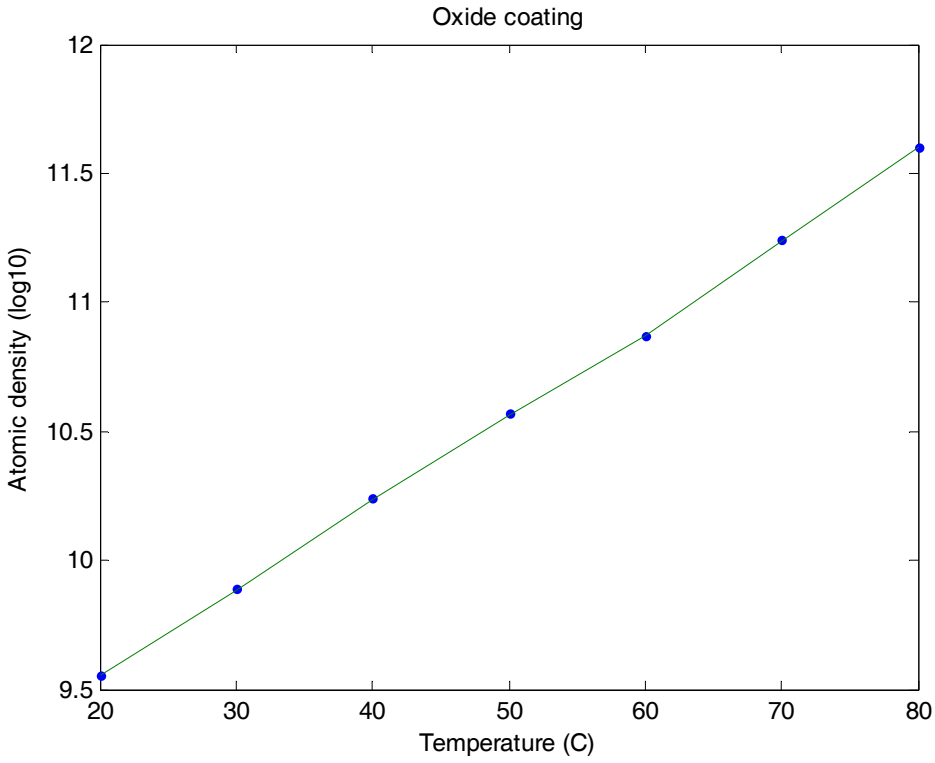
Oxide coating
Atomic density (log10)
Temperature (C)
12
11.5
11
10.5
10
9.5
20
30
40
50
60
70
80

(b)

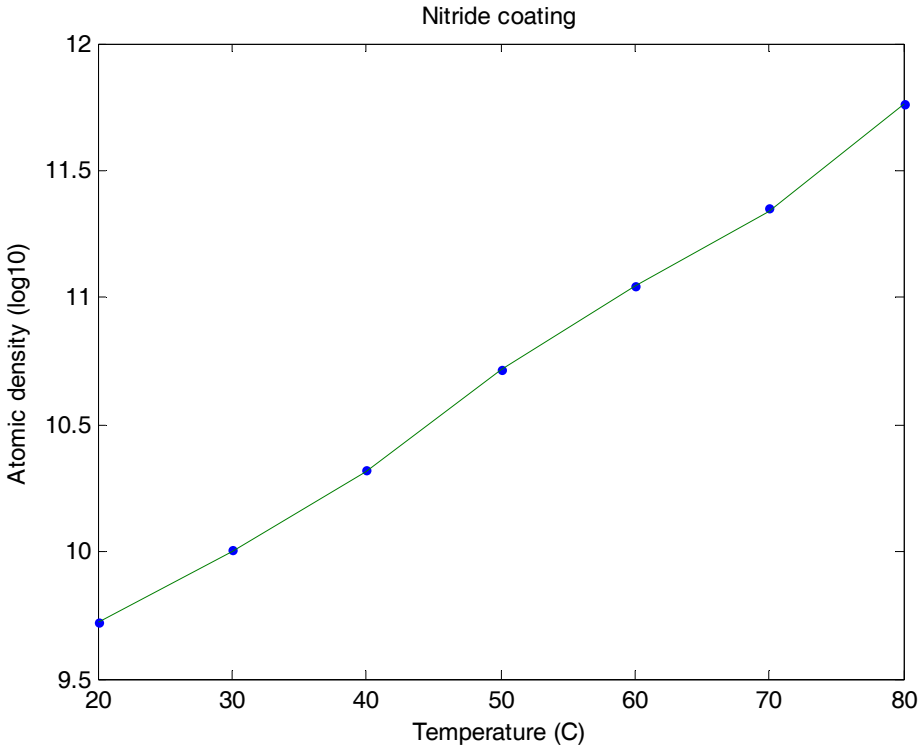
Nitride coating
Atomic density (log10)
Temperature (C)
12
11.5
11
10.5
10
9.5
20
30
40
50
60
70
80

(c)

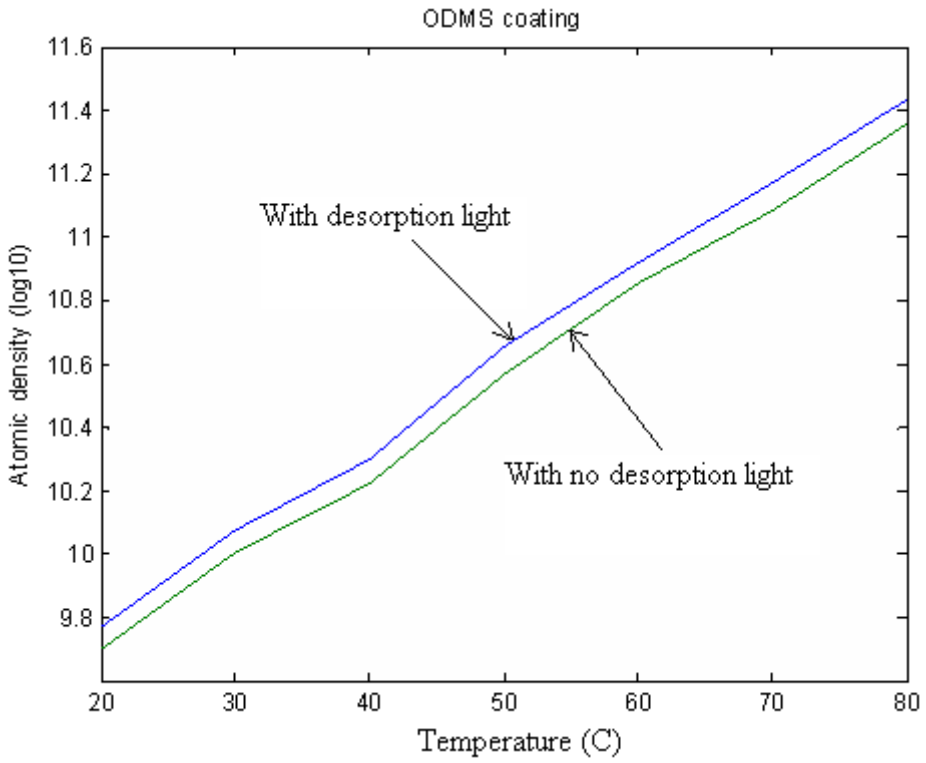

(d)

Figure 5.7 LIAD experiments in (a) no coating minicell (b) SiO_2 coating minicell (c) SiN coating minicell (d) ODMS coating minicell

As seen in figure 5.7, LIAD is only observed in ODMS coating minicell which indicates that it is a surface effect associated with the dynamic properties of the layer material.

The temperature dependence of the LIAD effect is also studied by doing the same LIAD experiment at different temperatures. Figure 5.8 indicates that the LIAD effect does not have obvious dependence on temperature.

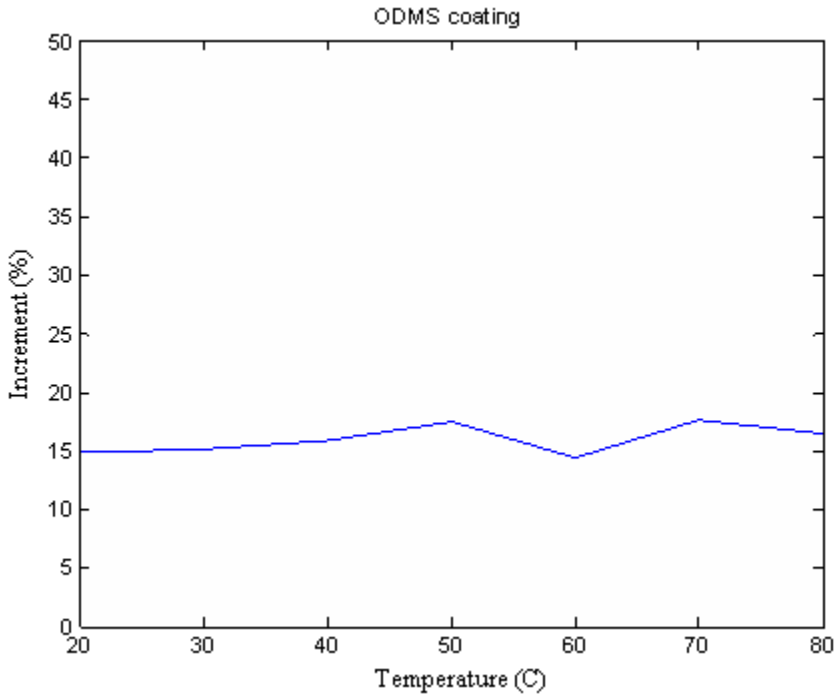

Figure 5.8 Light induced density increase v.s. temperature

The dependence of LIAD effect on the desorption laser power is investigated by varying the laser power from 20mW to 65mW. As seen in figure 5.9, the LIAD effect becomes more prominent when the desorption laser power is increased.

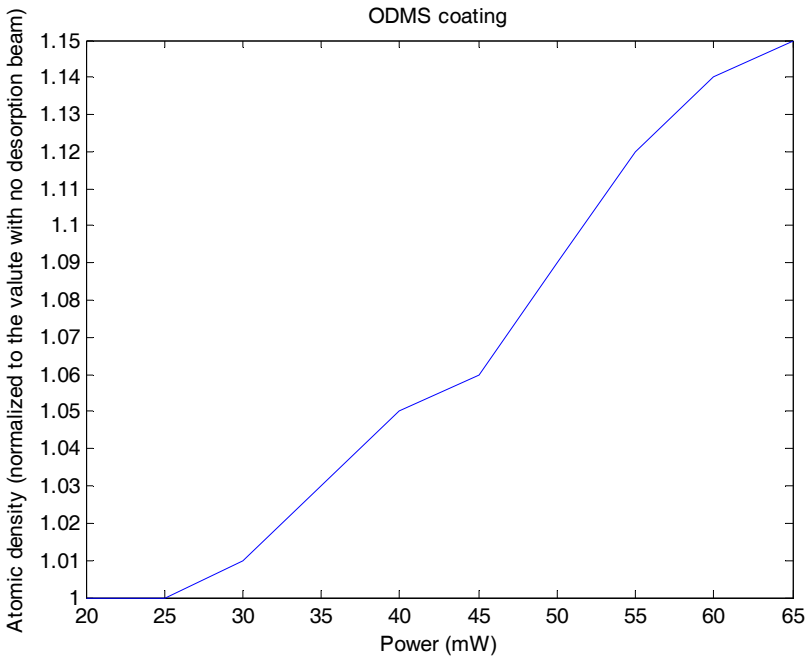

Figure 5.9 Atomic density increase v.s. desorption laser power

Finally, the dynamic properties of LIAD is investigated by measuring the atomic densities in different time frames after being exposed under the strong desorption beam.

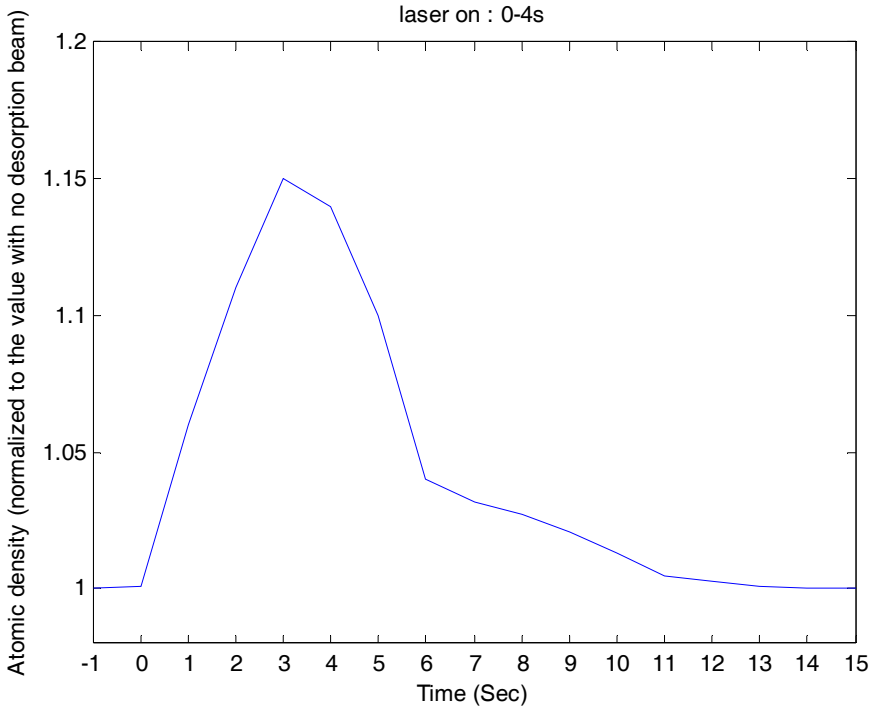

Figure 5.10 Dynamic LIAD v.s. exposure time

As seen in figure 5.10, the desorption beam is kept on for the first 4s. Then it is turned off. The maximum LIAD appears after about 3s after the desorption beam turning on and is reduced quickly after the desorption beam turning off.

For our Rb loaded ARROW device, LIAD is promising technique to increase the atomic density within the hollow core chamber after the ODMS monolayer is coated.

5.4 EIT in minicells

5.4.1 Lambda type EIT Setup in Rb loaded minicell

Lambda type EIT is conducted in the home-made rubidium cell with two rubidium D1 lasers. The probe is scanned around ^{85}Rb $S_{1/2}$ F=2 -> $P_{1/2}$ F'=3. And the coupling is on ^{85}Rb D1 line $S_{1/2}$ F=3 -> $P_{1/2}$ F'=3.

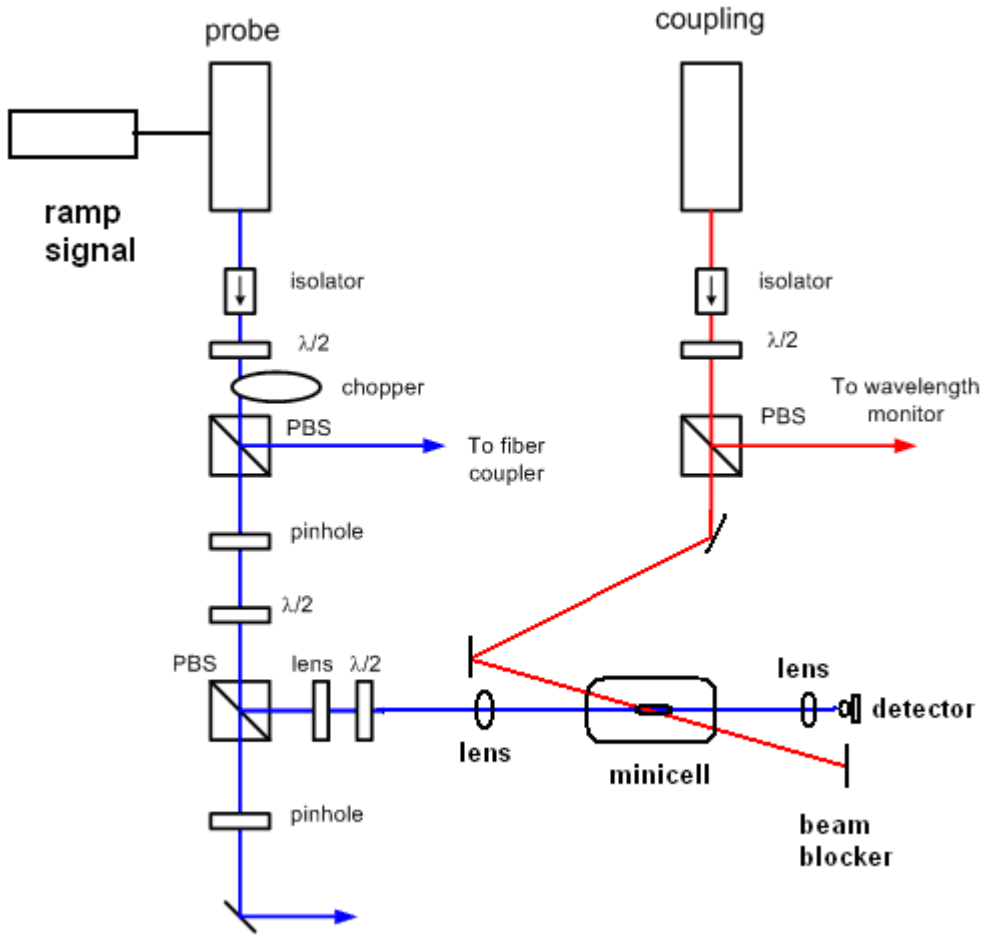

Figure 5.11 Lambda type EIT experiment setup in minicell

In this experiment, as minicells have very strong light scattering due to the curvature of the cell surface, we employ the spatial separation techniques to distinguish the weak probe beam from the strong coupling. Figure 5.11 illustrates the whole experimental setup for minicell EIT experiment (the separation angle between coupling and probe beams are not to scale. In the real experiment, the separation angle is about 2-3 degrees.) Two lenses are used to tightly focus the probe beam going through the minicell and focused on to the detector. In this experiment, the coupling laser is tuned at different powers to observe the influence of coupling power on the effect of EIT.

5.4.2 Experimental result

The coupling powers are set to be 10mW, 5mW and 1mW respectively to observe the changes of EIT transparencies as shown in figure 5.12.

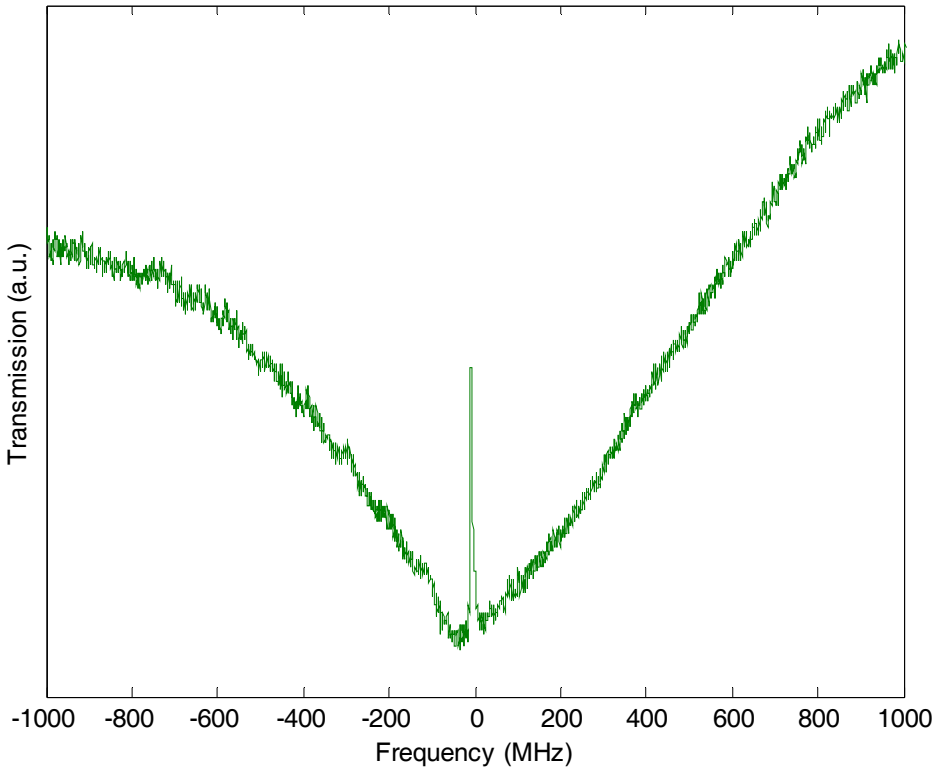
Transmission (a.u.)
-1000
-800
-600
-400
-200
0
200
400
600
800
1000
Frequency (MHz)

(a)

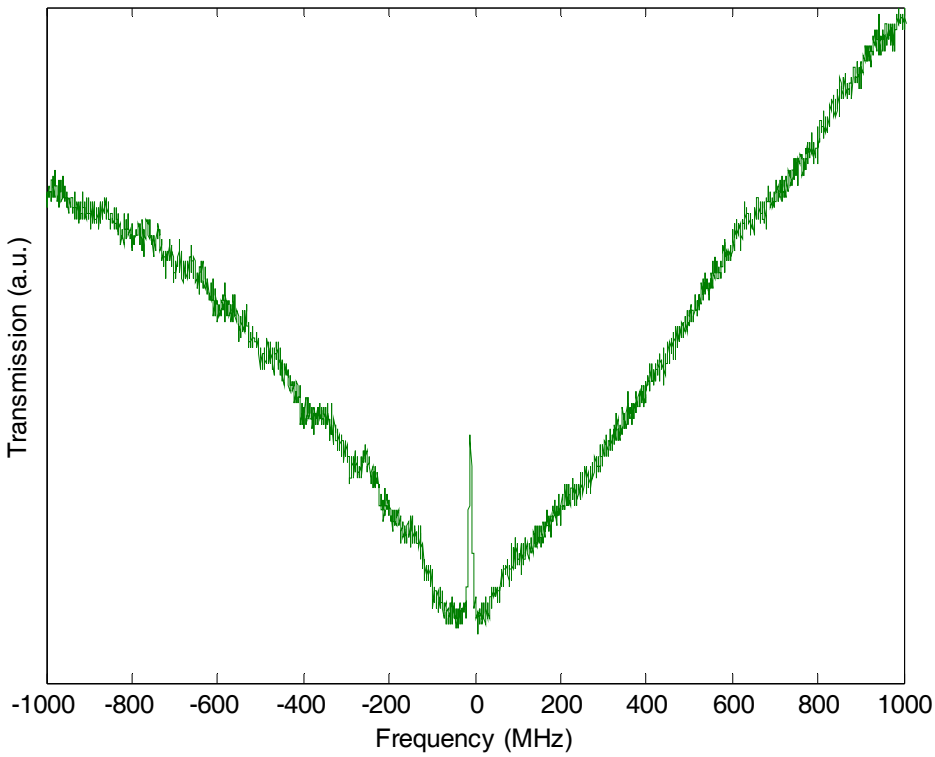
Transmission (a.u.)
-1000
-800
-600
-400
-200
0
200
400
600
800
1000
Frequency (MHz)

(b)

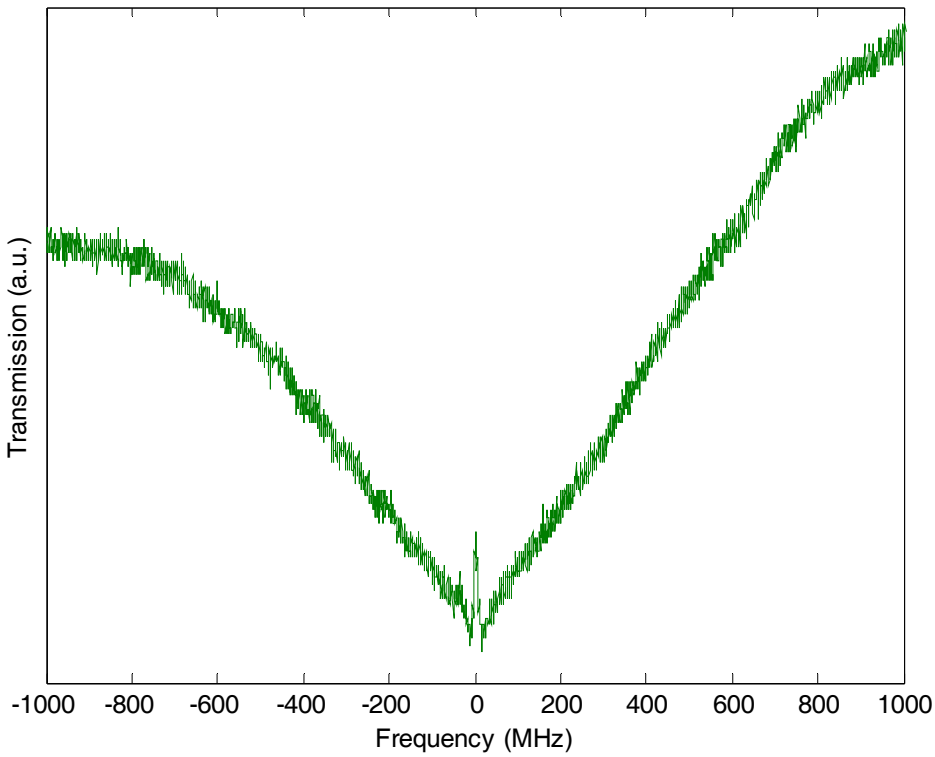

(c)

Figure 5.12 EIT spectra in minicells for different coupling powers: (a)P_c=10mW (b)P_c=5mW (c)P_c=1mW

The expected increase of the peak depth with the control laser Rabi frequency (intensity), showing that more than 65% transparency were easily achieved at room temperature. The EIT transparency percentage is plotted as the function of coupling Rabi frequency in figure 5.13 at the decoherence rate of 0.47MHz.

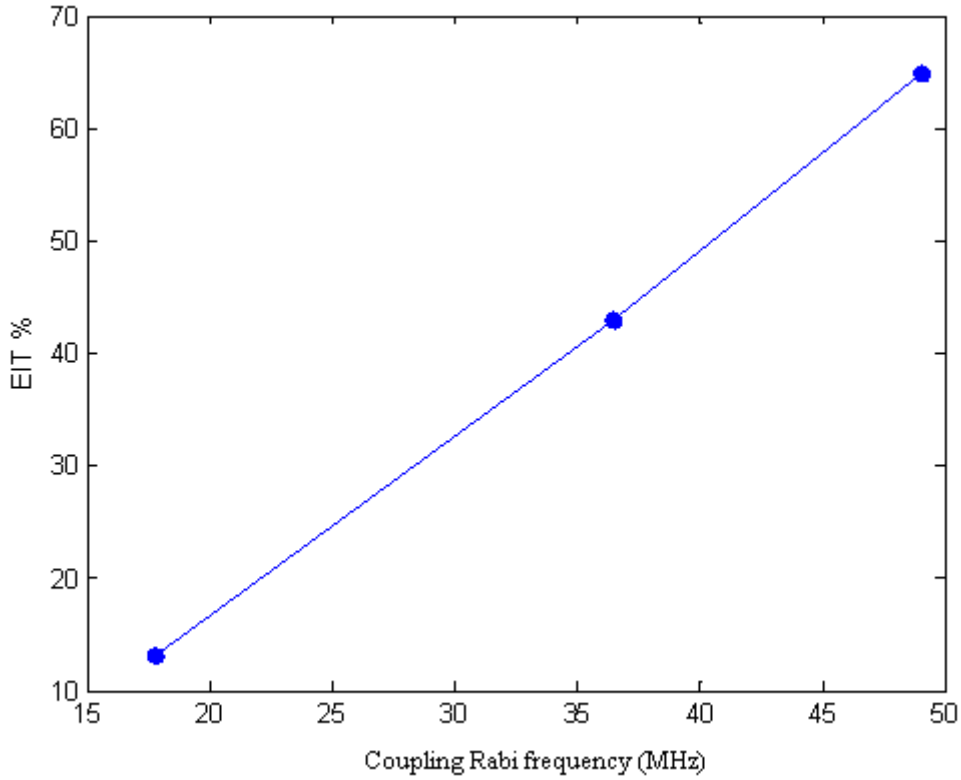

Figure 5.13 EIT transparency percentage (filled circles) vs coupling Rabi frequency.

5.5 EIT in Rb loaded ARROW

We finally conduct the EIT experiment in our Rb cell integrated ARROW waveguide. The detailed experiment process is presented and an analysis follows.

5.5.1 Experimental setup for EIT in Rb loaded ARROW

The experimental setup is illustrated in figure 5.14. Since the ARROW waveguide has

the polarization preference along the parallel direction [115], the probe beam cannot be distinguished by polarization difference between probe and coupling beams, and the monolithically integrated waveguide channel automatically collimates the alignment with both probe and coupling beams.

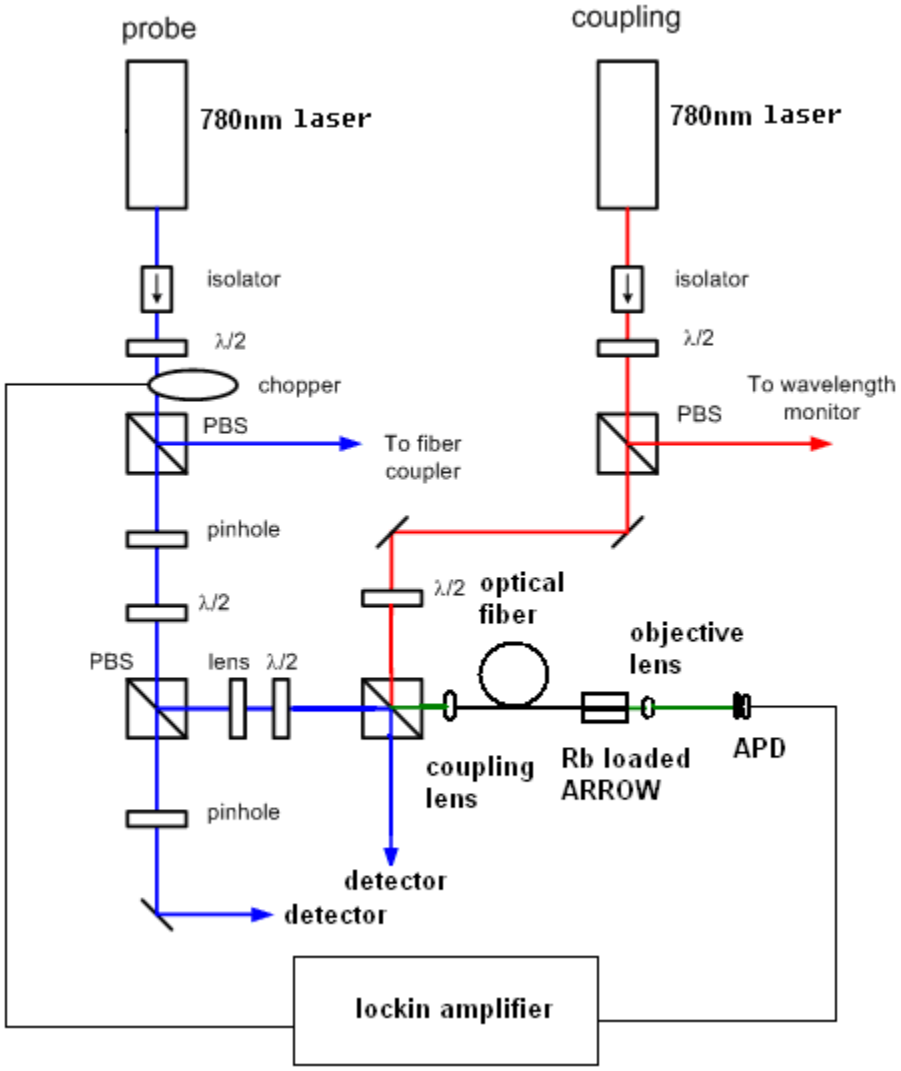

Figure 5.14 Experimental setup for EIT in Rb loaded ARROW

Therefore, a different method is employed to distinguish the probe beam from the strong coupling beam. In this setup, the probe is modulated by an optical chopper at the frequency of 1kHz. The output signal (input for lockin amplifier) and the modulation signal (input for reference) are fed into a lockin amplifier where an internal modulation and demodulation process is performed and hence the probe signal can be detected from the combined sum of both probe and coupling signals. This experiment is conducted at 80℃ with an ODMS coated Rb loaded ARROW.

The probe frequency is scanned around ^{85}Rb D2line $S_{1/2}$ F=2 -> $P_{3/2}$ F'=3. And the coupling frequency is locked on ^{85}Rb D2 line $S_{1/2}$ F=3 -> $P_{3/2}$ F'=3.

5.5.2 Experimental result

The input full coupling power is set to be 18.9mW and the probe power is about 1/5 of the maximum coupling power. The coupling power is tuned to be at 100%, 80%, 60%, 40% and 20% of original coupling power. As depicted in the theory introduction part (in figure 1.2) that when the coupling power is off, a normal transmission curve would appear with the atomic absorption dip around the transition. In our experiment with Rb loaded ARROWs, when the coupling power is turned on at its maximum input, a more than 40% transparency can be achieved.

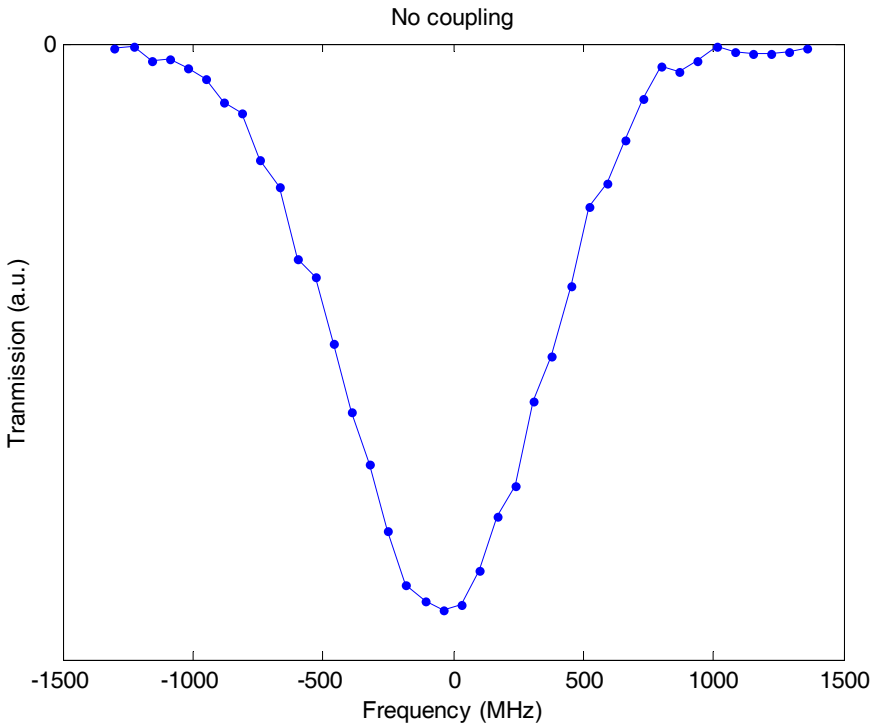
No coupling
0
Tranmission (a.u.)
-1500
-1000
-500
0
500
1000
1500
Frequency (MHz)

(a)

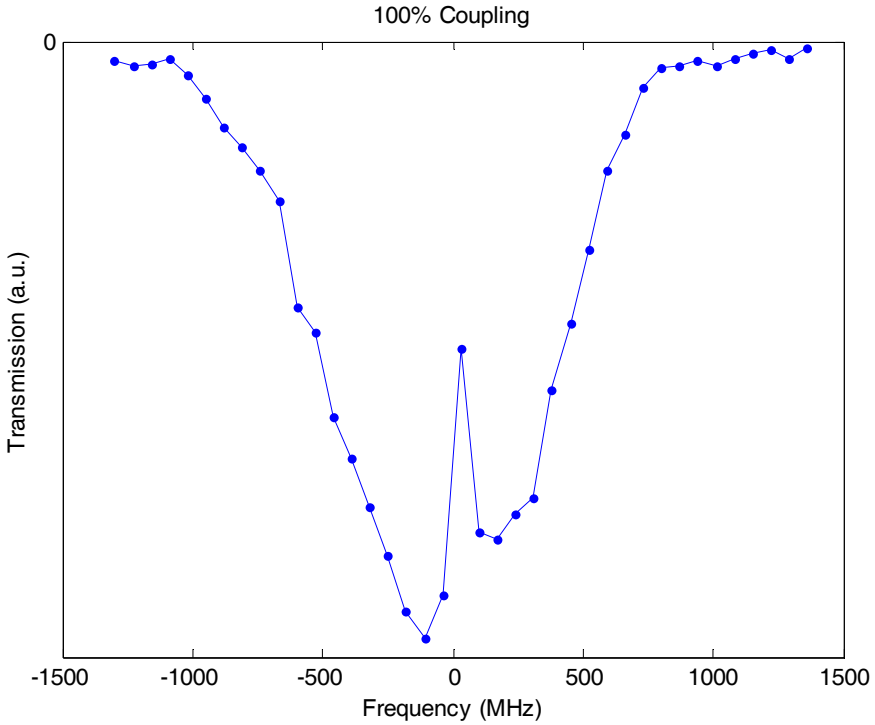
100% Coupling
0
Transmission (a.u.)
-1500
-1000
-500
0
500
1000
1500
Frequency (MHz)

(b)

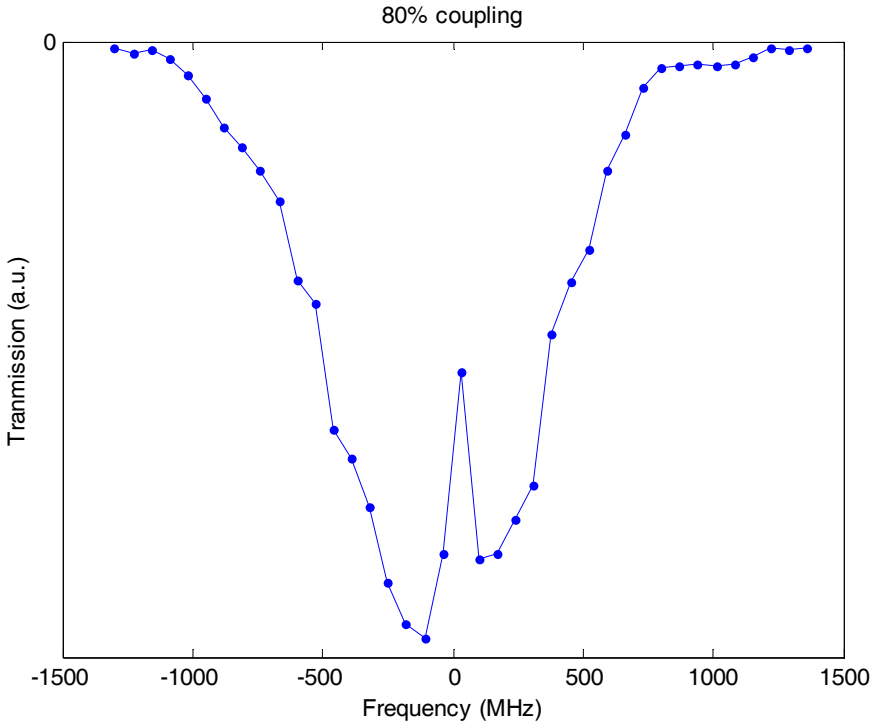
80% coupling
0
Tranmission (a.u.)
-1500
-1000
-500
0
500
1000
1500
Frequency (MHz)

(c)

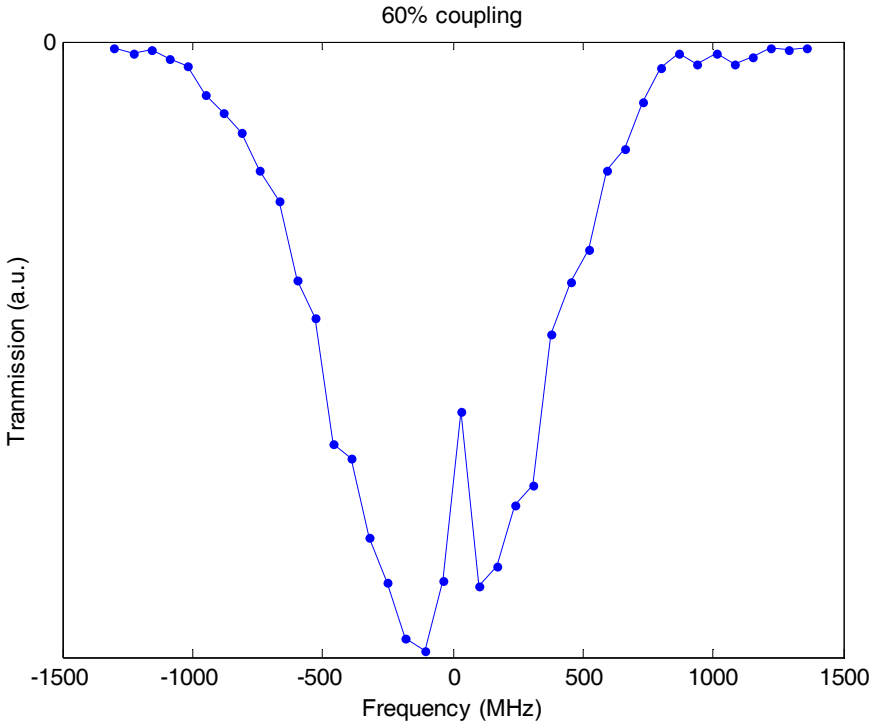
60% coupling
0
Tranmission (a.u.)
-1500
-1000
-500
0
500
1000
1500
Frequency (MHz)

(d)

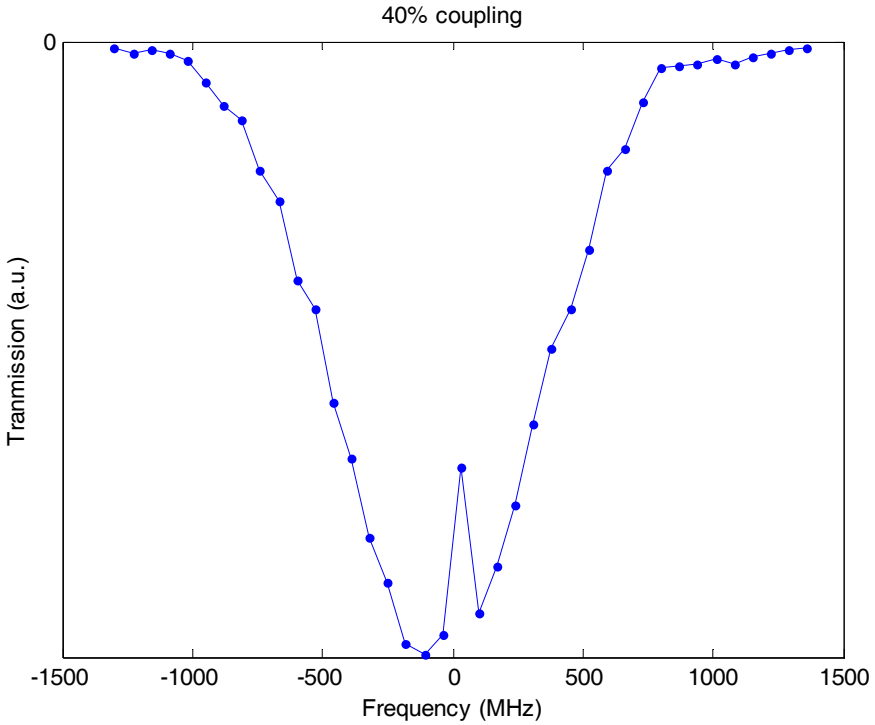
40% coupling
0
Tranmission (a.u.)
-1500
-1000
-500
0
500
1000
1500
Frequency (MHz)

(e)

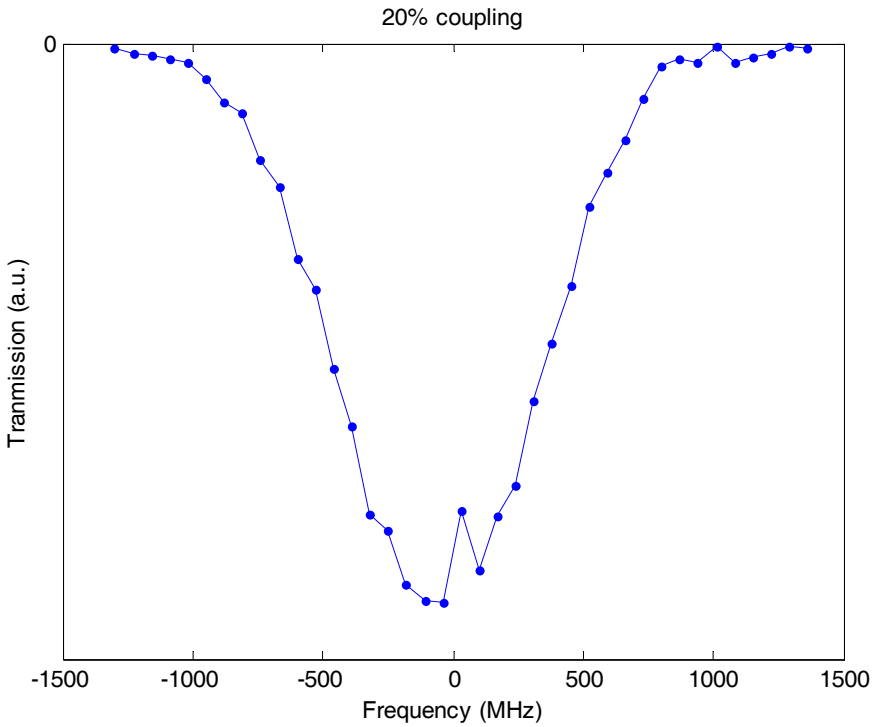

(f)

Figure 5.15 EIT spectra in Rb loaded ARROWs with different coupling powers

As the coupling power decreases from 100% full coupling power to 20% full coupling power, the transparency height gradually becomes lower and lower. The relation between the EIT depth in percentage and the coupling power is plotted in figure 5.16.

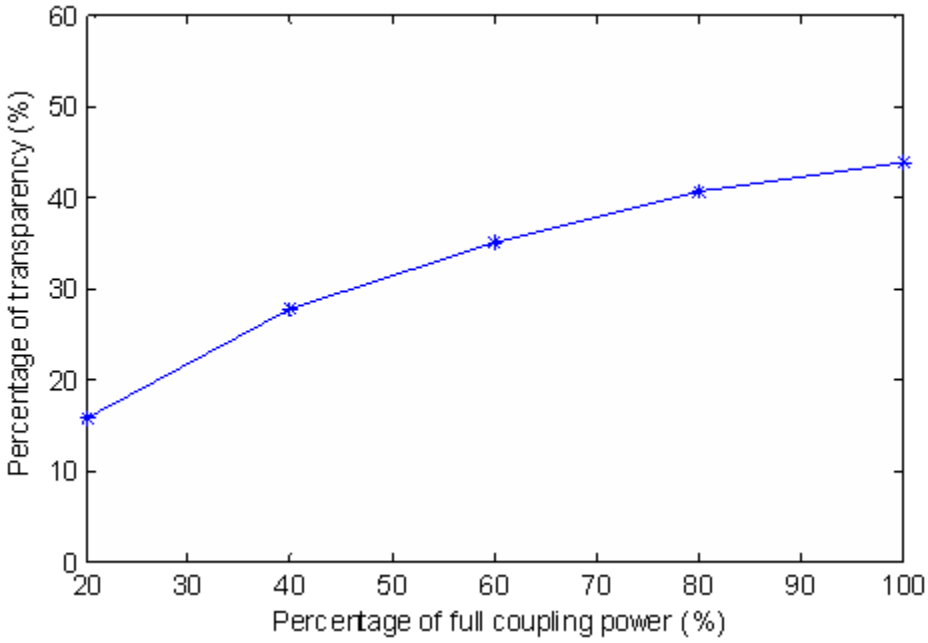

Figure 5.16 EIT depth vs coupling power in Rb loaded ARROW

5.6 Fitting of EIT spectrum

In this section, the fitting for the experimental data of EIT in Rb loaded ARROW are discussed. Several physical parameters such as dephasing rate and coupling Rabi frequency are extracted from the experimental data by employing a theoretical model [68].

5.6.1 Theory for fitting

The linear susceptibility in the Doppler broadened medium can be given by:

$$\chi = \frac{ic\mu_{21}^2 N_0 \sqrt{\pi}}{\hbar \omega_p u} e^{z^2} [1 - erf(z)] \tag{5.2}$$

Where $\Delta\omega_D$ is the Doppler width and expressed by:

$$\Delta\omega_D = \frac{2\omega_p}{c} u\sqrt{\ln 2} \tag{5.3}$$

And z is defined as:

$$z = \frac{c}{\omega_p u}[\gamma - i\Delta_1 + \frac{\Omega_c^2/4}{\gamma_{12} - i(\Delta_1 - \Delta_2)}] \tag{5.4}$$

Where $\gamma = \gamma_{13} + \gamma_{23} + \gamma_{12}$; γ_{13} and γ_{23} are the spontaneous decay rates of the excited state to the two ground states respectively. γ_{12} is the nonradiative decay rate between the two ground states.

The imaginary part of the linear susceptibility represents the absorption whereas the real part of the linear susceptibility indicates the refractive index.

5.6.2 The method for fitting

The flow chart for the fitting to EIT spectrum (implemented with Matlab) is illustrated in figure 5.17. Based on equations5.2, 5.3, 5.4 as shown in the previous section, the theoretical curves with the certain ranges (loops) of nonradiative decay rate and coupling Rabi frequency are compared with the experimental data to find the least

square value.

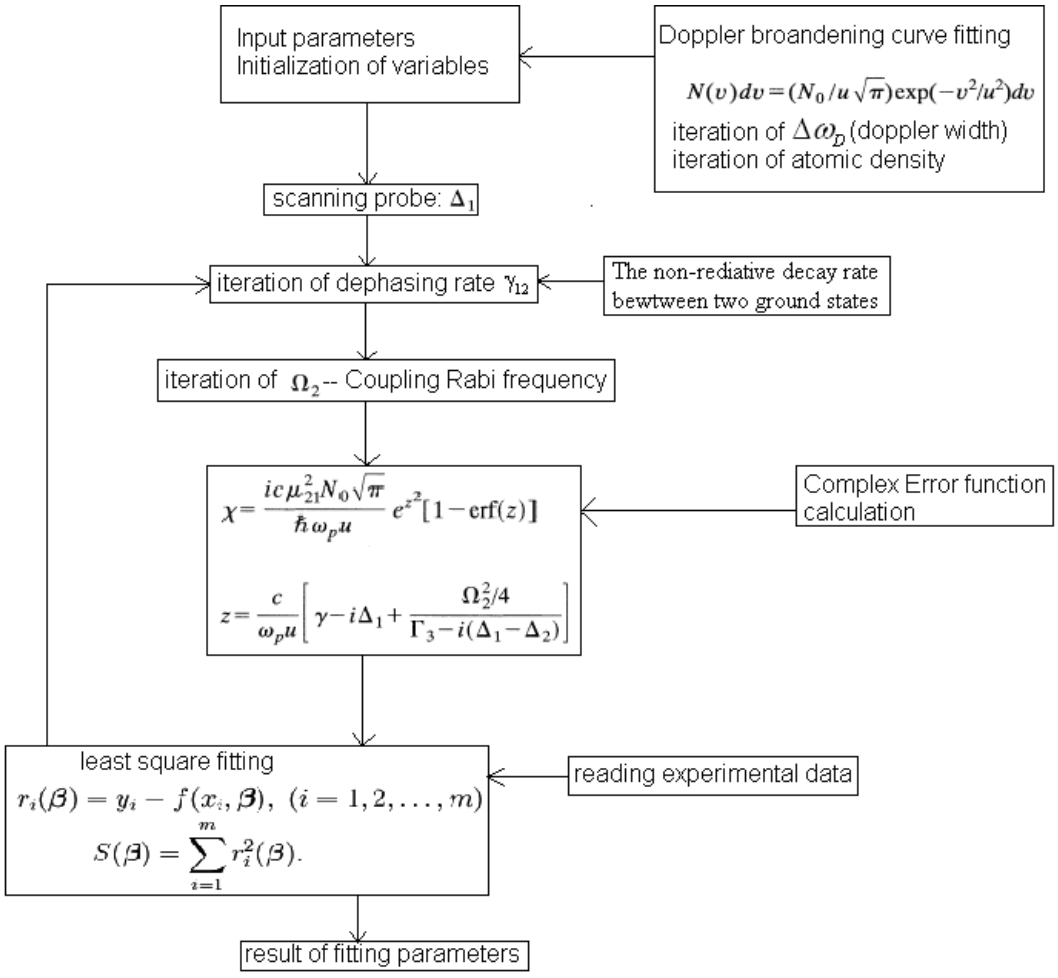

Figure 5.17 The flow chart for fitting of EIT spectrum

5.6.3 Fitting result

Fitting results for the EIT spectra at different coupling powers are illustrated in figure 5.18. The extracted coupling Rabi frequency with full coupling power is 191.7MHz

and the nonradiative rate is 28.5MHz which is a combination of the dephasing rate between the two ground states and the time-of-flight broadening due to the micro-scaled size of the mode area in the hollow core waveguide. The time-of-flight broadening can be subtracted to obtain the final dephasing rate around 4MHz.

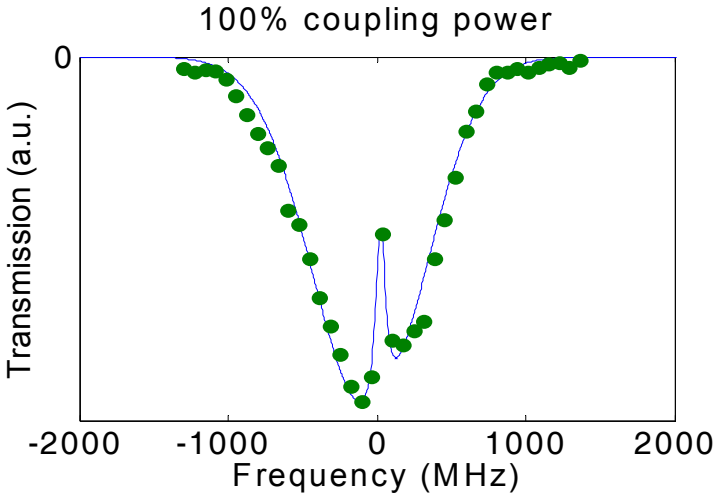

(a)

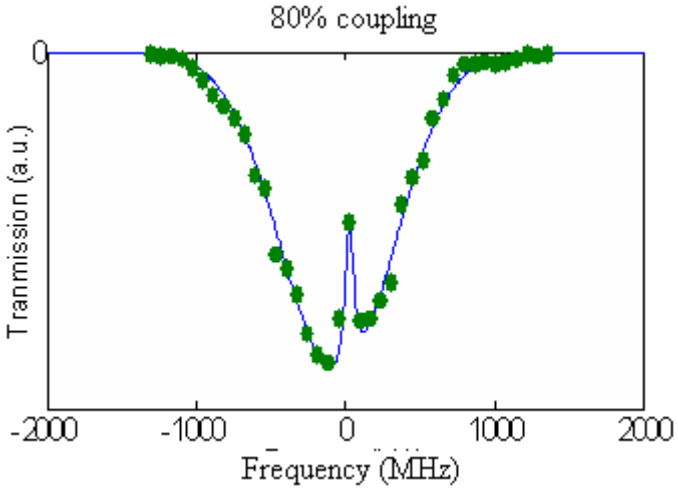

(b)

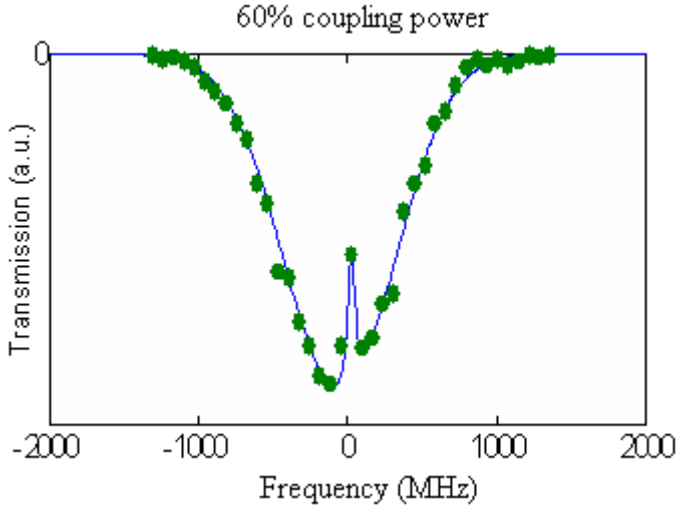
60% coupling power
0
Transmission (a.u.)
-2000
-1000
0
1000
2000
Frequency (MHz)

(c)

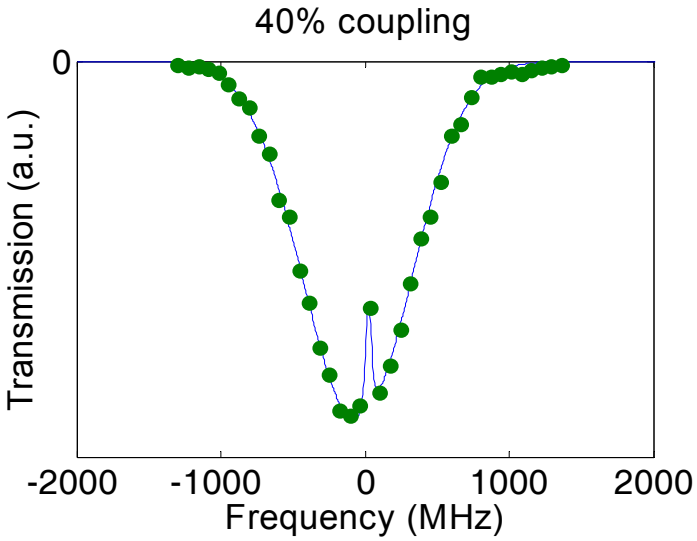
40% coupling
0
Transmission (a.u.)
-2000
-1000
0
1000
2000
Frequency (MHz)

(d)

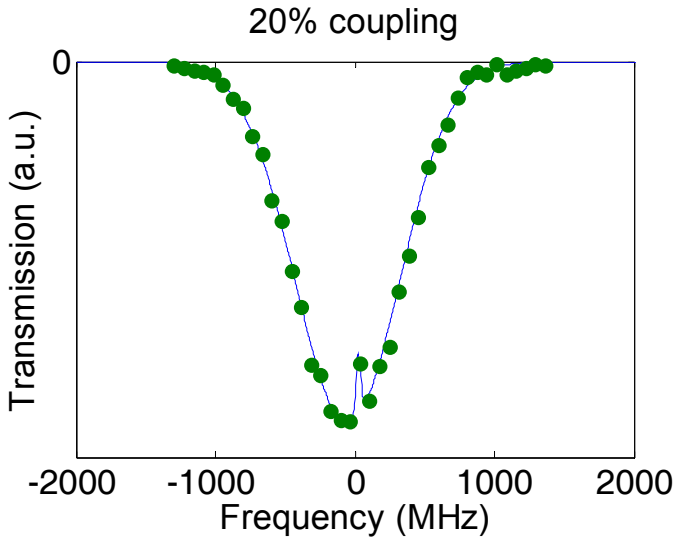

(e)

Figure 5.18 Fitting of EIT spectra in Rb loaded ARROWs. (a) Fitting with 100% coupling power (b) Fitting with 80% coupling power (c) Fitting with 60% coupling power (d) Fitting with 40% coupling power (e) Fitting with 20% coupling power

The extracted coupling Rabi frequencies and the EIT depths at different coupling powers with the same decoherence rate (28.5MHz) are listed in table 5.2.

Percentage of Coupling power	Coupling Rabi frequency	EIT transparency depth
100%	191.7 MHz	44%
80%	178.1 MHz	41%
60%	153.2 MHz	36%
40%	119.4 MHz	28%
20%	77.6 MHz	16%

Table 5.2 Fitting parameters of coupling Rabi frequencies and EIT transparency depths at different input coupling powers

5.6.4 Fitting with the consideration of waveguide loss.

In the previous section, the coupling frequency is assumed be a constant along the propagation distance. However, this is not practical, since in our waveguide with the original design, the intensity loss is always over 10/cm which gives a great decrease of the coupling Rabi frequency along the propagation distance. As shown in figure 5.19, the loss plays a very important role in observing the EIT effect.

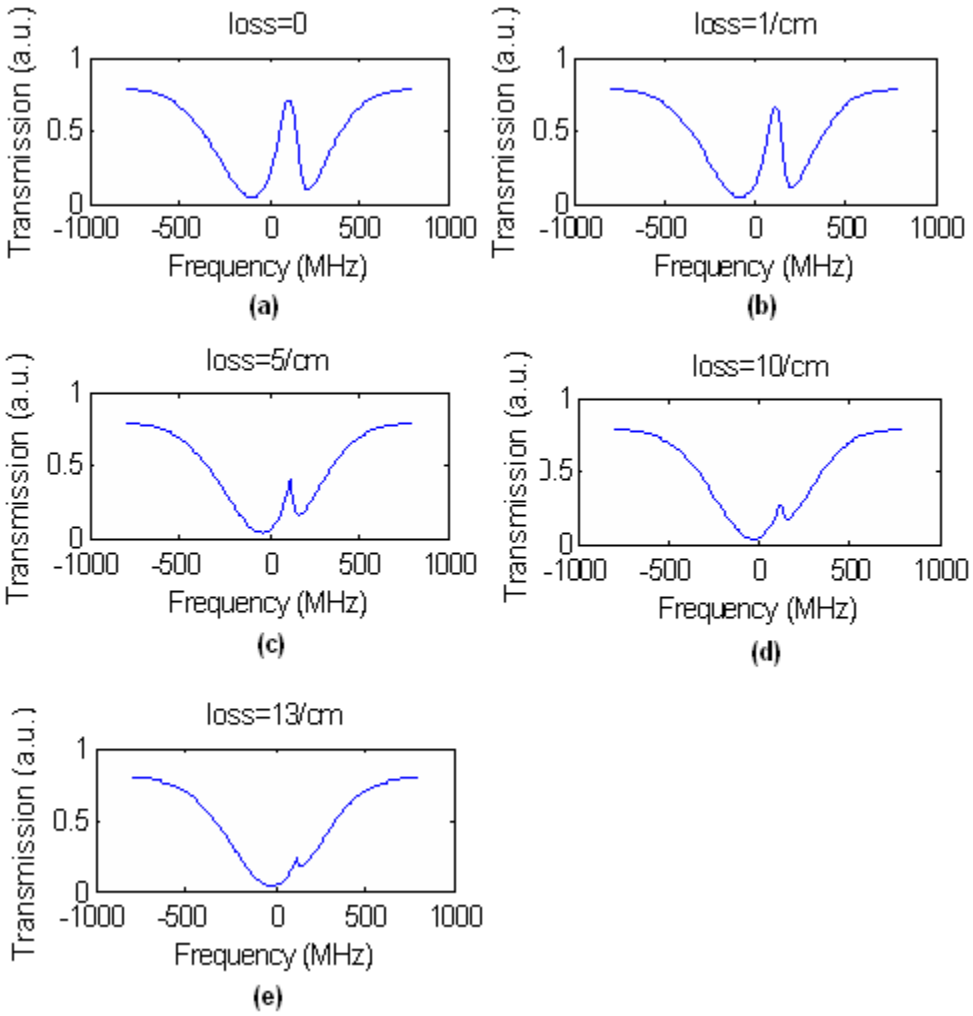

Figure 5.19 The calculated EIT spectra with different waveguide loss

It is obvious that with high waveguide loss, the EIT effect would be washed out due to the low intensity of coupling power.

Therefore, a more accurate fitting method is employed by considering the loss factor in the total EIT fitting process. The flow chart of this fitting method is illustrated in figure 5.20.

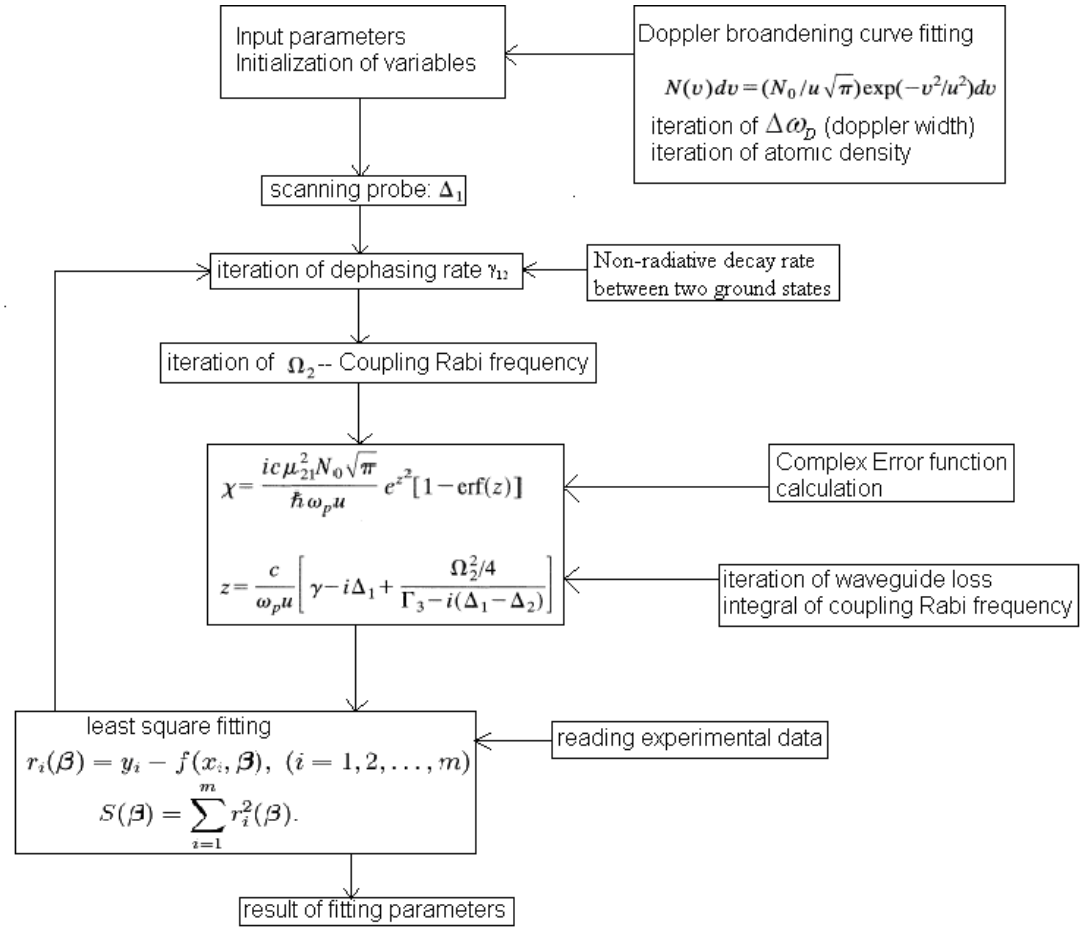

Figure 5.20 Flow chart of EIT spectrum fitting with waveguide loss

By introducing another free running parameter (waveguide loss), the Rabi frequency of coupling power is calculated by integrating its value along the propagation distance with the waveguide loss.

The results of the fitting with waveguide loss are illustrated in figure 5.21.

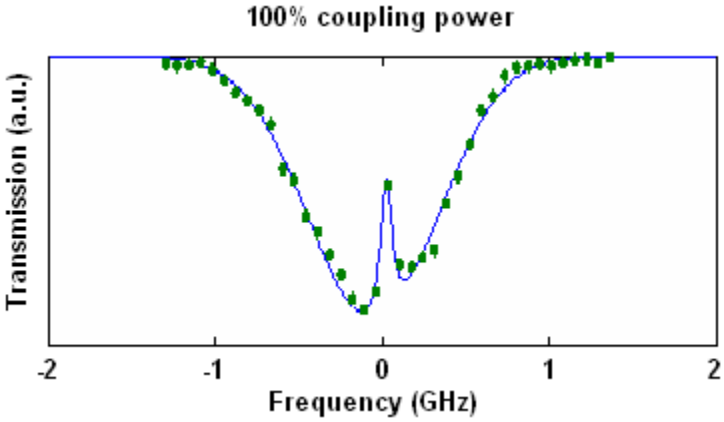
100% coupling power
Transmission (a.u.)
-2
-1
0
1
2
Frequency (GHz)

(a)

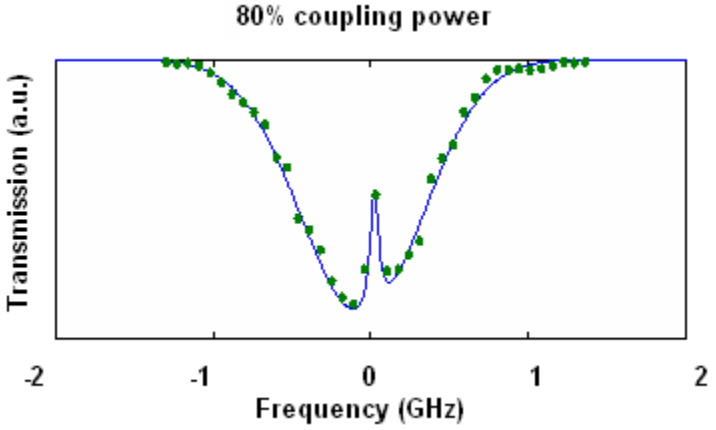
80% coupling power
Transmission (a.u.)
-2
-1
0
1
2
Frequency (GHz)

(b)

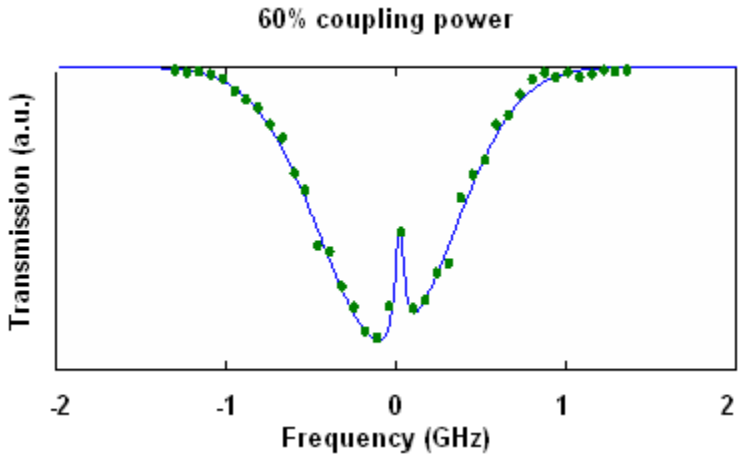
60% coupling power
Transmission (a.u.)
-2
-1
0
1
2
Frequency (GHz)

(c)

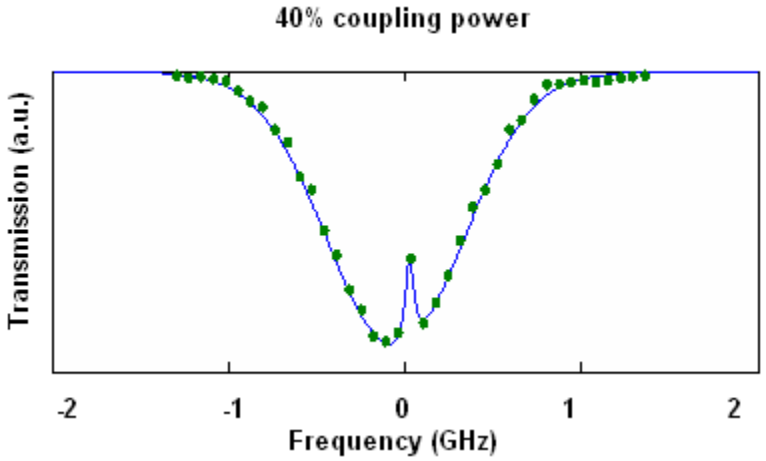
40% coupling power
Transmission (a.u.)
-2
-1
0
1
2
Frequency (GHz)

(d)

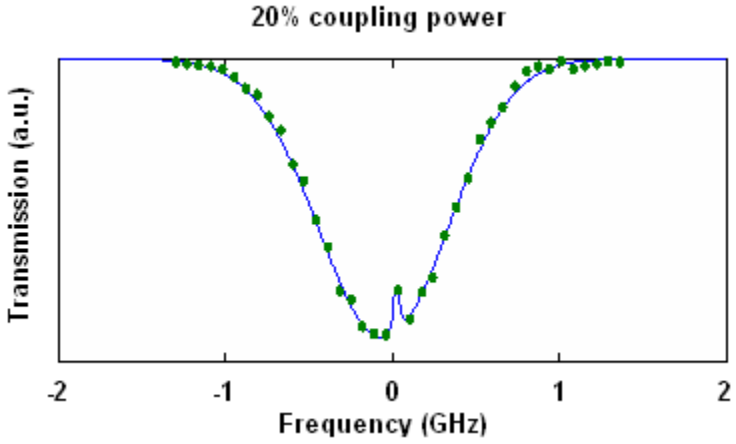

(e)

Figure 5.21 Fittings of EIT spectra with waveguide loss: (a) Fitting with 100% coupling power (b) Fitting with 80% coupling power (c) Fitting with 60% coupling power (d) Fitting with 40% coupling power (e) Fitting with 20% coupling power

From the above shown pictures in figure 5.21, the Rabi frequency of the initial input coupling powers are extracted as the following: Ω_c = 10.75 GHz with 100% full coupling power; Ω_c =9.57GHz with 80% full coupling power; Ω_c =8.11GHz with 60% full coupling power; Ω_c =6.79 GHz with 40% full coupling power; Ω_c =4.94 GHz. The estimated loss value for the waveguide is: 16.7/cm (assumed the same for all fittings and the interface loss is set to be 3dB at each connection between solid core and hollow core.)

The advantage of this improved simulation method can be more clearly observed in the next chapter for slow light experiments, as it will predict the pulse broadening more

accurately compared to the previous simulation method where a uniform Rabi frequency is assumed through the entire length of ARROW.

5.6.5 Experiment with coupling frequency detuning

With the similar experimental setup as shown in figure 5.22, it is interesting to conduct another EIT experiment where the probe laser is locked and the coupling laser is scanned and detected. The result of this coupling detuning EIT in Rb loaded ARROW is shown in figure 5.22. The EIT spectra by detuning the coupling frequency under different coupling powers are plotted in the following figure. The data are only collected with 100%, 80% and 60% full coupling powers because of the degradation of the Rb loaded ARROW after these experiments.

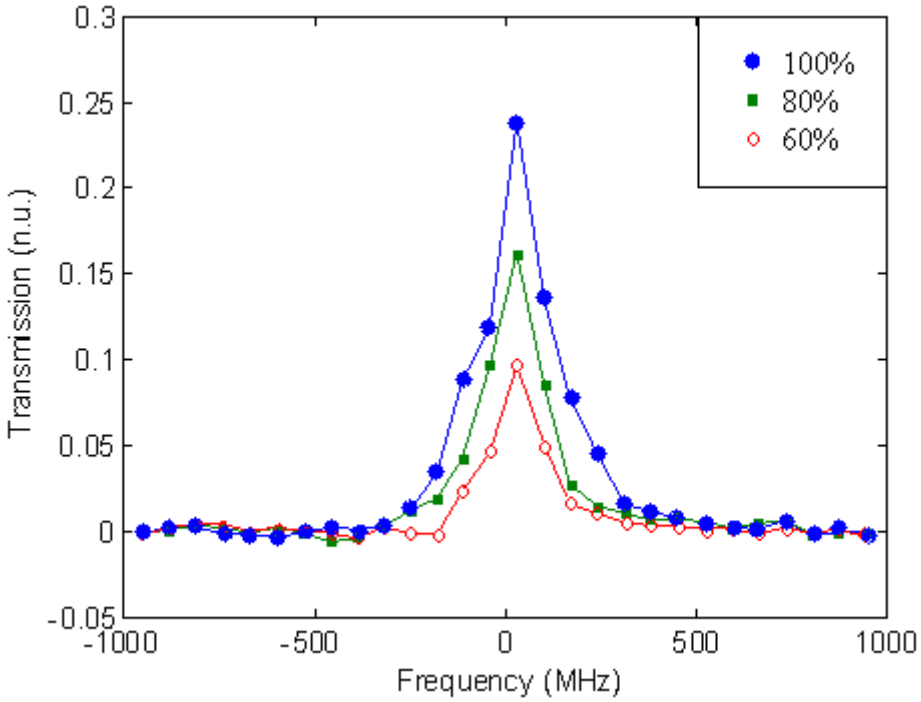

Figure 5.22 EIT spectra with coupling frequency detuning with different coupling powers (a) 100% coupling power (filled circles); (b) 80% coupling power (filled squares); (c) 60% coupling power (open circles))

The transparency increases with the increase of coupling power which agrees with the theoretical prediction. This type of EIT experiment has the advantage of removing the atomic absorption Doppler broadened profile in the background, which gives a clear EIT resonance at the corresponding atomic transition. This may find some interesting applications in laser locking technique for frequency stabilization.

5.7 Summary

In this chapter, both Lambda type and Vee type electromagnetically induced transparency experiment were discussed in bulk cell. LIAD which could possibly increase the atomic density in for future experiments is investigated with specialized minicell of different coatings.

The power dependence of the Lambda type EIT experiment is demonstrated in a minicell which verifies the possibility of conducting EIT in our Rb loaded ARROW waveguide. Finally, EIT is first demonstrated on chip with different coupling powers. The fitting procedures including the consideration of waveguide loss are discussed in the following sections to characterize the system performance of the Rb loaded ARROWs.

Chapter 6 Slow Light on a Chip

6.1 Slow light experiment in Rb loaded ARROW

6.1.1 Experimental setup

The experimental setup of slow light in Rb loaded ARROWs is illustrated in figure 6.1. To investigate slow light on the chip, the probe laser is modulated with an acousto-optic modulator (AOM) to create 20ns long pulses at a repetition rate of 5 MHz. A portion of the probe beam is routed directly to an oscilloscope while the remaining pulse traveled through the spectroscopy chip together with the cw coupling beam.

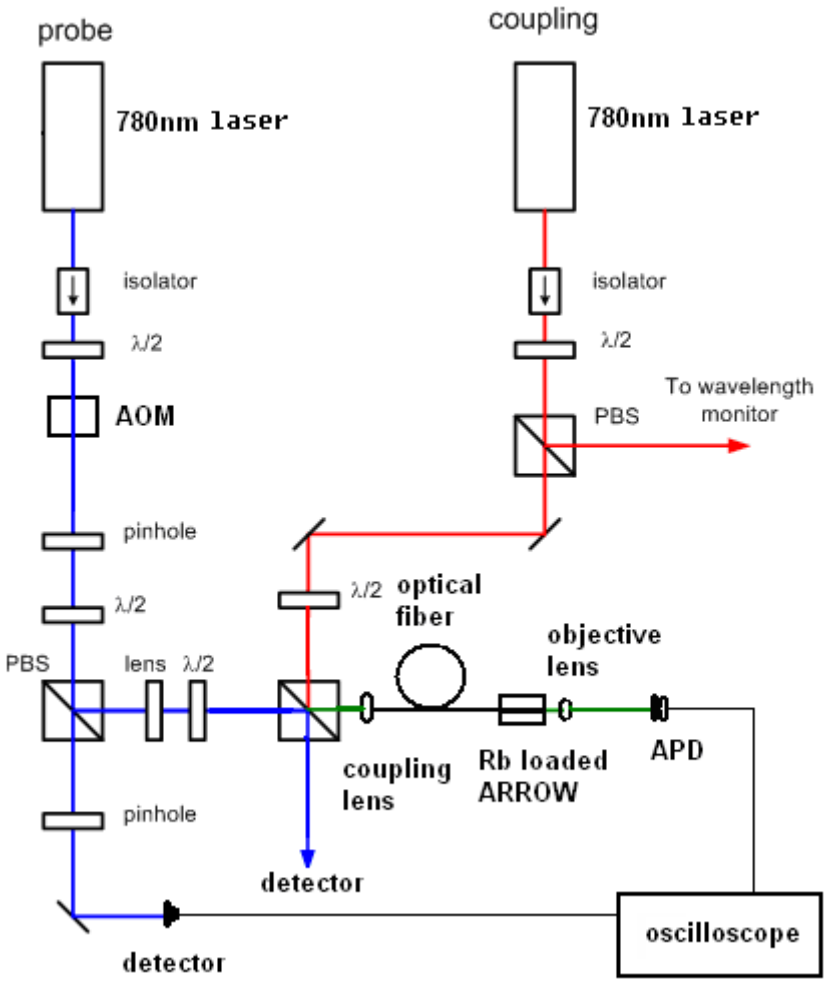

Figure 6.1 Experimental setup of slow light in Rb loaded ARROW

6.1.2 Experimental result

The coupling laser is locked to ^{85}Rb $5S_{1/2}$,F=3->$5P_{3/2}$, F=3. And the probe laser is scanned over ^{85}Rb $5S_{1/2}$, F=2-> $5P_{3/2}$, F=3 transition as shown in figure 6.2. The slow light experiment is conducted with different coupling powers. The initial coupling

power is 18.24mW and the initial probe power is 3.61mW.

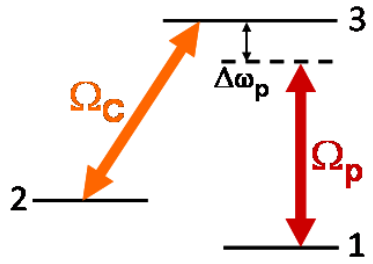

Figure 6.2 The Lambda type EIT used for slow light experiment

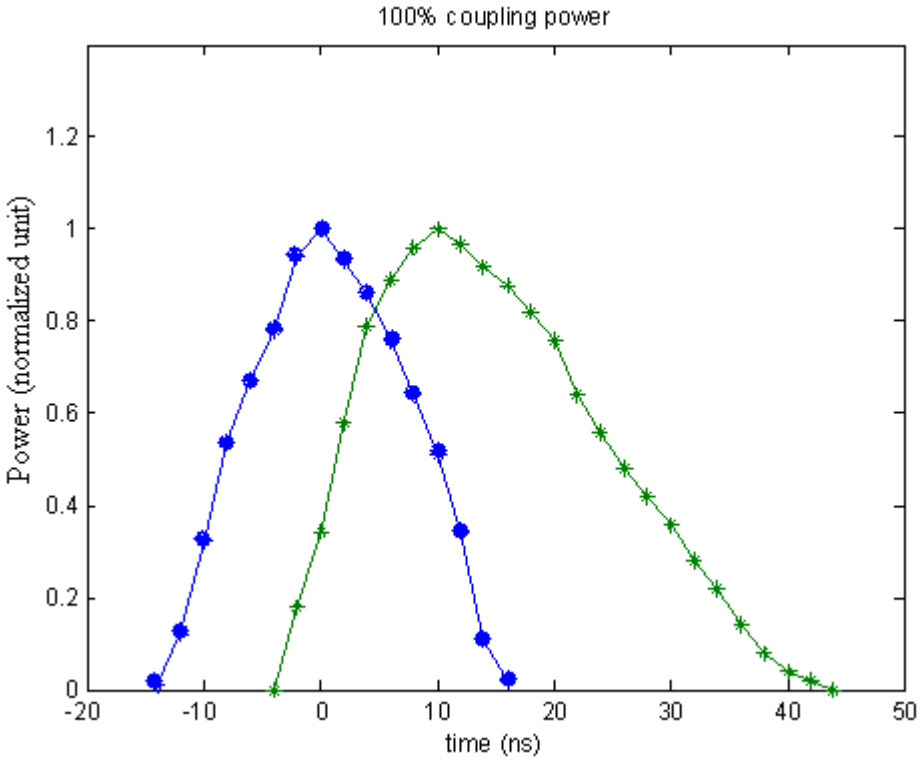

(a)

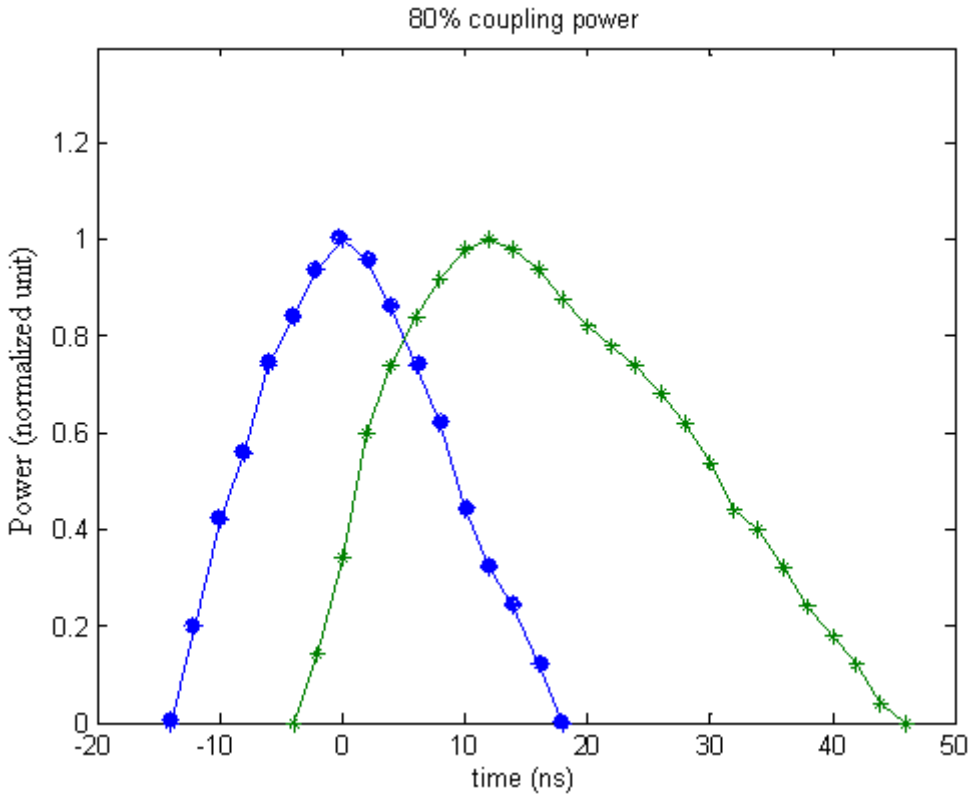
80% coupling power
Power (normalized unit)
time (ns)
0
0.2
0.4
0.6
0.8
1
1.2
-20
-10
0
10
20
30
40
50

(b)

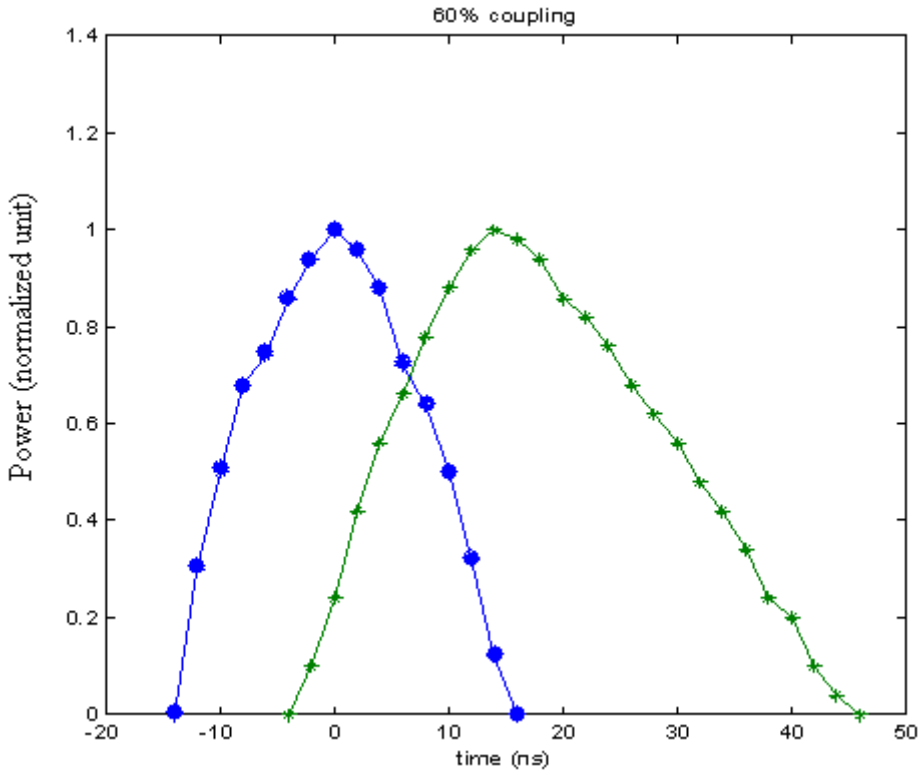
60% coupling
Power (normalized unit)
time (ns)
1.4
1.2
1
0.8
0.6
0.4
0.2
0
-20
-10
0
10
20
30
40
50

(c)

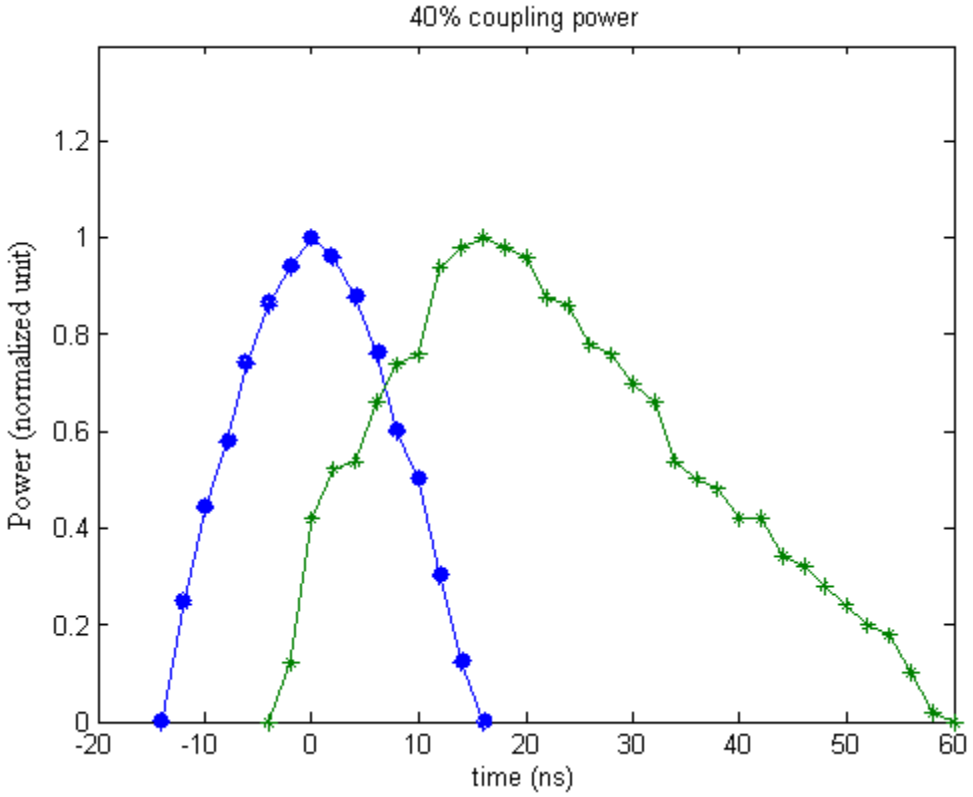

(d)

Figure 6.3 Experimental result of slow light with different coupling powers: (a) 100% full coupling power (b) 80% full coupling power (c) 60% full coupling power (d) 40% full coupling power

As shown in figure 6.4, with the decrease of coupling power, the pulse gets more delayed as expected. Meanwhile, with the more delay of the pulse, it experiences more severe broadening as illustrated in figure 6.5. (The estimation of pulse broadening will be addressed in the next section).

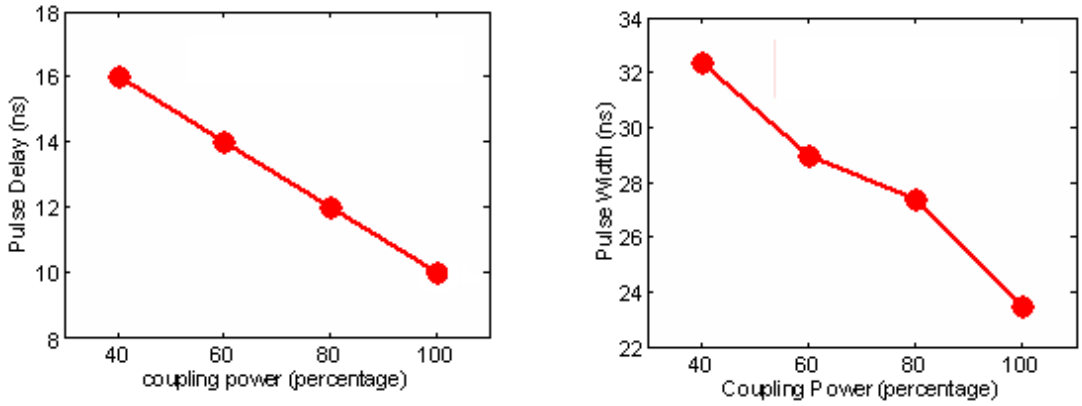

(a) (b)

Figure 6.4 (a) Pulse delay v.s. Coupling power (b) Pulse broadening vs Coupling power

6.2 Simulations of pulse propagation in slow light with Rb loaded ARROW

This effect of slowing down and broadening pulses is due to both group velocity dispersion $\beta_2(\omega)$ and frequency-dependent transmission $T(\omega)$ across the transparency peak. We can model the pulse propagation process in the frequency domain via:

$$E(t,L) = \int_{-\infty}^{\infty} E(\omega,0)T(\omega)e^{\frac{i}{2}\beta_2\omega^2 z}e^{i\omega t}d\omega \qquad (6.1)$$

Both $\beta_2(\omega)$ and $T(\omega)$ can be extracted from the EIT profile. The input pulse is

assumed to be a $Sech^2$ pulse, as illustrated in figure 6.5. where, (with τ (input pulse width) assumed to be 20ns.)

$$E(\omega,0) = \int_{-\infty}^{\infty} P_0 \sec h^2(\frac{t}{\tau}) \times e^{i\omega t} dt \quad (6.2)$$

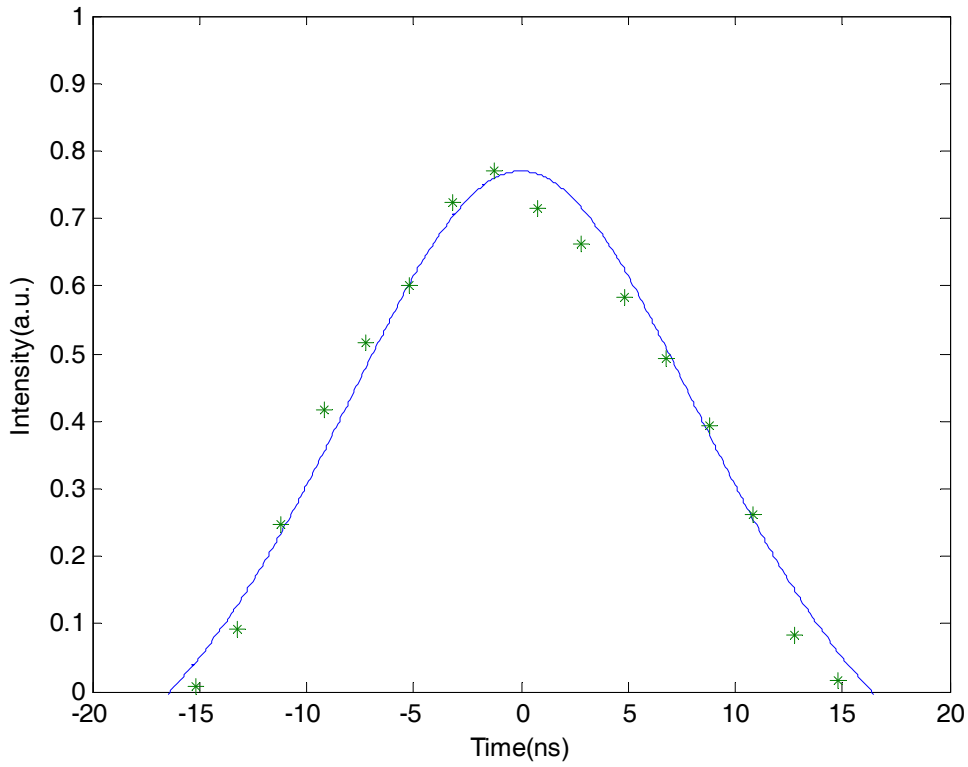

Figure 6.5 Reference pulse (input pulse) is plotted with $sech^2$ pulse shape compared to the experimental data.

The calculated $T(\omega)$ transmission curve (fitting parameters: coupling Rabi frequency: 201.6MHz ; Dephasing Rate: 4.04MHz) and β_2 (group velocity dispersion coefficient) with the full input coupling power is shown in figure 6.6.

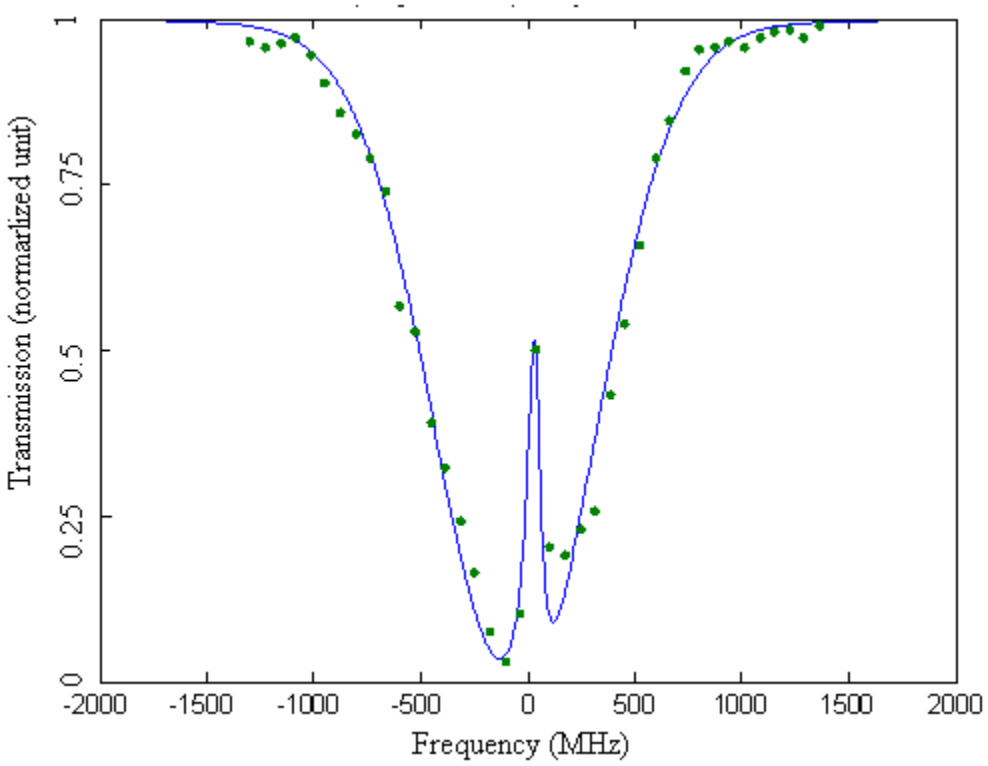
Transmission (normarlized unit)
0
0.25
0.5
0.75
1
-2000
-1500
-1000
-500
0
500
1000
1500
2000
Frequency (MHz)

(a)

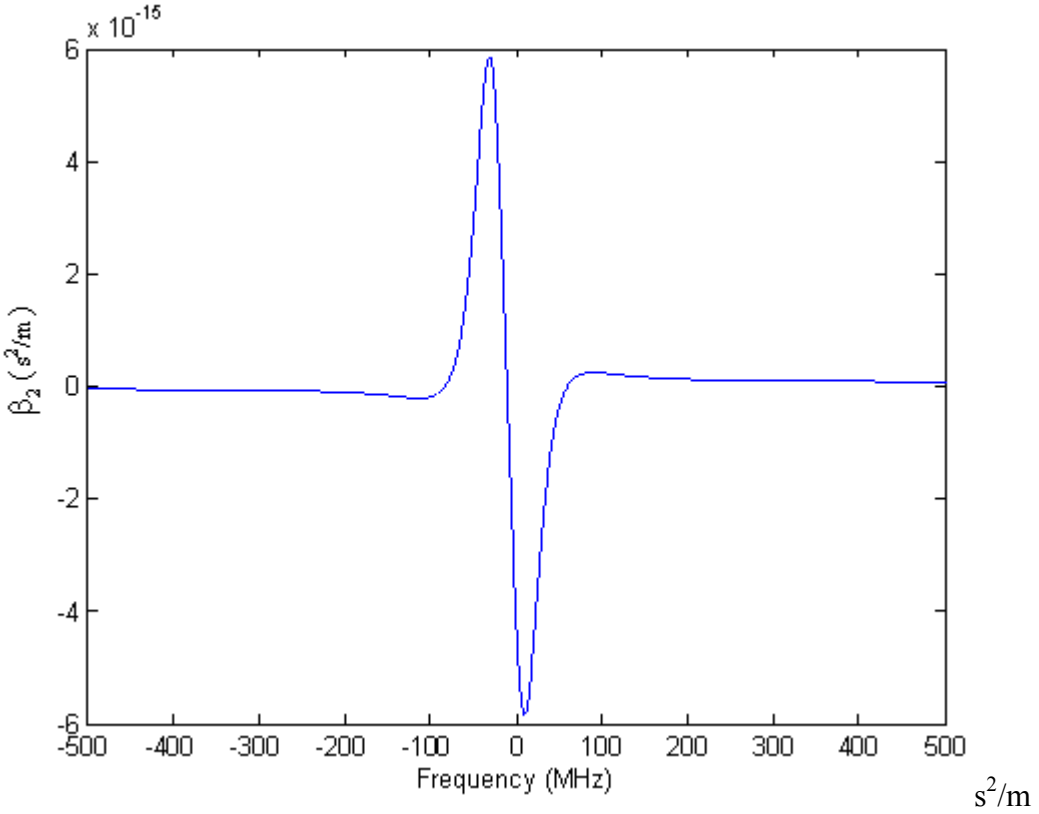

(b)

Figure 6.6 (a) Fitting of EIT spectrum with full coupling power and (b) β_2 (the second order derivative of refractive index respect to frequency) v.s. probe frequency with full coupling power

The pulse shape after the Rb loaded ARROW can be calculated without any free parameters from equation (6.1) and results are shown in figure 6.7.

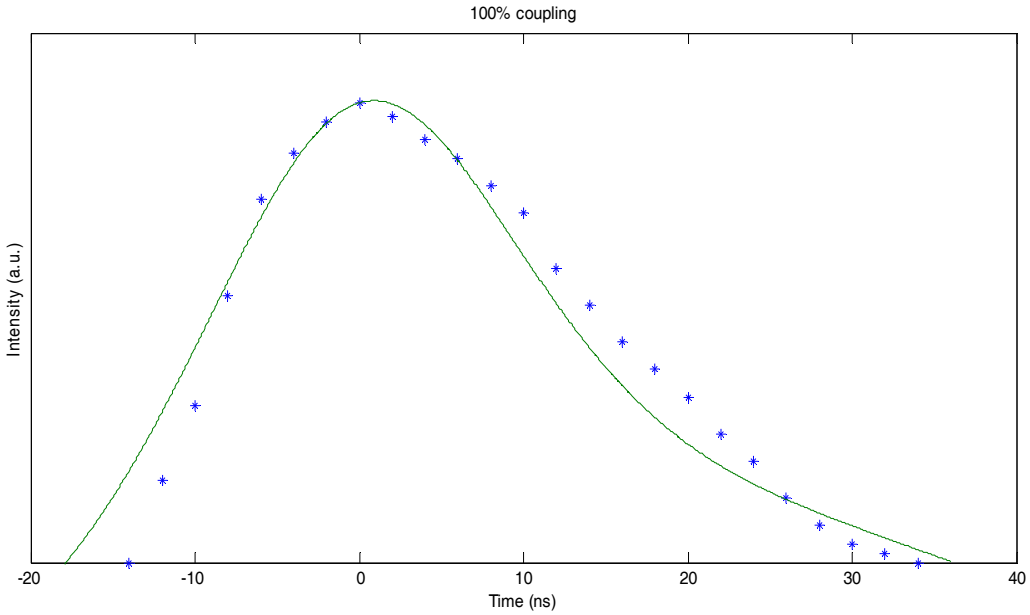

(a)

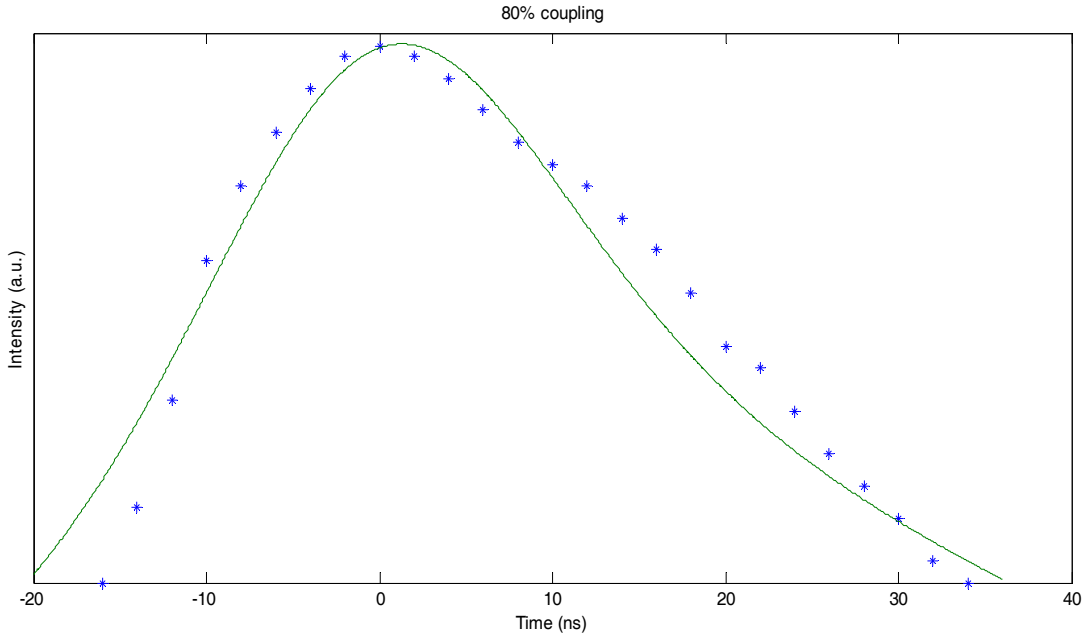
80% coupling
Intensity (a.u.)
-20
-10
0
10
20
30
40
Time (ns)

(b)

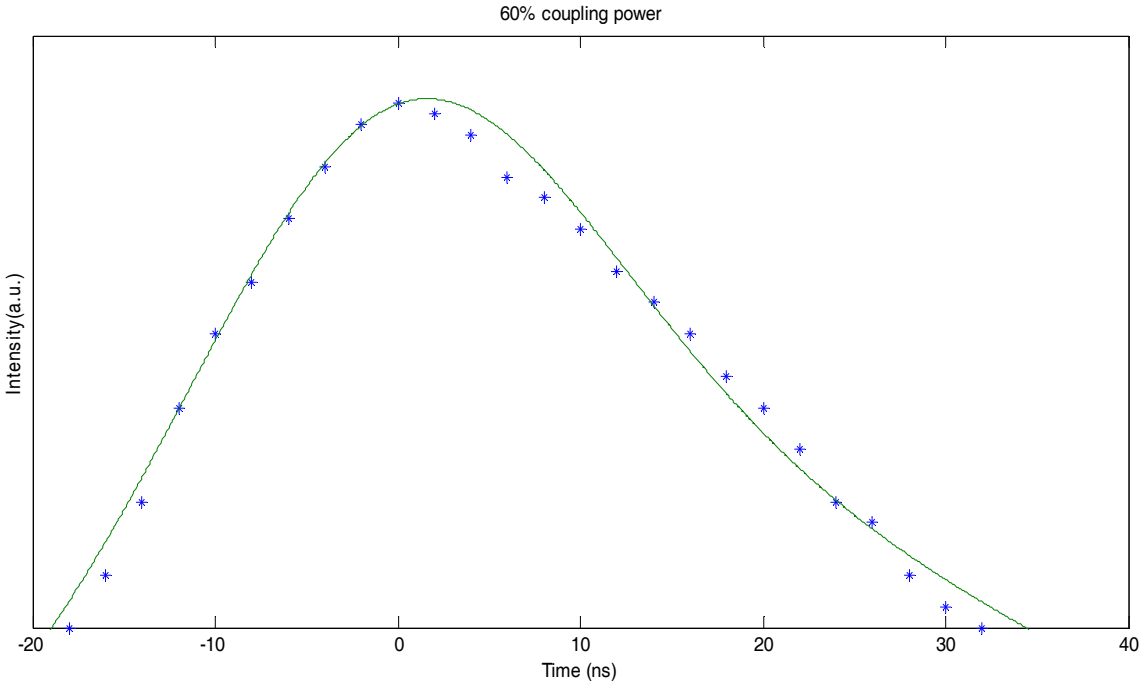
60% coupling power
Intensity(a.u.)
-20
-10
0
10
20
30
40
Time (ns)

(c)

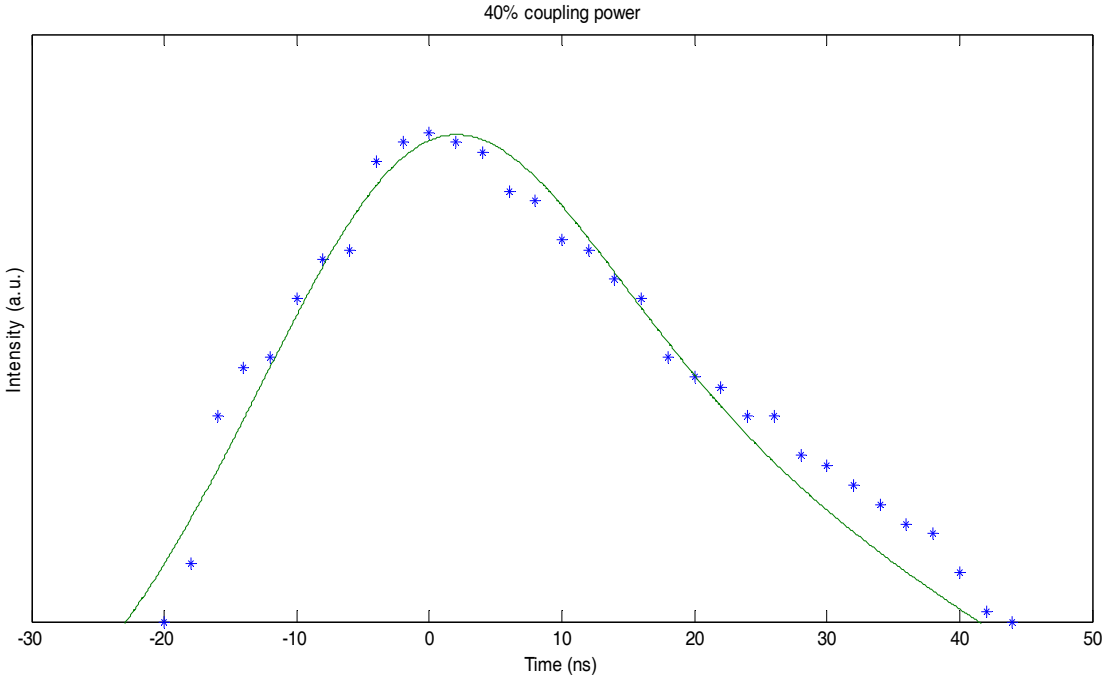

(d)

Figure 6.7 Simulations of output pulses from Rb loaded ARROWs: (a) 100% full coupling power (b) 80% full coupling power (c) 60% full coupling power (d) 40% full coupling power

As seen in figure6.6, the simulation results have a good agreement with the experimental data. A low pass filtering technique is employed as the final procedure to get rid of the high frequency oscillations generated by the fast Fourier transform (equation 6.1 is calculated in frequency domain.) during the whole calculation procedure.

This simulation is a changing-factor free calculation, in which there are no variables for experimental data fittings. All the Calculations are based on the experimental parameters, including the input pulse width (20ns) and the decoherece rate and intensity extracted based on the experimental data for both the EIT absorption curve and the dispersion curve.

The Fourier transform is employed because the calculation for a short light pulse in time domain can be extremely complicated and hence may take a relatively long computing time.

However, with the FFT algorithm used in this calculation, we can greatly reduce the complexity for this calculation. As a result, the computing time can be largely decreased due to this frequency-domain calculation. And the accuracy can still be maintained according to our final results.

Finally, after considering the influence of both the EIT absorption curve and the dispersion in the frequency domain of the pulse, the final result is conversed back to time domain by the reversed Fourier transform.

In figure 6.8, the simulation values and experimental data of group velocity and group

index are compared, which show a very good agreement. As seen in figure 6.8, a group index of as high as 1,200 is observed along with a commensurate reduction in group velocity.

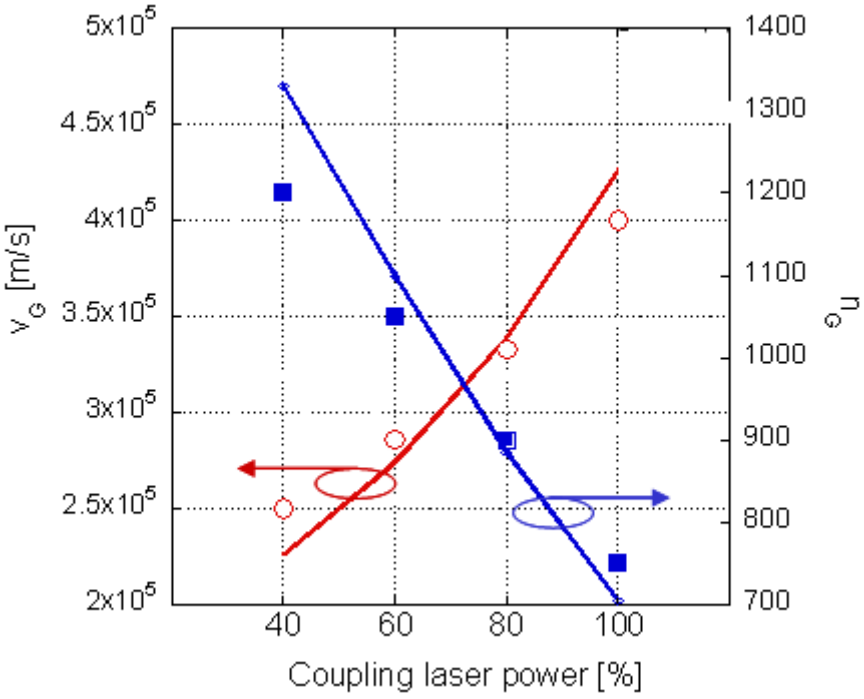

Figure 6.8 The group velocity and group index vs coupling power (experimental data of group velocity (open circles) and group index (filled squares) versus relative coupling laser power. The lines represent parameter-free calculations based extracted from the EIT spectrum)

The simulated result of pulse delay and broadening is compared with the experimentally measured values in figure 6.9.

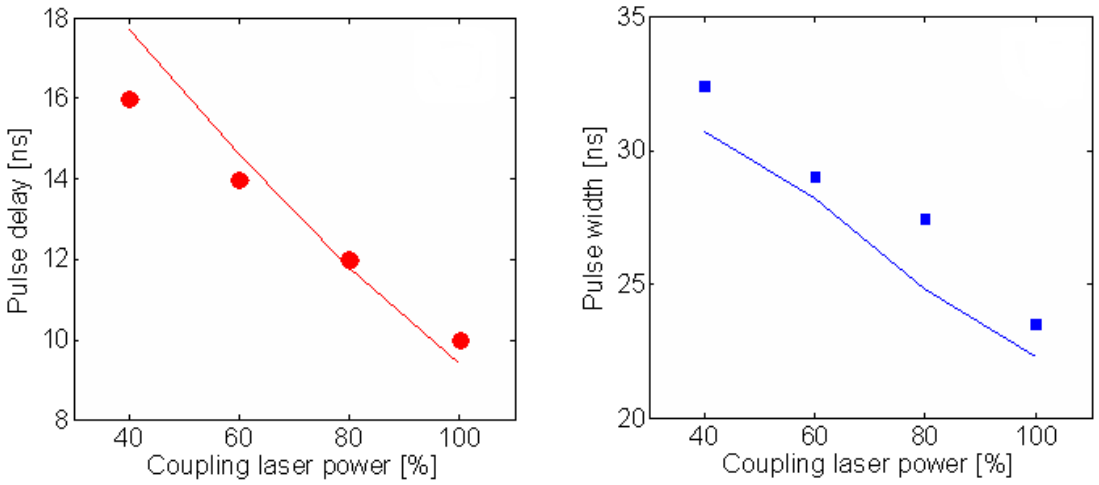

(b)

Figure 6.9 Experiment (symbols) and theory (lines) are compared for pulse delay and pulse width.

A good agreement between the simulated result and the experimental result indicates the rationality for assuming the input pulse with a sech^2 shape and calculating the pulse evolution in frequency domain by FFT.

6.3 Simulations of slow light experiment with waveguide loss

From the discussion in the previous chapter, we proposed an integration calculation to combine the loss effect of ARROW to fit experimental EIT spectrum. Here, we also replaced the single coupling Rabi frequency which was used for the calculations in section 6.2 by the integrated of the waveguide loss with the initial input Rabi frequency

(input coupling Rabi frequency: 10.81GHz with 11.5/cm loss).

The simulation results with waveguide loss are shown in figure 6.10.

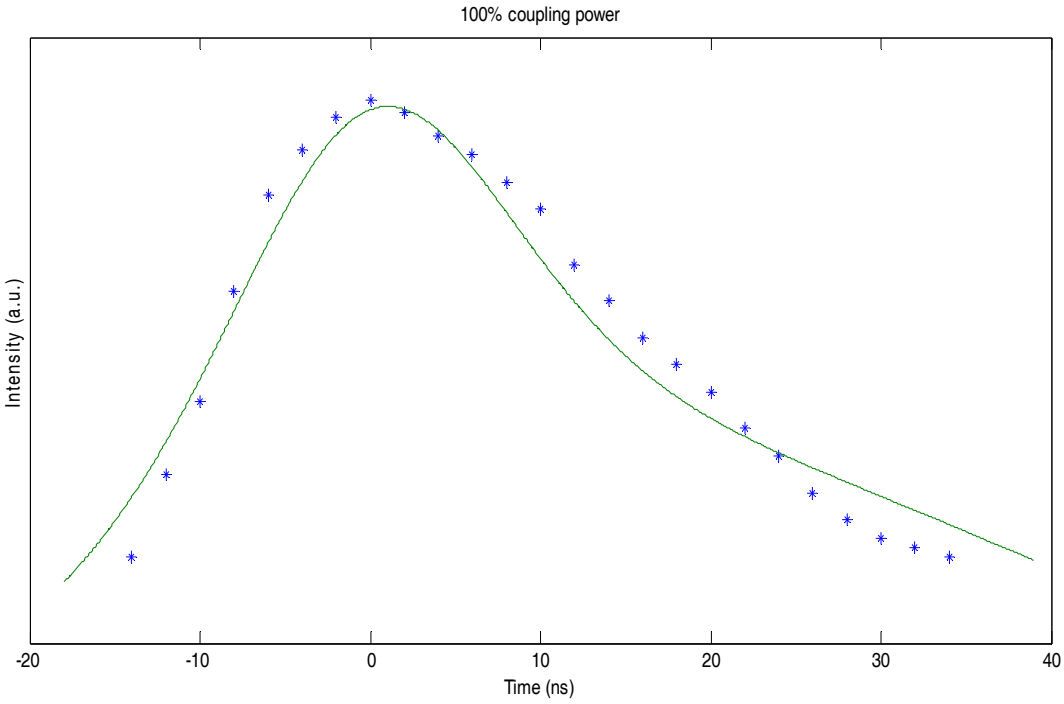

(a)

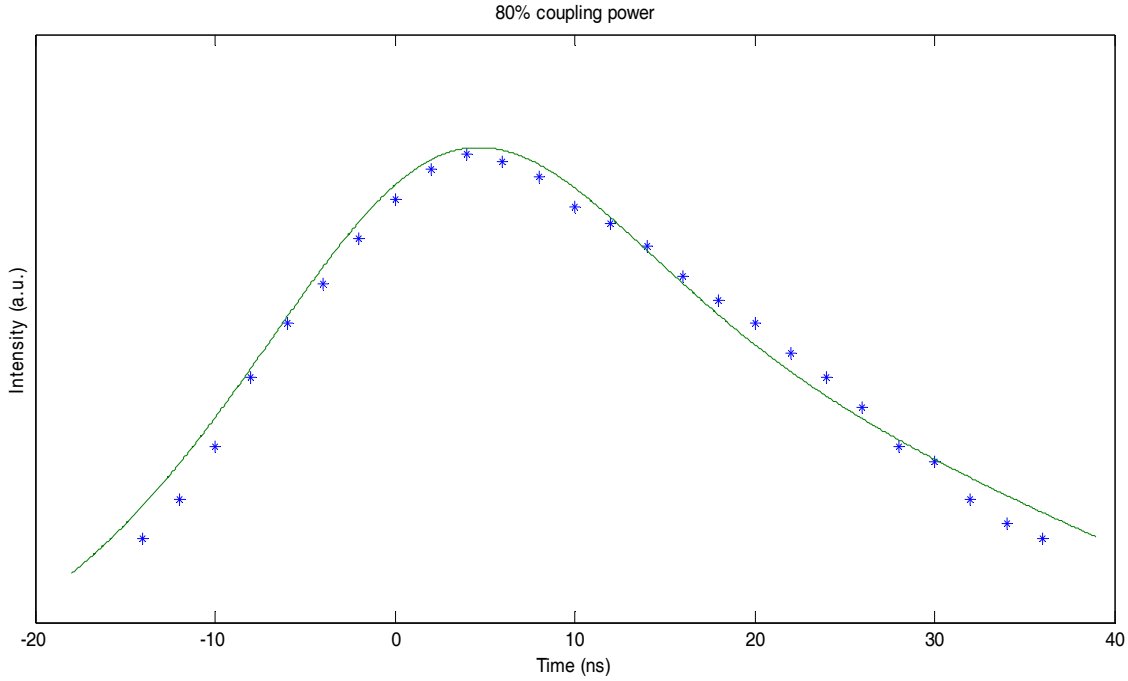

(b)

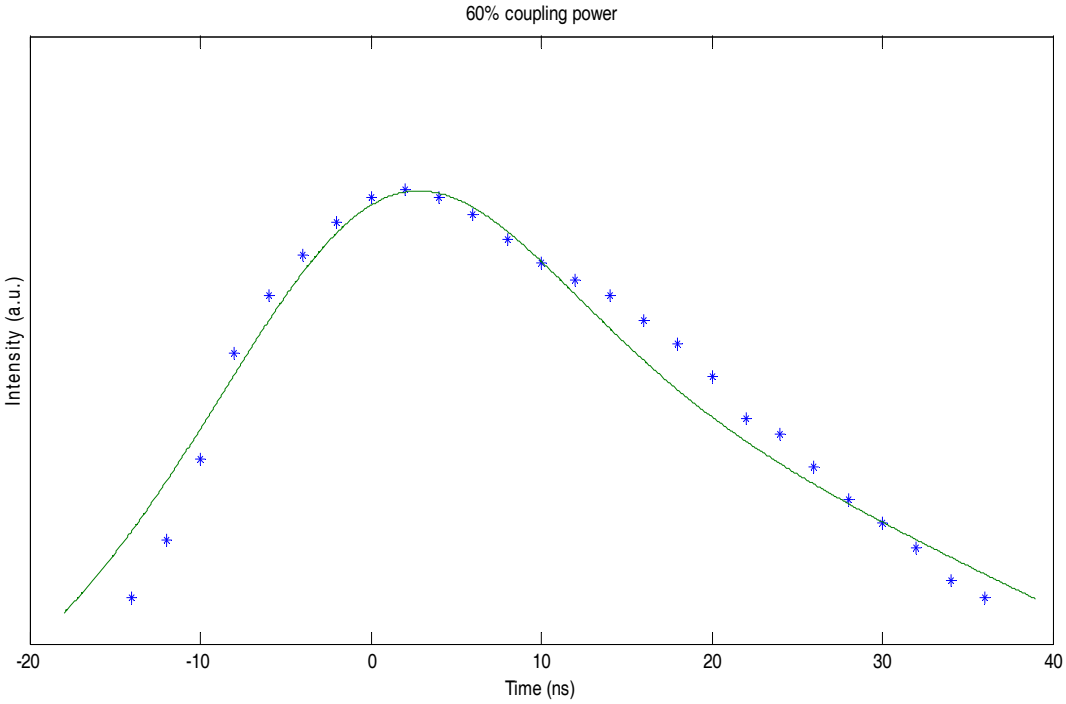

(c)

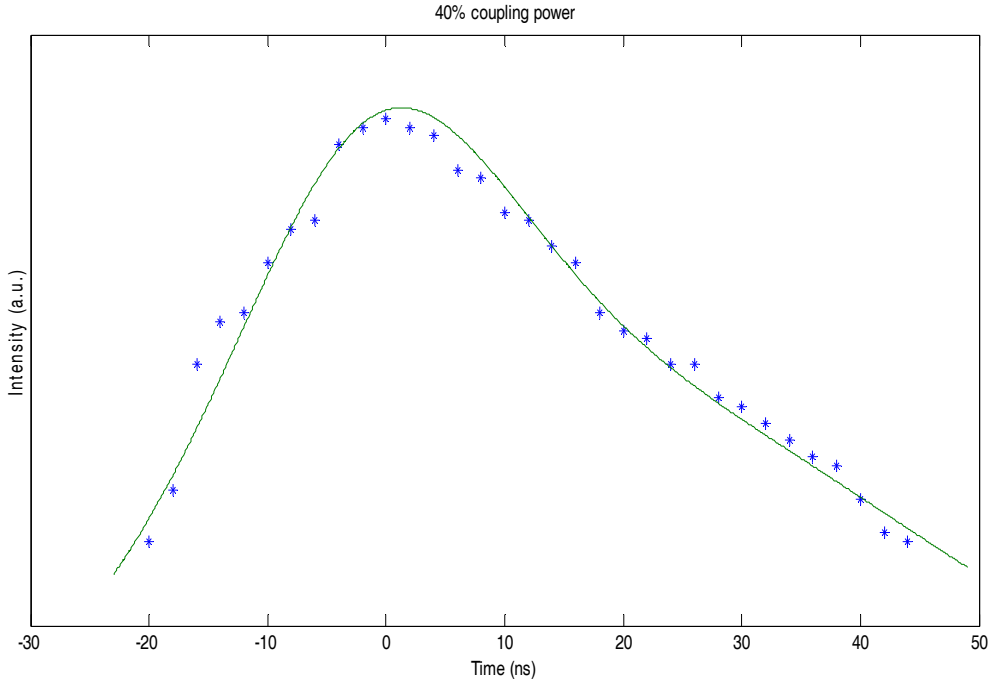

(d)

Figure 6.10 Simulations of output pulses with waveguide loss: (a) 100% full coupling power (b) 80% full coupling power (c) 60% full coupling power (d) 40% full coupling

From the comparison of figure 6.10 and figure 6.7, we can see that there is a better agreement between the simulation and experimental results for the waveguide loss integration method than the single coupling Rabi frequency method.

The calculations for pulse with both the waveguide loss integration method and the single coupling Rabi frequency method as well as the experimental data are plotted in figure 6.11.

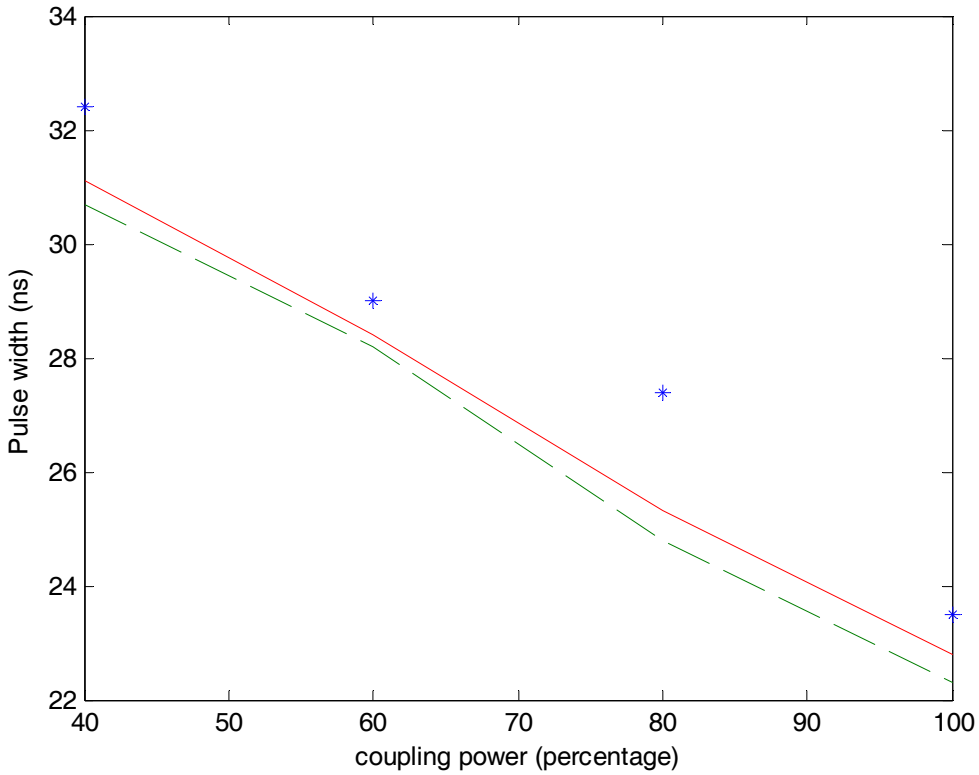

Figure 6.11 Pulse width with different coupling powers (stars: experimental data; solid line: calculations with waveguide loss; dashed line: calculations with single Rabi frequency)

As the comparison in figure 6.11 shows, the calculation with waveguide loss integration indicates a more accurate approach to investigate the slow light phenomenon in our Rb loaded ARROW.

6.4 Summary

Here, we have reported the first demonstration of atomic quantum state control in such an atomic spectroscopy chip. Rubidium atoms confined to hollow-core waveguides with micronscale cross sections exhibit robust quantum interference effects, a large group velocity reduction by a factor of 1,200, and optical pulse delays up to 18ns. These observations point the way to combining atomic quantum state control with solid-state photonics.

The demonstration of slow light and EIT via quantum state control on a fully self-contained atomic spectroscopy chip resulted in the lowest group velocities on a chip to date. The waveguide-based approach is compatible with additional, more conventional photonic structures and designs. Examples include multiple Rb cells in series or in parallel, or the exploitation of being able to microstructure the waveguide loss to create spatially varying EIT profiles and group velocities. In addition, the fact that such large EIT effects can be realized in photonic microsctructures indicates that further applications of electronic quantum state control are possible. Nonlinear optical effects are particularly attractive due to the combination of long propagation distances and small mode areas on the chip [120]. Examples include cross-phase modulation, quantum memory via parametric photon generation, or all-optical switches. Thus, the present results point the way towards chip-scale implementation of such quantum coherence enhanced nonlinear devices that operate at ultralow power levels.

Chapter 7 Summary and outlook

7.1 Summary of work

We have introduced a new way towards semiconductor-based devices that utilize quantum interference effects (EIT) and EIT assisted slow light effects. This approach combines the large magnitude of quantum interference effects in rubidium vapor with the numerous benefits of integrated optics. In order to combine these seemingly incompatible concepts, an integrated platform has been developed where both atomic vapor and light are confined to hollow channels on a chip. Miniaturization of the channel cross sections is particularly desirable for nonlinear optical devices whose efficiency scales inversely with mode area. Hollow-core ARROW waveguides are demonstrated as a highly promising approach towards this goal. We have described the basic principle of confining light in these waveguides, the effects of this confinement on the optical properties of confined rubidium atoms, and ways for optimizing the optical performance of the ARROWs. The results of fabrications of integrated vapor cells on a chip were presented.

A fully integrated EIT device required further development of these techniques. In particular, issues such as dephasing due to wall collisions in tightly confined spaces have been addressed and solved by coating an ODMS layer into the inner wall of the waveguide surface. The positive results of the testing for organic monolayer coatings

on the optical properties of the ARROW waveguides indicate that integrated rubidium cells are suitable for more demanding quantum coherence effects.

After various improvements of our self-contained Rb cell integrated ARROW waveguide, the linear and nonlinear (SAS) Rb spectroscopy has been demonstrated with our integrated optical device.

More importantly, the quantum coherence effect (electromagnetically induced transparency) has been demonstrated with our Rb cell integrated waveguide platform which would is pivotal step towards the development of novel quantum communication systems on a chip.

Based on this EIT technique, slowing down the group velocity of a light pulse has been finally achieved within our Rb loaded ARROWs which could possibly be used as the optical buffers in future quantum networks.

In addition to simply reducing the footprint of an atomic vapor cell, the integrated approach also possesses several advantages including strong confinement of the optical beam over long distances, simpler alignment especially for multibeam experiments, ability to place multiple cells on a single chip, and the addition of additional functionalities afforded by integrated optics such as intersecting waveguides, presenting a very intriguing and exciting prospect.

7.2 Remaining challenges

The dephasing rate can be even lowered in our device by reducing the experimental

temperature. Currently, all the EIT spectra are taken at 80℃ or higher in order to reach a reasonably high atomic density. This can be improved by reforming the fabrication techniques of the Rb cell integrated ARROW chips. In other words, by engineering the loss and sealing of Rb loaded ARROWs, EIT experiment can be done at lower temperatures. In turn, the speed of Rb atoms will reduce and result in a low dephasing rate due to the less collisions and lower flight rate.

Moreover, there are also other approaches to reducing the speed of Rb atoms, such as laser cooling or atomic trappings. [117,118]

7.3 Outlook

Recent reports on the use of low-level nonlinearities in bulk cells of Rb vapor for nonlinear optics and rudimentary quantum information processing demonstrate impressively that the potential of such devices is tremendous, such as optical data storage [57], optical switches [111] and paired photon generation [27]. The development of a suitable integrated environment will bridge the way towards practical implementations and presents exciting prospects for single-photon optics.

One example for nonlinear optics experiment based on EIT effect is parametric oscillation generation. The level scheme for this experiment is shown in figure 7.1. (pump: E_{14},E_c ; signal: E_p; idler: E_{24})

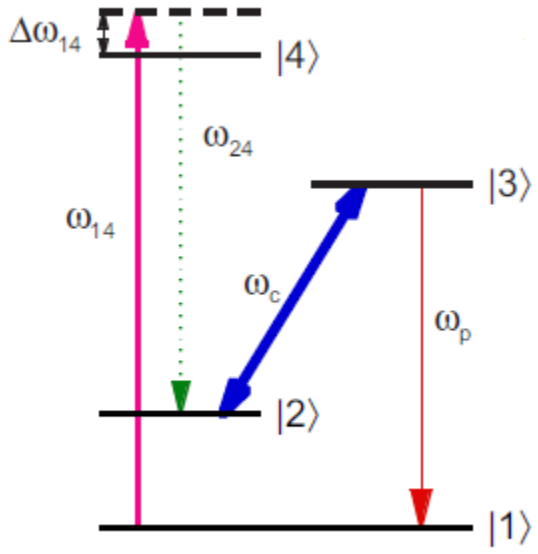

Figure 7.1 Four-level system for parametric oscillation generation

With this double Λ system, the fourth frequency ω_{24} is generated by [78]:

$$\omega_{24} = \omega_{14} + \omega_c - \omega_p \quad (7.1)$$

The generated wave can be expressed by the following equations:

$$\frac{\partial E_{24}}{\partial z} + \frac{1}{c}\frac{\partial E_{24}}{\partial t} = i\frac{\omega N}{2c}[\chi^{(1)}E_{24} + \chi^{(3)}E_{14}E_c E_p^*] \qquad (7.2)$$

where E14, E24, Ec, and Ep are the amplitudes of the lightwaves coupled to corresponding atomic transitions. N is the atomic density of the medium, and $\chi^{(1)}$ and $\chi^{(3)}$ are the linear and third-order susceptibilities are given by:

$$\chi_{24}^{(1)} = \frac{c}{\omega_{24}}\left(\frac{N\mu_{24}\gamma_{24}(\Delta_p - i\gamma_{13})|\Omega_{24}|^2}{(\gamma_{14}^2 - \Delta_{14}^2)(|\Omega_c|^2 - 4\Delta_p(\Delta_p - i\gamma_{13}))}\right)$$

$$\chi_{24}^{(3)} = \frac{4}{3}\frac{c}{\omega_{24}}\left(\frac{-N\mu_{24}}{(\omega_{14} - i\gamma_{14})(4\Delta_p(\Delta_p - i\gamma_{13}) - |\Omega_c|^2)}\right) \qquad (7.3)$$

Where μ_{24} is the dipole moment between level $|2\rangle$ and $|4\rangle$, γ_{24} is the spontaneous decay rate from level $|4\rangle$ to $|2\rangle$, γ_{14} is the spontaneous decay rate from level $|4\rangle$ to $|1\rangle$. γ_{13} is the spontaneous decay rate from level $|3\rangle$ to level $|1\rangle$. γ_{12} is the dephasing rate between two ground states $|1\rangle$ and $|2\rangle$. Δ_p is the probe laser detuning.

By using the experimental parameters extracted in section 6.2, the efficiency of parametric oscillation generation ($\eta = E_{24} / E_p$) is plotted as a function of pump power (assuming E_{14}=E_c) as shown in figure 7.2(a) and signal power (E_p) as shown in figure7.2(b).

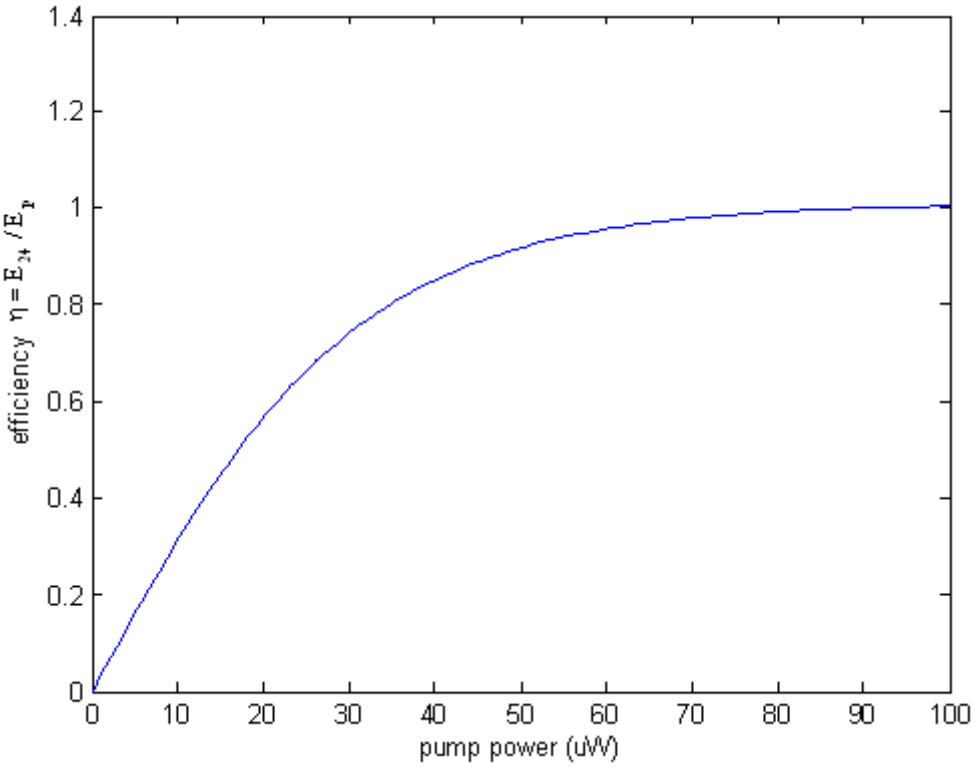
1.4
1.2
1
0.8
0.6
0.4
0.2
0
efficiency η = E24 / Ep
0
10
20
30
40
50
60
70
80
90
100
pump power (uW)

(a)

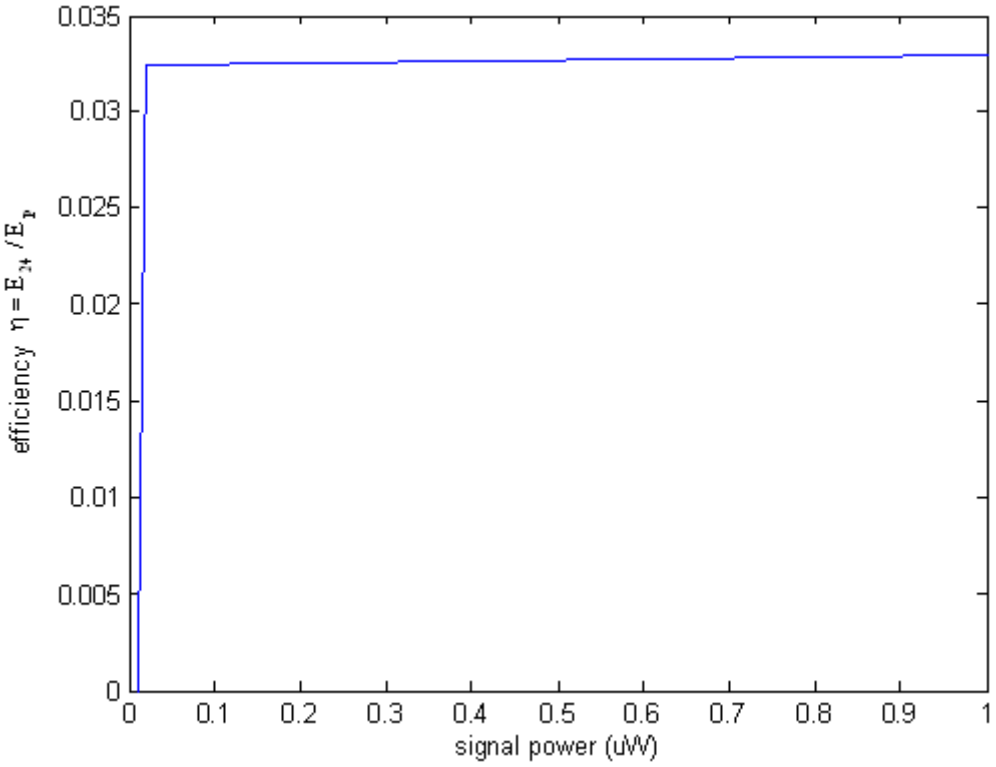

(b)

Figure 7.2 (a) The efficiency of parametric generation v.s. pump power (with the fixed signal power at 10nW). (b) The efficiency of parametric generation v.s. pump power.and signal power (with the fixed pump power at $1\,\mu W$).

As seen from figure 7.2 (a), with a few tens of μW of pump power, an input signal as low as 10nW will generate an idler light with almost 100% efficiency. It is interesting to notice that a saturation effect appears when the pump power reaches certain levels for this parametric generation (In this case, it is between $70 - 80\ \mu W$). In figure 7.2 (a), there is an interesting threshold phenomena with the increase of

signal power and after this threshold, the efficiency of idler generation changes slowly with the increase signal power (In this case, the threshold is about 20nW).

The above calculations give us some hints for realizing parametric oscillation generation in our Rb loaded ARROWs, such as what kind of power schemes are favorable to maximize the idler generation.

Moreover, the intersecting waveguide geometry is perfectly suited to quantum coherence-based nonlinear single-photon generation, because it allows the collection and detection of photons generated in a degenerate parametric process by the solid-core waveguides. In addition, different gases, functional waveguide geometries, and optical elements, such as distributed Bragg reflector (DBR) gratings, can be used on the ARROW platform, and some of the techniques described here may even be applied to nanophotonic structures, such as slot waveguides. All these options will stimulate further developments and new applications for this Rb cell integrated ARROW waveguide.

Appendix A Experimental Operations

A.1 Laser Operations

A.1.1 Vescent laser (trouble shooting)

When power module LED doesn't work:

(1) Fuse broken

On the power supply, first of all, check that if the fuse is blown. First unplug the other modules from the power supply (the external power bridges in the back). Check the fuse inside the power entry module in the back. Take out of the power plug and flip open the side to access the red fuse holder behind it. If it has blown, replace it.

(2) Power supply cable

Another problem can be sagging with the power supply. Check the power cable bringing power to the power supply. If it stops working, replace the power cable.

When laser module LED doesn't work:

(1) Interlocks

Disconnect the laser head from the laser controller. Put a 50-Ohm terminator over the laser to protect it. Disconnect everything from the laser controller except power. With the switch in the down / off position, the current monitor should show ~10mA of current that can be adjusted with the current knob.

Then flip the switch in the up / on position. The green light should be turned on for ~5 sec and then turn off. If the green light turns on for a few seconds, connect a 50-Ohm terminator as the 'laser' input and try again. During this process, if you do not see the green light turn on, there may be a problem with one of the interlocks. Check interlocks as the following instructions:

(a) Key interlock

The back panel key interlock: make sure it is turned on (to horizontal position). Wiggle the key to locate the problem. Also, keylock in the back needs to be turned all the way. It needs to be rotated the full 90 degrees to enable the laser.

(b) BNC interlock

The back panel BNC interlock: make sure it is tightly connected. Wiggle it to locate the problem.

(2) SMA cable/BNC cables

Try using a different SMA/BNC cables to drive the laser and see if that makes a difference or shake the cables and see the problem can be recreated.

(3) Laser Control

Connect the laser control module back to the power module with power bridges. Make sure that the laser current knob is turned up a little on the counting knob (typically more than “3”). If it is too low, there isn't enough current it through the diode for the laser controller to detect that current is flowing, and it activates a safety shut-off.

(4) Ramp Control

Connect the spectroscopy module back to the power module with power bridges. Turn on and off the ramp on the laser servo to check the status of laser operation. The ramp signal from the laser servo going into the laser controller (Servo In) can trigger a safety shut-off switch, which will cause the green status light to turn off and will prevent the laser from turning on.

(5) Internal circuit problem

Measure the testing points on the inside panel (T5, T8, T9)

Probe T5. It should be high if both the key interlock and the remote interlock are set up to allow the laser to turn on.

If T5 is high, probe T9. It should be high when the switch is in the up position and low when the switch is in the down position.

Finally, probe T8 -- it should go high when T9 goes high if (and only if) T5 is also high.

If any of the this doesn't work, it indicates an internal circuit problem which needs further diagnosis with Vescent photonics.

A.1.2 Newfocus laser

Frequency calibration:

Newfocus 795nm laser: 75MHz/0.1V

Newfocus 780nm laser: 70MHz/0.1V

A.2 Coupling lens calculation (fiber coupling, waveguide coupling)

Magnification	NA	f(mm)	Working distance(mm)
5×	0.1	25.4	13.0
10×	0.25	16.5	5.5
20×	0.4	9.0	1.7
40×	0.65	4.5	0.6
60×	0.85	2.9	0.3

Table A.1 Coupling lens calculation

A.3 Temperature calibration of Current control

Current (A)	T (C)
0.2	31.5
0.3	33.6
0.4	35.5
0.5	38.0
0.6	40.7
0.7	43.4
0.8	46.7

0.9	50.4
1.0	54.1
1.1	58.3
1.2	62.6
1.3	67.5
1.4	72.5
1.5	78.6
1.6	84.3
1.7	90.6
1.8	97.7
1.9	104.6
2.0	112.0

Table A.2 Calibration of TEC plate for ARROW chip testing

Current (A)	T (C)
0.2	31.1
0.3	35.9
0.4	43.9
0.5	55.6
0.6	63.7

0.7	71.4
0.8	78.7
0.9	86.4
1.0	93.1
1.1	102.3
1.2	110.6

Table A.3 Calibration of oven box for minicell testing

Appendix B

Compatibility testing of Rubidium with different materials

B.1 Aim

To test the compatibility of different materials with Rubidium

AL3 – Epoxy

AL4 – Gold

AL5 – Chromium

AL6 – Palladium

AL7 – Plexiglass

AL8 - Aluminum

AL9 –Tin

AL10 – Nickel

B.2 Method

laser source: 780nm, testing power = 1.12mW

Three cycles of heating cooling (from 20C to 80C, 10C for each step)

Spectra are recorded at each temperature to extract the atomic density

B.3. Result

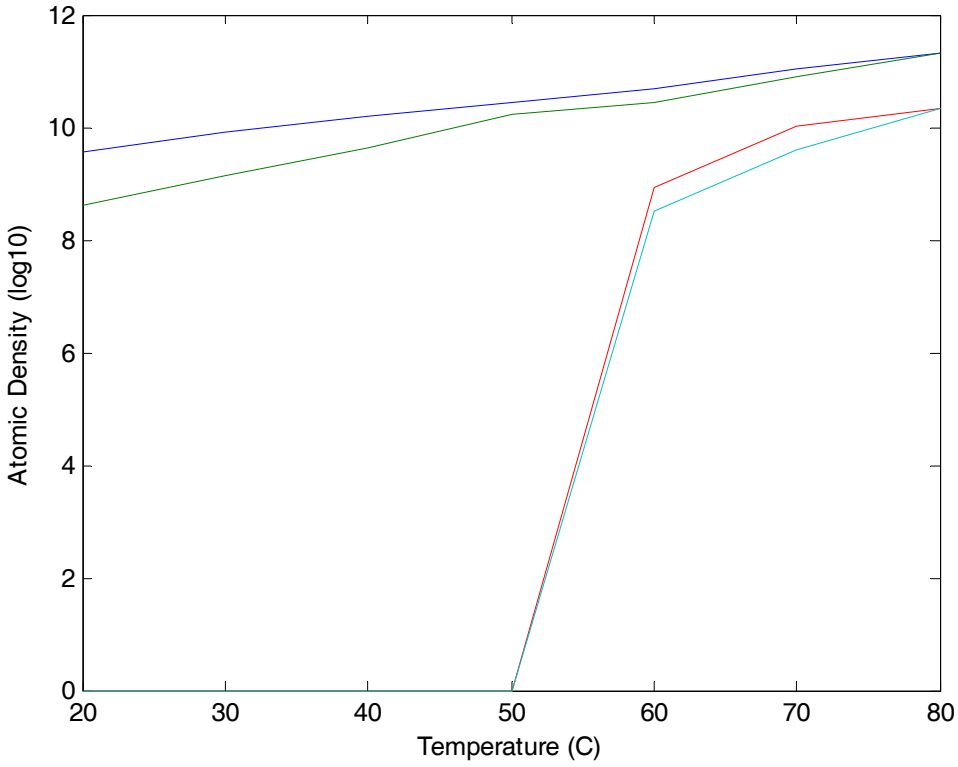

Figure B.1 AL3 – Epoxy (The absorption decreased dramatically after one cycle of heating and cooling, in the second round heating and cooling, absorption signal can only be observed when heated to 60c)

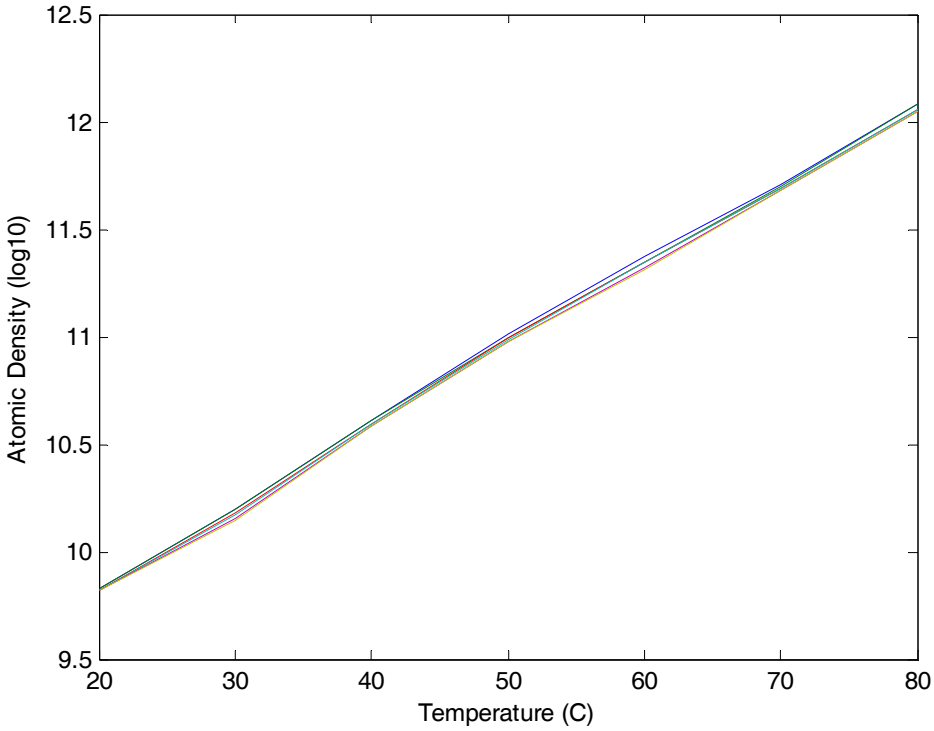

Figure B.2 AL4 – Gold (No degradation. There is less than 5% atomic density variation with three cycles of heating and cooling.)

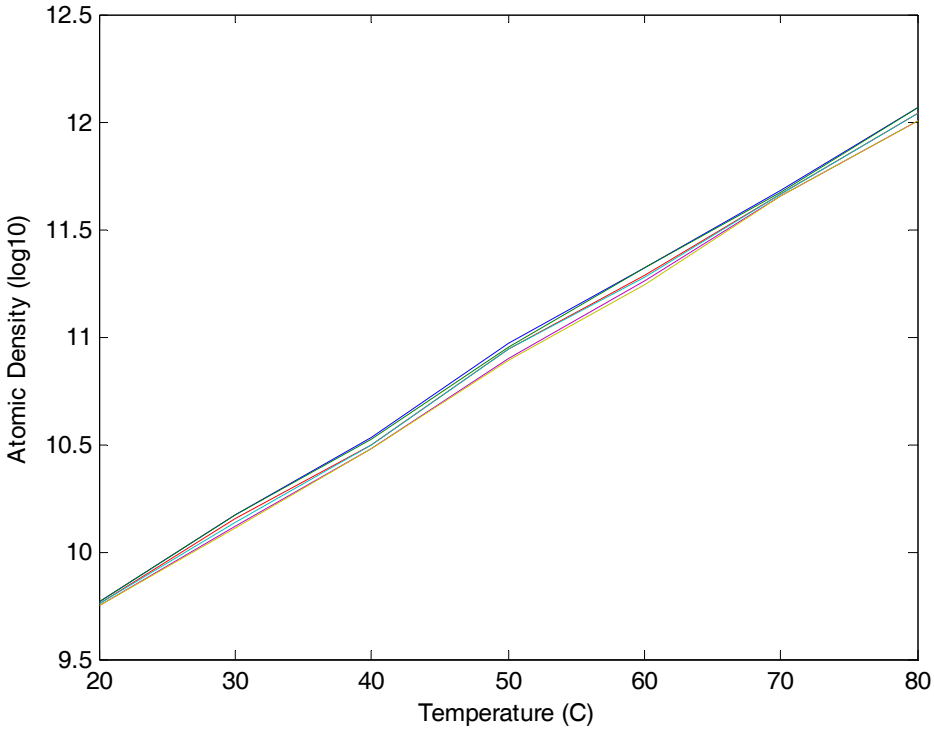

Figure B.3 AL5 – Chromium (No degradation. There is less than 5% atomic density variation with three cycles of heating and cooling.)

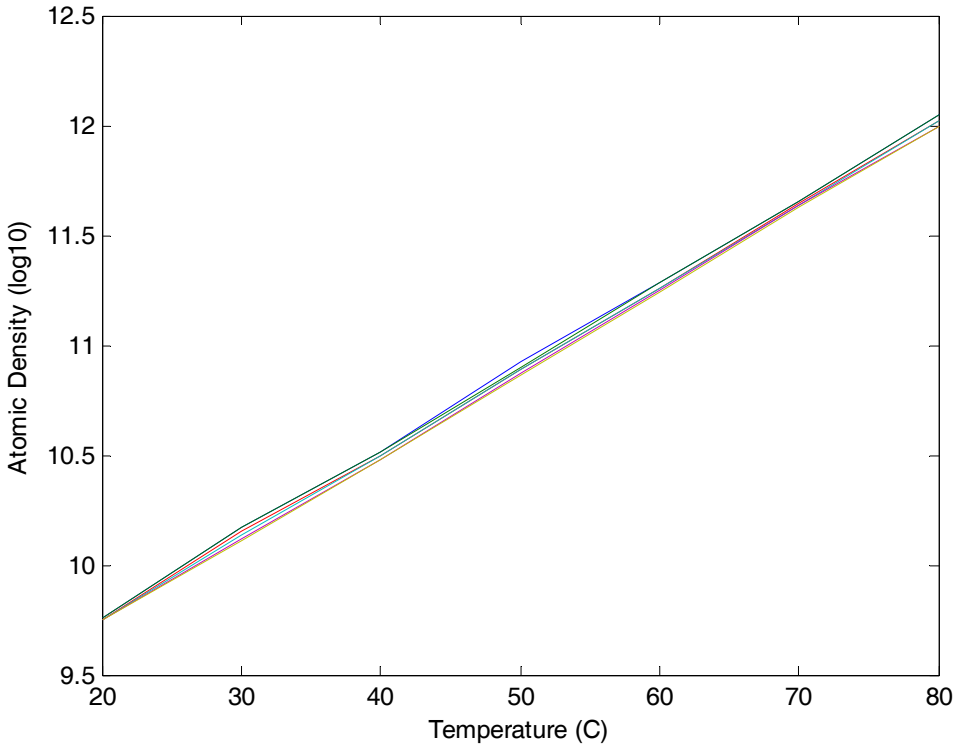

Figure B.4 AL6 – Palladium (No degradation. There is less than 5% atomic density variation with three cycles of heating and cooling.)

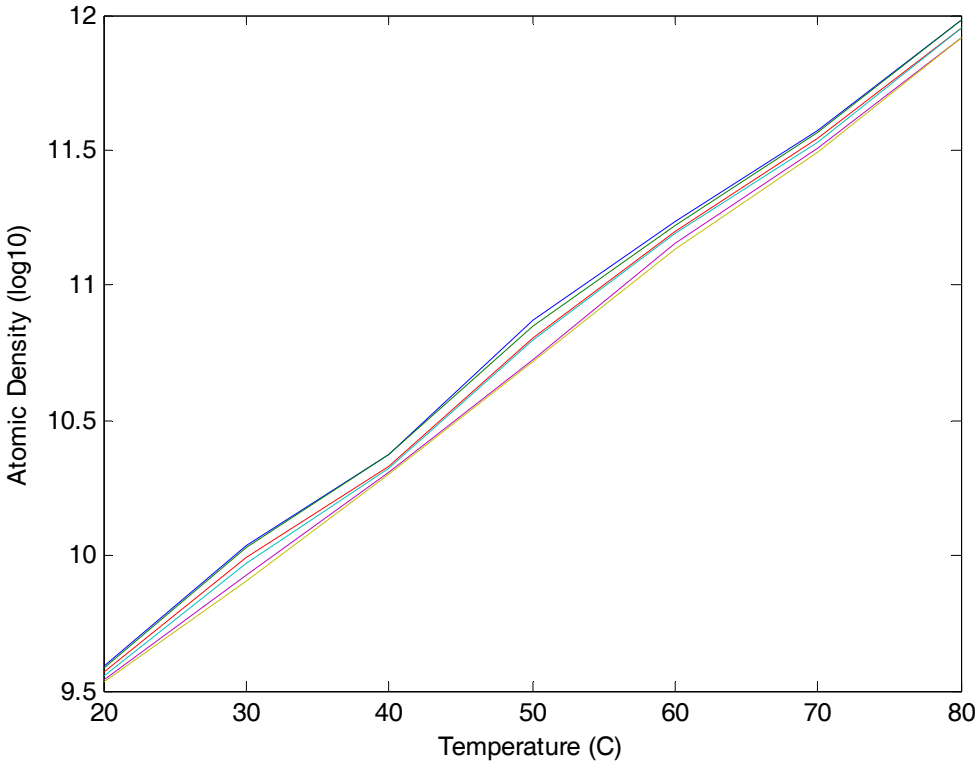

Figure B.5 AL7 – Plexiglass (Some degradation, 85.53% atomic density remains after three cycles of heating and cooling.)

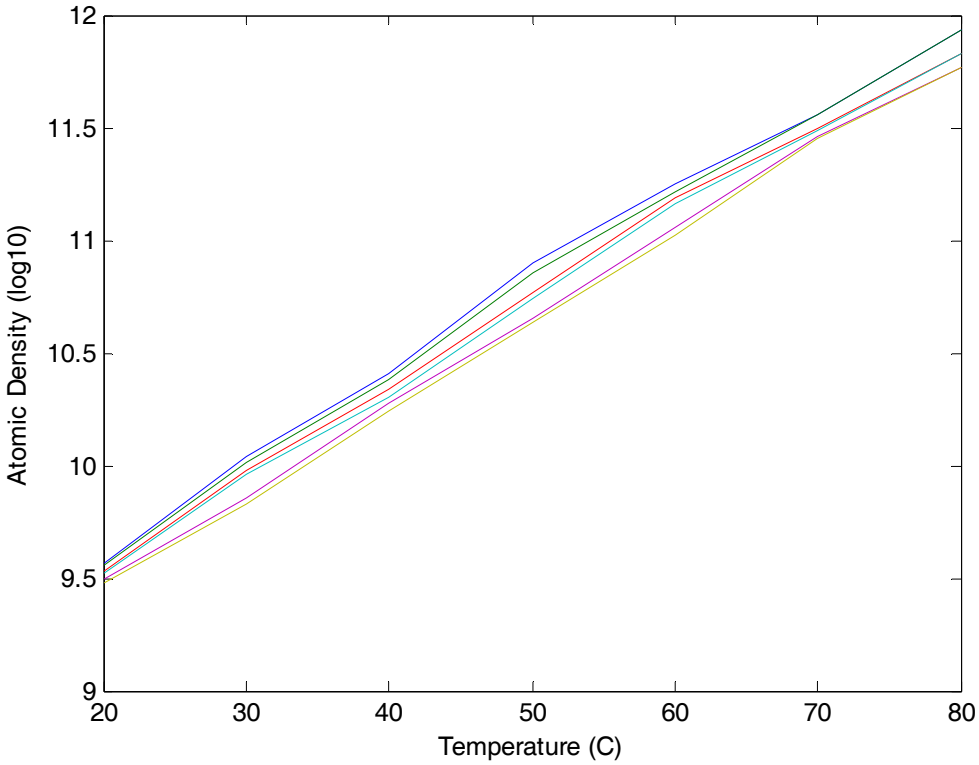

Figure B.6 AL8 - Aluminum (Some degradation, 81.13% atomic density remains after three cycles of heating and cooling.)

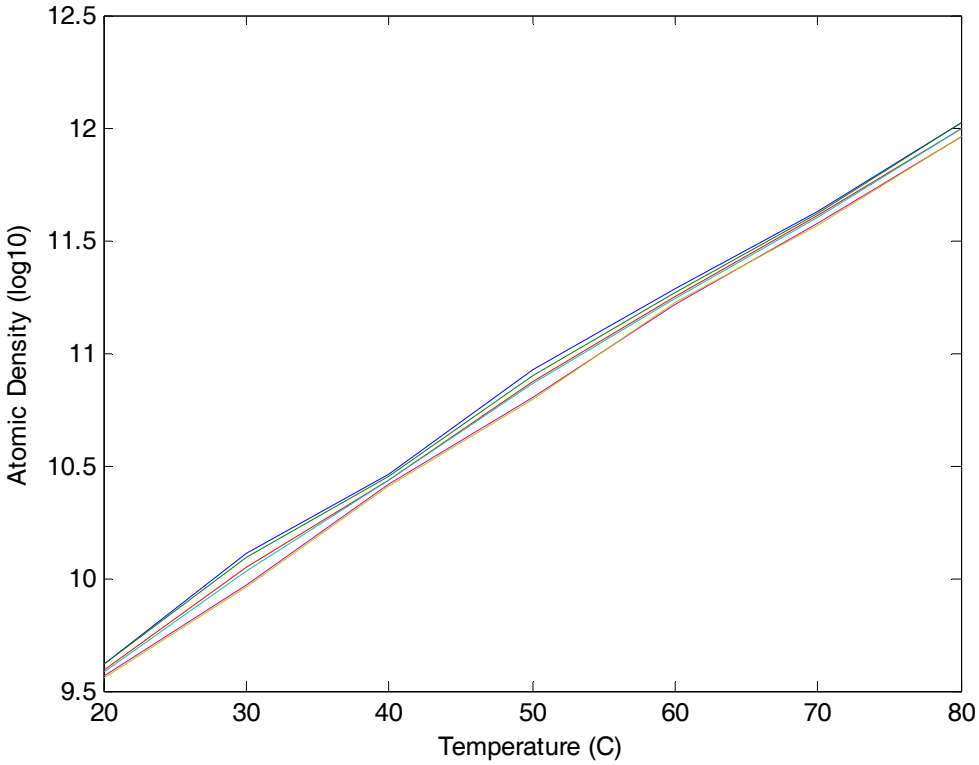

Figure B.7 AL9 –Tin (Some degradation, 85.92% atomic density remains after three cycles of heating and cooling.)

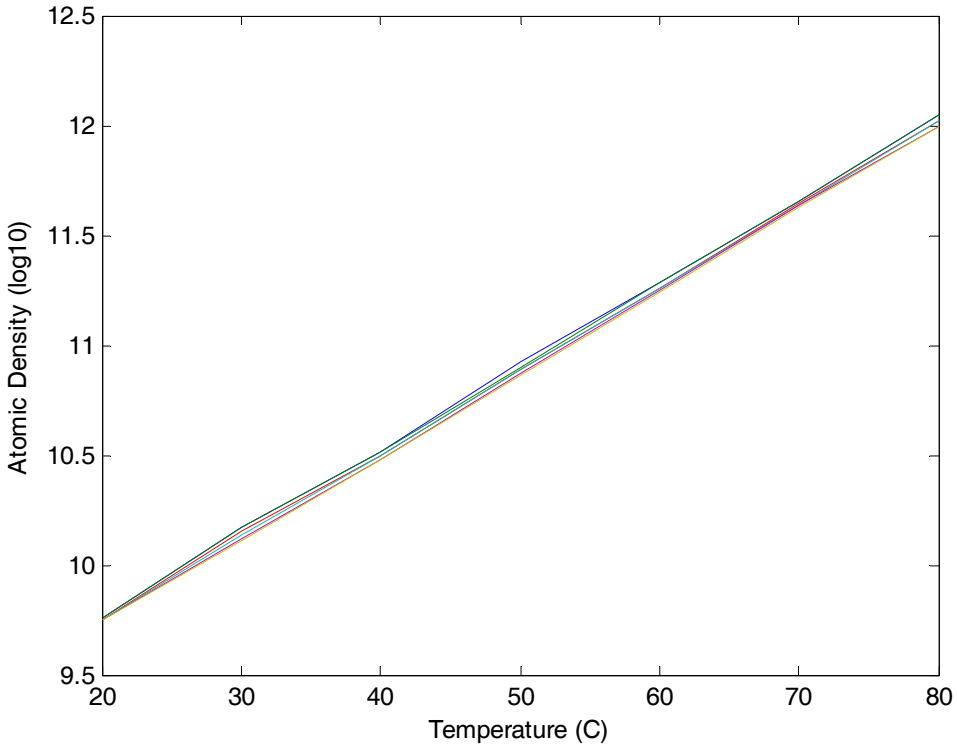

Figure B.8 AL10 - Nickel (No degradation. There is less than 5% atomic density variation with three cycles of heating and cooling.)

Material	Performance
Epoxy	Absorption decreased rapidly after one cycle of heating and cooling. **Large degradation.**
Gold	Less 5% atomic density decrease. **No degradation.**
Chromium	Less 5% atomic density decrease.

	No degradation.
Palladium	Less 5% atomic density decrease. **No degradation.**
Plexiglass	15% atomic density decrease. **Some degradation**
Aluminum	19% atomic density decrease **Some degradation**
Tin	15% atomic density decrease **Some degradation**
Nickel	Less 5% atomic density decrease. **No degradation**

Table B.1 Summary of material compatibility testing

Bibliography

1.R. T. Chen and G. F. Lipscomb, Eds., “WDM and Photonic Switching De-vices for Network Applications,” Proceedings of SPIE, vol. 3949, (2000).

2. C. Dragonne, “An N × N optical multiplexer using a planar arrangement of two star couplers,” IEEE Photon. Technol. Lett., 3, 812-815, (1991).

3. M. Kawachi, “Silica waveguide on silicon and their application to integrated-optic components,” Opt. Quantum Electron., 22, 391-416, (1990).

4. M. Kawachi, “Silica waveguide on silicon and their application to integrated-optic components,” Opt. Quantum Electron., 22, 391-416, (1990).

5. H. Ehler, M. Biletzke, B. Kuhlow, G. Przyrembel and U. H. P. Fischer, Optical Fiber Technol., 6, 344, (2000).

6. M. Saruwatari and K. Nawate, “Semiconductor laser to single mode fiber coupler,” Appl. Opt., 18, 1847, (1979).

7. M. Fok, Y. Deng, and P. Prucnal, "Asynchronous detection of optical code division multiple access signals using a bandwidth-efficient and wavelength-aware receiver," Opt. Lett. 35, 1097-1099 (2010).

8. P. Vorreau, S. Sygletos, F. Parmigiani, D. Hillerkuss, R. Bonk, P. Petropoulos, D. Richardson, G. Zarris, D. Simeonidou, D. Klonidis, I. Tomkos, R. Weerasuriya, S. Ibrahim, A. Ellis, D. Cotter, R. Morais, P. Monteiro, S. Ben Ezra, S. Tsadka, W. Freude, and J. Leuthold, "Optical grooming switch with regenerative functionality for transparent interconnection of networks," Opt. Express 17, 15173-15185 (2009).

9. D. Wang, T. Cheng, Y. Yeo, J. Liu, Z. Xu, Y. Wang, and G. Xiao, "All-optical modulation-transparent wavelength multicasting in a highly nonlinear fiber Sagnac loop mirror," Opt. Express 18, 10343-10353 (2010).

10. J. Singh, "Performance of asynchronous fiber-optic code division multiple access system based on three-dimensional wavelength/time/space codes and its link analysis," Appl. Opt. 49, 1355-1363 (2010).

11. G. Gao, J. Zhang, X. Cao, L. Wang, and W. Gu, "Dynamic quality of transmission optimization and global impairments control in reconfigurable transparent WDM networks: schemes and demonstrations," Chin. Opt. Lett. 8, 270-274 (2010).

12. W. Yang, S. Paredes, H. Schriemer, and T. Hall, "Protection of Dynamic and Flexible Bandwidth on Demand in Metro Agile All-Optical Ring Networks," J. Opt. Commun. Netw. 1, A160-A169 (2009).

13. R. Casellas, R. Martínez, R. Muñoz, and S. Gunreben, "Enhanced Backwards Recursive Path Computation for Multi-area Wavelength Switched Optical Networks Under Wavelength Continuity Constraint," J. Opt. Commun. Netw. 1, A180-A193 (2009).

14. L. Peng and Y. Kim, "Investigation of the Design of MAC Protocols for TT-TR-Based WDM Burst-Switched Ring Networks," J. Opt. Commun. Netw. 1, A25-A34 (2009).

15. B. Bathula and J. Elmirghani, "Constraint-Based Anycasting Over Optical Burst Switched Networks," J. Opt. Commun. Netw. 1, A35-A43 (2009).

16. A. Cianfrani, V. Eramo, A. Germoni, C. Raffaelli, and M. Savi, "Loss Analysis of Multiple Service Classes in Shared-per-Wavelength Optical Packet Switches," J. Opt. Commun. Netw. 1, A69-A80 (2009).

17. S. Khaleghi, S. Khaleghi, and K. Jamshidi, "Performance Analysis of a Spectrally Phase-Encoded Optical Code Division Multiple Access Packet Network," J. Opt. Commun. Netw. 1, 213-221 (2009).

18. D. Barth, P. Berthomé, D. Chiaroni, J. Fourneau, C. Laforest, and S. Vial, "Mixing Convergence and Deflection Strategies for Packet Routing in All-Optical Networks," J. Opt. Commun. Netw. 1, 222-234 (2009).

19. M. Rodelgo-Lacruz, C. López-Bravo, F. González-Castaño, F. Gil-Castiñeira, and H. Chao, "Not-Aligned Optical Cell Switching Paradigm," J. Opt. Commun. Netw. 1, B70-B80 (2009).

20. L. Meng, C. Assi, M. Maier, and A. Dhaini, "Resource Management in STARGATE-Based Ethernet Passive Optical Networks (SG-EPONs)," J. Opt. Commun. Netw. 1, 279-293 (2009).

21. H. Kankaya and N. Akar, "Exact Analysis of Single-Wavelength Optical Buffers With Feedback Markov Fluid Queues," J. Opt. Commun. Netw. 1, 530-542 (2009).

22. Y. Pointurier, M. Brandt-Pearce, and S. Subramaniam, "Analysis of Blocking Probability in Noise- and Cross-Talk-Impaired All-Optical Networks," J. Opt. Commun. Netw. 1, 543-554 (2009).

23. M. Murakami, T. Seki, and K. Oda, "Optical Signal Channel Power Stability in a Transparent Optical Network Using Large-Scale Photonic Cross Connects and Automatic Gain Control EDFAs," J. Opt. Commun. Netw. 2, 20-27 (2010).

24. I. Moraes and O. Duarte, "Using the Network Load for Admission Control in OBS Networks: A Multilink Approach," J. Opt. Commun. Netw. 2, 137-147 (2010).

25. Y. Deng, Z. Wang, K. Kravtsov, J. Chang, C. Hartzell, M. Fok, and P. Prucnal, "Demonstration and Analysis of Asynchronous and Survivable Optical CDMA Ring Networks," J. Opt. Commun. Netw. 2, 159-165 (2010).

26. H. Schmidt and A. Imamoglu: "Giant Kerr nonlinearities using electromagnetically induced transparency", Optics Letters, 21, 1936-38, (1996).

27. V. Bali, D. A. Braje, P. Kolchin, G. Y. Yin, and S. E. Harris, “Generation of Paired Photons with Controllable Waveforms”, Phys.Rev. Lett. 94, 183601 (2005).

28. M S Bigelow et al. “Observation of Ultraslow Light Propagation in a Ruby Crystal at Room Temperature”Phys. Rev. Lett. 90 113903 (2003).

29. Seong-Min Ma, Hua Xu, and Byoung Seung Ham, "Electromagnetically-induced transparency and slow light in GaAs/AlGaAs multiple quantum wells in a transient regime," Opt. Express 17, 14902-14908 (2009)

30. F. Benabid, P. Light, F. Couny, and P. Russell, "Electromagnetically-induced transparency grid in acetylene-filled hollow-core PCF," Opt. Express 13, 5694-5703 (2005)

31. "Experimental Demonstration of Electromagnetic Induced Transparency and Dispersion Effects in Cs Atom Vapour," J.X. Zhang, R.F. Dong, H. Chang, C.D. Xie, K.C. Peng, and Min Xiao, Chin. Phys. Lett. 18, 1586 (2001).

33 8L. Liew, S. Knappe, J. Moreland, H. Robinson, L. Hollberg, and J. Kitching, Appl. Phys. Lett. 84, 2694 (2004).

34 M. M. Kash, V. Sautenkov, A. Zibrov, L. Hollberg, G. Welch, M. Lukin, Y. Rostovtsev, and M. O. Scully, Phys. Rev. Lett. 82, 5229 (1999).

35.D. F. Philips, A. Fleischhauer, A. Mair, R. Walsworth, and M. D. Lukin, Phys. Rev. Lett. 86, 783 (2001).

36. Yong-qing Li and Min Xiao, "Enhancement of nondegenerate four-wave mixing based on electromagnetically induced transparency in rubidium atoms," Opt. Lett. 21,

1064-1066 (1996)

37. V. Bali , D. A. Braje, P. Kolchin, G. Y. Yin, and S. E. Harris, “Generation of Paired Photons with Controllable Waveforms”, Phys.Rev. Lett., 94, 183601 (2005).

38. Xudong Yang, Shujing Li, Chunhong Zhang, Hai Wang，”Enhanced cross-Kerr nonlinearity via electromagnetically induced transparency in a four-level tripod atomic system,” Journal of the Optical Society of America B 26, 1423 (2009)

39. P. Yeh, A. Yariv, and C-S. Hong, J. Opt. Soc. Am., 67, 423, (1977).

40. Y. Fink, J.N. Winn, S. Fan, C. Chen, J.Michel, J.D.Joannopoulos, and E.L.Thomas, Science, 282, 1679, (1998).

41. P.Russell, Laser Focus World, 38, 77, (2002).

42. G.R. Hadley, J.G. Fleming, and S-Y. Liu, Opt. Lett., 29, 809, (2004).

43. J.N. Winn, Y. Fink, S. Fan, and J.D. Joannopoulos, Opt. Lett., 23, 1573, (1998).

44. “Active control of slow light on a chip with photonic crystal waveguides”, Yu. A. Vlasov, M.O'Boyle, H. Hamann and S. J. McNab. Nature November 3 (2005)

45. M.A. Duguay, Y. Kokubun, T.L. Koch, and L. Pfeiffer,. Appl. Phys. Lett. 49, 13 (1986)

46. Pochi Yeh, Optical Waves in Layered Media, Chapter 4,5,6 1 Wiley (1988).

47. J.L Archambault, R.J.Black, Journal of Lightwave technology, vol 11, No.3 March (1993).

48. Y. Okamura,et al., “A novel technique to measure the propagation loss of integrated optical waveguides” Appl. Opt., 22, 3892-3894, (1983).

49. M.D. Himel and U.J. Gilbson, "Measurement of Planar Wave- guide Losses Using a Coherent Fiber Bundle," Appl. Opt., vol. 25, 4413-4416, (1986).

50. Yan Zhou, et al., “Low-loss measurement in partially buried opticalwaveguideson glass with a plastic prism”Appl. Opt., 36, 5089-5090, (1997).

51. Roberta Ramponi, Roberto Osellame, and Marco Marangoni, “Two straightforward methods for the measurement of optical losses in planar waveguides”Review of Scientific Instruments, 73, 1117-1120, (2002).

52. A. Imamoglu and S.E. Harris, “Lasers without inversion: interference of dressed lifetime-broadened states”, Opt. Lett., 14, 1344, (1989).

53. S.E. Harris, J.E. Field, A. Imamoglu, “Nonlinear optical processes using electromagnetically induced transparency”, Phys. Rev. Lett., 64, 1107 (1990).

54. B.S. Ham, M.S. Shariar, and P.R. Hemmer, Opt. Lett., 22, 1138, (1997).

55. M.D. Lukin, P.R. Hemmer, M. Loffler, and M.O. Scully, “Resonant enhancement of parametric processes via radiative interference and induced coherence”, Phys. Rev. Lett., 81, 2675, (1998).

56. A.Zibrov, M.D. Lukin, and M.O. Scully, “Nondegenerate parametric self-oscillation via multiwave mixing in coherent atomic media”, Phys. Rev. Lett., 83, 4049, (1999).

57. M.D. Eisaman, L. Childress, A. Andre, F. Massou, A.Zibrov, and M.D. Lukin, “Shaping quantum pulses of light via coherent atomic memory”, Phys. Rev. Lett., 93, 233602, (2004).

58. S. Knappe, V. Gerginov, P. D. D. Schwindt, V. Shah, H. G. Robinson, L. Hollberg, J. Kitching. “Atomic vapor cells for chip-scale atomic clocks with improved long-term frequency stability,” Opt. Lett., 30, 2351 (2005).

59. L. Liew, S. Knappe, J. Moreland, H. Robinson, L. Holberg, and J. Kitching, “Microfabricated alkali atom vapor cells,” Appl. Phys. Lett., 84, 2694 (2004).

60. S. Knappe, H. G. Robinson, and L. Hollberg, “Microfabricated saturated absorption laser spectrometer,” Optics Express 15, 6293 (2007).

61. F. Benabid, G. Antonopoulos, J. C. Knight, P. St. J. Russell, “Stokes amplification regimes in quasi-cw pumped hydrogen-filled hollow-core photonic crystal fiber,” Phys. Rev. Lett., 95, 2139031 (2005).

62. S. Ghosh, A. R. Bhagwat, C. K. Renshaw, S. Goh, A. L. Gaeta, B. J. Kirby, “Low-Light-Level Optical Interactions with Rubidium Vapor in a Photonic Band-Gap Fiber,” Phys. Rev. Lett. 97, 023603, (2006).

63. R. Thapa, K. Knabe, M. Faheem, A. Naweed, O. Weaver, and K. L. Corwin, “Saturated absorption spectroscopy of acetylene gas inside large-core photonic bandgap fiber,” Optics Letters 31, 2489, (2006).

64. P. S. Light, F. Benabid, F. Couny, M. Maric, and A. N. Luiten, “Electromagnetically

induced transparency in Rbfilled coated hollow-core photonic crystal fiber," Optics Letters 32, 1323, (2007).

65. S. Ghosh, A. R. Bhagwat, C. K. Renshaw, S. Goh, A. L. Gaeta, B. J. Kirby, "Low-Light-Level Optical Interactions with Rubidium Vapor in a Photonic Band-Gap Fiber," Phys. Rev. Lett. 97, 023603, (2006).

66. P. S. Light, F. Benabid, F. Couny, M. Maric, and A. N. Luiten, "Electromagnetically induced transparency in Rbfilled coated hollow-core photonic crystal fiber," Optics Letters 32, 1323, (2007).

67. A.R. Hawkins, J.F. Hulbert, B.T. Carroll, B. Wu, and H. Schmidt, "Fabrication methods for compact atomic spectroscopy", Proc. SPIE 6898, 689817 (2008).

68. Y. Q. Li and Min Xiao, Phys. Rev. A 51, R2703 (1995).

69. Slepkov, Aaron D; Bhagwat, Amar R; Venkataraman, Vivek; Londero, Pablo; Gaeta, Alexander L, Generation of large alkali vapor densities inside bare hollow-core photonic band-gap fibers, Optics Express,16,18976 (2008).

70. Ghosh, Saikat and Bhagwat, Amar R. and Renshaw, C. Kyle and Goh, Shireen and Gaeta, Alexander L. and Kirby, Brian, Low-Light-Level Optical Interactions with Rubidium Vapor in a Photonic Band-Gap Fiber, PRL 97,023603 (2006).

71. Alexandrov, E. B. and Balabas, M. V. and Budker, D. and English, D. and Kimball, D. F. and Li, C.-H. and Yashchu, Light-induced desorption of alkali-metal atoms from paraffin coating, PRA 66,042903 (2002).

72. Braje, Danielle A. and Balifmmode Vlatko and Goda, Sunil and Yin, G. Y. and Harris, Frequency Mixing Using Electromagnetically Induced Transparency in Cold Atoms PRL 93,183601 (2004).

73. L. V. Hau, S. E. Harris, Z. Dutton, and C. H. Behroozi, "Light speed reduction to 17 metres per second in an ultracold atomic gas," Nature 397, 594–596 (1999).

74. D. F. Philips, A. Fleischhauer, A. Mair, R. L. Walsworth, and M. D. Lukin, "Storage of light in atomic vapor," Phys. Rev. Lett. 86, 783–786 (2001).

75. J. R. Pierce, TravelingWave Tubes, Van Nostrand, (1950).

76. S. L. McCall and E. L. Hahn, "Self-induced transparency by pulsed coherent light," Phys. Rev. Lett. 18, 908–911 (1967).

77. D. Grischkowsky, "Adiabatic following and slow optical pulse propagation in

rubidium vapor," Phys. Rev. A 7, 2096 (1973).

78. S. E. Harris, J. E. Field, and A. Imamoglu, "Nonlinear optics using electromagnetically induced transparency," Phys. Rev. Lett. 64, 1107–1110 (1990).

79. M. M. Kash, V. A. Sautenkov, A. S. Zibrov, L. Hollberg, G. R.Welch, M. D. Lukin, Y. Rostovtsev, E. S. Fry, and M. O. Scully, "Ultraslow group velocity and enhanced nonlinear optical effects in a coherently driven hot atomic gas," Phys. Rev. Lett. 82, 5229–5232 (1999).

80. R. M. Camacho, M. V. Pack, and J. C. Howell, "Low-distortion slow light using two absorption resonances," Phys. Rev. A 73, 063812 (2006).

81. M. S. Bigelow, N. N. Lepeshkin, and R.W. Boyd, "Observation of ultraslow light propagation in a ruby crystal at room temperature," Phys. Rev. Lett. 90, 113903 (2003).

82. M. S. Bigelow, N. N. Lepeshkin, and R. W. Boyd, "Superluminal and slow light propagation in a room-temperature solid," Science 301, 200–202 (2003).

83. R. M. Camacho, M. V. Pack, and J. C. Howell, "Slow light with large fractional delays by spectral hole-burning in rubidium vapor," Phys. Rev. A 74, 033801 (2006).

84. K-J. Boller, A. Imamoglu, and S. E. Harris, "Observation of EIT," Phys. Rev. Lett. 66, 2593–2596 (1991).

85. S. E. Harris, J. E. Field, and A. Kasapi, "Dispersive properties of EIT," Phys. Rev. A. 46, R39–R32 (1992).

86. A. Kasapi, M. Jain, G. Y. Jin, and S. E. Harris, "EIT: propagation dynamics," Phys. Rev. Lett. 74, 2447–2450 (1995).

87. N. M. Litchinitser, B. J. Eggleton, and G. P. Agrawal, "Dispersion of cascaded fiber gratings in WDM lightwave systems," J. Lightwave Technol. 16, 1523–1529 (1999).

88. S.Wang, H. Erlig, H. R. Fetterman, E. Yablonovitch, V. Grubsky, D. S. Starodubov, and Feinberg, "Group velocity dispersion cancellation and additive group delays by cascaded fiber Bragg gratings in transmission," IEEE Microw. Guid.Wave Lett. 8, 327–329 (1998).

89. J. B. Khurgin, J. U. Kang, and Y. J. Ding, "Ultrabroad-bandwidth electrooptic modulator based on a cascaded Bragg grating," Opt. Lett. 25, 70–72 (2000).

90. R. W. Boyd, Nonlinear Optics, 2nd ed. (2003).

91. K. Y. Song, M. G. Herráez, and L. Thevenaz, “Observation of pulse delaying and advancementin optical fibers using stimulated Brillouin scattering,” Opt. Express 13, 82–88 (2005).

92. Y. Okawachi, M. S. Bigelow, J. E. Sharping, Z. Zhu, A. Schweinsberg, D. J. Gauthier, R. W. oyd, and A. L. Gaeta, “Tunable all-optical delays via Brillouin slow light in an optical fiber,” Phys. Rev. Lett. 94, 153902 (2005).

93. M. D. Stenner, M. A. Neifeld, Z. Zhu, A. M. C. Dawes, and D. J. Gauthier, “Distortion management in slow-light pulse delay,” Opt. Express 13, 9995–10002 (2005).

94. A. Minardo, R. Bernini, and L. Zeni, “Low distortion Brillouin slow light in optical fibers using AM modulation,” Opt. Express 14, 5866–5876 (2006).

95. Z. Shi, R. Pant, Z. Zhu, M. D. Stenner, M. A. Neifeld, D. J. Gauthier, and R. W. Boyd, “Design of a tunable time-delay element using multiple gain lines for increased fractional delay with high data fidelity,” Opt. Lett. 32, 1986–1988 (2007).

96. K. Y. Song, K. S. Abedin, K. Hotate, M. G. Herraez, and L. Thevenaz, “Highly efficient Brillouin slow and fast light using As2Se3 chalcogenide fiber,” Opt. Express 14, 5860–5865 (2006).

97. A. Zadok, A. Eyal, and M. Tur, “Extended delay of broadband signals in stimulated rillouin cattering slow light using synthesized pump chirp,” Opt. Express 14, 8498–8505 (2006).

98. T. Schneider, R. Henker, K. U. Lauterbach, and M. Junker, “Comparison of delay enhancement mechanisms for SBS-based slow light systems,” Opt. Express 15, 9606–9613 (2007).

99. M. G. Herraez, K. Y. Song, and L. Thevenaz, “Arbitrary-bandwidth Brillouin slow light in optical fibers,” Opt. Express 14, 1395–1400 (2006).

100. Z. Zhu, A. M. C. Dawes, D. J. Gauthier, L. Zhang, and A. E. Willner, “Broadband SBS slow light in an optical fiber,” J. Lightwave Technol. 25, 201–206 (2007).

101. T. Schneider, M. Junker, and K.-U. Lauterbach, “Potential ultra wide slowlight bandwidth enhancement,” Opt. Express 14, 11082–11087 (2006).

102. K. Y. Song and K. Hotate, “25 GHz bandwidth Brillouin slow light in optical fibers,” Opt. Lett. 32, 217–219 (2007).

103. L. Yi, L. Zhan, W. Hu, and Y. Xia, “Delay of broadband signals using slow light in stimulated Brillouin scattering with phase-modulated pump,” IEEE Photon. Technol. Lett. 19, 619–621 (2007).

104. L. Thevenaz, “Slow light in optical fibers,” Nat. Photonics 2, 474–481 (2008).

105. J. E. Sharping, Y. Okawachi, and A. L. Gaeta, “Wide bandwidth slow light using a Raman fiber amplifier,” Opt. Express 13, 6092–6098 (2005).

106. Y. Okawachi, M. A. Foster, J. E. Sharping, A. L. Gaeta, Q. Xu, and M. Lipson, “All-optical slow-light on a photonic chip,” Opt. Express 14, 2317– 2322 (2006).

107. A. Schweinsberg, N. N. Lepeshkin, M. S. Bigelow, R. W. Boyd, and S. Jarabo, “Observation of superluminal and slow light propagation in erbiumdoped optical fiber,” Europhys. Lett. 73, 218–224 (2006).

108. H. Shin, A. Schweinsberg, G. Gehring, K. Schwertz, H. J. Chang, R. W. Boyd, Q.-H. Park, and D. J. Gauthier, “Reducing pulse distortion in fastlight pulse propagation through an erbium-doped fiber amplifier,” Opt. Lett. 32, 906–908 (2007).

109. D. Dahan and G. Eisenstein, “Tunable all optical delay via slow and fast light propagation in a Raman assisted fiber optical parametric amplifier: a route to all optical buffering,” Opt. Express 13, 6234–6249 (2005).

110. S. Lee, K. Lee, J. Ahn, Reversed peaks of saturated absorption spectra of atomic rubidium, Japanese Journal of Applied Physics, 48 032301, (2009)

111. Andrew M. C. Dawes, Lucas Illing, Susan M. Clark, Daniel J. Gauthier, All-Optical Switching in Rubidium Vapor, Science, Vol. 308. no. 5722, pp. 672 – 674, (2005)

112. S. Sensam, Irfan Ali-Khan, G.Y. Yin, S.E. Harris, Resonant Sum Frequency Generation with Time-Energy Entagled Photons. Phys. Rev. Lett. 102, 053602, (2009).

113. S.E. Harris, Y. Yamamoto, Photon Switching by Quantum Interference, Phys. Rev. Lett. 81, 3611-3614, (1998).

114. Doppler Free Spectroscopy, lab handout, MIT (2000). Website: http://web.mit.edu/afs/athena/course/8/8.13/JLExperiments/JLExp_48.pdf

115. D. Yin, J.P. Barber, A.R. Hawkins, and H. Schmidt, "Integrated ARROW waveguides with hollow cores", Optics Express, 12, 2710, (2004).

116 J. B. Khurgin “Expanding the bandwidth of slow-light photonic devices based on coupled resonators” Opt. Lett. Vol.30. No.5, p146 (2005).

[117] A. Ashkin, "Trapping of Atoms by Resonance Radiation Pressure," Phys. Rev. Lett. 40, 729 (1978).

[118] S. Chu et al., "Three-Dimensional Viscous Confinement and Cooling of Atoms by Resonance Radiation Pressure," Phys. Rev. Lett. 55, 48 (1985).

[119] W. Yang, D.B. Conkey, B. Wu, D. Yin, A.R. Hawkins, and H. Schmidt, "Atomic spectroscopy on a chip", Nature Photonics 1, 331 (2007).

[120] B. Wu, J.F. Hulbert, K. Hurd, E.J. Lunt, A.R. Hawkins, and H. Schmidt, “Slow light on a chip via atomic quantum state control”, to appear in Nature Photonics (2010).

[121] http://mxp.physics.umn.edu/s05/Projects/S05Rb/theory.htm.

ON-CHIP ATOMIC SPECTROSCOPY

by

Donald B. Conkey

A thesis submitted to the faculty of

Brigham Young University

in partial fulfillment of the requirements for the degree of

Master of Science

Department of Electrical and Computer Engineering

Brigham Young University

April 2007

BRIGHAM YOUNG UNIVERSITY

GRADUATE COMMITTEE APPROVAL

of a thesis submitted by

Donald B. Conkey

This thesis has been read by each member of the following graduate committee and by majority vote has been found to be satisfactory.

Date	Aaron R. Hawkins, Chair
Date	Stephen M. Schultz
Date	Richard. H. Selfridge

BRIGHAM YOUNG UNIVERSITY

As chair of the candidate's graduate committee, I have read the thesis of Donald B. Conkey in its final form and have found that (1) its format, citations, and bibliographical style are consistent and acceptable and fulfill university and department style requirements; (2) its illustrative materials including figures, tables, and charts are in place; and (3) the final manuscript is satisfactory to the graduate committee and is ready for submission to the university library.

Date	Aaron R. Hawkins Chair, Graduate Committee

Accepted for the Department

Date	Michael J. Wirthlin Graduate Coordinator

Accepted for the College

Date	Alan R. Parkinson Dean, Ira A. Fulton College of Engineering and Technology

ABSTRACT

ON-CHIP ATOMIC SPECTROSCOPY

Donald B. Conkey

Department of Electrical and Computer Engineering

Master of Science

This thesis presents the integration of atomic vapor cells with anti-resonant reflecting optical waveguides (ARROWs) fabricated on silicon chips. These potentially provide a compact platform for a number of optical applications, including the study of quantum coherence effects such as electromagnetically induced transparency and single-photon nonlinearities, as well as frequency stabilization standards. The use of hollow waveguides allows for light propagation in low index (vapor) media with compact mode areas. ARROWs make particularly attractive waveguides for this purpose because they can be interfaced with solid core waveguides, microfabricated on a planar substrate, and are effectively single mode. ARROW fabrication utilizes an acid-removed sacrificial core surrounded by alternating plasma deposited dielectric layers, which act as Fabry-Perot reflectors.

To demonstrate the effectiveness of the ARROW as a vapor cell, a platform consisting of solid and hollow core waveguides integrated with rubidium vapor cells was developed. A variety of sealing techniques were tested for vapor cell integration with the ARROW chip and for compatibility with rubidium. Rubidium was used because it is of particular interest for studying quantum coherence effects. Liquefied rubidium was transferred from a bulk supply into an on-chip vapor cell in an anaerobic atmosphere glovebox. Optical absorption measurements confirmed the presence of rubidium vapor within the hollow waveguide platform. Further analysis of the measurements revealed high optical density of rubidium atoms in the hollow core. Saturated absorption spectroscopy measurements verified that the on-chip integrated vapor cell was suitable for common precision spectroscopy applications.

ACKNOWLEDGMENTS

I am grateful to the individuals who have supported me throughout the preparation of this thesis. Foremost I would like to thank Dr. Hawkins for providing me with this research opportunity and for continual support throughout my undergraduate and graduate years. I would also like to thank John Barber, who trained me in many microfabrication techniques essential to the fabrication of ARROWs. Thanks to our collaborators at the University of California at Santa Cruz, Dr. Schmidt, Wenge Yang, and Bin Wu, who have provided excellent optical measurements, device characterizations and insights. Special thanks to John Hulbert and Becky Brenning for aiding me with the tedious testing and fabrication of vapor cells. I am indebted to Evan Lunt and Brian Phillips who have helped me with the ARROW fabrication process and have finished devices for me when I was not physically able. I would especially like to thank my best friend and wife, Emily, for all the love and encouragement she has given me.

TABLE OF CONTENTS

1 Introduction 1

1.1 Overview 1

1.2 Contributions 3

2 Atomic Spectroscopy 5

2.1.1 Absorption Spectroscopy 5

2.1.2 Atomic Energy Level Splitting 7

2.1.3 Rubidium Energy Structure 9

2.1.4 Saturated Absorption Spectroscopy 11

2.2 Atomic Vapor Cells 13

2.3 Vapor Cell Integration Advantages 14

2.3.1 NIST Reference Cell 16

2.3.2 Photonic Band-gap Fiber 18

3 ARROWs 21

3.1 Principle 21

3.2 Fabrication 22

3.3 Variations in Design 26

3.4 ARROWs for Vapor Cell Integration 27

4 Vapor Cell Integration with ARROW 31

4.1 ARROW Vapor Cell Platform 31

4.2 Vapor Cell Attachment 32

4.3 Leak Rates for the Vapor Cells 32
4.4 Rubidium Incorporation into Vapor Cell 35
4.5 Self Assembling Monolayer Coating 37
5 Optical Measurements 41
5.1 Vapor Cell 41
5.2 Vapor Through Channel 43
5.3 Absorption Spectroscopy in ARROW 44
5.4 Temperature Dependence in ARROW 46
5.5 Detection of 90 Degree Scattering in ARROW 48
5.6 Saturation Absorption Spectroscopy in ARROW 50
6 Conclusions 53
6.1 Summary 53
6.2 Future Work 53
References 55
APPENDIX A Process Flow 61
APPENDIX B ARROW Designs 65
APPENDIX C Publications 69

LIST OF TABLES

3. 1 A comparison of the overall volume, optical volume, and intensity in bulk cells, NIST cells and the ARROW.....29

4. 1 Effectiveness of passivation layers in lowering the surface energy of PECVD silicon nitride. 39

B. 1 The ARROW design for a pedestal ARROW with oxide conformality 1.32.....65

B. 2 The ARROW design for a regular ARROW with oxide conformality 1.32. 66

B. 3 The ARROW design for a pedestal ARROW with oxide conformality 1.4.....66

B. 4 The ARROW design for a regular ARROW with oxide conformality 1.4. 67

LIST OF FIGURES

2. 1 Basic setup for absorption spectroscopy. 6

2. 2 The absorption spectrum of rubidium's two natural isotopes around the D_2 transition. Frequency is labeled to show the frequency difference between the dips, with the first dip used as a reference. 7

2. 3 The energy structure of rubidium showing its few lowest energy levels. 8

2. 4 The difference in the split ground state energy level of rubidium's natural isotopes. These transitions correspond to the absorption peaks in Figure 2.2. 10

2. 5 Saturation absorption spectroscopy setup. 11

2. 6 The energy structure of rubidium, detailing its hyperfine transitions. 12

2. 7 The saturation absorption spectrum of a D_2 transition in ^{87}Rb showing two Lamb dips. 13

2. 8 A conventional atomic vapor cell. 14

2. 9 A hollow waveguide allows for small mode confinement and long interaction lengths. Conventional cells do not allow for both. 15

2. 10 The fabrication process for the NIST reference cell [10]. 17

2. 11 Absorption spectrum of cesium in the NIST reference cell, frequency units show the difference in frequency between dips [10]. 18

2. 12 SEM of a photonic band-gap fiber. 19

2. 13 Saturation absorption spectrum in photonic band-gap fiber [27]. 19

3. 1 Cross section illustration of an ARROW waveguide. 22

3. 2 ARROW platform. 22

3. 3 Bottom dielectric layers and sacrificial core deposited. 24

3. 4 Top dielectric layers deposited over core, with a thick top oxide layer. 24

3. 5 Solid-core waveguides etched into the thick, top oxide layer. 24

3. 6 Sacrificial cores exposed through etching. 25

3. 7 sacrificial cores etched out in selective acid etch. 25

3. 8 SEM cross section of an ARROW looking into the hollow core. 25

3. 9 SEM cross section of a pedestal ARROW..... 26

3. 10 SEM cross section of an arched-core ARROW. 27

3. 11 The interface (2) between the solid core (1) and the hollow core waveguides (3) allows the integrated vapor cell to be sealed. 28

4. 1 The integrated vapor cell platform using ARROWs..... 31

4. 2 Leak rates of various sealing techniques tested for possible integration with hollow waveguide. 34

4. 3 Photograph of the integrated vapor cell platform with an ARROW. 36

4. 4 Diagram showing process used to incorporate rubidium into the vapor cell, a) fabricated hollow channel, b) vapor cell is integrated onto the waveguide chip, and c) in an inert atmosphere rubidium is incorporated into the cell..... 37

4. 5 ODMS Self assembled monolayer on the silicon nitride surface. 38

5. 1 Test platform for the rubidium filled vapor cell absorption test. 42

5. 2 Measured absorption spectrum from the rubidium filled vapor cell around the D_2 line. 42

5. 3 Test platform for measuring rubidium absorption in empty vapor cell connected to rubidium filled vapor cell through hollow channel. 43

5. 4 Measured absorption peaks in the empty vapor cell connected to rubidium filled vapor cell through hollow channel..... 44

5. 5 Absorption spectroscopy setup using the ARROW. 45

5. 6 Absorption spectrum from the rubidium vapor filled ARROW. 45

5. 7 The temperature dependence of rubidium atoms in ARROWs and bulk cells. 47

5. 8 The optical density of rubidium vapor as a function of temperature in an ARROW device. 48

5. 9 The test setup for the scattering measurement. 49

5. 10 The output spectrum of light which scattered 90 degrees in the ARROW. The rubidium absorption peaks of ^{85}Rb are visible. 49

5. 11 Setup for the saturation absorption spectroscopy easurement. 50

5. 12 Absorption spectrum with the pump beam turned on and off. When the pump beam is on saturated absorption spectroscopy's characteristic Lamb dips are present. 51

1 Introduction

1.1 Overview

Large vapor cells are used to investigate a variety of quantum interference effects. Atomic clocks [1], nonlinear frequency generation [2], gas phase sensing [3], precision spectroscopy [3, 4], low-level switching [5], and the use of electromagnetically induced transparency [6] in slow light [7, 8], and quantum communications [9] are many of the effects that can be observed when light interacts with atomic vapor in these cells. In these conventional bulk vapor cells there is a tradeoff between small beam areas and finite focal depth. Hollow waveguides decouple this tradeoff and allow for long intensities over large distances. This long interaction length with the atomic vapor makes hollow waveguides ideal platforms for observation of quantum interference effects. Many gases and molecular vapors can be optically investigated, but alkali vapors are of particular interest for quantum interference effects.

On chip vapor cells would miniaturize and simplify the measurement apparatus used to observe the aforementioned effects. Several miniaturized cells already exist: the NIST miniature vapor cell [1, 10] and photonic bandgap fibers have been integrated with rubidium vapor [2]. In this thesis a platform based on hollow anti-resonant reflecting optical waveguides (ARROWs) integrated with atomic vapor cells is described. ARROWs coupled with solid-core waveguides for off-chip fiber optical access form

monolithically integrated chips. With a footprint of less than 1 cm^2 and a cell volume over seven orders of magnitude smaller than bulk cells, ARROW chips are very small. ARROWs also have a micron sized mode area, which enables high intensities over near centimeter lengths on chip.

This thesis discusses the effectiveness of hollow core ARROWs for use as an integrated vapor cell platform, specifically for absorption spectroscopy applications. The introduction chapter provides background information about absorption spectroscopy, saturation absorption spectroscopy, and some current apparatuses for investigating photon-atom interactions. These other apparatuses include atomic vapor cells, the NIST cell, and photonic band-gap fibers. Chapter Three briefly discusses ARROW principles and fabrication techniques. The benefits of using ARROWs as integrated vapor cells are also described. Chapter Four explains how the ARROW is modified to contain atomic vapor. Chapter Five presents optical measurements and certain characteristics of the rubidium vapor in the hollow core waveguide.

The measurements show the effectiveness of sealing techniques and transferring rubidium atoms through a hollow channel. Absorption spectroscopy measurements of rubidium vapor in the hollow core ARROW, as well as optical density measurements of rubidium in an ARROW show the effectiveness of photon-atom interactions in the hollow core. The advantages of the planar integration of a vapor cell are shown with a scattering measurement. Finally, saturation absorption spectroscopy is demonstrated. All of these demonstrate that an ARROW device satisfies key requirements for integrated atomic spectroscopy.

1.2 Contributions

The research presented in this thesis represents a collaborative effort with the University of California at Santa Cruz (UCSC). My responsibility has been the design, development, and integration of vapor cells with the ARROW waveguide. Fabrication of the ARROW waveguides for integration with vapor cells was also performed by me in the BYU Integrated Microfabrication Laboratory (IML). UCSC performed the optical design and testing of the ARROWs, as well as the testing of the integrated ARROW vapor cells. This thesis focuses on the integration of the ARROW device for atomic spectroscopy. Significant optical test results from UCSC are included, as they show the performance of the integrated vapor cell.

This research provides a unique contribution to integrated optics and atomic spectroscopy. From this research two peer-reviewed journal articles have been published [11,12], with another currently being reviewed [13] and five conference presentations have been given [14-18], including an invited talk [18]. These papers and presentations and this thesis lay the foundation for the work to come in utilizing the full-potential of the ARROW as a platform for atomic spectroscopy and quantum interference effects.

2 Atomic Spectroscopy

2.1.1 Absorption Spectroscopy

As electromagnetic energy from a laser beam propagates through a sample of atomic vapor, atoms absorb the energy from the photons. Consequently, the photons which lose their energy to the atomic vapor are not detected in the output. The resulting output spectrum contains dips around the frequencies of the absorbed photons (Figure 2.2). These frequencies reveal the atomic energy structure of the atom and the density of the atoms in the sample. The relative intensity of the transmitted light varies proportionally to the molar concentration of the vapor and the thickness of the sample. These can be determined by the Beer-Lambert Law:

$$I_1 = I_0 * \exp(-\alpha * L). \quad (1)$$

I_1 and I_0 are the resulting and incident intensities. α is the absorption coefficient, which depends on the density of atoms. L is the path length of the light through the atomic vapor.

Absorption spectroscopy for alkali atoms is best explained in a simple hydrogen-like atomic energy level scheme. Alkali atoms have the same outer electronic configuration as hydrogen. The inner shells of alkali atoms are all full of electrons and

closed, therefore they can be neglected. The outer, valence shell only has one electron, like hydrogen. Without the presence of an external field the valence electron will stay at its lowest energy level, which is referred to as the ground state. This is ideal, because when there are an equal number of atoms in both excited and ground states, photons are as likely to be spontaneously emitted as absorbed. The laser signal would not attenuate and yield any dips in its transmission in this case. The attenuation of the signal can be maximized when all atoms are in the ground state.

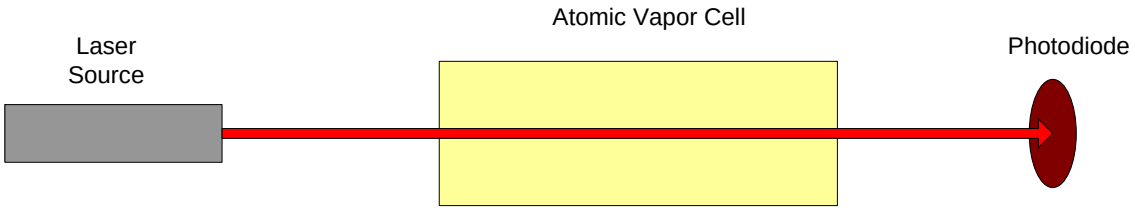

Figure 2. 1 Basic setup for absorption spectroscopy.

To measure an absorption spectrum, the simple configuration shown in Figure 2.1 is used. The atomic vapor cell would be full of whichever atoms are to be analyzed. A laser would be selected that could scan through the natural frequency of the atoms. When the transmission spectrum is observed, there is a smooth absorption curve around the true natural absorption frequency. Figure 2.2 shows a sample absorption plot from rubidium. The four dips are from four separate energy transitions and will be explained later. Each dip spreads out in a Gaussian curve due to thermal motions in individual atoms in the gas. If an atom is moving toward the beam the frequency from the perspective of the atom is red-shifted. Thus, it will absorb light at a frequency less than the natural frequency of the atom. The same is true for atoms moving away from the beam, although they blue-shift

the frequency. These cause absorption in a wider spectrum than just the natural frequency. This is referred to as Doppler broadening. It does not pose a problem when looking at absorption dips several nanometers apart.

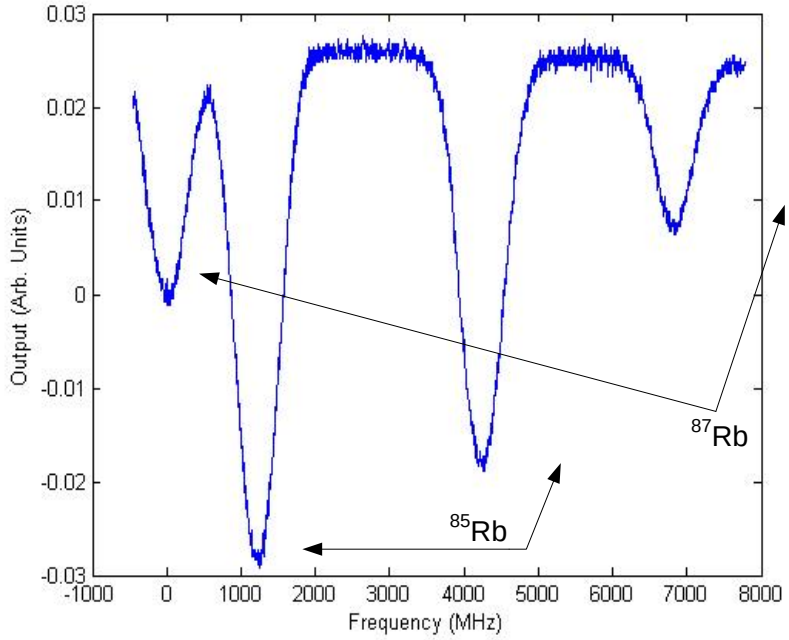

Figure 2. 2 The absorption spectrum of rubidium's two natural isotopes around the D_2 transition. Frequency is labeled to show the frequency difference between the dips, with the first dip used as a reference.

2.1.2 Atomic Energy Level Splitting

Energy levels are split in two ways, fine and hyperfine splitting. The first, fine splitting, comes about through an electromagnetic interaction between an electron and its nucleus. From the electrons perspective, the nucleus spins around it. This sets up a magnetic field which interacts with the magnetic moment of the electron, thus altering its energy. The energy changes based on the orientation of the electrons spin relative to the angular momentum of the orbit. The difference of wavelengths from fine splitting is

typically on the order of nanometers. Figure 2.3 shows the few lowest energy levels of rubidium. The first excited energy state is fine split into two energy levels: $5^2P_{1/2}$ and $5^2P_{3/2,}$ with a 15 nm difference in wavelength. The rubidium energy level structure will be discussed further in the next section.

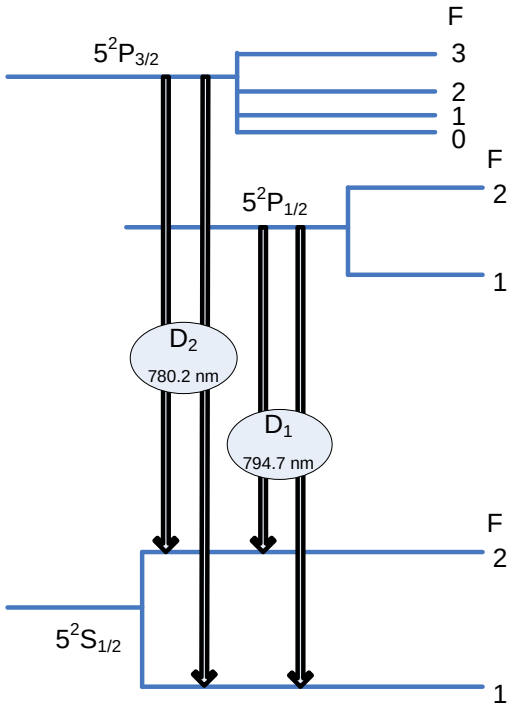

Figure 2. 3 The energy structure of rubidium showing its few lowest energy levels.

Hyperfine splitting is the second way in which energy levels split. The magnetic moment of the valence electron changes as it interacts with the magnetic moment of the nucleus. The hyperfine splitting comes from the difference in energy of the orientations of the magnetic dipoles. It is characterized by the angular momentum quantum number F. Figure 2.3 shows how $5^2S_{1/2}$ and $5^2P_{1/2}$ are split into two, and $5^2P_{3/2}$ is split four hyperfine levels. As the name suggests, hyperfine splitting is on a much smaller scale than fine splitting, 10^{-3} nm. In fact, it is smaller than the Doppler broadened spectrum of a single

line. This means that, because of Doppler broadening, absorption spectroscopy does not have high enough resolution to show the hyperfine levels. Therefore, special means, such as saturated absorption spectroscopy, are required to observe the hyperfine splitting of atomic energy levels.

2.1.3 Rubidium Energy Structure

Rubidium is commonly used for investigation of atomic energy levels. Rubidium is an alkali atom and has all the benefits of the hydrogen-like structure alkali atoms possess as discussed in the previous section. It also has natural absorption wavelengths around 780 nm, which is a wavelength of readily available lasers. Also, much noteworthy research on quantum interference has been done using it [19]. Furthermore, rubidium provides a wavelength reference and a three level energy scheme used for many quantum interference effects [19, 20]. These characteristics make rubidium highly used in slow light research as well [19].

The ground state of rubidium, denoted $5^2S_{1/2}$ contains one valence electron. It is also split into two hyperfine sublevels (Figure 2.4). The first excited state of rubidium is also split, but is characterized by a fine split. These two states are denoted $5^2P_{1/2}$ and $5^2P_{3/2,}$ and are separated by 15 nm in wavelength. The transitions that may take place as electromagnetic energy interacts with the atoms are denoted D_1 and D_2 (Figures 2.3). The D_1 transition corresponds to a 795 nm wavelength and represents the transition between the $5^2S_{1/2}$ and the lower energy excited state $5^2P_{1/2}$. The D_2 transition corresponds to the transition between $5^2S_{1/2}$ to the higher energy excited state $5^2P_{3/2,}$ and has a wavelength of 780 nm.

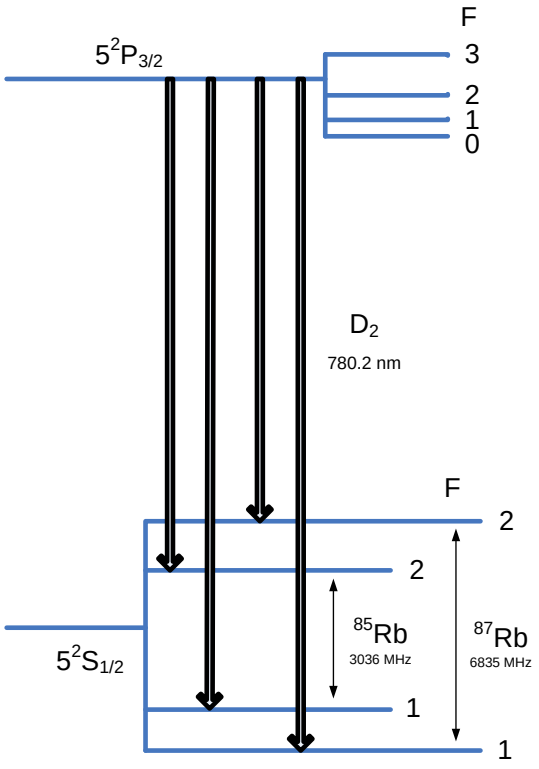

Figure 2. 4 The difference in the split ground state energy level of rubidium's natural isotopes. These transitions correspond to the absorption peaks in Figure 2.2.

Another reason rubidium is good for absorption spectroscopy is its two naturally occurring isotopes, which are both in reasonable abundance. Rubidium 85 is at 72 percent abundance, and rubidium 87 takes in the other 28 percent. This is advantageous because it means that there are actually four groups of transitions, a D_1 and D_2 transition for both ^{85}Rb and ^{87}Rb. Figure 2.4 shows how the hyperfine splitting of the ground state differs between isotopes. All of the transitions represented in Figure 2.4 can be seen in the absorption spectrum plot in Figure 2.2. Notice how the frequency difference between dips corresponds to the frequency difference shown in Figure 2.5. Also, notice how the more abundant rubidium 85 absorbs more light than rubidium 87.

2.1.4 Saturated Absorption Spectroscopy

A second laser beam propagating through and saturating the atomic transitions reveals the hyperfine structure of atoms. This second beam has the same frequency as the first, because it comes from the same source. However, it has a different intensity and propagates through the atomic vapor in the opposite direction. Figure 2.5 shows a setup used for saturated absorption spectroscopy. The more intense saturation beam excites the atoms to an excited state. Due to the fast rate of emission and absorption transitions the strong resonant laser field causes the ground state and the excited state populations to equilibrate. This effectively saturates the transition. The less intense probe beam does not have many atoms available to excite, because the saturation beam has already excited them. This leaves transmission dips in the absorption peaks called Lamb dips. Each Lamb dip corresponds to a hyperfine energy transition. Figure 2.6 shows the possible hyperfine energy transitions possible in rubidium vapor. Figure 2.7 shows a saturated absorption spectrum of the D_2 transition in rubidium. Notice how the absorption dip has two Lamb dips, each corresponding to an allowed energy transitions of rubidium shown in Figure 2.6.

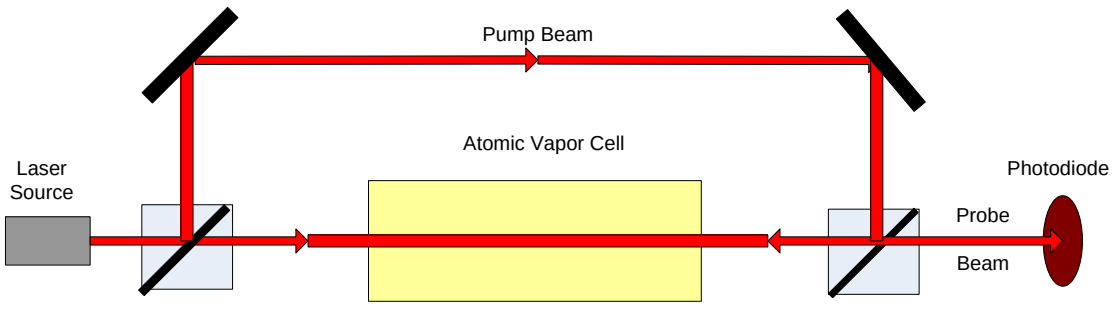

Figure 2. 5 Saturation absorption spectroscopy setup.

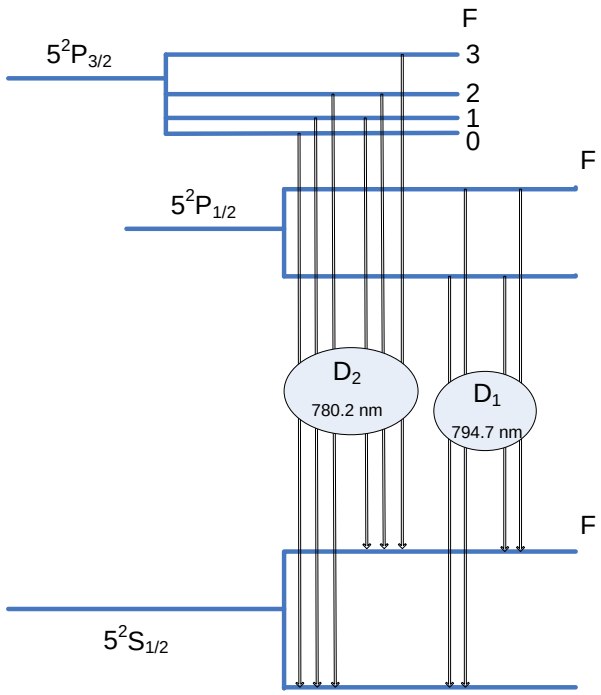

Figure 2. 6 The energy structure of rubidium, detailing its hyperfine transitions.

A key element to saturated absorption spectroscopy is tuning the frequency to the center of the natural frequency. If the lasers are not tuned to the center, both beams will be absorbed. The saturation beam will have no effect on the probe beam, because the two beams have excited different atoms in the Doppler profile. For example, if the laser wavelength is less than the center of the absorption peak, the saturation beam only excites atoms moving toward the beam with some velocity. From the atoms perspective the wavelength of the beam is actually at its resonant frequency, because the velocity red shifted the beam's frequency. At the same time the probe beam propagates in the opposite direction. The probe beam can only excite atoms moving with the same velocity in the opposite direction, because of the Doppler shift and the opposite propagation direction. Both of the beams have affected different atoms. The laser wavelength must be exactly at the transition frequency to observe increased transmission in the probe beam.

The probe beams Lamb result completely from atoms with zero velocity. Therefore, the linewidth of Lamb dips is not determined by Doppler broadening, but by the transition. This allows greater resolution and the small hyperfine transitions to be seen. Scanning through the natural frequency allows the absorption dips and the Lamb dips to be shown (Figure 2.7).

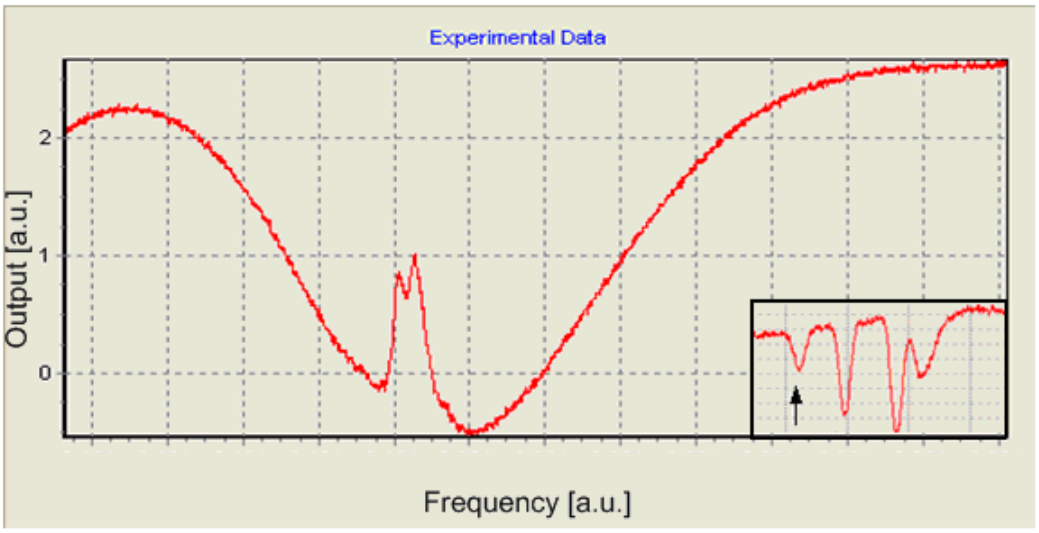

Figure 2. 7 The saturation absorption spectrum of a D_2 transition in ^{87}Rb showing two Lamb dips.

2.2 Atomic Vapor Cells

Atomic vapor cells are the primary source for atomic vapors used in alkali vapor absorption spectroscopy and other photon-atom interaction processes. These cells have been used for these measurements for several decades. In fact, the fabrication of the cells has not changed very much since Bouchiat and Brossel started applying coatings to cells in 1966 [21-23]. The coatings prevent the alkali atoms in the cell from adsorbing onto the surface of the glass walls [21]. This allows for more atoms to be in the optical beam path.

The coated walls also help the atoms maintain phase coherence despite atom-wall collisions, which is essential to produce many quantum optical effects.

Fabricating conventional atomic vapor cells requires a complex system of glassware attached to a bulk rubidium ampoule, a vacuum, several valves, and the cell. Glassblowers typically form this complex apparatus. To coat the cells a rod with paraffin flakes is inserted into the cell and the cell is vacuumed out. The rod is within the glass pipe network and does not affect the vacuum. Then, in an oven, the temperature is increased to evaporate the paraffin onto the walls. Following the rod's removal from the cell, rubidium is moved toward the cell from its bulk ampoule using a blown air heat gun. The bulk rubidium stays out of the cell to keep it from interacting with the paraffin. The cell is then separated from the glass apparatus by melting the glass pipe just above the rubidium [23]. Figure 2.8 shows a conventional atomic vapor cell.

Figure 2. 8 A conventional atomic vapor cell.

2.3 Vapor Cell Integration Advantages

Integrating the vapor cell into a hollow waveguide increases the interaction length of light with vapor and decreases the mode size of the interacting beam; both effects significantly enhance the nonlinear effects. A spot size comparable to the absorption

cross section of the atom, $3\lambda^2/2\pi$, is necessary for low level quantum interference effects [24] and to enhance nonlinear effects [11]. For the D_2 transition in rubidium the absorption cross section is approximately 3 μm^2, which corresponds to a .6 μm spot size. A beam with a 4 μm waist provides a close match and gives a 31 μm focal depth [11]. A longer interaction length would also enhance the nonlinear effects. However, increasing the focal depth of the beam increases the beam waist, making it much larger than the absorption cross section. Thus, the focal depth and the spot size of beams are coupled and the interaction with vapor in a conventional cell is limited. Integrating the cell into a hollow waveguide allows for long interaction lengths as well as small mode confinement. As long as the light is confined within the absorption cross section-sized core the light will interact with the alkali vapor and significantly enhance the nonlinear effects throughout its length. For example, integrating the alkali vapor into a hollow waveguide 7 mm long would increase the nonlinear interaction length 225 times over a conventional cell. Not only would the nonlinear interaction length increase, the overall size would decrease, thus making it more viable for commercial use.

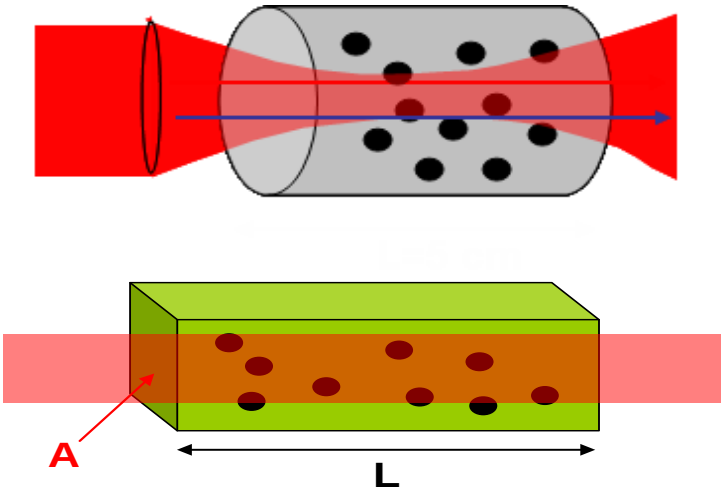

Figure 2. 9 A hollow waveguide allows for small mode confinement and long interaction lengths. Conventional cells do not allow for both.

2.3.1 NIST Reference Cell

The National Institute of Standards and Technology (NIST) recently developed its own miniaturized vapor cell. The cell was created mainly for use as a miniaturized atomic clock [10], although it also has potential uses as a magnetometer, an apparatus for spectroscopy, and as a frequency reference cell. The cell could not be fabricated using traditional glass blowing techniques, because of the desired small scale [10]. To fabricate the cell on the millimeter scale, silicon micromachining was used. This actually lowered the cost and created a device that was more highly reproducible than any glass blown device [10]. The atomic frequency reference came from either rubidium [25] or cesium [10, 26] atoms in the cell. Both of these atoms react with many materials and cannot be handled in the air. Therefore a special fabrication method was developed to avoid specimen contamination.

The devices are fabricated using micromachined silicon and borosilicate glass anodically bonded together. To begin the fabrication process double-sided polished <100> wafers were photolithographically patterned and etched. Then, using high temperature and a high electric field, a similarly sized piece of borosilicate glass was anodically bonded to the silicon. This caused oxide to form at the interface and create a hermetic seal [10]. At this stage a small cavity has been formed, which the alkali atoms can be placed into. Figure 2.10 shows the steps to fabricating an NIST cell.

The alkali atoms were introduced into the cavity in two ways. The first method involved using chemical reactions of BaN_6 in H_2O and Alkali-Cl to form an elemental alkali atom in an ultra high vacuum environment [10]. The ultra high vacuum environment allows for fairly precise control of the pressure and the gases in the

environment. After the elemental alkali atoms have been formed the chamber can be backfilled with a buffer gas to an appropriate pressure. In this environment the top borosilicate glass piece is anodically bonded onto the cell cavity.

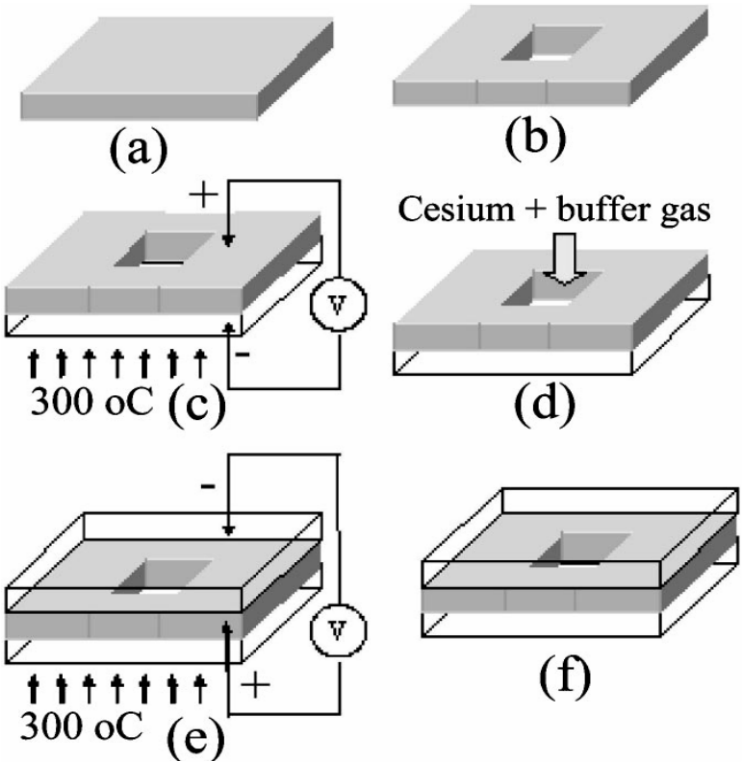

Figure 2. 10 The fabrication process for the NIST reference cell [10].

The second method for incorporating alkali atoms into the cell cavity utilizes an anaerobic glovebox filled with dry nitrogen [10]. This method works well for cesium which is liquid at room temperature. A nanoliter pipette transfers the liquid cesium directly from an ampoule to the cell cavity. The cavity is then placed in a low vacuum bell jar, in which the buffer gas is added and the top borosilicate glass is anodically

bonded to the cell cavity. Figure 2.11 shows cesium absorption spectroscopy peaks from the cell. Although, the NIST cell does miniaturize the conventional atomic vapor cell, it does not improve the interaction length of the beam with the atoms.

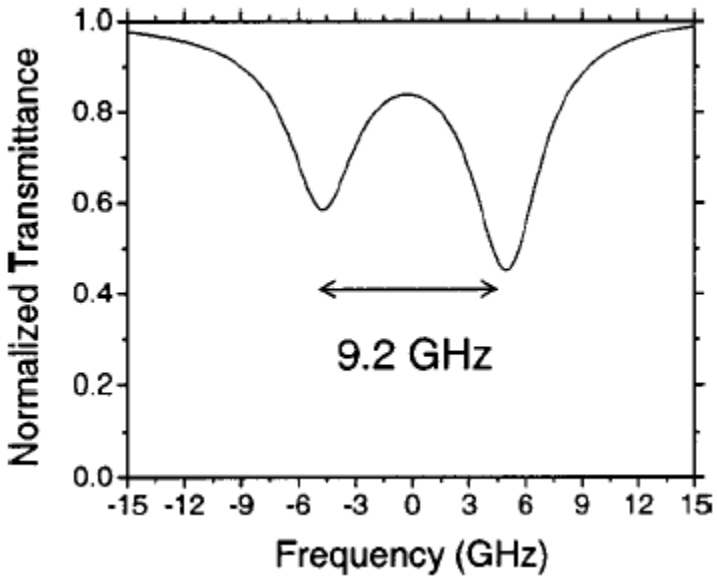

Figure 2. 11 Absorption spectrum of cesium in the NIST reference cell, frequency units show the difference in frequency between dips [10].

2.3.2 Photonic Band-gap Fiber

Photonic band-gap fibers (Figure 2.12) have been integrated with rubidium and other atomic vapors for saturated absorption spectroscopy (Figure 2.13) [27] and to exhibit other optical effects [28]. Photonic band-gap fibers confine high intensities of light in a hollow region using photonic structures which surround a hollow core. To incorporate rubidium vapor into the photonic band-gap fiber the fiber must first be prepared with monolayer coatings [24]. Like paraffin in conventional cells, these coatings limit the number of atoms which adsorb onto the silica walls of the fiber. After the

coating, the ends of the fiber are placed in separate vacuum cells. One cell contains rubidium, which diffuses down the length of the fiber [24]. The optical measurements take place while the fiber is hooked up to the vacuum cells. However, the fibers must be sealed in the optical path and the non-planar setup of the fiber limits the optical interaction to a single dimension.

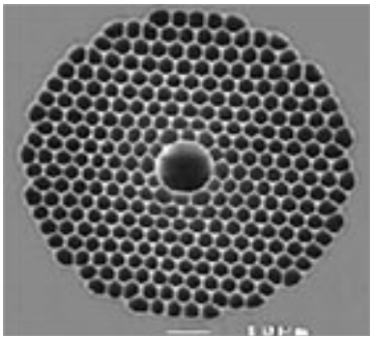

Figure 2. 12 SEM of a photonic band-gap fiber.

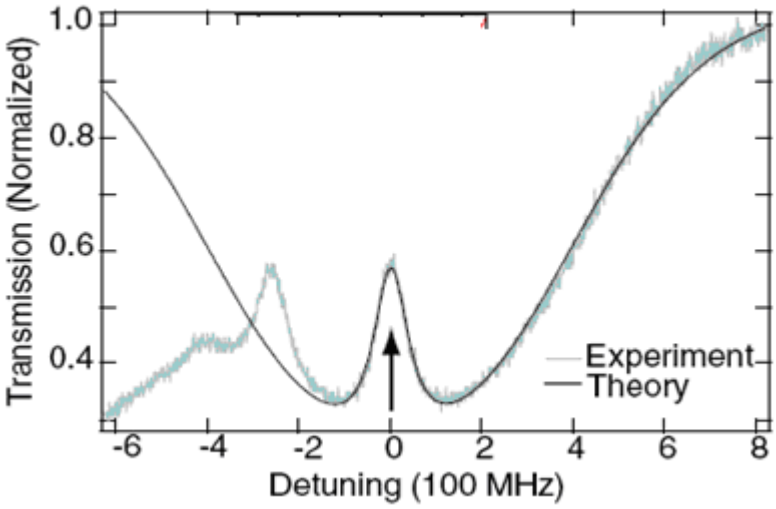

Figure 2. 13 Saturation absorption spectrum in photonic band-gap fiber [27].

3 ARROWs

3.1 Principle

Unlike conventional waveguides, ARROWs do not guide light through total internal reflection at a single boundary [29]. Conventional optical waveguide designs require that light propagates in a high index medium surrounded by a lower index one, this allows total internal reflection. If the core had a lower index of refraction, light would quickly leak into the surrounding higher index material. ARROWs allow light to propagate in lower index media by utilizing Fabry-Perot reflectors in the transverse direction. The Fabry-Perot reflectors act like mirrors, exhibiting high reflectivity when operating at anti-resonance [29]. The finite transmission of the cladding layers makes the ARROW a leaky waveguide. However, the loss reduces when more dielectric layers are added. Each additional layer decreases the loss by approximately three times [30]. The ARROW is also effectively a single mode waveguide since higher order modes are suppressed by high optical losses [29]. To achieve the anti-resonant, highly reflective condition the dielectric layers must be deposited to a fairly precise thickness determined by Equation 2 [29]:

$$t_j = \frac{\lambda}{4n_j}(2M+1)\left[1-\frac{n_c^2}{n_j^2}+\frac{\lambda^2}{4n_j^2 d_c^2}\right]^{-1/2}. \qquad (2)$$

In the equation n_j and n_c are the index of refraction of the jth layer and the core, respectively, d_c is the thickness of the core, λ is the wavelength, and M is an integer representing the anti-resonance order. These correspond with Figure 3.1, which shows a cross section of an ARROW.

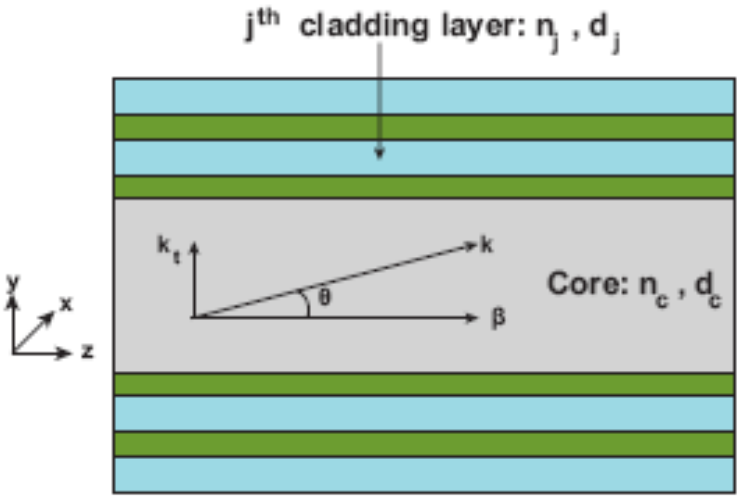

Figure 3. 1 Cross section illustration of an ARROW waveguide.

3.2 Fabrication

Figure 3. 2 ARROW platform.

The ARROW fabrication process utilizes standard semiconductor processes [30, 31]. This makes fabrication of multiple devices simultaneously possible. ARROWs are fabricated on <100> crystal orientation silicon wafers to allow the devices to be cleaved perpendicular to the waveguides. The process for fabricating the device shown in Figure 3.2 begins by depositing the bottom dielectric layers of silicon dioxide and silicon nitride using plasma enhanced chemical vapor deposition (PECVD). Each layer thickness is deposited according to Equation 2. Following the bottom layers the sacrificial core is fabricated using SU-8 spun on to a specified thickness, patterned, and developed (Figure 3.3). The top dielectric layers are then deposited over and around the sacrificial core using PECVD (Figure 3.4). The top oxide layer is deposited thicker than the other layers, but still at an anti-resonant thickness. This thick oxide layer provides structural strength for the waveguide [32]. Ridge waveguides etched into the top, thick silicon dioxide layer provide a means for coupling light into the hollow core without exposing the hollow waveguide to the surrounding air [33], which is essential to atomic vapor cell success. The solid-core, ridge waveguide is patterned with an SU-8 mask and etched using a reactive ion etcher (Figure 3.5). The next step is to expose the sacrificial cores to air to allow them to be etched and removed. This is also done in the reactive ion etcher with the pattern masked by SU-8 (Figure 3.6). To complete the ARROW and make it hollow, a highly selective acid bath etches the sacrificial core (Figure 3.7). The openings in Figure 3.7 can now be used to attach a reservoir that does not interfere with the optical beam path. Figure 3.8 shows a cross section of a completed ARROW.

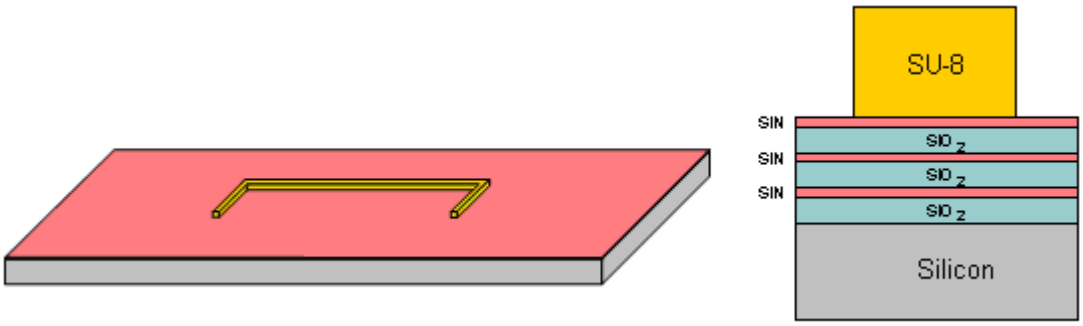

Figure 3. 3 Bottom dielectric layers and sacrificial core deposited.

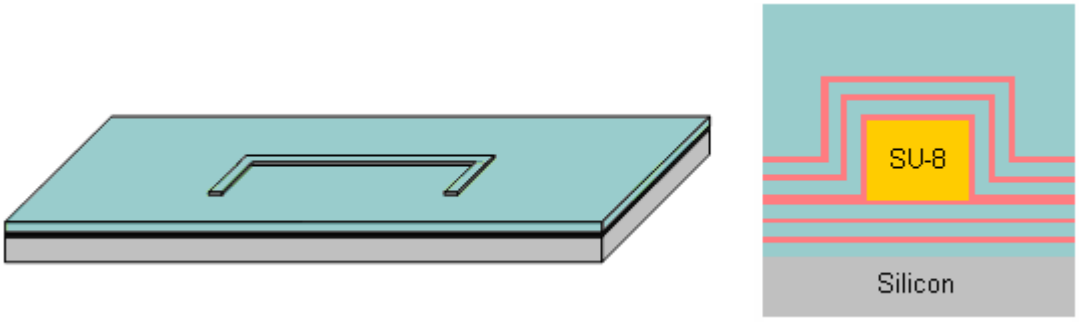

Figure 3. 4 Top dielectric layers deposited over core, with a thick top oxide layer.

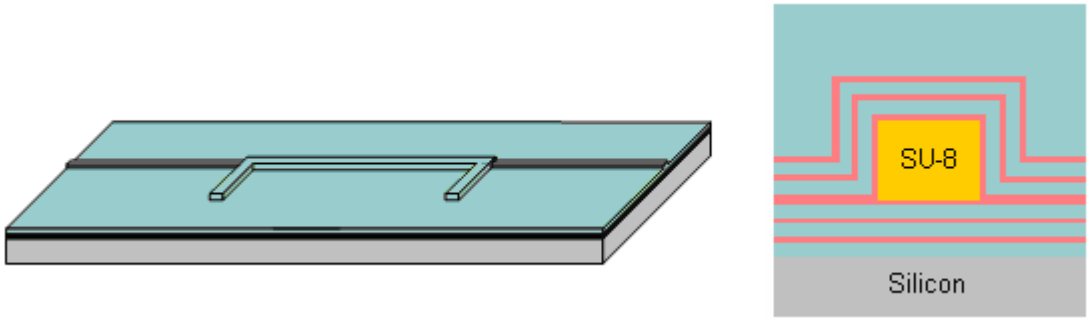

Figure 3. 5 Solid-core waveguides etched into the thick, top oxide layer.

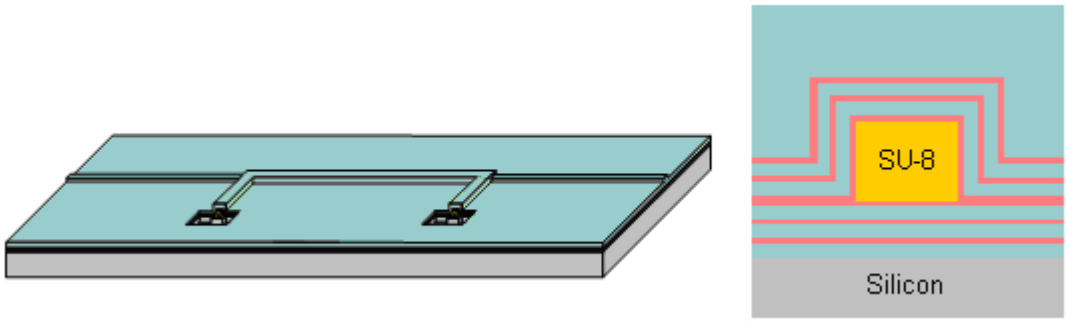

Figure 3. 6 Sacrificial cores exposed through etching.

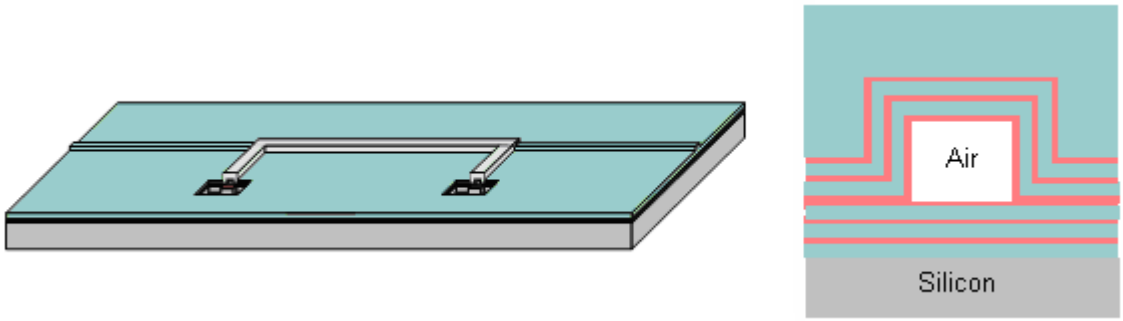

Figure 3. 7 sacrificial cores etched out in selective acid etch.

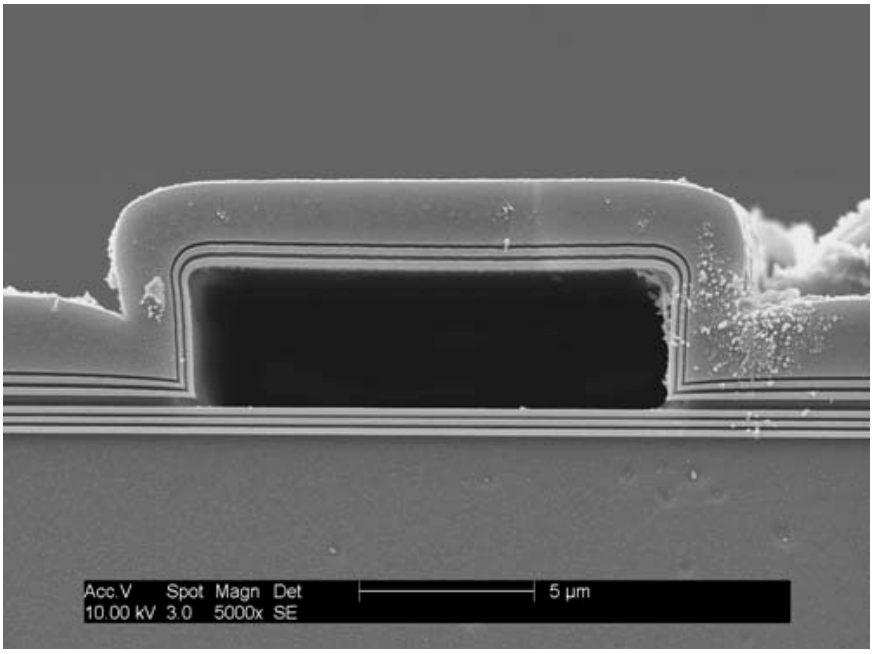

Figure 3. 8 SEM cross section of an ARROW looking into the hollow core.

3.3 Variations in Design

Several different geometries can be fabricated to give hollow waveguides unique characteristics. The fabrication process outlined above (Section 3.2) yields a rectangular core (Figure 3.8) [30, 34]. The thick top oxide layer extends laterally out from the waveguide as can be seen in the figure. This high index layer yields a higher loss in the waveguide than if air were laterally extending out from the waveguide. Fabricating the ARROW on a raised pedestal creates a waveguide where air extends laterally from the waveguide [30, 34]. This is realized by adding a single step to the fabrication process. Before depositing the bottom dielectric layers the pedestal is etched into the silicon. This places the lateral extensions of the waveguide above the thick top oxide layer [30, 34]. Figure 3.9 shows a cross section of a pedestal ARROW.

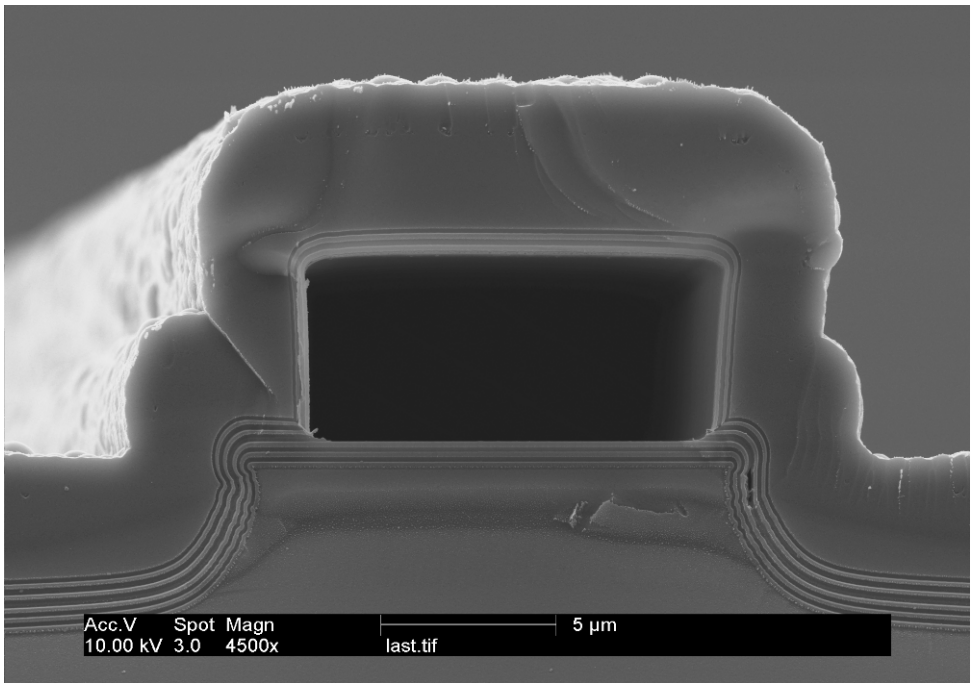

Figure 3. 9 SEM cross section of a pedestal ARROW

The shape of the core can also be changed to give different waveguiding properties. Fabrication processes have been developed to make an arched core ARROW (Figure 3.10) [35]. The arched core ARROW improves the structural strength of devices, provides lower loss, and is less polarization dependent than rectangular cores [36].

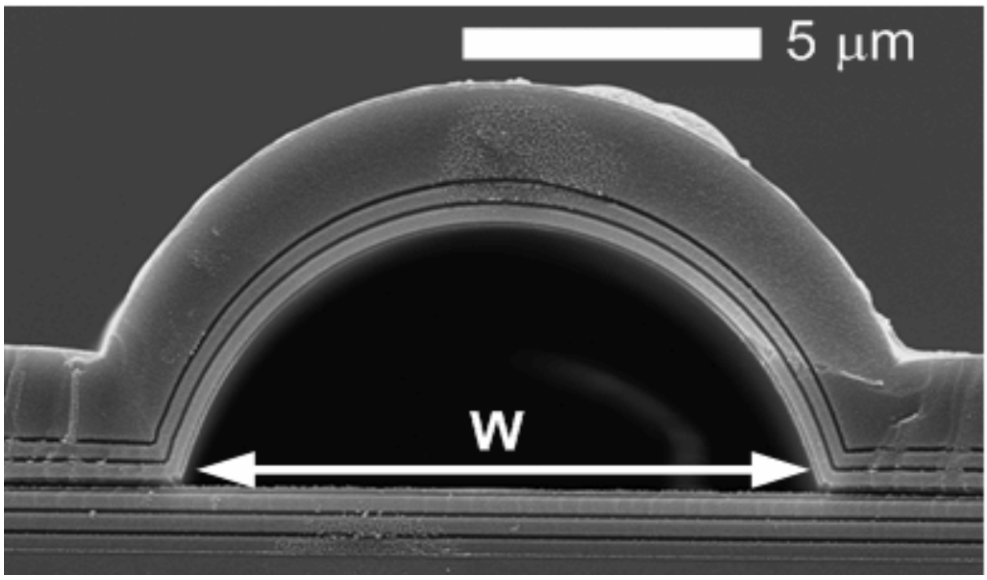

Figure 3. 10 SEM cross section of an arched-core ARROW.

3.4 ARROWs for Vapor Cell Integration

ARROWs provide attractive platforms for atomic vapor cell integration. Like photonic band-gap fibers, ARROWs decouple the tradeoff between small beam area and finite focal depth. The ARROW provides long interaction distances, with a high optical density of atoms, which provides large intensities over these distances. Also, the hollow waveguide aligns any beams propagating through its core, taking away the hassle of aligning multiple beams in an atomic vapor cell. However, unlike photonic band-gap

fibers ARROWs are a fully planar, monolithically integrated device, which utilizes standard semiconductor fabrication techniques. Monolithic integration of the ARROW provides intersecting solid core waveguides with the hollow core ARROW. This waveguide intersection provides a means for resonant fluorescence detection, simplified Doppler-free spectroscopy, and parametric generation. Also, the interface between the hollow core ARROW and the solid core waveguides is essential for sealing the hollow core and allowing beams from off chip to interact with atoms in the sealed, hollow core (Figure 3.11). Also, with a footprint of about 1 cm^2, the ARROW device is smaller than both the NIST cell and photonic band-gap fibers. The ARROW also provides significant improvement to the overall volume, optical volume, and intensity of the interacting, propagating beam. Table 3.1 provides a comparison between the volumes and intensities of the bulk atomic vapor cell, the NIST cell, and the ARROW. As the table shows the ARROW provides several orders magnitude of improvement over the bulk and NIST cells volume and overall volume.

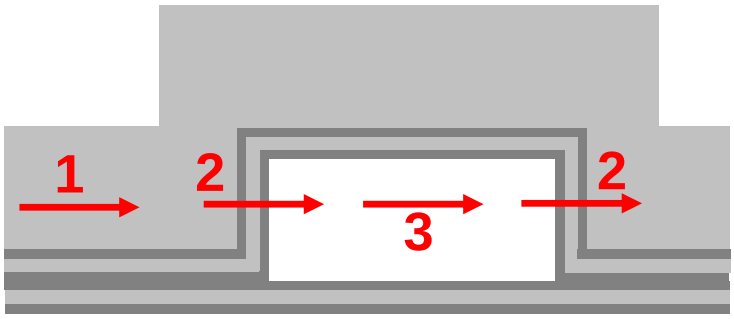

Figure 3. 11 The interface (2) between the solid core (1) and the hollow core waveguides (3) allows the integrated vapor cell to be sealed.

Table 3. 1 A comparison of the overall volume, optical volume, and intensity in bulk cells, NIST cells and the ARROW.

	dimensions [um x um x um]	**V [pl]**	**Vopt [pl]**	**I [norm.u.]**
Bulk cell	25,000 x 25,000 x 50,000	3.1×10^{10}	4×10^{7}	1
NIST cell	1000 x 1000 x 1000	1,000,000	23,000	35
ARROW	5 x 12 x 7000	420	200	62,000
ARROW Improvement	**Mode area: 19 l2**	7.4×10^{7} (bulk) 2,400 (NIST)	3×10^{5} (bulk) 115 (NIST)	62,000 (bulk) 1,700 (NIST)

4 Vapor Cell Integration with ARROW

4.1 ARROW Vapor Cell Platform

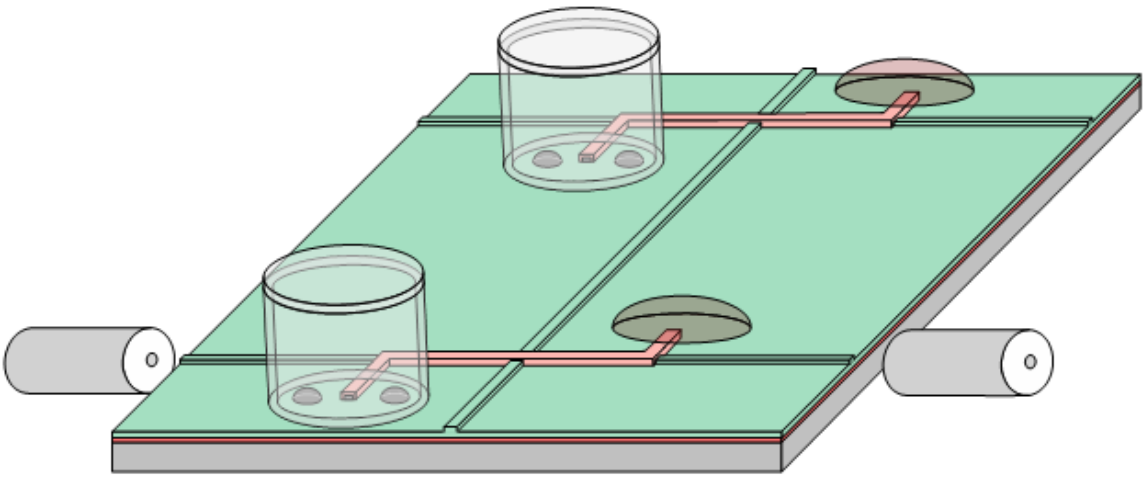

Figure 4. 1 The integrated vapor cell platform using ARROWs.

The ARROW platform was designed to be integrated with vapor cells. Figure 4.1 shows many of the features used in the design of the integrated platform. The hollow core waveguides are designed in an S-shaped pattern. This design allows vapor cell integration without covering the light-guiding segment of the hollow waveguide. Also, the sealed end of the hollow core waveguide can be sealed away from the light-guiding segment of the waveguide. Ridge waveguides etched into the thick, top oxide layer allow light to be coupled into the hollow core waveguide without exposing the hollow cores to air (Figure 3.11). All coupling of light onto the chip is done with the ridge waveguides. Ridge

waveguides can also be used for intersections which would be useful for applications like resonance fluorescence detection, parametric generation, and Doppler-free spectroscopy [37]. Also, multiple devices can be put on the same chip, as Figure 4.1 shows.

4.2 Vapor Cell Attachment

The integration of vapor cells with the hollow waveguide presents unique challenges. The most common method for transferring vapor into a vapor cell is to move a solid source of alkali atoms to the inside of the vapor cell. Once the alkali atoms are in the vapor cell, it must provide a stable, hermetically sealed, and inert environment. Any oxygen initially in the cell or leaking in will contaminate the vapor or the bulk sample. The seal must be stable for long periods of time to ensure that the device is usable for that time. To seal the vapor cell to the substrate the vapor cell must seal onto the flat substrate as well as over the waveguides which rise to at least ten microns above the substrate. This generally means that some type of epoxy, which can flow around the waveguide and seal, is required to seal the vapor cell over the waveguide. Also, some way of adjusting the pressure within the cell would be desirable for quantum interference effects. This would reduce the number of collisions between rubidium and buffer gas atoms and lower the coherence dephasing rate of the alkali atom.

4.3 Leak Rates for the Vapor Cells

Using the device specifications described in Section 4.2 several sealing techniques were tested for compatibility with the integrated cell platform. Here a representative

sampling of the techniques is presented. The techniques and materials presented were tested for their unique characteristics. Sealing adhesives tested include silicone and five-minute epoxy. Rubber stopper sleeves, which fit tightly around glass tubes, were also tested to determine how well natural rubber would seal. Butyl rubber o-rings sealed tightly with screws were tested, as were Swagelok fittings, which showed how well a metal-metal connection would seal.

The vapor cell seals were tested by measuring the leak rate of helium gas out of the cell. The devices were fabricated and sealed in a helium filled glovebox which left helium gas inside each vapor cell. The vapor cells were then tested in a helium leak detector. The leak rate of helium gas out of the cell determined how well the sealing mechanism worked.

The vapor cells used to test the sealants, silicone and epoxy, were fabricated in the same way. A 4 mm outer diameter and 2 mm inner diameter glass tube cut to 1 cm in length was used as the vapor cell. To seal the glass tube, two 1 cm square glass pieces were attached to both sides of the cut glass tube using either silicone or five minute epoxy. This process took place in a helium atmosphere glovebox, thus leaving helium gas inside the cell. The helium leak detector measured a leak rate of 3.225×10^{-7} mbarL/s for the silicone cells and 0.134×10^{-7} mbarL/s for the epoxy. The silicone leak rate proved to be the worst leak rate out of all the designs.

The rubber stopper sleeve vapor cell leak rate offers some improvement in leak rate over the silicone. The rubber stopper sleeve works by fitting snugly over the end of a 4 mm outer diameter glass tube. The end of the glass tube not sealed with the rubber stopper sleeve was sealed with a 1 cm square glass piece epoxied to the glass tube. The

epoxy use was justified by its low leak rate. Many types of adhesives were used to seal the stopper sleeve to the glass tube. However, these proved to be no better than just fitting the stopper sleeve over the glass tube, showing that the rubber stopper sleeve had a higher leak rate than the sealants. The helium leak detector measured leak rates of 1.991×10^{-7} mbarL/s for this vapor cell.

The screws with o-ring and Swagelok cells both had low leak rates. Tapped holes drilled into bulk aluminum, but not all the way through, served as the cell for the screw and o-ring vapor cells. This allowed the cells to be isolated with no paths for helium leakage, other than through the o-ring. In the glovebox, a screw with a butyl o-ring was screwed into the tapped hole. The o-ring provided a good seal for the helium remaining inside the cell. This method yielded leak rates similar to those of the epoxy: 0.137×10^{-7} mbarL/s. To test the metal-metal sealed vapor cell, both sides of small Swagelok fittings were sealed in the glovebox. No leaks were detected with these seals.

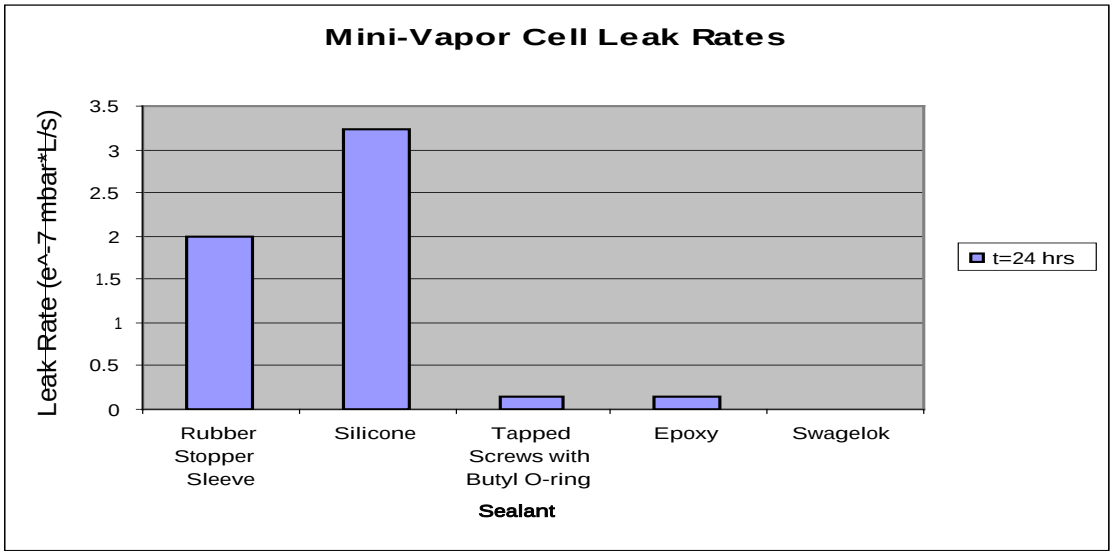

Figure 4. 2 Leak rates of various sealing techniques tested for possible integration with hollow waveguide.

These tests revealed that the epoxy, o-ring/screw, and Swagelok cell fabrication methods would provide the best seal. However, the sensitivity of the alkali atoms to the vapor cell required further testing. To do this vapor cells were created and the rubidium was monitored. Rubidium's contamination was apparent as its color within the cell would change from silvery to white, green, or violet. These tests revealed that epoxy could only be used as a sealant as long as it had cured before the alkali atoms were introduced to the cell: the outgassing of the epoxy as it cured contaminated the alkali sample. Also, certain metals used for the o-ring and screw technique would contaminate the sample: aluminum turned the rubidium white and brass turned it green. Stainless steel proved to be the most compatible with the alkali atom sample. The cells used for the measurements discussed in the following sections were fabricated using the epoxy as well as the o-ring/screw fabrication techniques.

4.4 Rubidium Incorporation into Vapor Cell

Rubidium incorporated into the vapor cell serves as the alkali vapor in this apparatus. Despite rubidium's benefits for quantum interference it has many characteristics which make it difficult to use. Rubidium is known to ignite in air, react violently in water, and react with many other materials. Even moisture in the air contaminates rubidium and slight amounts of oxygen oxidize it. For this reason all transferring of rubidium is done within the inert atmosphere of a glovebox.

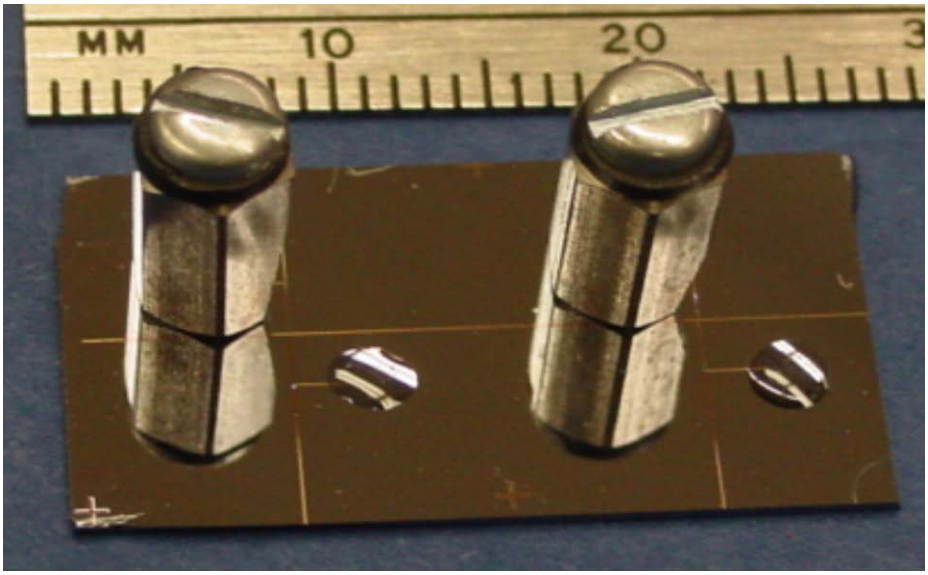

Figure 4. 3 Photograph of the integrated vapor cell platform with an ARROW.

Rubidium integration onto the hollow waveguide platform utilizes the stainless steel and epoxy vapor cell discussed at the end of Section 4.3 (Figure 4.3). The stainless steel vapor cell is modified to fit on the platform. The modification involves thinning one of the side walls so the vapor cell does not overlap the ARROW waveguide on the chip. After cleaning and dehydration baking the stainless steel standoff, it is epoxied to the ARROW chip over an open end of the hollow channel (Figure 4.4b). A dab of epoxy over the channel's remaining open end is necessary for the cell to be sealed. Passing the waveguide into the glovebox's inert atmosphere prepares the device for rubidium incorporation. Once the bulk rubidium in an ampoule liquefies at 39 C, stainless steel implements transfer small amounts to the inside of the stainless steel vapor cell. Sealing the vapor cell occurs once a stainless screw is screwed into the standoff. An o-ring placed on the screw seals the vapor cell and the hollow channel (Figure 4.4c). This completely fabricated vapor cell can now be tested for atomic spectroscopy.

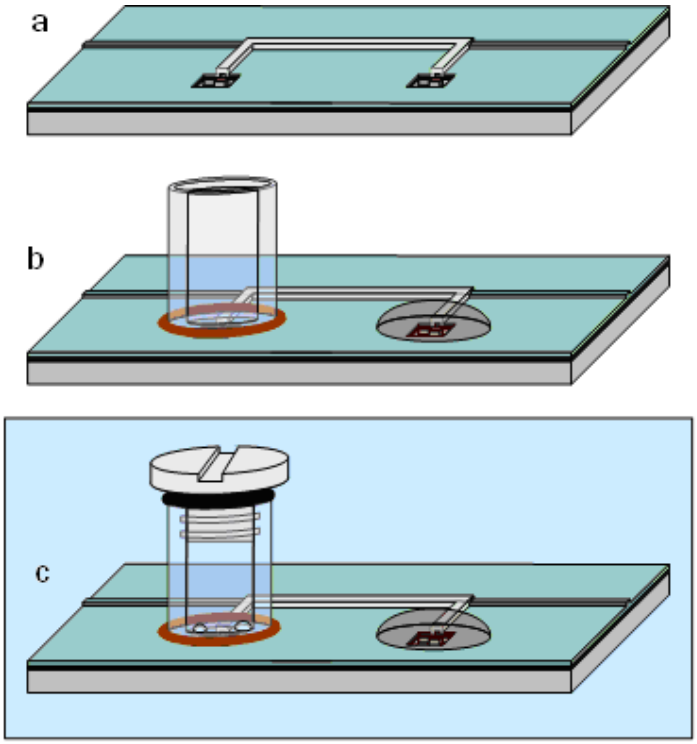

Figure 4. 4 Diagram showing process used to incorporate rubidium into the vapor cell, a) fabricated hollow channel, b) vapor cell is integrated onto the waveguide chip, and c) in an inert atmosphere rubidium is incorporated into the cell.

4.5 Self Assembling Monolayer Coating

Of particular concern for rubidium filled cells is adsorption of rubidium to the silica glass walls [29]. Rubidium within cells will adhere to the walls and lose their effectiveness in interacting with the light. Also, spin-decoherence, which occurs as rubidium atoms interact with the walls, makes creating quantum interference effects difficult. The adsorption of the rubidium has been addressed in large rubidium cells by coating cell walls with paraffin or siloxane monolayers [29, 38]. These passivate the

surface of the silica glass. This decreases both the occurrence of rubidium atoms adhering to the wall and the number of rubidium atom interactions with the cell wall, thus increasing the effectiveness of the vapor cell as a quantum interference device. Similar adsorption problems occur with the silicon nitride wall surface in the ARROW devices. Fortunately, the same methods which improved the problem can do the same for the silicon nitride walls. A paraffin layer, the passivation coating layer on conventional cells, does not provide an attractive passivation coating. Paraffin coatings are typically done through evaporation in a vacuum. The small, confined dimensions of the ARROWs make it difficult to evaporate paraffin inside the channel. However, siloxane monolayers, such as octadecyldimethylmethoxysilane (ODMS) can be formed in the liquid state (Figure 4.5) [39]. For this reason siloxane monolayers are the preferred method for passivation of ARROW walls.

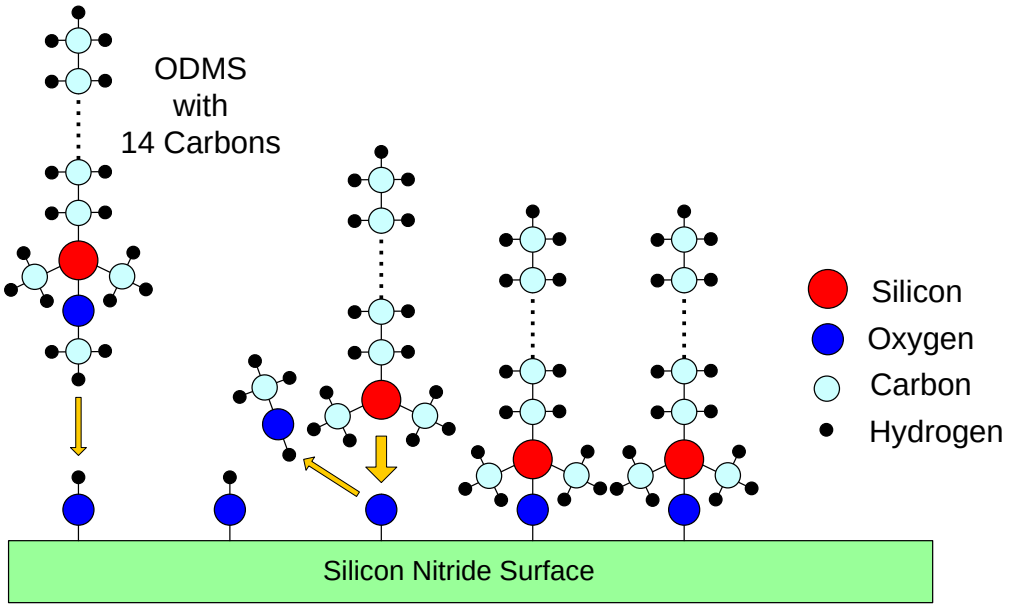

Figure 4. 5 ODMS Self assembled monolayer on the silicon nitride surface.

The effectiveness of self-assembled monolayers is well documented; however it's effectiveness on PECVD silicon nitride surfaces is not. Dyne pen tests were used to find the effectiveness of these coatings on the PECVD silicon nitride surface. Dyne pens come in several different dyne level fluids. The surface energy of the surface can be found by applying a thin layer of dyne pen solutions to the surface and noting the time taken for the solution to bead. If, for example, a 50 dyne pen is applied to the surface and it beads within two seconds, the surface energy is 50 dynes/cm. If the 50 dyne fluid takes longer than two seconds to bead, higher dyne level pens should be used until the fluid beads within two seconds. Using this technique for uncoated PECVD silicon nitride yielded a surface energy of 60 dynes/cm. Dyne tests were then conducted on ODMS, HMDS, paraffin, Surpass 4000, and Ultratol Dynamic coated samples. The results can be seen in Table 4.1. Tests showed the surface energy can be reduced using ODMS, HMDS, or paraffin. ODMS is the preferred method of surface passivation, because of the difficulty of depositing paraffin and the limited adherence time of HMDS.

Table 4. 1 Effectiveness of passivation layers in lowering the surface energy of PECVD silicon nitride.

	Uncoated	**ODMS**	**HMDS**	**Paraffin**	**Surpass 4000**	**Ultratol Dynamic**
PECVD Nitride surface energy	60 dynes/cm	50 dynes/cm	40 dynes/cm	40 dynes/cm	>60 dynes/cm	>60 dynes/cm

A method for coating the walls of the hollow channel waveguide is still being developed. Currently, straight hollow channels can be coated with little affect on its waveguiding properties. However, coating the S-shaped channels used for the integrated vapor cell platform ruins the waveguiding. The self-assembled monolayers will coat the corners too thickly and block the transmission path of the laser.

5 Optical Measurements

5.1 Vapor Cell

Before integrating the vapor cells with the hollow waveguides, the vapor cells effectiveness was tested. Several effects could ruin the vapor cell by contaminating the rubidium: leaks in the cell, outgassing of any adhesives used in the fabrication, dirty glass, or reaction with the metal. Any of these would destroy the rubidium absorption spectrum. Tests to measure the rubidium absorption spectrum in these vapor cells proved the effectiveness of the vapor cell.

Several techniques were employed for making the vapor cells for testing. The results presented here used 4 mm outer diameter and 2 mm inner diameter glass tubes cut down to 1 cm lengths. The ends of these cut tubes were flattened, polished, cleaned, and then attached to a glass substrate using epoxy. Rubidium droplets were transferred to the cell in the inert atmosphere of a glovebox as discussed in Section 3.4. Placing a rubber stopper sleeve over the glass tube completed the fabrication. A laser probed through the glass reservoir to test for the rubidium absorption spectrum. The absorption platform was set up as seen in Figure 4.1. Figure 4.2 shows the absorption spectrum through this cell (bottom curve) compared to a bulk rubidium cell (top curve). The less pronounced absorption peaks are a result of the smaller size of these vapor cells compared to the bulk cell.

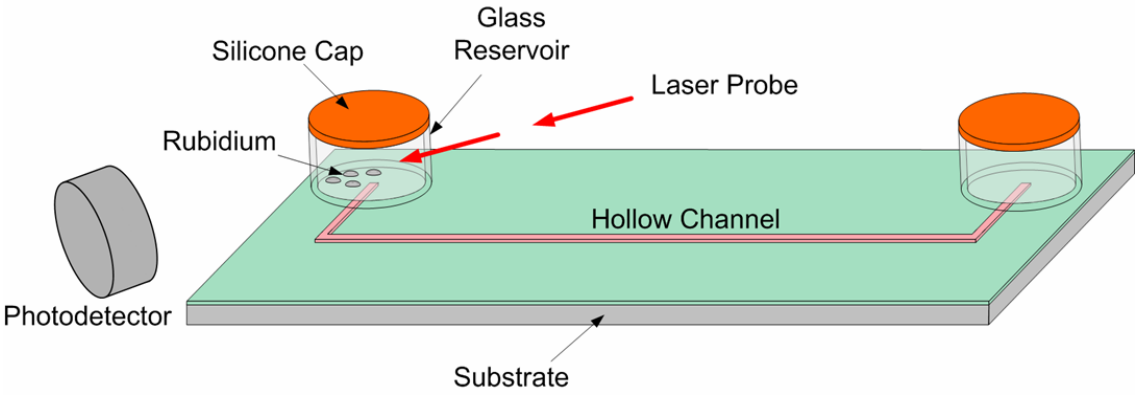

Figure 5. 1 Test platform for the rubidium filled vapor cell absorption test.

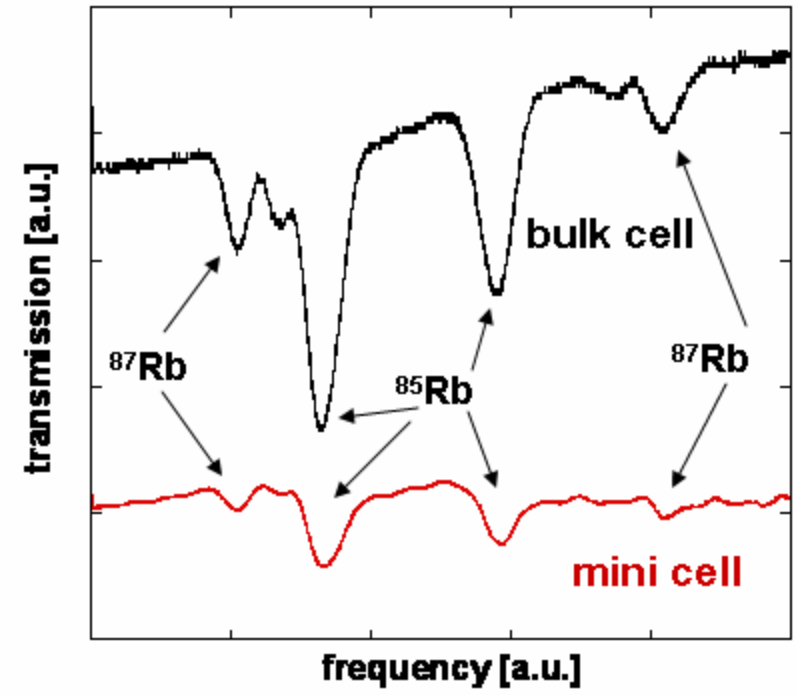

Figure 5. 2 Measured absorption spectrum from the rubidium filled vapor cell around the D_2 line.

5.2 Vapor Through Channel

After obtaining a rubidium absorption spectrum in a vapor cell a test was developed to verify whether rubidium vapor would travel through an ARROW-sized channel to another vapor cell. This platform utilized a hollow channel fabricated using techniques similar to those discussed in Section 2.2, except that the channel did not have alternating dielectric layers. Cut glass tube vapor cells were placed on the platform using epoxy, just as in the experiment above. Likewise, the rubidium was placed in the vapor cell using the same technique. However, rubidium was placed in only one cell.

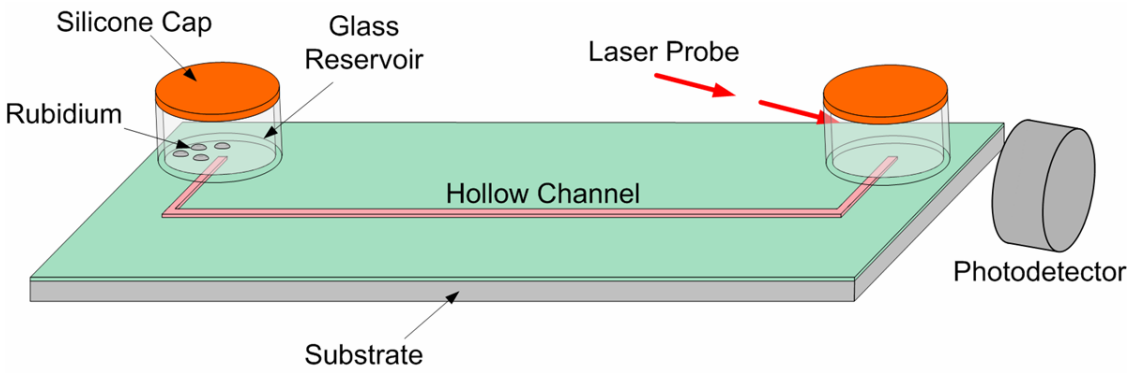

Figure 5. 3 Test platform for measuring rubidium absorption in empty vapor cell connected to rubidium filled vapor cell through hollow channel.

For the experiment a laser was probed through the vapor cell that rubidium was not placed in. Figure 4.3 shows the experiment platform. Absorption was detected on the output of the vapor cell as seen in Figure 4.4. This showed the rubidium vapor traveled through the small dimensions of the hollow channel.

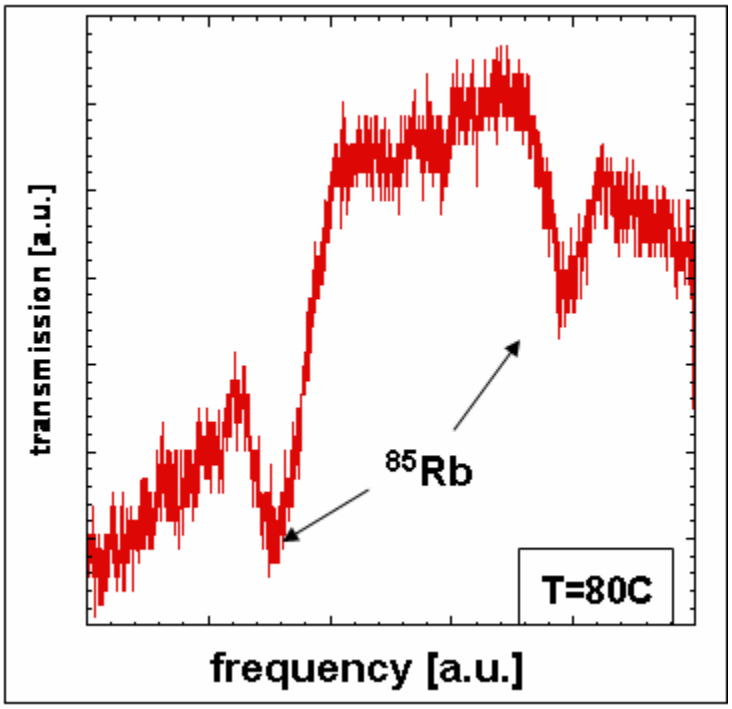

Figure 5. 4 Measured absorption peaks in the empty vapor cell connected to rubidium filled vapor cell through hollow channel.

5.3 Absorption Spectroscopy in ARROW

The next experiment probed through the ARROW channel integrated with rubidium atoms to look for absorption dips. The devices used for testing were fabricated using the ARROW fabrication techniques discussed in Section 2.2. After the ARROW devices were ready a vapor cell was epoxied to an open end of the ARROW as discussed in Section 3.4. The devices were tested by coupling the laser into the solid core waveguide. After passing through the solid core the laser light passed through the solid to hollow core interface. Once in the hollow core waveguide the light interacted with the rubidium atoms. The light propagated out of the hollow core and back into a solid core waveguide. A detector placed on the opposite end of the device detected the light coming

out. Figure 4.5 shows the experiment platform used. Figure 4.6 shows the absorption spectrum of the rubidium D_2 line around 780 nm. Both the ^{85}Rb and ^{87}Rb absorption peaks are visible.

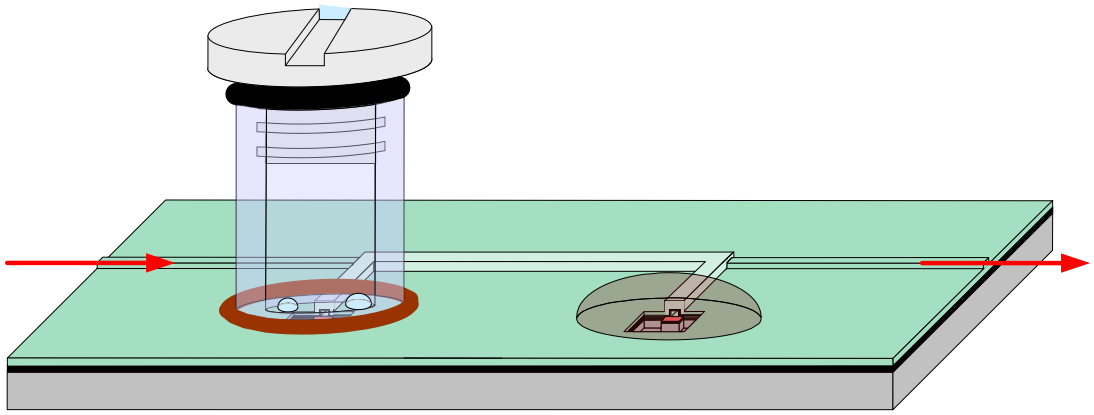

Figure 5. 5 Absorption spectroscopy setup using the ARROW.

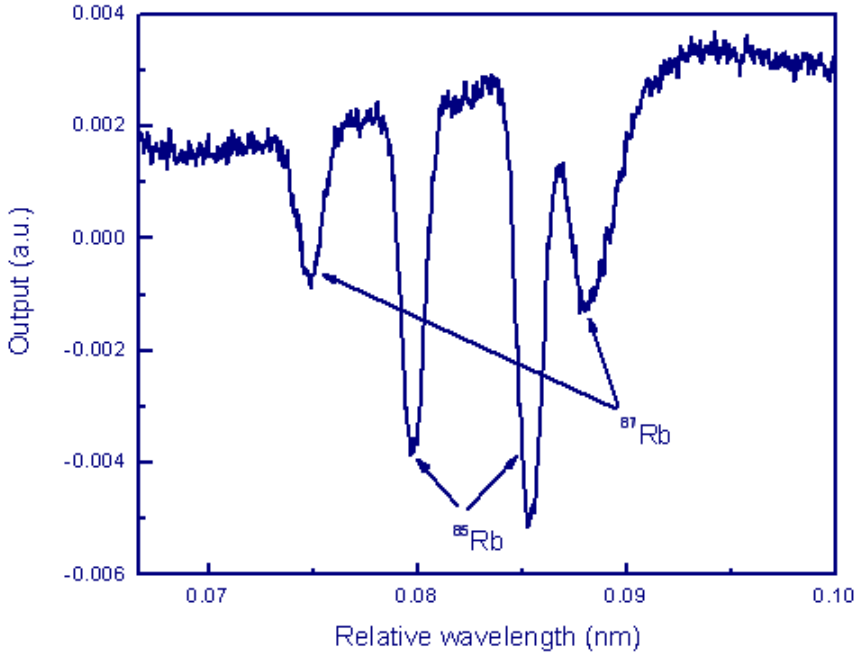

Figure 5. 6 Absorption spectrum from the rubidium vapor filled ARROW.

5.4 Temperature Dependence in ARROW

The temperature dependence of the rubidium absorption in the ARROW's hollow core followed the same trend as the absorption in a bulk cell. Figure 4.7 shows the temperature dependence of rubidium absorption in ARROWs compared to the dependence in a bulk cell. The figures were compiled by first recording absorption spectrums for different temperatures. A single absorption peak was then selected to do the calculations with, the inset in Figure 4.7 shows the peak selected. In this case the peak with the highest frequency near the D_2 transition was selected. For every temperature the far-resonant, I_0, and the on-resonant, I_1, output values were obtained. I_1 and I_0 are related by Equation 1:

$$I_1 = I_0 * \exp(-\alpha * L). \quad (1)$$

In the equation α is the absorption coefficient and L is the ARROW hollow core length. Using Equation 3 and the measured values of I_1 and I_0, α is calculated. Theoretically,

$$\alpha = N * \sigma. \quad (3)$$

In Equation 3, N is the density of rubidium atoms in the cross section and σ is the absorption cross section, which is calculated theoretically. Using, the calculated value of σ and the previously obtained value for α, the density of rubidium atoms in the ARROW is calculated and plotted (Figure 4.7).

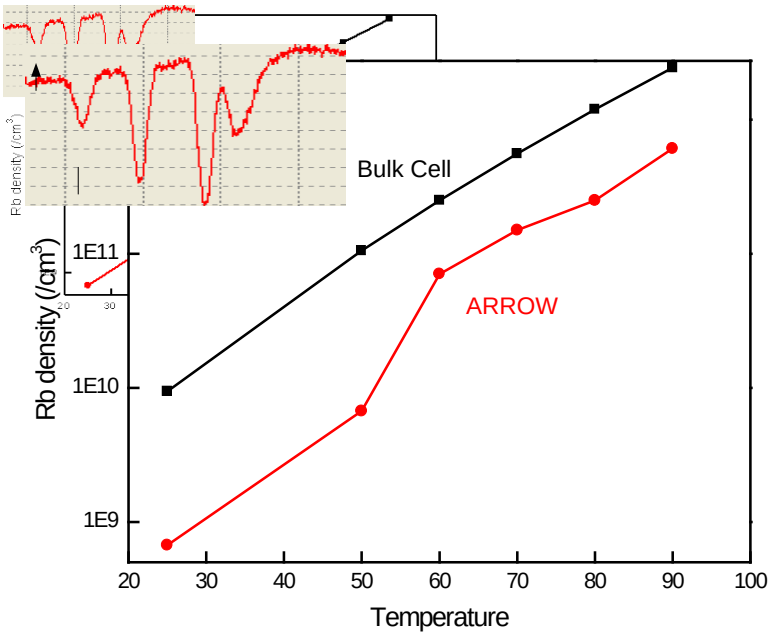

Figure 5. 7 The temperature dependence of rubidium atoms in ARROWs and bulk cells.

High optical densities were measured in the ARROW. Equation 4 shows how the optical density is obtained:

$$OD = \alpha * L. \tag{4}$$

Using the far-resonant, I_0, and the on-resonant, I_1, output values with Equation 1 gives the optical density. For temperatures above 80 C an optically dense medium can be created with optical densities as high as 2.14. With optical densities this high the ARROW device has potential for detecting nonlinear quantum coherence effects [13].

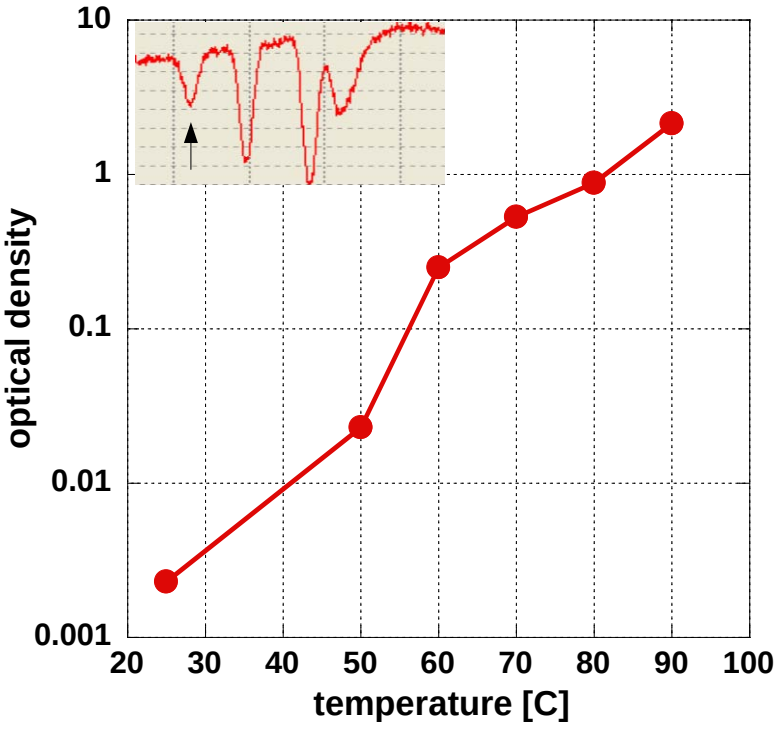

Figure 5. 8 The optical density of rubidium vapor as a function of temperature in an ARROW device.

5.5 Detection of 90 Degree Scattering in ARROW

To show the effective use of the solid core waveguide which intersects the hollow core ARROW a scattering measurement was taken. A probe beam coupled onto the chip into one of the intersecting solid core waveguides. The beam propagated through the solid core waveguide and crossed through the hollow core device. A photodetector detected the output from the solid core waveguide which couples directly into the hollow core waveguide. Light propagating through the hollow core coupled into this solid core waveguide and was detected. The light detected by the photodetector scattered 90 degrees in the ARROW. The output spectrum shows the rubidium absorption dips, showing that

the light did travel through the rubidium-filled hollow core. The intersecting waveguide is essential for use in resonant fluorescence detection, simplified Doppler-free spectroscopy, and parametric generation.

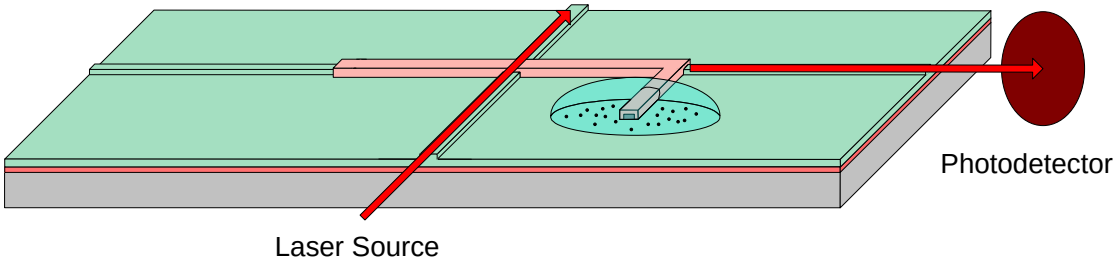

Figure 5. 9 The test setup for the scattering measurement.

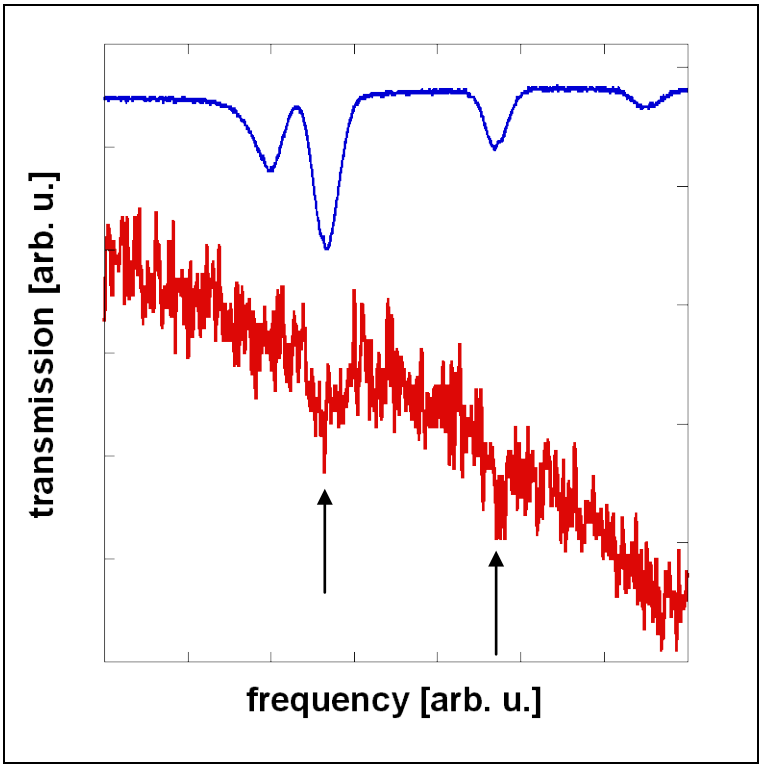

Figure 5. 10 The output spectrum of light which scattered 90 degrees in the ARROW. The rubidium absorption peaks of ^{85}Rb are visible.

5.6 Saturation Absorption Spectroscopy in ARROW

The device for the saturation absorption spectroscopy measurement was fabricated in the same way as the device for the absorption spectroscopy. A stainless steel standoff was modified and epoxied over one of the channel openings of the ARROW. Epoxy placed over the other opening sealed the hollow channel. In the helium filled glovebox rubidium was transferred to the stainless standoff, which was sealed off with a screw and o-ring. A single external cavity diode laser tuned to 780 nm was split into two beams, a pump and a probe beam. The pump beam was approximately twenty times more intense than the probe beam. These beams were coupled onto the chip on opposite sides and propagated in opposite directions through the rubidium vapor filled hollow core (Figure 4.11). This setup follows the typical setup for saturation absorption spectroscopy shown in Figure 1.5 and discussed in Section 1.2.4.

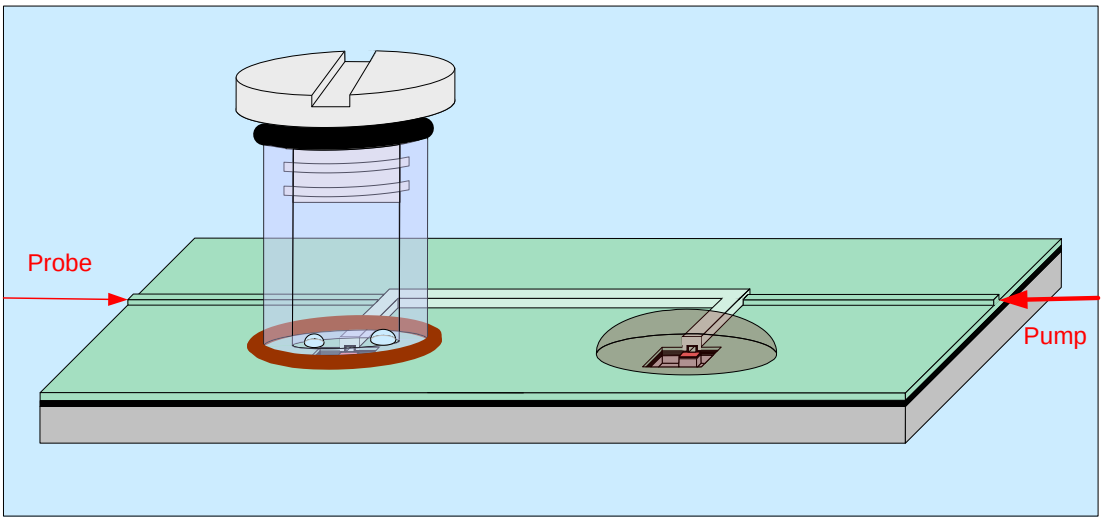

Figure 5. 11 Setup for the saturation absorption spectroscopy easurement.

As expected the more intense pump beam saturated the transitions. The probe beam saw Lamb dips characteristic of saturated absorption spectroscopy. Figure 4.12 shows the absorption of the probe beam as a function of frequency with the pump beam both on and off. When the probe is turned on the Lamb dips are present. The saturated absorption spectrum does not show all of the hyperfine transitions shown in the plot in Figure 1.7. Unfortunately, in the ARROW device most of the Lamb dips were overwhelmed by the absorption peaks.

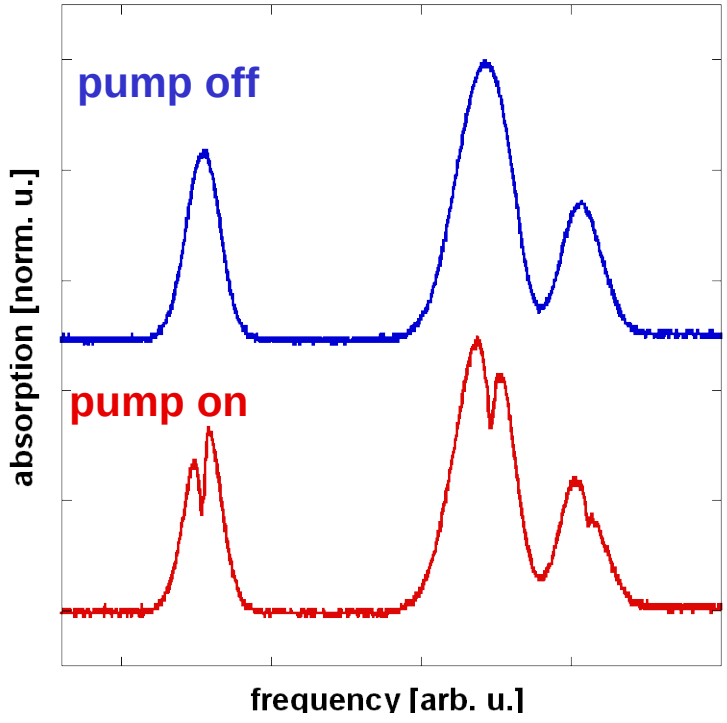

Figure 5. 12 Absorption spectrum with the pump beam turned on and off. When the pump beam is on saturated absorption spectroscopy's characteristic Lamb dips are present.

6 Conclusions

6.1 Summary

Miniaturization and simplification of quantum interference investigation can be accomplished using hollow ARROW waveguide platforms. Using the ability to seal vapor cells onto planar waveguides, rubidium vapor can be integrated into the hollow waveguides. Through experimentation, epoxies were able to seal the atomic vapor cells onto the platform. Further tests showed the effectiveness of rubidium transferring through the length of the waveguide and thus the effectiveness of the channels in containing an atomic vapor. Atomic absorption spectroscopy through the hollow waveguide showed the rubidium absorption peaks around the D_2 line. Further analysis of the absorption peaks revealed a high density of rubidium atoms in the hollow core, which corresponded to a high optical density. Scattering measurements showed the versatility of the planar device setup. Finally, saturated absorption spectroscopy measurements showed the hollow core ARROW was suitable for a common precision spectroscopy application.

6.2 Future Work

Improvement on the ARROW integrated atomic vapor cell platform in the near future will focus on three main areas. The first is finding better self assembling monolayer coatings. No coatings were consciously deposited on the walls of the hollow

cores in the devices fabricated for the absorption measurements. It is believed that the epoxy used to seal the channel and to attach the stainless standoff outgassed and coated the walls. However, this coating failed once the device was heated above 100 C. Other work must be done to decrease the buffer gas pressure in the cell. With the current fabrication technique the buffer gas pressure can not be adjusted. The pressure of the hollow core is equivalent to the pressure in the glovebox when it is sealed. The glovebox is typically kept at a pressure higher than 760 Torr to ensure that oxygen does not leak in. The higher pressure in the core increases broadening of the absorption peaks. Also, the lifetime of the devices is relatively short. New means of sealing the rubidium into the cell will have to be employed to increase the lifetime.

References

[1] S. Knappe, V. Gerginov, P. D. D. Schwindt, V. Shah, H. G. Robinson, L. Hollberg and J. Kitching, "Atomic vapor cells for chip-scale atomic clocks with improved long-term frequency stability," *Opt. Lett.*, vol. 30, pp. 2351, 2005.

[2] F. Benabid, G. Antonopoulos, J. C. Knight and P. St. J. Russell, "Stokes amplification regimes in quasi-cw pumped hydrogen-filled hollow-core photonic crystal fiber," *Phys. Rev. Lett.*, vol. 95, pp. 213903, 2005.

[3] T. W. Hansch, J. Alnis, P. Fendel, M. Fischer, C. Gohle, M. Herrmann, R. Holzwarth, N. Kolachevsky, T. Udem and M. Zimmermann, "Precision spectroscopy of hydrogen and femtosecond laser frequency combs." *Philos. Transact. A Math Phys. Eng. Sci.*, vol. 363, pp. 2155-2163, 2005.

[4] W. Demtroder, *Laser Spectroscopy.*, 3rd ed. Springer, 2003.

[5] A. M. C. Dawes, L. Illing, S. M. Clark and D. J. Gauthier, "All-optical switching in rubidium vapor," *Science*, vol. 308, pp. 672, 2005.

[6] S. E. Harris, "Electromagnetically induced transparency," *Phys. Today*, vol. 50, pp. 36, 1997.

[7] M. D. Lukin, "Colloquium: Trapping and manipulating photon states in atomic ensembles," *Rev. Mod. Phys.*, vol. 75, pp. 457-472, 2003.

[8] L. V. Hau, S. E. Harris, Z. Dutton and C. H. Behrroozi, "Light speed reduction to 17 metres per second in an ultracold atomic gas," *Nature*, vol. 397, pp. 594, 1999.

[9] M. D. Eisaman, A. Andre, F. Massou, M. Fleischhauer, A. S. Zibrov and M. D. Lukin, "Electromagnetically induced transparency with tunable single-photon pulses," *Nature*, vol. 438, pp. 837-841, 2005.

[10] L. Liew, S. Knappe, J. Moreland, H. Robinson, L. Holberg and J. Kitching, "Microfabricated alkali atom vapor cells," *Appl. Phys. Lett.*, vol. 84, pp. 2694, 2004.

[11] H. Schmidt and A. R. Hawkins "Electromagnetically induced transparency in alkali atoms integrated on a semiconductor chip", *Appl. Phys. Lett,* vol. 86, pp. 032106, 2005.

[12] H. Schmidt, D. Yin, W. Yang, D. B. Conkey, J. P. Barber, A. R. Hawkins, B. Wu "Towards Integration of quantum interference in alkali atoms on a chip", *Proceedings of the SPIE* 6130, 2006, pp. 1-11.

[13] W. Yang, D. B. Conkey, R. Brenning, A. R. Hawkins, and H. Schmidt "Atomic Spectroscopy on a Chip", In review *Nature Photonics.*

[14] D. Yin, A. R. Hawkins, and H. Schmidt, "Design of integrated hollow-core waveguides for EIT on a chip," presented *at OSA Annual Meeting,* Tucson, AZ, October 15-20, 2005.

[15] H. Schmidt, D. Yin, W. Yang, D. B. Conkey, J. P. Barber, A. R. Hawkins, "Towards integration of quantum interference in alkali atoms on a chip," SPIE Photonics West, January 23-25, San Jose, CA, 2006.

[16] W. Yang, D. Yin, B. Wu, H. Schmidt, D. B. Conkey, E. J. Lunt, A. R. Hawkins, "Monolithically integrated atomic vapor cell for quantum optics on a chip," 90th OSA Annual Meeting, October 8-12, Rochester, NY, 2006.

[17] D.B. Conkey, R.L. Brenning, A.R. Hawkins, W. Yang, B. Wu, H. Schmidt, "Microfabrication of integrated atomic vapor cells," Photonics West, January 20-25, San Jose, CA, 2007.

[18] H. Schmidt, W. Yang, B. Wu, D. Yin, D. B. Conkey, J. Hulbert, and A. R. Hawkins, "Rubidium spectroscopy on a chip," Invited talk, Photonics West, January 20-25, San Jose, CA, 2007.

[19] J. P. Marangos, "Topical review: Electromagnetically induced transparency," *J. Modern Optics,* vol. 45, pp. 471-503, 1998.

[20] Y. Li and M. Xiao, "Electromagnetically induced transparency in a three-level Λ-type system in rubidium atoms," *Phys. Rev. A,* vol. 51, pp. R2703-R2706, 1995.

[21] M. A. Bouchiat and J. Brossel, "Relaxation of optically pumped Rb atoms on paraffin-coated walls," *Phys. Rev.,* vol. 147, pp. 41-54, 1966.

[22] H. G. Robinson and C. E. Johnson, "Narrow 87Rb hyperfine-structure resonances in an evacuated wall-coated cell," *Appl. Phys. Lett.,* vol. 40, pp. 771-773, 1982.

[23] M. Klein, I. Novikova, D. F. Phillips and R. L. Walsworth, "Slow light in paraffin-coated Rb vapor cells," *J. Modern Optics,* vol. 53, pp. 2583-2591, 2006.

[24] S. Ghosh, J. E. Sharping, D. G. Ouzounov and A. L. Gaeta, "Resonant optical interactions with molecules confined to hollow core photonic band-gap fibers," *Phys. Rev. Lett.,* vol. 94, pp. 093902, 2005.

[25] S. Knappe, V. Velichansky, H. Robinson, L. Liew, J. Moreland, J. Kitching and L. Holberg, "Atomic vapor cells for miniature frequency references," in *2003 IEEE International Frequency Control Symposium and PDA Exhibition Jointly with the 17th European Frequency and Time Forum,* 2003, pp. 31-32.

[26] S. Knappe, P. D. D. Schwindt, V. Gerginov, V. Shah, H. G. Robinson, L. Hollberg and J. Kitching, "Microfabricated atomic clocks and magnetometers," in *Proceeding of the 17th International Conference on Laser Spectroscopy,* 2005, pp. 1-10.

[27] R. Thapa, K. Knabe, M. Faheem, A. Naweed, O. L. Weaver and K. L. Corwin, "Saturated absorption spectroscopy of acetylene gas inside large-core photonic bandgap fiber," *Opt. Lett.,* vol. 31, pp. 2489-2491, 2006.

[28] S. Ghosh, A. R. Bhagwat, C. K. Renshaw, S. Goh and A. L. Gaeta, "Low-light-level optical interactions with rubidium vapor in a photonic band-gap fiber," *Phys. Rev. Lett.,* vol. 97, pp. 023603, 2006.

[29] M. A. Duguay, Y. Kokubun and T. L. Koch, "Antiresonant reflecting optical waveguides in SiO2-Si multilayer structures," *Appl. Phys. Lett.,* vol. 49, pp. 13-15, 1986.

[30] J. P. Barber, "Fabrication of hollow optical waveguides on planar substrates," dissertation, 2006.

[31] J. P. Barber, D. B. Conkey, J. R. Lee, N. B. Hubbard, L. L. Howell, D. Yin, H. Schmidt and A. R. Hawkins, "Fabrication of hollow waveguides with sacrificial aluminum cores," *IEEE Photon. Tech. Lett.,* vol. 17, pp. 363, 2005.

[32] N. B. Hubbard, L. L. Hubbard, J. P. Barber, D. B. Conkey, A. R. Hawkins and H. Schmidt, "Structural models and design rules for on-chip micro-channels with sacrificial cores," *J. Micromech. Microeng.,* vol. 15, pp. 720-727, 2005.

[33] H. Schmidt, D. Yin, J. P. Barber and A. R. Hawkins, "Hollow-core waveguides and 2D waveguide arrays for integrated optics of gases and liquids," *IEEE J. Sel. Top. Quant. Electron.,* vol. 11, pp. 519, 2005.

[34] D. Yin, J. P. Barber, E. J. Lunt, A. R. Hawkins and H. Schmidt, "Optical characterization of arch-shaped ARROW waveguides with liquid cores," *Optics Express,* vol. 13, pp. 10566-10570, 2005.

[35] J. P. Barber, E. J. Lunt, Z. A. George, D. Yin, H. Schmidt and A. R. Hawkins, "Integrated hollow waveguides with arch-shaped cores," *IEEE Photon. Tech. Lett.,* vol. 18, pp. 28-30, 2006.

[36] D. Yin, J. P. Barber, A. R. Hawkins and H. Schmidt, "Waveguide loss optimization in hollow-core ARROW waveguides," *Optics Express*, vol. 13, pp. 9331-9336, 2005.

[37] S. Briaudeau, D. Bloch and M. Ducloy, "Sub-Doppler spectroscopy in a thin film of resonant vapor," *Phys. Rev. A*, vol. 59, pp. 3723-3735, 1999.

[38] J. C. Camparo, "Alkali <I-S> wall relaxation in dichlorodimethylsilane coated resonance cells," *J. Chem. Phys.*, vol. 88, pp. 1533-1539, 1987.

[39] C. R. Kessel and S. Granick, "Formation and Characterization of a Highly Ordered and Well-Anchored Alkylsilane Monolayer on Mica by Self-Assembly," *Langmuir*, vol. 7, pp. 532-538, 1991.

APPENDIX

APPENDIX A Process Flow

This appendix describes the general process for fabrication of hollow ARROW waveguides. The optional step includes a raised silicon pedestal etch before waveguide formation. The bulk of this flow comes from John Barber. More information on the ARROW fabrication process can be found in his dissertation [30].

1) (Optional) Pedestal process:
    a. Pattern SU8 using the pedestal etch mask with a target thickness of 10 μm.
    b. Oxygen plasma descum for 90 seconds.
    c. Perform an RIE silicon etch using CF_4 gas in the Anelva DEM-451 machine for 50 minutes.
    d. Perform a 5 minute oxygen plasma descum.
    e. Remove SU-8 residue in Nano-Strip at 90°C for 60 minutes, followed by a DI water rinse.
    f. Measure pedestal height and width using the profilometer. If incorrect, scrap the wafer and start over, adjusting the etch time as needed. The correct height should be equal to the total thickness of all PECVD deposited top layers.
2) Remove native oxide in HF or buffered oxide etch (BOE), 1 minute or until the wafer dewets, followed by a DI water rinse.
3) Bottom dielectric layer deposition:

a. Clean and season both PECVD chambers for the appropriate film type.
b. Place a bare silicon test wafer in the PECVD chamber and deposit a test film (1 minute, 45 second deposition for oxide, 10 minute deposition for nitride).
c. Measure the test wafer using the ellipsometer and calculate the film growth rate.
d. For nitride, adjust the refractive index of the film by changing the ammonia (NH_3) flow rate. An increased ammonia flow lowers the refractive index. Run more test wafers as necessary to achieve the desired refractive index.
e. Place the wafer in the PECVD chamber and deposit the desired film using the measured growth rate from above to calculate the correct deposition time.
f. Blow particles off of the wafer with a nitrogen gun and perform an SC-1 clean to remove remaining particles.
g. Repeat steps a through f for each required dielectric layer.

4) Deposit and pattern the sacrificial core using the appropriate process for SU-8.
5) Perform a 1 minute oxygen plasma descum.
6) Deposit the upper dielectric layers using the process in step 4 above, but omit the SC-1 clean between layers.
7) Solid-core waveguide formation:
    a. Pattern SU-8 with a target thickness of 5 μm using the appropriate mask.
    b. Perform a 1 minute oxygen plasma descum.

c. Perform an RIE oxide etch in the Anelva DEM-451 for 9 minutes.

8) Core expose etch:
    a. Do a 2 minute oxygen plasma descum followed by a Nano-Strip etch at 90°C for 30 minutes and a DI water rinse.
    b. Pattern SU-8 with a target thickness of 10 μm using the appropriate mask.
    c. Perform a 1 minute oxygen plasma descum.
    d. Perform an RIE oxide etch in the Anelva DEM-451 for 45 minutes.
    e. Perform a 5 minute oxygen plasma descum.
9) Place wafer in Nano-Strip etchant to remove the sacrificial core material
    a. Hotplate temperature should be 90°C for Nano-Strip
    b. Nano-Strip should be replaced every 24-48 hours with fresh solution. Care must be taken during the core removal etch to avoid breaking the waveguides. Slowly siphon off the old acid without disturbing the wafer.
10) Carefully remove the etchant from the beaker and rinse the waveguides with DI water 6 times by slowly adding water, gently agitating, and draining the water. After rinsing, soak the pieces in DI water for 24 hours, followed by 2 more DI water rinses. Dry the waveguides by placing the beaker on a hotplate at 90°C for 30 minutes or until the remaining water has evaporated.
11) Inspect the waveguides using a microscope and cleave as desired.

APPENDIX B ARROW Designs

The ARROW designs presented in this appendix are specifically designed for air-core ARROWs where the index of the core is 1. Occasionally the design must be redesigned because of new PECVD growth conformalities. The PECVDs have different growth rates in the vertical and horizontal directions. Conformality is measured as a ratio between the vertical growth rate and the horizontal growth rate. The two older designs (Tables B.3 and B.4) were designed for an oxide conformality of 1.4. The newer designs (Tables B.1 and B.2) have a conformality of 1.32.

Table B. 1 The ARROW design for a pedestal ARROW with oxide conformality 1.32.

Specifications		Layer Structure	
		Layer	Thickness (nm)
Wavelength	780 nm	Oxide 6	3020
Core	Air	Nitride 6	100
Core Shape	Rectangle	Oxide 5	140
Nitride Index	2.10	Nitride 5	260
		Oxide 4	220
Conformality (Vertical : Horizontal)		Nitride 4	270
Nitride	1.2	Core	5 μm
Oxide	1.32	Nitride 3	106
Pedestal		Oxide 3	548
		Nitride 2	106
		Oxide 2	548
Designed February 2007		Nitride 1	106
		Oxide 1	548
		Substrate	-

Table B. 2 The ARROW design for a regular ARROW with oxide conformality 1.32.

Specifications		Layer Structure	
		Layer	Thickness (nm)
Wavelength	780 nm	Oxide 6	3040
Core	Air	Nitride 6	392
Core Shape	Rectangle	Oxide 5	308
Nitride Index	2.10	Nitride 5	120
		Oxide 4	216
Conformality (Vertical : Horizontal)		Nitride 4	250
Nitride	1.2	Core	5 µm
Oxide	1.32	1.2	106
Regular		1.32	548
		Nitride 2	106
		Oxide 2	548
Designed February 2007		Nitride 1	106
		Oxide 1	548
		Substrate	-

Table B. 3 The ARROW design for a pedestal ARROW with oxide conformality 1.4.

Specifications		Layer Structure	
		Layer	Thickness (nm)
Wavelength	780 nm	Oxide 6	4178
Core	Air	Nitride 6	90
Core Shape	Rectangle	Oxide 5	124
Nitride Index	2.10	Nitride 5	134
		Oxide 4	110
Conformality (Vertical : Horizontal)		Nitride 4	352
Nitride	1.2	Core	5.8 µm
Oxide	1.4	Nitride 3	111
Pedestal		Oxide 3	546
		Nitride 2	111
		Oxide 2	546
Designed January 2006		Nitride 1	111
		Oxide 1	546
		Substrate	-

Table B. 4 The ARROW design for a regular ARROW with oxide conformality 1.4.

Specifications		Layer Structure	
		Layer	Thickness (nm)
Wavelength	780 nm	Oxide 6	3402
Core	Air	Nitride 6	139
Core Shape	Rectangle	Oxide 5	379
Nitride Index	2.10	Nitride 5	162
		Oxide 4	216
Conformality (Vertical : Horizontal)		Nitride 4	303
Nitride	1.2	Core	5.8 μm
Oxide	1.4	Nitride 3	110
Regular		Oxide 3	550
		Nitride 2	110
		Oxide 2	550
Designed January 2006		Nitride 1	110
		Oxide 1	550
		Substrate	-

APPENDIX C Publications

Archival Journal Publications

1. W. Yang, D. B. Conkey, R. Brenning, A. R. Hawkins, and H. Schmidt, “Atomic Spectroscopy on a Chip”, In review *Nature Photonics*

2. H. Schmidt, D. Yin, W. Yang, D. B. Conkey, J. P. Barber, A. R. Hawkins, B. Wu, "Towards Integration of quantum interference in alkali atoms on a chip", *Proceedings of the SPIE* 6130, pp. 1-11, 2006.

3. B. A. Peeni, D. B. Conkey, J. P. Barber, R. Kelly, M. L. Lee, A. T. Wooley, and A. R. Hawkins, "Planar Thin Film Device for Capillary Electrophoresis", *Lab on a Chip,* vol. 5, pp.501-505, 2005.

4. N.B. Hubbard, L.L. Howell, J.P. Barber, D.B. Conkey, A.R. Hawkins, and H. Schmidt, "Mechanical models and design rules for on-chip micro-channels with sacrificial cores", *J. of Micromech. Microeng.*, vol. 15, pp. 720-727, 2005.

5. J.P. Barber, D.B. Conkey, J.R. Lee, N.B. Hubbard, L.L. Howell, H. Schmidt, and A.R. Hawkins, "Fabrication of Hollow Waveguides with Sacrificial Aluminum Cores,” *IEEE Phot. Tech. Lett., vol 17*, pp. 363-365, 2005.

Conference Publications

1. D.B. Conkey, R.L. Brenning, A.R. Hawkins, W. Yang, B. Wu, H. Schmidt, "Microfabrication of integrated atomic vapor cells," Photonics West, January 20-25, San Jose, CA, 2007.

2. H. Schmidt, W. Yang, B. Wu, D. Yin, D.B. Conkey, J. Hulbert, and A.R. Hawkins, "Rubidium spectroscopy on a chip", Invited talk, Photonics West Conference, San Jose, CA, Jan 21-25, 2007.

3. W. Yang, D. Yin, B. Wu, H. Schmidt, D. B. Conkey, E. J. Lunt, A. R. Hawkins, "Monolithically Integrated Atomic Vapor Cell for Quantum Optics on a Chip," 90th OSA Annual Meeting, October 8-12, Rochester, NY, 2006.

3 spaces before and after figures/tables and their caption

4. H. Schmidt, D. Yin, W. Yang, D. B. Conkey, J. P. Barber, A. R. Hawkins, "Towards integration of quantum interference in alkali atoms on a chip," SPIE Photonics West, January 23-25, San Jose, CA, 2006.

5. J. P. Barber, D. B. Conkey, M. M. Smith, J. R. Lee, B. A. Peeni, Z. A. George, A. R. Hawkins, D. Yin, and H. Schmidt, "Hollow waveguides on planar substrates with selectable geometry cores," Conference on Lasers and Electro-Optics/International QUantum Electronics Conference, May 22-25, Baltimore, MD, 2005.

6. B. A. Peeni, D. B. Conkey, A. T. Woolley, M. L. Lee, and A. R. Hawkins, "Electro-osmotic Pumps Constructed Using Sacrificial Etching," 28th International Symposium on Capillary Chromatography and Electrophoresis, May 22-25, Las Vegas, NV, 2005.